BRNO UNIVERSITY OF TECHNOLOGY

VYSOKÉ UČENÍ TECHNICKÉ V BRNĚ

CENTRAL EUROPEAN INSTITUTE OF TECHNOLOGY BUT

STŘEDOEVROPSKÝ TECHNOLOGICKÝ INSTITUT VUT

UTILIZATION OF POROUS ANODIC ALUMINA FOR FABRICATION OF NANOSTRUCTURED LAYERS AND THEIR PHOTOELECTROCHEMICAL AND OPTICAL APPLICATIONS

VYUŽITÍ PORÉZNÍ ALUMINY PRO PŘÍPRAVU NANOSTRUKTUROVANÝCH VRSTEV A JEJICH FOTOELEKTROCHEMICKÉ A OPTICKÉ APLIKACE

DOCTORAL THESIS
DIZERTAČNÍ PRÁCE

AUTHOR AUTOR PRÁCE	Ing. Tomáš Lednický
SUPERVISOR ŠKOLITEL	Dr.techn. Ing. Mária Bendová

BRNO 2021

ABSTRACT

Porous anodic alumina (PAA) is an oxide layer formed by anodic oxidation of aluminium. In addition to its vast industrial use, its popularity has exponentially expanded into the field of nanotechnology due to the discovery of the self-ordering growth of PAA, leading to a honeycomb-like nanostructure. Together with a simple fabrication and tuneable properties, PAA represents an inexpensive alternative to the nanoscale world. In the same spirit, this PhD thesis deals with methods utilizing the PAA to fabricate functional nanostructures.

The first part of the thesis is focused on the PAA-assisted formation of titanium dioxide (TiO_2) nanocolumn arrays and their possible application as photoanodes for the water-splitting reaction. TiO_2 nanocolumns are formed by anodisation of superimposed Al layer over titanium substrate being so-called ‘PAA-assisted anodisation’. The present study demonstrates the electrochemical properties and photoelectrochemical performance of nanocolumns formed from nitrogen-enriched substrates modified by various thermal treatments. The major finding was that their hollow morphology causes their poor performance. This issue was addressed by developing a novel anodising strategy that originates from the extensive study of anodising parameters and their effect on the morphology and stability of nanocolumns.

The second part demonstrates the fabrication of well-ordered gold nanoparticles (AuNPs) on a transparent substrate as a localized surface plasmon resonance (LSPR) sensor element. A key-stone of this multidisciplinary method is a combination of a self-ordering behaviour of PAA that produces the template for controlled solid-state dewetting (SSD) of a subsequently deposited thin film of gold. This work includes the detailed technical aspects of complete fabrication, starting with the template production from an aluminium sheet to forming AuNPs and their transfer to a transparent substrate. This part is concluded with the characterization of fabricated AuNP nanocomposites with a practical comparison of their bulk refractive index sensitivity and stability in time. Results show this large-scale and inexpensive technique can easily compete with other, more demanding, AuNP fabrication technologies.

KEYWORDS

porous anodic alumina, fabrication, nanostructures, titanium dioxide, gold nanoparticles, photoelectrochemistry, localized surface plasmon resonance.

ABSTRAKT

Porézní anodická alumina (PAA) je oxidová vrstva vytvořená anodickou oxidací hliníku, která má široké průmyslné využití. Její popularita zaznamenala exponenciální nárůst zejména v oblasti nanotechnologií, k čemu přispělo objevení jejího samouspořádání do struktury o nanorozměrech připomínající včelí plástev. Její jednoduchá příprava a laditelné vlastnosti z ní tvoří levný způsob výroby nanostruktur. Ve stejném duchu se tato disertační práce zabývá metodami přípravy funkčních nanostruktur za využití PAA.

První část je zaměřena na výrobu pole nanosloupců z oxidu titaničitého (TiO_2) a jejich možné použití jako fotoanody pro štěpení vody. TiO_2 nanostloupce jsou tvořeny anodizací hliníkové vrstvy na titanovém substrátu, také nazývanou PAA-asistovaná anodizace. Táto studie demonstruje elektrochemické vlastnosti a fotoelektrochemickou aktivitu nano sloupců vytvořených z dusíkem obohacených substrátů, které byly následně různě termálně modifikovány. Hlavním poznatkem studie je, že špatné vlastnosti jsou způsobeny dutou morfologií nanosloupců. Tento poznatek vedl k rozsáhle studii zabývající se dopadem anodizačných podmínek na morfologii ale i stabilitu vytvořených nanosloupců, jejímž výsledkem byla nová strategie anodizace.

Druhá část prezentuje výrobní proces přípravy uspořádané vrstvy zlatých nanočástic na transparentním substrátu pro jejich použití jako optického senzoru využívající efekt rezonance lokalizovaných povrchových plasmonů. Základem této multidisciplinární metody je využití kombinace samouspořádání PAA k výrobě šablony a následného procesu řízeného smáčení v pevné fázi tenké vrstvy zlata. Táto práce detailně popisuje technologické aspekty přípravy; od samotné výroby šablon z hliníku, přes vytváření zlatých nanočástic, až po jejich přenos na transparentní substrát. Na závěr této práce jsou kompozity z nanočástic charakterizovány, přičemž je porovnána jejich citlivost na změnu indexu lomu okolí a jejich stálost. Ze závěrů vyplývá, že tato poměrně velkoplošná a levná metoda je konkurence schopná i v oblasti senzorické citlivosti.

KLÍČOVÁ SLOVA

porézní anodická alumina, výroba, nanostruktury, oxid titaničitý, zlaté nanočástice, photoelektrochemie, rezonance lokalizovaných povrchových plasmonů.

LEDNICKÝ, Tomáš. *Utilization of porous anodic alumina for fabrication of nanostructured layers and their photoelectrochemical and optical applications*. Brno, 2021. Available also at: https://www.vutbr.cz/studenti/zav-prace/detail/135699. Doctoral Thesis. Vysoké učení technické v Brně, Středoevropský technologický institut VUT, Central European Institute of Technology BUT. Supervisor Mária Bendová.

DECLARATION

I declare that I have written my doctoral thesis on the theme of "UTILIZATION OF POROUS ANODIC ALUMINA FOR FABRICATION OF NANOSTRUCTURED LAYERS AND THEIR PHOTOELECTROCHEMICAL AND OPTICAL APPLICATIONS" independently, under the guidance of the doctoral thesis supervisor and using the technical literature and other sources of information which are all quoted in the thesis and detailed in the list of literature at the end of the thesis.

As the author of the doctoral thesis I furthermore declare that, as regards the creation of this doctoral thesis, I have not infringed any copyright. In particular, I have not unlawfully encroached on anyone's personal and/or ownership rights and I am fully aware of the consequences in the case of breaking Regulation § 11 and the following of the Copyright Act No 121/2000 Sb., and of the rights related to intellectual property right and changes in some Acts (Intellectual Property Act) and formulated in later regulations, inclusive of the possible consequences resulting from the provisions of Criminal Act No 40/2009 Sb., Section 2, Head VI, Part 4.

Brno 30.04.2021 Ing. Tomáš Lednický

ACKNOWLEDGEMENT

I would like to express my gratitude to my supervisor Dr. Mária Bendová who gave me this opportunity. I am thankful for her supervision, kind attitude, support, and handful of patience while teaching me more systematic approach through my stubbornness. My sincere gratitude and enormous respect go to Dr. Attila Bonyár (BUTE, Hungary) who unconditionally joined this journey with his endless support, enthusiasm, and especially his never-ending trust in me. Moreover, I am profoundly grateful for his help on this work; his hard-working and humble attitude that has been always an ideal inspiration for me.

The results in this thesis reflect several collaborations I have been lucky to take part in. In addition to the one with Dr. Attila Bonyár, I am grateful to Prof. Achim Walter Hassel for his opportunity to do an internship in his group at Johannes Kepler University Linz. I would like to thank Dr. Andrei Ionut Mardare for his help with my integration during the stay, and Michael Pichler for his technical support. Moreover, I am grateful to Dr. Jan Macák for possibility to do some measurements in his labs in Pardubice, and even more to Dr. Miloš Krbal for doing them.

I would like to thank all my colleagues who not only helped me directly or indirectly but also created a joyful scientific ground for work. Namely, my friend Dr. Radim Zahradníček who was always ready to give all of his ideas, solutions and give his best in table tennis matches. Then, Dr. Ondřej Man for his useful consultations, Dr. Lukáš Flajšman, Dr. Alexandr Otáhal and Jakub Sadílek for their advice and broad technical help. This way I would also like to express my gratitude to CEITEC staff, members of the former Labsensnano research group, and especially members of Nano Research Infrastructure for doing their best to keep machines in the operating state and making the research more accessible.

Personally, I would like to thank Dr. Milena Setka who managed to survive few last years with me in the office and did not go crazy. For similar accomplishments and revision of this work, a big thanks goes to my friend and roommate Dr. Štepan Kuchař. I would like to thank all my friends for their enriching company outside of science and their persistent nagging about the period of my PhD study. Last but not least, from the bottom of my heart I would like to thank my family and especially my parents, who supported me from the very beginning.

I also thank the funding agencies who supported this work. The internship was supported by Erazmus+ program of European Union, part of the work was carried out with the support of CzechNanoLab infrastructure (ID LM2018110, MŠMT, 2020–2022), CEITEC Brno University of Technology, and part of the research leading to the presented results has been supported by the Czech Science Foundation (GAČR) project no. 15-23005Y.

Brno 30.04.2021 Ing. Tomáš Lednický

CONTENTS

PREFACE

Porous anodic alumina (PAA) has enchanted me already during my early years at the university, researching it for my bachelor and master thesis. Its beauty comes from its fascinating forming behaviour leading to a nanosized honeycomb-like structure. Its unique properties have attracted a lot of scientists trying to tame them for their benefit. There is no wonder, I accepted the opportunity to continue researching this area for my PhD degree.

This thesis summarizes two of such researches done during my PhD program. While each of them has a different application, both are experimental works focused on the fabrication of nanostructures utilizing the PAA. Despite the traditional approach, I decided to keep these topics separated to highlight the versatility of the PAA, and also to stress out the multidisciplinarity of the applications. The research done in the first part was supervised by Dr. Mária Bednová, while the research in the second part was done in the collaboration with Dr. Attila Bonyár.

In the process of writing, I did my best to underline the experimental aspect of the work. I tried to keep introduction and theory parts to minimum as it has been already done a thousand times, and rather refer to some of the excellent literature that has already done an excellent job. My intent was to focus more on the most recent state of the art, and give the maximum devotion to experimental parts. My aim was to objectively present all significant results regardless of their success character, and thus give the reader the full overview of development process including also dead ends and failed attempts. I believe this information is an inevitable part of scientific research that should not be omitted; or as sayings goes, ‘there is no light without darkness’.

Even though, some part of the research present in this thesis have been already published (list of publications), this thesis was written as an independent work with more detail result part. However, some studied done solely by my colleagues can be found only in the original publications if needed.

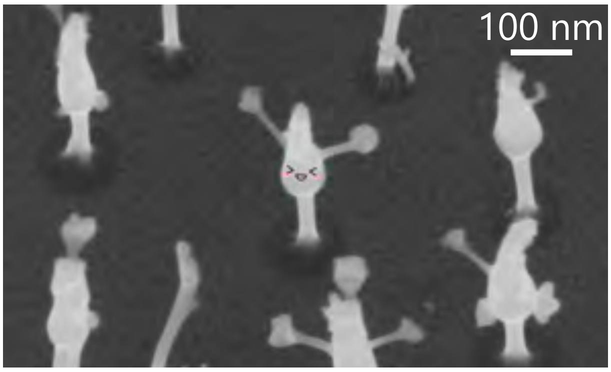

‘A picture is worth a thousand words.’

Frederick R. Barnard

Part I

Photoelectrochemistry on TiO_2 nanostructures

‘If nothing else works, then a total pig-headed unwillingness to look facts in the face will see us through.’

Blackadder Goes Forth
GENERAL MELCHETT

Introduction

In recent decades, modern society has realised the severity of upcoming economic problems related to the depletion of fossil fuels as well as the environmental and health impacts arising from fossil fuel combustion. Therefore, an enormous effort has been invested in finding and developing ecologically clean, energy-efficient, safe, sustainable, and viable technologies as an alternative to fossil fuels.

Since the beginning, hydrogen has received considerable attention as a promising next-generation energy carrier and a clean-burning fuel. However, even nowadays, there are many challenges, which complicate the utilisation and especially the commercialisation of hydrogen as an environmentally friendly substitution for fossil fuels.[1] Neglecting the significant issues concerning hydrogen storage and transport, current commercialised hydrogen production techniques suffer from a reliance on fossil fuel sources, harsh process conditions, and high costs.

Therefore, alternative methods that utilise renewable energy sources for hydrogen production, such as hydropower, wind power, or sunlight, have been explored during the last decades. Figure 1 shows a diagram representing hydrogen production pathways from renewable energy sources. Among these energies, hydrogen production from biomass is not considered a substantial source due to greenhouse gas generation as a by-product. Therefore, solar energy has been considered the most promising source due to its lesser location dependence than wind and hydropower energy.

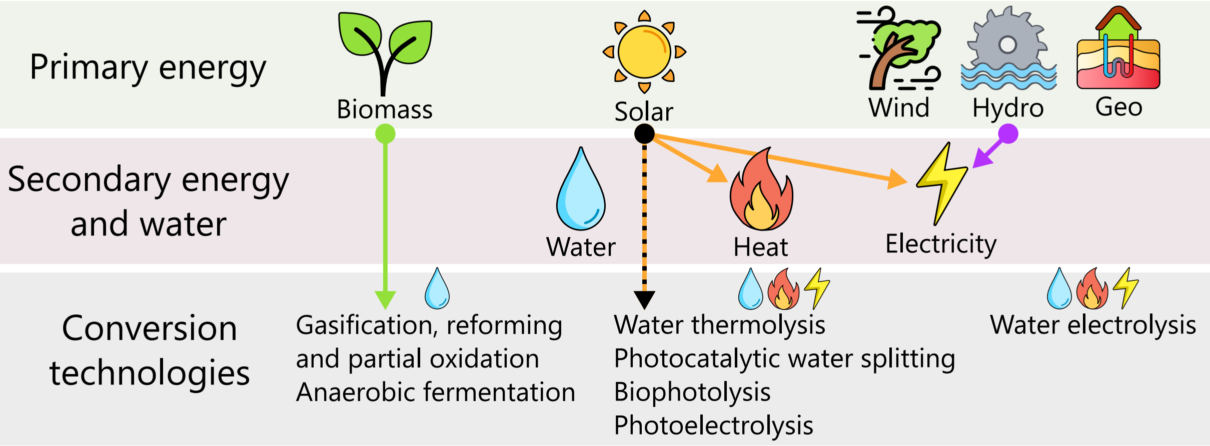

Figure 1: Main hydrogen production pathways from renewable energy sources. Modified according to ref. [2].

The combination of solar energy with plentiful water resources provides a good platform for hydrogen generation called solar water splitting. Hydrogen production via solar water splitting can be generally categorised into three types: 1) thermochemical water splitting, 2) photobiological water splitting, and 3) photocatalytic water splitting. The last is the most promising and investigated method of hydrogen production. Compared with the other two techniques, it has the following advantages: i) reasonable solar-to-hydrogen efficiency, ii) low process cost, iii) the ability to achieve separate hydrogen and oxygen evolution during the reaction, and iv) small reactor systems suitable for household applications, thus providing for excellent market potential.

Photocatalysis is defined as a chemical reaction induced by photo-irradiation in the presence of a photocatalyst. Such materials will facilitate chemical reactions without being consumed or transformed. The basic working principle of a simple photoelectrochemical cell (PEC) is illustrated in Figure 2:B. Here, TiO_2 (photocatalyst) represents the photoanode and Pt the counter electrode. The photoanode irradiation by light of energy greater than the bandgap of TiO_2 (n-type semiconductor) excites an electron from the valence band into the conduction band. This creates an electron (e^-)–hole (h^+) pair. We can help to split this pair by adding a potential bias. When an anodic potential is applied, these electrons migrate through the bulk to reach the Pt counter electrode, where they are used to reduce H^+ into H_2. Meanwhile, the holes which reach the interface between the TiO_2 surface and electrolyte can oxidise water, forming O_2 (illustrated in Figure 2:B2).

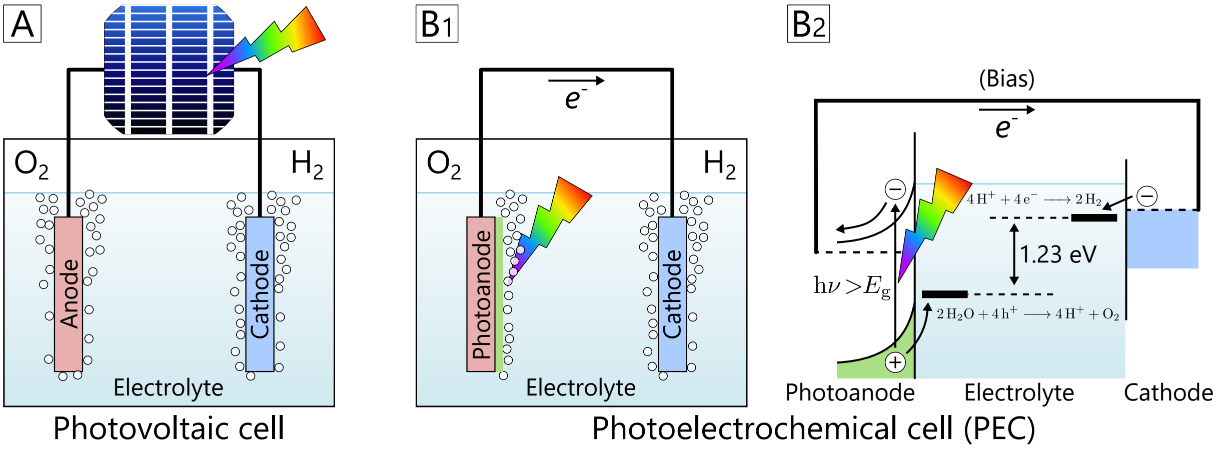

Figure 2: Schematic illustration of solar-driven electrochemical water splitting cells: (A) photovoltaic electrolysis, (B1) photoelectrochemical water splitting cell, and (B2) working principle of water splitting PEC with n-type semiconductor photoanode. Adapted and modified from ref. [3].

Here, the photocatalyst (photoanode) undeniably plays a crucial role as a photoelectrochemically active material. Therefore, uncompromising demands on material properties are required to be able to achieve a viable device. Similar to materials used in solar cells, photocatalyst should have a high quantum efficiency over the solar spectrum. This requires a narrow bandgap, high optical absorption, excellent internal quantum efficiency, and a sufficient transfer of charge carriers to the electrolyte. Additionally, photocatalysts need to support water splitting reactions and thus have to be chemically stable with suitable valence and conduction band energies to match the redox reactions.

Moreover, these materials usually need to have well-tuned structural parameters such as surface area, crystallinity, or particle size to achieve the maximum number of active sites for oxide evolution reaction (OER). Finally, they also should be inexpensive. The problem is that no known material or combination of materials meets all these requirements yet.

However, there are many promising material candidates which meet a part of the requirements. One of them is titanium dioxide (TiO_2), which is well known to be the most practical and prevalent photocatalyst, for it is chemically stable, abundant, nontoxic, and cost-effective. The appropriate electronic band structure and excellent surface activity endow TiO_2 with promising potential in hydrogen production, photovoltaics, photocatalysts, lithium-ion batteries, fuel cells, gas sensors, detoxification, and supercapacitors. These applications can be roughly divided into 'energy' and 'environmental' categories. Although TiO_2 possesses such a promising potential, its relatively poor charge transport property and wide bandgap (3.0–3.2 eV), which can utilise only a fraction of the available solar energy (5–7 %), are the two main limitations for its application in catalysis and energy harvesting.

Therefore, in recent years, many scientists dedicated their work to overcome these limits. It is no surprise that TiO_2-related materials have been a 'hot' topic of a vast amount of scientific research focused on their formation [4–10], properties [5, 9, 11–16], and applications [5, 7, 9–11, 17–26], which is proven by multiple excellent reviews dedicated to the TiO_2 topic.

This work has similar objectives; it focuses on TiO_2-based nanomaterials and their possible utilisation as a photocatalyst for the water splitting reaction. Specifically, it studies the formation and properties of TiO_2 nanocolumn arrays prepared by an unconventional electrochemical process called porous anodic alumina (PAA)-assisted anodisation. The main benefit of this method is a relatively novel approach to modify TiO_2 material composition and thus tune its electrical and optical properties. As pointed out, this work aims to narrow the wide bandgap of TiO_2 and improve its relatively poor electrical properties, which are the biggest obstacles in TiO_2 development as a photocatalyst. Positive results could initiate an evolution in hydrogen production and be a necessary trigger to an inevitable breakthrough in the current energy and fossil fuels economics towards more environmentally friendly solutions.

This part of the thesis is divided into two thematical chapters: theoretical/review and experimental chapter, including results and discussion. The first chapter aims to provide a minimum academic background and the current state of the art. It begins with a short introduction to water splitting, the role of TiO_2, its properties, and the possibility of increasing its photocatalytic performance further. The following sections introduce the porous anodic alumina (PAA), a specific PAA-assisted anodising case, and the current progress in this field. This chapter concludes with the motivation of this work.

The second (experimental) part is written to give the reader a systematic demonstration of formation and properties of TiO_2-based nanostructures. It begins with the fabrication overview of the nanocolumns that extends to evaluating their morphology and stability. The following sections discuss the electrochemical properties and photoelectrochemical performance of the formed nanostructures. This part is closed with the summarised conclusion and future outlooks.

1 THEORY & REVIEW

1.1 Titanium dioxide for photoelectrochemical water splitting

This section will briefly introduce the water splitting and semiconductor behaviour as a photo-anode within a photoelectrochemical cell (PEC). It relates to titanium dioxide (TiO_2) properties, which play an important role in the good photocatalytic performance of photoanode. In the end, a short overview of important historical milestones and recent approaches to overcome some of the TiO_2 limitations will be presented. The following sections are inspired by the excellent PhD research of J. C. Alexander [4] that I highly recommended as an extensive and comprehensive work dealing with TiO_2 and water splitting applications.

1.1.1 The water splitting reaction

The general reaction of interest is the solar splitting of water into its constituent parts of H_2 and O_2:

$$H_2O \xrightarrow{h\nu} H_2 + \frac{1}{2}O_2. \tag{1.1}$$

This reaction splits into two half-reactions:

$$(\textbf{HER}) \quad {H_2}^{+} + 2\,e^{-} \longrightarrow H_2, \tag{1.2}$$

$$(\textbf{OER}) \quad H_2O + 2\,h^{+} \longrightarrow 2\,H^{+} + \frac{1}{2}O_2. \tag{1.3}$$

In the hydrogen evolution reaction (HER), two protons are donated by the water molecule and then reduced with two electrons to produce one molecule of hydrogen. This reaction defines the zero of the reversible hydrogen electrode (RHE) scale. In the oxygen evolution reaction (OER), the water molecule is oxidised by two positively charged holes to produce oxygen. Thus, for each complete O_2 molecule, a total of four holes is required to oxidise two water molecules. As such, water splitting is often called a four-electron process. TiO_2 can be used as a photo-anode to drive the OER. Water absorbs onto TiO_2 both molecularly and dissociatively, depending on the configuration of surface atoms.

Water splitting into H_2 and O_2 is an uphill reaction. It needs the standard Gibbs free energy change ΔG° of $-237\,\mathrm{kJ\,mol^{-1}}$. In practice, the energy can be delivered in the form of the reducing/oxidising potential difference of photogenerated charge carriers in a solar cell such as a PEC. The reversible potential is given by:

$$E^\circ = -\frac{\Delta G^\circ}{nF} = 1.23\,\mathrm{V}, \tag{1.4}$$

where n is the electron stoichiometry of the elementary reaction (Equation 1.2) (with a value of 2 in this case), and F is Faraday's constant. Therefore, the minimum required reversible potential is 1.23 V if no additional heat is provided to the system. However, in practice, higher potentials are necessary to cause the reaction to depart from the equilibrium due to resistive losses in the circuit and the need to drive the reaction at an economically reasonable rate. This overpotential at the anode, η_a, and the cathode, η_c, is illustrated in Figure 1.1:D.

1.1.2 The semiconductor photoelectrolysis cell

One of several photoelectrolysis approaches uses semiconductor–electrolyte junctions to produce internal electric fields required for efficient separation of the electron–hole pairs. The holes subsequently oxidise water to oxygen in the anode region, and electrons reduce water or hydrogen ions in the cathode region. In this work, we cover only the configuration when anode and cathode are separated electrodes.

When a semiconductor electrode comes into contact with an electrolyte containing a redox system, equilibrium is achieved if the electrochemical potential is constant throughout the whole system; i.e., the Fermi levels of the semiconductor and the redox system must be equal on both sides of the interface. The thermodynamic equilibration lasts while charges cross the interface until a corresponding potential difference occurs. This charge migration forms a depletion layer (space charge layer) within a thin surface region of the semiconductor. The energy bands are bent upward or downward depending on the doping of the semiconductor. Figure 1.1:A–B illustrates such a situation for an n-type semiconductor (TiO_2).

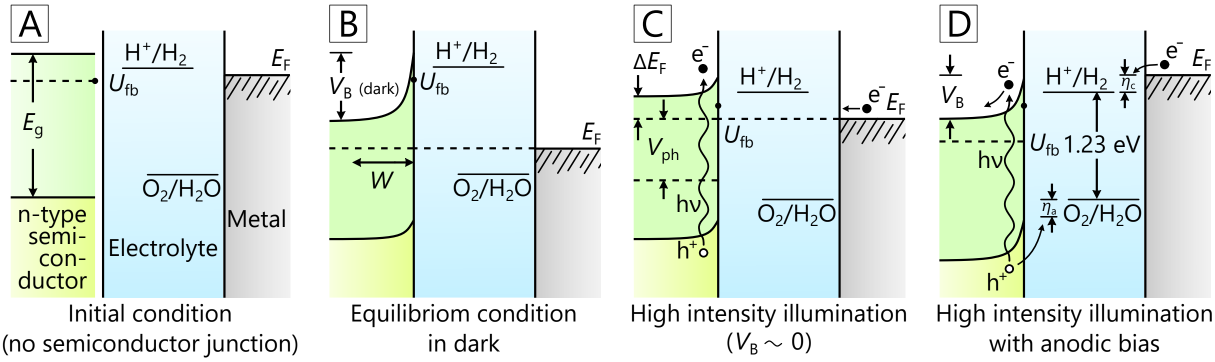

Figure 1.1: Sequence of energy level diagrams for an n-type semiconductor–metal photoelectrolysis cell from the initial condition (no contact) to the final state of the water photoelectrolysis with an external bias. Taken and modified from ref. [27].

The width of the space charge layer W is determined by the band bending V_B

$$W = \left(\frac{2\varepsilon_\mathrm{r}\varepsilon_0 V_\mathrm{B}}{eN_\mathrm{d}}\right)^{\frac{1}{2}}, \tag{1.5}$$

where e is the elementary charge, ε_0 is the vacuum permittivity, ε_r is the relative permittivity of the material, and N_d is the donor density (for an n-type semiconductor). The width is usually 1–1000 nm, depending on the carrier density (doping concentration) and the relative permittivity of the semiconductor.

Similarly, the Helmholtz double-layer forms on the electrolyte side of the interface. This layer additionally contributes to the potential shift and capacitance across the interface (not included in the diagram). The Helmholtz layer is formed either by absorption of ions or molecules, by oriented dipoles, or by forming surface bonds between the solid and the solution species. The width of the Helmholtz layer is usually a few atomic/molecular layers, typically 0.4–0.6 nm, and the capacitance of the order of 10 μF cm^{-1}.[28] The presence of the diffuse double layer (Gouy layer) can be neglected in the electrolyte with a sufficiently high ionic concentration.

Under illumination (Figure 1.1:C), the Fermi level in the semiconductor bulk rises to flat-band potential (U_{fb}). With the two electrodes shorted together, the maximum Fermi level possible in the cell is the flat-band potential. In Figure 1.1:C, U_{fb} is below the H^+/H_2 redox potential. Hence, even with the illumination intensity sufficient to completely flatten the semiconductor bands, the evolution of H_2 still cannot occur at the counter metal electrode because the Fermi level is below the H^+/H_2 redox potential. An external anodic bias (E_{b}) must be applied to raise the Fermi level in the metal counter electrode, as shown in Figure 1.1:C. The bias also provides the overvoltage at the metal cathode (η_c), required to sustain the current flow. Additionally, it increases the band bending in the semiconductor to maintain the required charge separation rate.[27]

1.2 Quantum efficiency of photoelectrodes

The quantum efficiency of a photoelectrochemical reaction, that is, the number of charge carriers (measured in the external circuit) per each photon absorbed, depends on i) the efficiency with which the minority carriers are collected at the surface, and on ii) the competition between surface recombination and the charge transfer reaction. The total photocurrent density j_{tot} is the sum of the current densities due to carriers generated in the depletion layer j_{dl} and those generated inside the bulk that diffuse into the depletion layer and are transported to the interface, j_{diff}. This simplified situation is shown in Figure 1.2. Overall, the collection efficiency depends on the penetration depth of the light defined as $1/\alpha(\lambda)$ (where $\alpha(\lambda)$ is the absorption coefficient), the minority carrier diffusion length L_{p} (in the case of holes), and the thickness of the depletion layer, W.

For the simple case in which surface recombination can be disregarded, that is, all carriers reaching the surface are transferred to the solution, an illuminated Schottky diode can be used to calculate the quantum efficiency:

$$Q = \frac{j_{\mathrm{p}}}{\phi_{\mathrm{a}}} = 1 - \frac{e^{-\alpha W}}{1 + \alpha L_{\mathrm{p}}}, \tag{1.6}$$

where j_{p} is the flux of holes towards the surface and ϕ_{a} is the absorbed photon flux.[30] Therefore, the term on the right-hand side represents the fraction of carriers lost due to

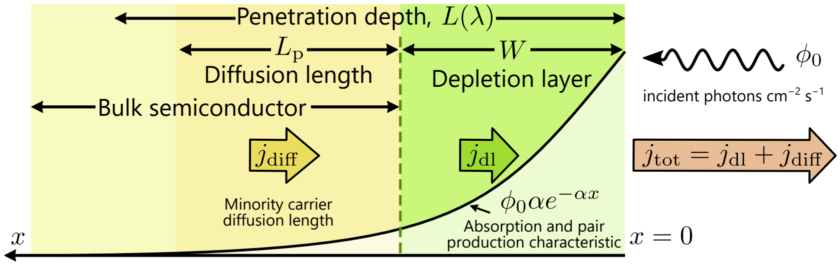

Figure 1.2: Photocurrent model, according to Gärtner.[29] The width of the depletion layer and the diffusion length of holes are shown in addition to the exponential absorption of incident photons.[4]

recombination inside the semiconductor. From this equation, it is clear that to ensure a significant quantum efficiency; it is necessary to achieve $1/\alpha(\lambda) < W$ or $1/\alpha(\lambda) < L_p$. This condition is usually satisfied for direct-bandgap semiconductor; hence its $\alpha(\lambda)$ is large, and thus the penetration depth of the light is small. In an indirect semiconductor like TiO_2, however, $\alpha(\lambda)$ is usually much smaller. For example, the penetration depth of the light ($\lambda = 380\,\mathrm{nm}$) is approx. 250 nm in an n-TiO_2 single crystal that results (for $W = 20\,\mathrm{nm}$ and $L_p = 10\,\mathrm{nm}$) in the quantum efficiency of only 11 %. However, it is necessary to note that the diffusion length (L_p) of the minority carrier diverges in literature from 100 nm [31] to less than 10 nm [32].

1.3 Photoelectrode materials

The situation depicted in Figure 1.1 describes most of the semiconductors studied to date. For these semiconductors, an external bias is required to generate H_2 and O_2 in a photoelectrolysis cell. A potential bias can be applied either by an external voltage source or by immersing the electrodes in solutions of different chemical potentials. Several oxide semiconductors such as $SrTiO_3$, $KTaO_3$, and ZrO_2 have U_{fb} above the H^+/H_2 potential; therefore, no external bias is required to generate H_2 and O_2. Unfortunately, these oxides have wide bandgaps (>3.4 eV), which result in very low solar absorptivity; hence they are inefficient (<1 %) in systems for solar energy conversion. Other semiconductors with an appropriate bandgap, such as CdS, CdSe, or GaAs, are either unstable to oxidative decomposition during O_2 evolution or have an unsuitable position of band edges (shown in the energy level diagram in Figure 1.3).

In the case of TiO_2, the situation is more promising since its bandgap (3.2 and 3.0 eV for anatase and rutile, respectively)[35] is not as large as other oxides, and it also has a favourable band edge alignment with water redox potentials. Also, the redox potential for water oxidation to oxygen is more anodic than that for the oxidation of TiO_2 to O_2. This situation makes the water oxidation reaction more thermodynamically favoured than the TiO_2 oxidative decomposition, making TiO_2 very stable.[33]

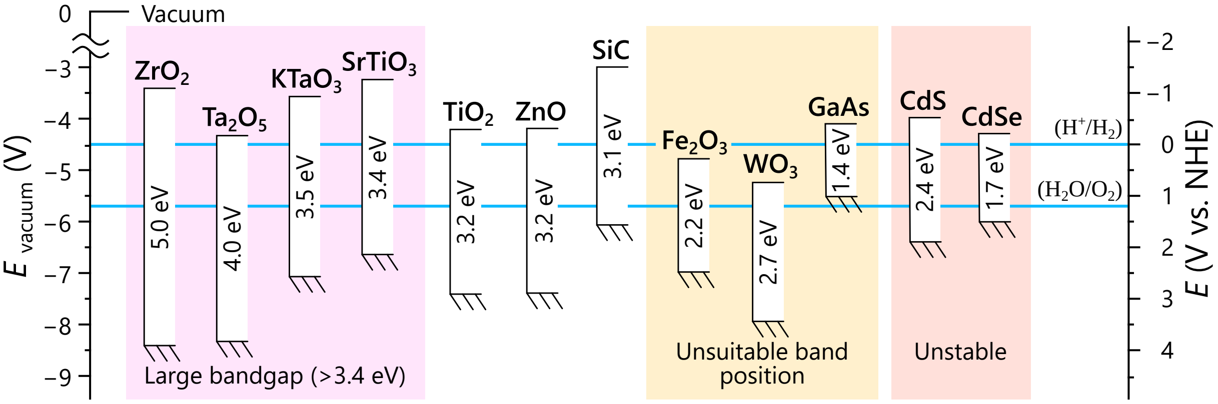

Figure 1.3: Diagram of energy levels of commonly used semiconductors in contact with aqueous electrolyte at pH 1. The position of the H^+/H_2 and H_2O/O_2 redox couples are indicated.[26, 33, 34]

1.4 Overview of TiO_2 photocatalysts

One of the earliest works investigating TiO_2 photoinduced electrochemical properties is that of Renz [36], who reported in 1921 that titania is partially reduced during illumination by sunlight in the presence of an organic compound. Since then, only several reports observing photo-induced oxidation on TiO_2 were published. However, the most significant breakthrough was made in the late 1960s by Fujishima and Honda. They found that oxygen gas evolved on titania at potentials very much shifted from the thermodynamic expectations (according to ref. [37], an original paper in Japanese ref. [38]). A few years later, in 1972, they demonstrated a complete photoelectrochemical water splitting. They used a single-crystal TiO_2 (rutile) photoanode and Pt cathode with external bias and simultaneously achieved both oxygen and hydrogen evolution.[39] After this pioneering work published at the time of 'the oil crisis', which also represented the first report on the efficient hydrogen production from water utilising solar energy and TiO_2, the field of photoelectrochemistry started to receive much wider attention due to its implications for solar energy conversion. Since then, there has been a massive boom in research efforts to understand the fundamental processes and to enhance the efficiency of TiO_2 materials. A more detailed history of this field can be found in excellent reviews of Fujishima [37] and Schneider [15].

Besides photoelectrochemical water splitting, TiO_2 has attracted much attention thanks to its unique properties. It found a way to many promising areas ranging from pigments, corrosion-protective and optical coatings, photovoltaics, photocatalysis, gas sensors, water and air purification, CO_2 reduction, organic synthesis, self-cleaning and anti-fogging surfaces, bone implants.

Although TiO_2 has excellent stability, nontoxicity, and low cost, however, its relatively wide bandgap (3.02 and 3.20 eV for rutile and anatase, respectively)[22] hinders TiO_2

utilisation of solar energy only to the ultraviolet (UV) part that represents only 4 % intensity of the whole solar spectrum.[26] Besides, TiO_2 photocatalytic efficiency suffers from a fast charge carrier recombination and a relatively short carrier lifetime. Most TiO_2-based cells even make insufficient use of the UV spectrum, and the peak energy conversion efficiencies reported have been 0.6 % or less over the whole solar spectrum. Therefore, various strategies for increasing solar-to-hydrogen (STH) efficiency have been developed using TiO_2 as a base material. Popular options are morphology and crystallinity control of nanostructured TiO_2, material doping, surface decoration with cocatalysts, and heterojunction formation.[40] This work covers some strategies modifying the morphology, crystallinity, and doping of TiO_2 materials.

A primary factor limiting the efficiency of these devices is the mismatch between the optical path length required for light absorption and the charge diffusion lengths. If a photogenerated charge is to participate in a chemical reaction, it must reach the semiconductor/electrolyte interface before it recombines. In an anatase TiO_2 film, to absorb 90 % of the light above the bandgap, the film thickness is in the order of 1 µm, but the minority carrier (hole) diffusion length is only around 10–100 nm. This consideration highlights the importance of engineering systems with both high optical density and high surface-to-volume ratio. Promising candidates are one-dimensional (1–D) TiO_2 nanostructures (e.g., nanotubes, nanocolumns, nanowires) for their enhanced optical absorption.[25] Also, a comparative study shows that ordered arrays of TiO_2 outperform colloidal TiO_2 materials in the field of photocatalytic, sensing, and photoelectrolysis applications.[41] Since 1999, when Zwilling [42] first demonstrated that titanium anodic oxidation in fluoride ions containing electrolyte leads to TiO_2 nanotubular structure, it has become a great success story.[7, 26, 43] On the other side, the research of TiO_2 nanowires/nanocolumns has spread across many fabrication techniques.[44]

In addition to decreasing the distance that the charge carrier needs to travel, it is also efficient to increase its diffusion length. Here, the crystallinity of TiO_2 plays a very significant role. As-formed TiO_2 nanostructures typically have an amorphous structure, which usually comprises numerous defects such as impurities, dangling bonds, and microvoids. These defects can behave as recombination centres for the photogenerated electron–hole pairs, resulting in a decrease in photocatalytic activity. It is already well known that annealing leads to the relaxation of the mechanical stress and growth of crystalline grains. In the case of TiO_2, it can also change the crystal structure from amorphous to anatase (>280 °C) or rutile (>500 °C).[9, 45–47] Therefore, annealing produces a more suitable crystal structure and reduces the bandgap due to the phase transformation (amorphous<anatase<rutile). Moreover, it is possible to increase the concentration of oxygen vacancies in TiO_2 by annealing in an oxygen-deficient (vacuum) or reducing (H_2) environment, and thus to increase the doping concentration (n-type).[48, 49] Tuning bandgap and the width of the depletion layer is a fundamental advantage of doping.[50, 51]

Although TiO_2 has excellent stability, nontoxicity and low cost, its relatively large band gap (3.02 eV and 3.20 eV for rutile and anatase, respectively [22]) hinder TiO_2 utilization of solar energy only to the ultraviolet (UV) spectrum which represent 4 % of the whole solar spectrum [26]. In addition, TiO_2 photocatalytic efficiency suffers from a fast charge carrier recombination and a relatively short carrier lifetime. Most TiO_2-based cells make insufficient use of even the UV spectrum, however, and the peak energy conversion efficiencies reported have been 0.6 % or less over the whole solar spectrum. Therefore, various strategies for increasing solar-to-hydrogen (STH) efficiency have been developed using TiO_2 as a model material, such as morphology and crystallinity control of nanostructured TiO_2, doping, surface decoration with cocatalysts, and heterojunction formation.[40] In this work we cover and investigate only the morphology, crystallinity and doping of TiO_2 materials.

A primary factor limiting the efficiency of these devices is the mismatch between the optical path length required for light absorption and the charge diffusion lengths. If a photo-generated charge is to participate in a chemical reaction, it must be able to reach the semiconductor/electrolyte interface before it recombines. In an anatase TiO_2 film, the film thickness to absorb 90 % of the light above the band gap is on the order of 1 µm, but the minority carrier (hole) diffusion length is only around 10 nm. This consideration highlights the importance of engineering systems with both a high optical density and high surface-to-volume ratio. One–dimensional (1–D) TiO_2 nanostructures such as nanotube or nanocolumn/nanowire arrays are promising candidates for their enhanced optical absorption.[25] Comparative studies also show that ordered arrays of TiO_2 nanowires/nanotubes outperform colloidal TiO_2 for photocatalytic, sensing, and photoelectrolysis applications [41]. Since 1999, when Zwilling [42] first demonstrated that titanium anodic oxidation in a fluoride ions containing electrolyte leads to TiO_2 nanotubular structure, it has become a great success story.[7, 26, 43] On the other side, the research of TiO_2 nanowires/nanocolumns has spread across a vast number of fabrication techniques.[44] This give a great opportunity to bring and study relatively novel ideas. One of such novelties could be the fabrication method; we use in this study anodising of an Al/Ti superimposed metal layers to grow TiO_2 nanocolumn arrays.[52, 53] This, so–called porous anodic alumina (PAA)-assisted formation, leads to the TiO_2 growth which is restricted within the PAA's nanopores (described in more detail in the result section).

In addition, to enhance the photocatalytic efficiency, we have to increase the charges diffusion length. Here, the crystallinity of TiO_2 plays a very significant role. As-formed TiO_2 nanocolumns typically have an amorphous structure, which usually comprises numerous defects such as impurities, dangling bonds, and microvoids that can behave as recombination centres for the photo-generated electron-hole pairs, resultsing in a decrease of the photocatalytic activity. It is already well-known that annealing leads to relaxation and growth of grains. In the case of TiO_2, it can also change the crystal structure from amorphous to anatase (>280 °C) or to mixture of anatase and rutile (>550 °C).[9] Benefit of annealing is not only a better crystallinity but also a smaller band gap can be achieved due to a phase conversion. In addition, by annealing in an oxygen deficient (vacuum) or reducing gas (H_2) environment it is possible to increase the oxygen vacancy concentration in TiO_2, and thus to increase the doping concentration (n-type).[48, 49] A great advantage is that by controlling the doping concentration, we can tune the band gap, position of the Fermi level, and the width of the depletion layer.[50, 51]

Another method for bandgap engineering is direct TiO_2 doping (the information in this paragraph refers to ref. [22]). By replacing Ti atoms with other cations (e.g., Ni^{3+}, V^{5+}, Cr^{3+}), we can introduce an impurity level in the forbidden band. This intermediate energy level can act as either an electron acceptor or a donor, allowing TiO_2 to absorb visible light. It should be noted that doping can enhance photocatalytic activity while having no impact on light absorption (e.g., Nd^{3+}). Anion doping (e.g., C, N, F, P, S) is another approach to extend the light absorption of TiO_2 into the visible region. Unlike cation doping, anion doping hardly affects the conduction band of TiO_2. It usually reconstructs the valence band and shifts it upward to narrow the bandgap of TiO_2. Among the mentioned dopants, nitrogen seems to be the most suitable doping element,[54–56] and thus, the reason it was studied in this work.

To conclude this section, bandgap engineering is crucial for the effective utilisation of solar energy. On the other hand, it is also necessary to tune the morphological parameters concerning material properties such as the doping concentration, depletion layer thickness, and the hole diffusion length to take advantage of TiO_2 optical properties. Figure 1.4 illustrates an example of a suitable and improper design of the nanocolumn to the depletion. In this way, the goal is to overcome the short diffusion length of holes in TiO_2 by employing a depletion layer being as thick as possible (Figure 1.4:A) while avoiding complete depletion of the nanocolumns (Figure 1.4:B). Another work utilised for TNTs is to fabricate structures with material thickness lower than the diffusion length of the charge carrier (<10 nm).[41]

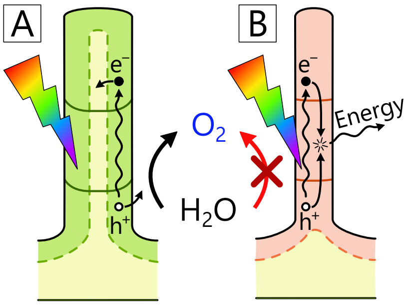

Figure 1.4: Schematic representation of the depletion layer distribution in a nanocolumn. (A) The width of the depletion layer is smaller than the column radius, so the depletion layer envelopes the nanocolumn. Otherwise, (B) the whole column is depleted, and photogenerated charge carrier separation is hindered.

1.5 Porous anodic alumina

This section discusses the brief origin, formation, structure, and growth of porous anodic alumina (PAA). It is intended as a short glimpse into the state-of-the-art, to introduce the reader to the context of the experimental section. For a more in-depth exploration of fabrication and application possibilities, see related publications.[57–67]

1.5.1 Introduction

In an ambient atmosphere, aluminium becomes rapidly coated with a compact native oxide layer with a thickness of a few nanometres. This thin but sturdy oxide layer protects the aluminium from further oxidation. Even though aluminium has good corrosion resistance, corrosion of the metal can easily occur in rather aggressive environments, containing corrosive compounds such as chlorides and sulphates. In 1857, Buff [68] first found that aluminium can be electrochemically oxidized in an aqueous solution to form an oxide layer that is thicker than the native one. This process was called 'anodisation' because the to be processed aluminium part serves as an anode in an electrolytic cell.[58]

In general, the anodic aluminium oxide (AAO) film can form two different morphologies (shown in Figure 1.5): compact barrier-type oxide film and porous-type oxide film. Which one forms during anodising primarily depends on the nature of the electrolyte. More acidic electrolytes (e.g., sulphuric acid, phosphoric acid, oxalic acid) usually form porous-type films, while neutral (with pH around 7, e.g., phosphate buffer, borate buffer) electrolytes form barrier-type films.

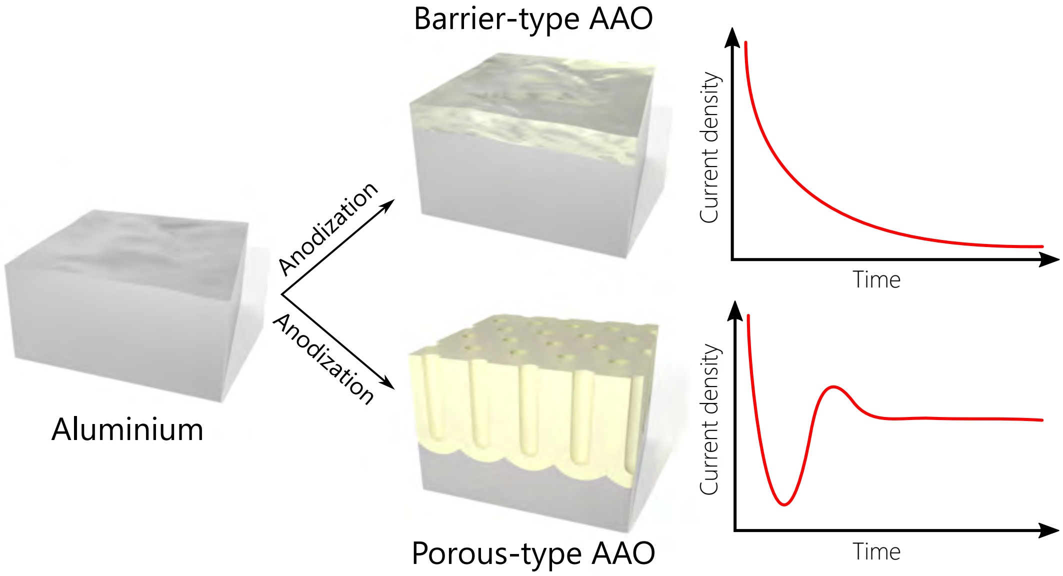

Figure 1.5: Schematic illustration of the barrier- and porous-type anodic oxides formed by the anodisation of aluminium. On the right side of the scheme, typical trends of current density versus time during potentiostatic anodising for a given oxide type are presented.

Those two types differ in the thickness of the film produced and in the thickness controlling parameters. Aside from the electrolyte temperature, the barrier-type film thickness is controlled solely by the voltage applied, whereas the porous-type film thickness depends on the current density and time.[59] The maximum film thickness attainable for the barrier-type film is restricted to a voltage below the oxide breakdown voltage, which corresponds to approximately 1 µm of oxide thickness. In comparison to barrier-type, during porous-type development, the oxide growth is accompanied by a local field-assisted oxide dissolution that leads to the characteristic porous structure. The thickness of the porous films depends on time and can easily grow over hundreds of micrometres.

PAA films were first reported by Keller et al.,[69] who described the formation of nanopore arrays grown perpendicularly to the aluminium surface with relatively low regularity. After almost 50 years, a phenomenon of self-ordering nature of PAA was demonstrated by Masuda and Fukuda [70] by long-time anodising of high purity (99.99 %) aluminium in 0.3 M oxalic acid at 40 V. One year later, Masuda and Satoh [71] presented the so-called two-step anodisation process that leads to the formation of ideal PAA structure with highly ordered, straight and uniform pores throughout the whole PAAs thickness. Since then, the novel and tuneable structural features of PAA have been intensively exploited for their utilization as a template for biosensing [57, 58, 62] but essentially as PAA-assisted synthesis of a diverse range of nanostructured materials.[58, 60, 61, 63, 72, 73]

1.5.2 PAA morphology

The morphology of the ideal PAA, illustrated in Figure 1.6, may be described as a close-packed array of columnar hexagonal cells in a honeycomb arrangement. Each hexagonal cell contains a central pore perpendicular to the substrate closed by a thin barrier of the oxide layer at the oxide/metal interface with an approximately hemispherical morphology. In general, the structure of PAA is often described by several structural parameters, such as pore diameter (D_p), the cell size or interpore distance (D_c), barrier layer thickness (t_b), and porosity (P). These structural parameters of PAA are known to be dependent on the anodising conditions: the type of electrolyte, anodising potential (U), current density (j), temperature (T).[58, 64]

Cell size D_c or interpore distance, together with pore alignment, are the only PAA parameters, which influence the final morphology of the aluminium templates used in this work (Part II). It is generally accepted that cell size mainly depends on the anodising potential (U) with a proportional constant (ζ_c) close to 2.5 nmV^{-1} (Figure 1.7). This relation is especially the case for mild anodising [58] (hard anodising is not discussed in this work) in sulphuric, oxalic, and phosphoric acid electrolytes.[64, 74] Besides the anodising potential, it was reported that cell size also depends on the temperature [75–77] or concentration [78, 79] of electrolyte.

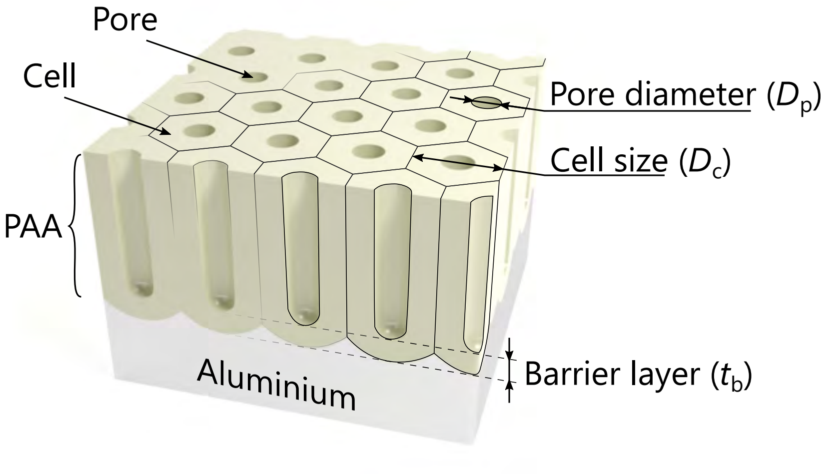

Figure 1.6: Schematic 3D model of a perfectly ordered honeycomb-like PAA on Al substrate.

Other parameters do not play a significant role in determining the Al template morphology and do not significantly impact the technological processes (considering our work). Nevertheless, the pore diameter (D_p) is still one of the most attractive and versatile parameters of PAA. Primarily, the pore diameter depends on the anodising potential, while further widening may occur due to enhanced chemical dissolution of AAO related to a high temperature, aggressive electrolytes, or even long anodising time.[58] Therefore, the pore diameter may differ throughout the thickness of the PAA. The proportional constant ζ_p varies with regards to the used electrolyte. The most commonly used acids (sulphuric, oxalic, and phosphoric acid) are usually in the range of 0.9–1.3 $\mathrm{nmV^{-1}}$, but it is much smaller for weaker acids (e.g. malonic, citric, selenic).[63, 64] Even though the anodising conditions determine the pore diameter, it can be easily altered by post-treatment procedures involving widening by chemical etching [82–85] or narrowed by using the atomic layer deposition (ALD) technique [86, 87].

The barrier layer thickness (tb) depends directly on the anodising potential with a rate close to $1\,\mathrm{nm\,V^{-1}}$ for a large variety of electrolytes and anodising conditions.[64] Nielsch et al.[74] suggested that for optimal self-ordering conditions of anodising, the barrier layer thickness is approximately half of the interpore distance ($t_b = D_c/2$).

1.5.3 Growth of self-ordered PAA

Since most PAA structural parameters are related to the anodising potential, it is no wonder that the potentiostatic (constant potential) anodisation is commonly used for the fabrication of self-ordered PAA. The growth kinetics of PAA with normal development of current density during potentiostatic anodising is illustrated in Figure 1.8:A. When a constant anodic potential is applied, a thin barrier oxide layer is formed over the aluminium surface (stage I). This initial stage resembles the barrier-type anodisation when the current drops with increasing thickness of the oxide layer that behaves as resistance in a series cir-

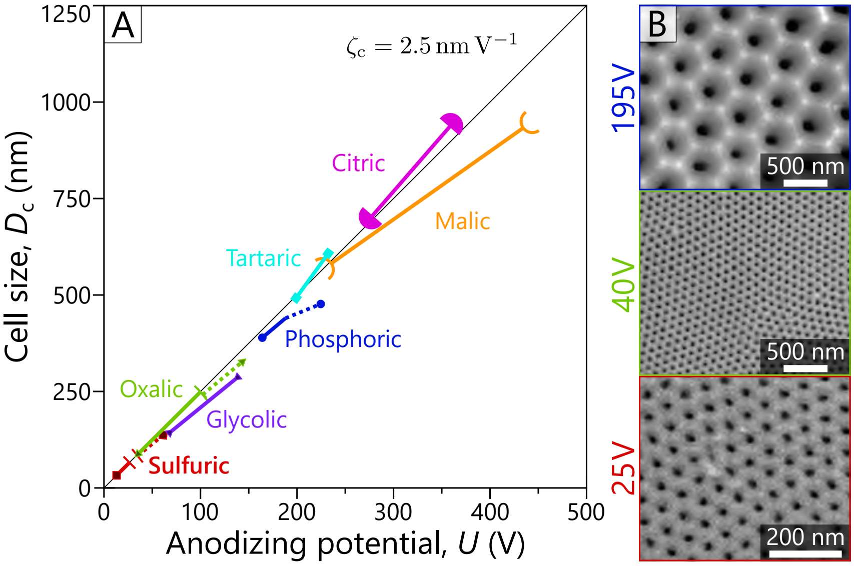

Figure 1.7: (A) anodising potential influence on the cell size D_c (interpore distance) for PAA formed in various electrolytes (mild anodising – full lines, hard anodising – dashed lines). Adapted from ref. [64, 80]. (B) SEM images of PAA surface (from top) formed in phosphoric, oxalic, and sulphuric acid by a two-step anodisation process. Adapted from ref. [81].

cuit. In the following stage (stage II), the formation of individual penetration paths takes place. These paths are usually based on defects, which can originate from the aluminium material (e.g. surface defects, grain boundaries, morphology features) or are formed during the compact oxide growth (oxide non-uniformity, stress-induced cracks)[58]. The local increase in the electric field strength at these paths leads to enhanced field-assisted oxide dissolution and eventually to the formation of individual pores. All these naturally lead to a significant rise in the overall current density.

After this pore initiation, further pore growth can lead to several outcomes with respect to anodising conditions.[67, 88] However, only the self-ordered regime is used and described in this thesis. The first phase of pore growth (stage III), also called unsteady-state growth, is typically associated with a descending current due to decreased pore density. During this phase, the growth of individual pores is influenced by the electric field and mechanical stress induced by neighbouring pores and volume expansion of the oxide. When the anodising conditions are appropriately selected, pores will be gradually self-ordered into the most favourable hexagonal lattice giving PAA a characteristic honeycomb-like structure. The last phase (stage IV) consists of a steady-state growth that prolongs existing pores, and a very modest pore rearrangement that improves the lattice order.

The self-ordering behaviour of pores within the PAA is one of the most attractive properties that has been intensively utilized in academic research for a wide variety of nanotechnology applications for over two decades. The first application to produce a nanohole gold film was proposed by Masuda and Fukuda [70], which included a demon-

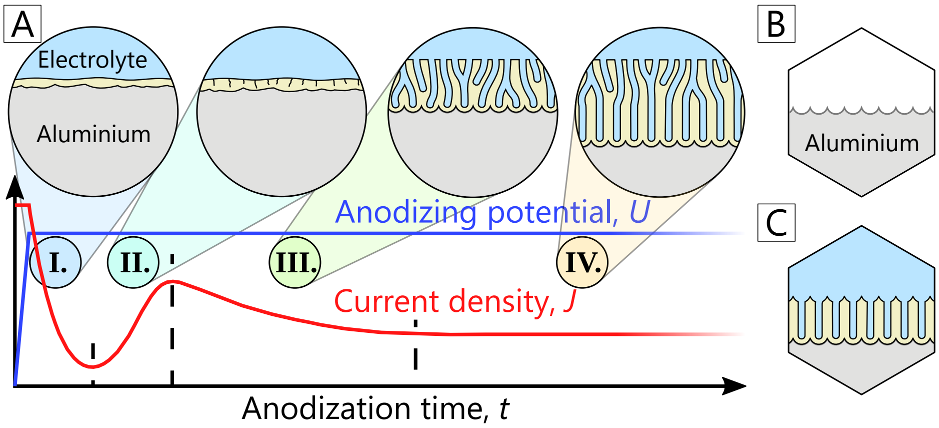

Figure 1.8: (A) Schematic diagram of PAA growth kinetics in potentiostatic conditions with stages of PAA development. Inspired by ref. [58, 64]. (B) Selective removal of the disordered PAA layer. (C) Re-anodising of textured aluminium.

stration of the so-called 'two-step anodisation' process. Even though two-step anodisation is not utilized in this work, its first two steps represent the complete fabrication of aluminium templates used for AuNPs fabrication (Part II).

The typical two-step process consists of long anodisation forming a PAA with a disordered top layer and a self-organized bottom layer (Figure 1.8:A). This whole PAA layer is subsequently selectively removed, revealing the aluminium surface textured by a hexagonal array of spherical concaves (Figure 1.8:B). Re-anodising this textured aluminium under the same conditions as employed for the first anodisation leads to a pore governed nucleation at the centres of each concave. Because the nucleation sites already match the well-ordered steady-state alignment, pores continue with their coherent growth perpendicular to the surface (Figure 1.8:C). In general, PAA formed by two-step anodisation (and so the textured aluminium) exhibits a poly-domain structure that is a natural consequence of random pore nucleation and domain growth (illustrated in Figure 1.9:1–4). Although the lateral size of the defect-free domain rapidly increases during the self-organized phase (stage III) and can be increased further with the anodising time later during steady-state growth (stage IV), it is only limited to tens of cells over several micrometres (shown in Figure 1.9:B).[74, 89, 90]

Since the first demonstration of the self-ordering of PAA, many studies have been conducted to explore the optimum conditions for the best possible pore ordering. These findings indicate that the self-ordering regime occurs only within a relatively narrow window of anodising conditions. First reports given by Masuda and co-workers demonstrated that optimum anodising parameters for best ordering are (electrolyte temperature 0 °C): sulphuric acid ($0.3\,\mathrm{M}$ H_2SO_4) at $U = 25\,\mathrm{V}$ ($D_c = 65\,\mathrm{nm}$)[93]; oxalic acid ($0.3\,\mathrm{M}$ $H_2C_2O_4$) at $U = 40\,\mathrm{V}$ ($D_c = 103\,\mathrm{nm}$)[70]; and phosphoric acid ($0.3\,\mathrm{M}$ H_3PO_4) at $U = 195\,\mathrm{V}$ ($D_c = 500\,\mathrm{nm}$)[94]. Afterwards, Nielsch et al.[74] proposed that self-ordering of pores requires 10 % porosity regardless of the specific anodising conditions. However, later re-

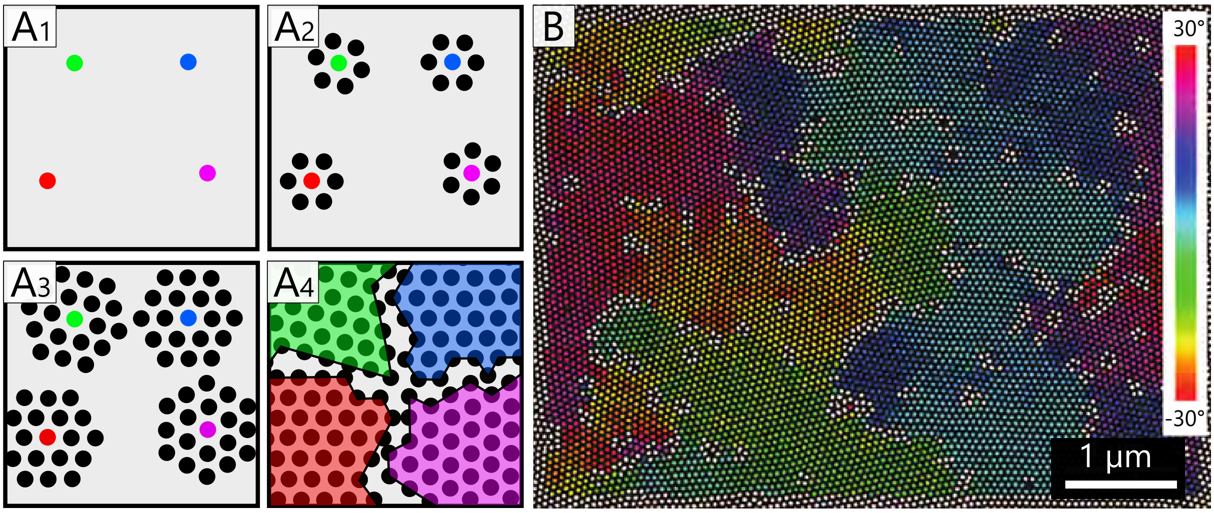

Figure 1.9: (A1–4) Model of defect-free domains expansion with hexagonal lattice. Adapted from ref. [91]. (B) Colour-coded SEM image of PAA formed by anodising in 0.3 M H_2SO_4 at 25 V for 24 h, showing a poly-domain structure. Reproduced from ref. [92].

ports [58] showed that ordering strongly depends on the anodising potential [89, 95, 96], electrolyte concentration [78, 97], electrolyte temperature [75, 96, 98], anodising time [74, 90], and even aluminium crystal orientation [89, 96, 99].

Unfortunately, there is no simple rule to achieve the best ordering, except for the crystal orientation that has to be [001]. In the case of anodising potential, ideal values are 25 and 40 V for sulphuric and oxalic acid (0.3 M), shown in Figure 1.10:A, respectively. On the other hand, the effect of the electrolyte composition/concentration and temperature is far more complex. The reason is that these parameters influence each other, as shown in Figure 1.10:B, but also influence anodising potential and rate of oxide growth. The anodising time plays a significant role in the pore ordering since the self-ordering process is governed by mechanical stress.[100, 101] This effect is still relatively weak, and good alignment can be observed predominantly in the very late stages of PAA growth. However, with increasing thickness of the PAA, the anion concentration is expected to decrease due to insufficient diffusion through the PAA, and thus a maximum [74] is expected.

Finally, the pore ordering is related to the initial pore nucleation that strongly depends on the aluminium surface morphology. Pores preferentially nucleate in defect areas, such as grooves, pits, or grain boundaries. While these defects can be effectively reduced by aluminium annealing and polishing (shown later in the experimental chapter 2), the primary pore nucleation over the surface and domain orientation is still a random event (Figure 1.8:A1–4). Despite a vast amount of reports controlling the pore nucleation by pre-patterning the aluminium surface, e.g., nanoimprinting [58, 102–104], the methods used are relatively expensive and time-consuming than simple aluminium anodising.

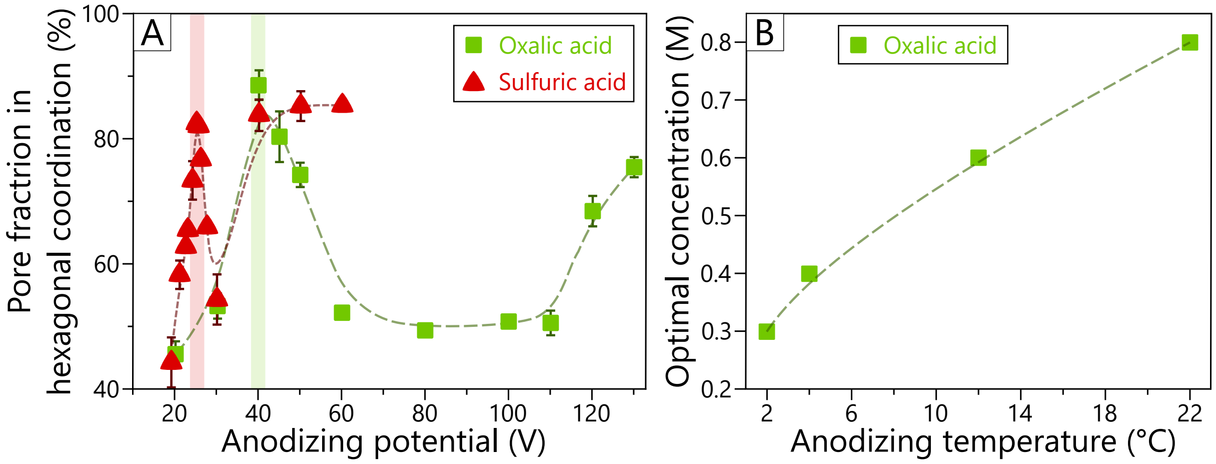

Figure 1.10: (A) Dependence of pore fraction in hexagonal coordination on the anodising potential in 0.3 M oxalic and 0.3 M sulphuric acids at 1 °C. Reproduced from ref. [95]. (B) Optimal oxalic acid concentrations, which can result in the best pore ordering of PAA at 40 V as a function of anodising temperature. Reproduced from ref. [97].

Conclusion

This section introduced the porous anodic alumina (PAA) and its formation by anodising aluminium. Its focus was to discuss the self-ordering behaviour of pores and the factors influencing it, and its outcomes will be used later in the experimental sections for creating PAA using sulphuric and oxalic acid.

1.6 Porous anodic alumina assisted anodisation

Porous anodic alumina (PAA)-assisted anodisation is the principal fabrication technique used in this part to form nanostructure surfaces. Briefly, it combines the porous anodisation of an aluminium film that is superimposed over the substrate layer from which the nanostructures are grown. Because this is primarily an experimental work, this topic will be introduced to cover the basics but will only refer to original publications for more detailed theoretical explanations.

1.6.1 Anodic oxidation of superimposed metallic layers

Anodic oxidation of metals is practically a straightforward process. In reality, it requires just an electric current to flow through the metal electrode immersed in an electrolyte. If the current is not spontaneous, then it can be achieved by applied anodic potential. This accessibility lends to extensive fundamental studies on metal oxidation. While some early works at the turn of the '70s and '80s of the previous century were directed towards the kinetics of the process and the properties of the oxide films,[105] others aided by improved surface analysis methods focused on the atomic migrations occurring within the oxide/metal films.[106, 107] During these times, a novel approach was adopted by Perrier, Rigo, and Siejka, based on anodisation of superimposed layers of different metals.[108–110]

Briefly, Perrier et al. have found that if two metals are superimposed in one way, when the order of their oxides is conserved after anodisation, then when we switch their order, the anodisation will result in a partially (mixed) or fully inverted order of oxides. This process is governed by several factors: oxide resistivity, transport number, relative metal migration, oxide structure, Pilling–Bedworth ratio. Discussing just the oxide resistivity is sufficient for further illustration, while the rest can be found in a comprehensive work of Pringle.[111]

Anodisation of a superimposed layer system begins with forming a thin uniform oxide on the surface of the superimposed metal. The oxide layer thickens until it reaches the interface between the two metals. What happens then depends on the relative resistivities of two oxides, with the results shown schematically in Figure 1.11. In effect, the situation is analogous to the superposition of two liquids of different densities. When the less dense liquid or resistive oxide is superimposed, the system is stable, and the order is conserved, as indicated in Figure 1.11:A. However, when the situation is reversed, the system is unstable; the instability is relieved by a Rayleigh–Taylor effect with the consequences shown in Figure 1.11:B. The Rayleigh–Taylor effect arises in the anodisation of superimposed layers due to perturbations in the thickness of the more resistive superimposed layer. Any variation in thickness of the layer concentrates the current at the thin spots due to their lower resistance. Here, the less resistivity underlying substrate oxide extends in the form of fingers into the superimposed oxide. The result is an accelerating build-up of anodising current at the thin spots and eventual penetration of the superimposed layer by the fingers of the substrate oxide, as indicated in Figure 1.11:B2. This process may stop here, creating a partial mixture of both oxides (an example shown in Figure 1.11:B3); or continue further with a complete switching the oxide positions (Figure 1.11:B).

Further in-depth research of anodising behaviour of the superimposed metal layers can be found either in the experimental studies of Siejka (Al-Nb/Nb-Al, Nb-Ta/Ta-Nb)[108–110], and Wood (Al-Zr [112], Al-Ta [113]) or the theoretical works of Pringle [111, 114].

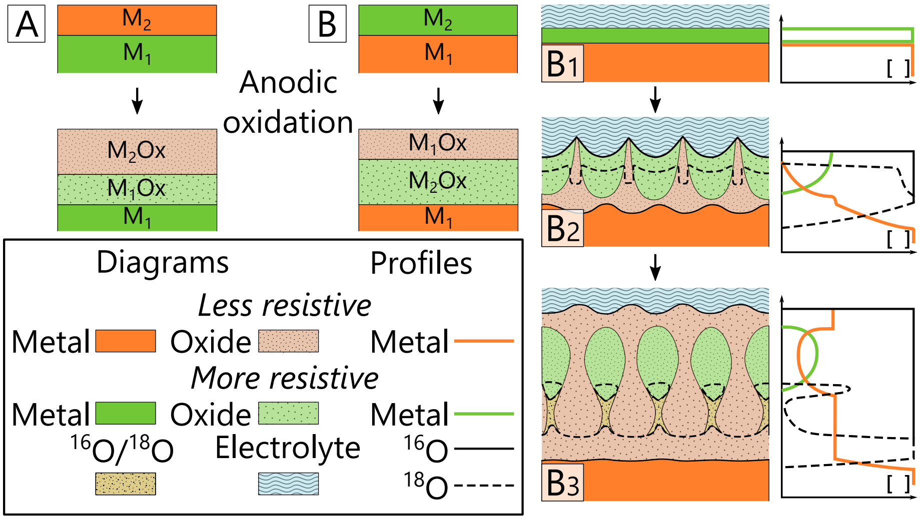

Figure 1.11: Schematic representation of the two extreme situations for the anodisation of metallic bilayer systems: (A) preserved and (B) inverted order of oxides (MO_x) after anodisation. (B1–3) Schematic diagrams with corresponding element concentration profiles show (B2) finger penetration and (B3) oxide mesh formation when the superimposed metal oxide is more resistive. Adapted and modified from ref. [108, 111, 114] . More information about the ^{18}O trace analysis can be found in the referenced articles.

1.6.2 The PAA-assisted anodisation

The PAA-assisted anodisation combines the porous anodic oxidation of the aluminium layer (section 1.5) with the anodisation of superimposed layers. The substrate (the underlying layer under aluminium) is usually another valve metal (e.g., Nb, Ta, Ti, W, Zr). Since the resistivity of the aluminium oxide is in general higher than that of the oxide of the other valve metals, this situation relates to the reversed, unstable circumstances leading to the migration and mixing of the underlying oxide (Figure 1.11:B). In contrast to the barrier-type anodising of superimposed layers (illustrated in Figure 1.11:B1–3), in the case of the PAA-assisted anodising, the anodised area and the growth of the underlying oxide are confined by the preformed porous mask of the overlying PAA layer. Figure 1.12 illustrates this process. Such a situation is similar to numerous separated barrier-type anodising processes co-occurring at the bottom of each pore, characteristically called the barrier layer (details in section 1.5), despite a few differences, such as the geometry, chemical composition, and nanosized lateral dimensions. The PAA-assisted anodisation has a similar development in a single pore area compared to its flat analogy.

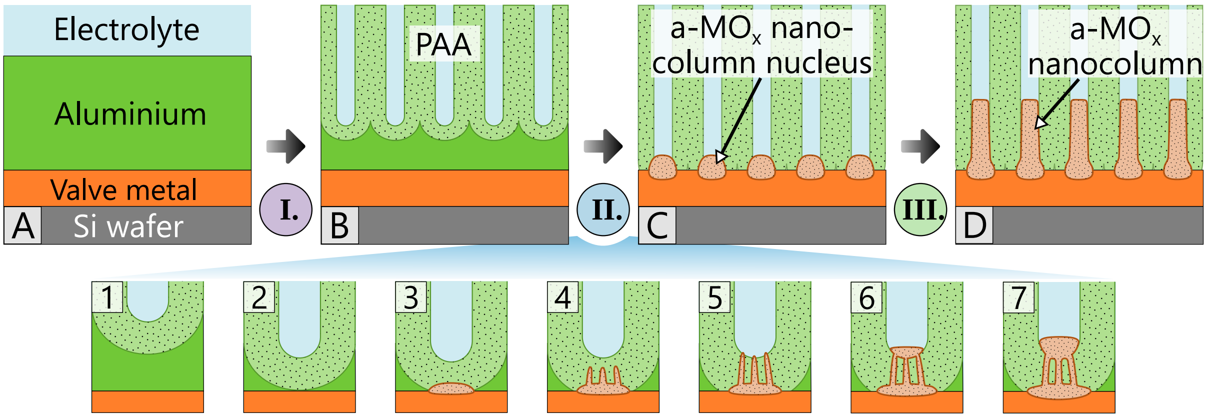

Figure 1.12: Schematic illustration of (A–D) exemplary PAA-assisted anodising of an Al/valve metal bilayer resulting in the formation of PAA-embedded a-MO$_x$ nanocolumns. (1–7) A detailed schematic of an example of nuclei growth. The roman numbers mark anodisation stages (used later in the text and illustrated in Figure 2.1): I.) aluminium anodising, II.) substrate anodising, and III.) substrate re-anodising. Schematic inspired by results in the experimental section (chapter 2).

Figure 1.12 represents a schematic illustration of PAA-assisted anodisation of an aluminium/valve-metal (Al/M) bilayer. During this process, the porous anodising of Al overlayer forms a layer of PAA (Figure 1.12:B). After the whole Al layer is consumed and the PAA reaches the underlying metal layer (Figure 1.12:2), the growth of underlying anodic metal oxide (a-MO$_x$) occurs (Figure 1.12:3). Afterwards, the less resistive substrate oxide penetrates the more resistive barrier layer, possibly in the form of fingers (Figure 1.12:4–5), similarly to the flat analogy (Figure 1.11:B2). When the substrate oxide thoroughly penetrates the barrier layer, it may form a cap at the bottom of the pore (Figure 1.12:6–7). The final structure (Figure 1.12:7), resembling a tooth by its shape, is again analogous to the flat case (Figure 1.11:B3), where a part of alumina from the barrier layer is trapped within the a-MO$_x$ structure.

Furthermore, the anodisation process can be extended into the so-called re-anodisation stage (Figure 1.12, stage III.). During this stage, the anodising potential is increased and leads to additional growth of the oxide cap that fills the interior of the pore, inheriting its columnar shape (Figure 1.12:D). Since the thickness of the a-MO$_x$ strongly depends on the formation potential,[115] moderating it provides an excellent method to control the length of oxide structures.

1.6.3 State-of-the-art of PAA-assisted anodising of Ti and its alloys

The PAA-assisted anodisation of valve metals can be utilised to fabricate a well-ordered array of a-MO$_x$ structures. The first known report of this technique dates back to 1986 by Surganov et al.[116] Here, the authors anodised an Al/V/Al sandwich layer where the incorporated vanadium layer was used as a tool to penetrate through the PAA barrier layer resulting in the open-through pore structure. Later, in the '90s, the PAA-assisted anodisation was successfully employed to fabricate the first nanostructured arrays of a-MO$_x$.[117, 118] This research was afterwards continued and pioneered by Mozalev.[52, 119–122]

In the last two decades, the PAA-assisted anodisation was successfully employed on valve metals such as tungsten (W) [122–125], niobium (Nb) [120, 121], zirconium (Zr) [126, 127], tantalum (Ta) [117, 128], titanium (Ti) [52, 53, 118, 119, 129–135], and even titanium nitride (TiN) [119, 136]. These reports show that the intermixing of the PAA barrier layer and substrate oxide can take various forms, which strongly depend on the substrate composition and the anodisation parameters. Instead of the tooth-like structure with multiple thin fingers [121, 132, 133], it is also possible to form wineglass-like structures with only one thin pivoting oxide protrusion [137], column-like structures with a smooth transition between the bottom and cap part [53, 122], or even conical structures [128].

In the rest of this section, the reader will be introduced to two of the recent studies by Bendová et al.[119, 138] These specific studies are especially relevant because the present work follows up their research focused on the study of the formation and properties of titanium oxide nanocolumns formed by PAA-assisted anodisation on various substrates. Moreover, the present work was primarily motivated by pointed-out challenges and limits, as will be discussed later. This section will also serve the purpose of demonstrating the technique of PAA-assisted anodising and formation of titanium oxide nanocolumns in more detail.

Figure 1.13 and Figure 1.14 summarise a few of the most relevant results. Figure 1.13:A shows how the applied anodising potential can control simply the length of nanocolumns during the re-anodising stage. Comfortably, this relation is approximately linear, but it also slightly differs due to the substrate composition, as shown in the SEM images (Figure 1.13:B) and the graph (Figure 1.13:C).

One of the most critical findings of the study is that the morphology and even the chemical composition of nanocolumns depend on the substrate composition (in more detail in ref. [119, 138]) and re-anodising potential. Figure 1.13:D schematically illustrates three selected types of observed morphologies for various TiN$_x$ substrates and selected re-anodising potentials. For further reference, a nanocolumn can be divided into three parts (from the top, see illustration in Figure 1.13:D): 1) column body – filling the pore interior and positioned above the initial barrier layer, 2) the root/s – which penetrate the barrier

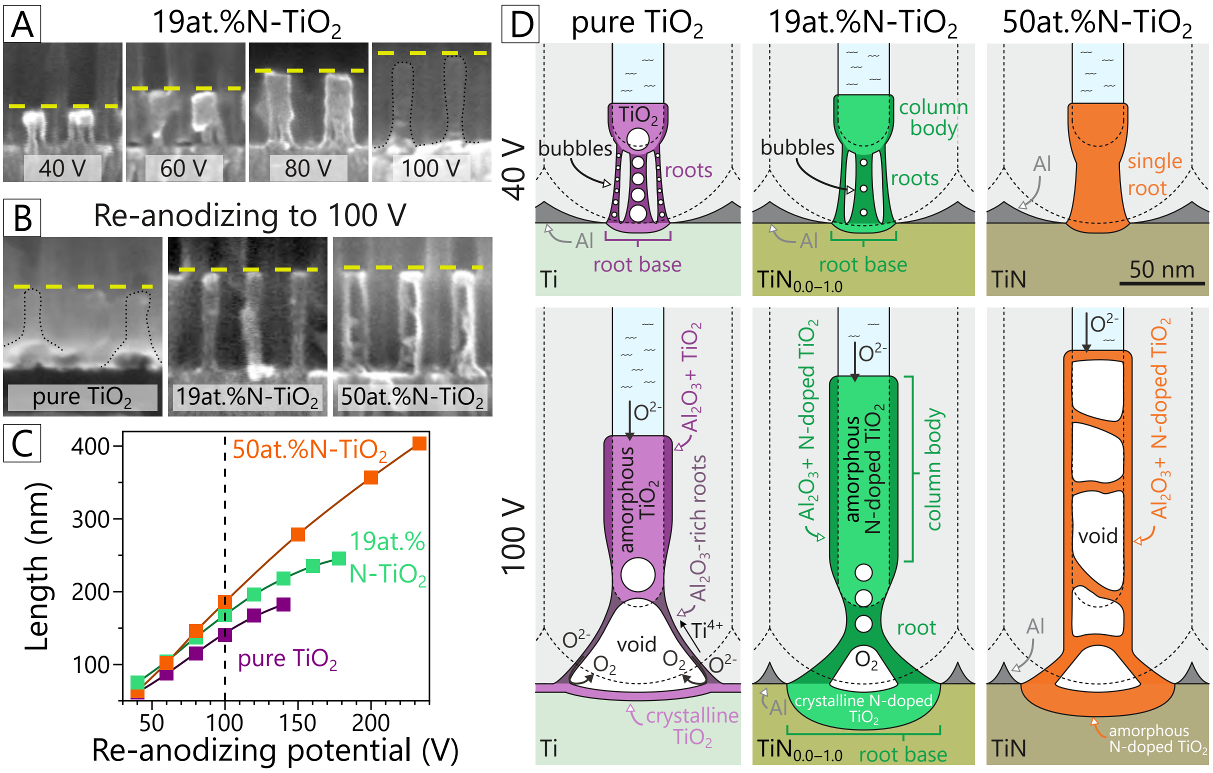

Figure 1.13: Cross-section SEM images of selected PAA-embedded N-doped TiO$_2$ nanocolumns: (A) 19 at%.N-TiO$_2$ grown at various re-anodising potentials and (B) of various substrate doping re-anodised to 100 V. The yellow dash line marks the column top. (C) The length of N-doped TiO$_2$ columns vs re-anodising potential for substrates of selected nitrogen concentrations. (D) Schematic model of columns formation from various substrates at two significant growth stages (40 and 100 V) with expected ionic transport processes. Reproduced and adapted with permission from ref. [119].

layer and connect the column body with the bottom part – 2) root base. The morphology and chemical composition of nanocolumns are tied to their electrical and optical properties. However, they play a crucial role in the fabrication process as they determine the final yield of the free-standing nanocolumns after removing the supporting PAA. The PAA removal is usually performed by selective wet etching that preferentially attacks the alumina, leaving the remaining components (e.g., Al, Ti, TiO$_2$) intact. However, the mechanical stability of nanocolumns can be weakened by a partial intermixing of alumina within the a-MO$_x$ structure. These presumably less chemically stable alumina mixtures are then etched away together with the rest of the PAA, crippling the mechanical integrity of nanocolumn structures. Because structural weakness and alumina intermixing concentrate in the root area, they make it the weakest part.

The stability of a single column has only two resulting states: a free-standing column that survived the etching or a broken column that did not. Since the PAA is not well-ordered, this unevenness forms columns of slightly different properties and creates a good

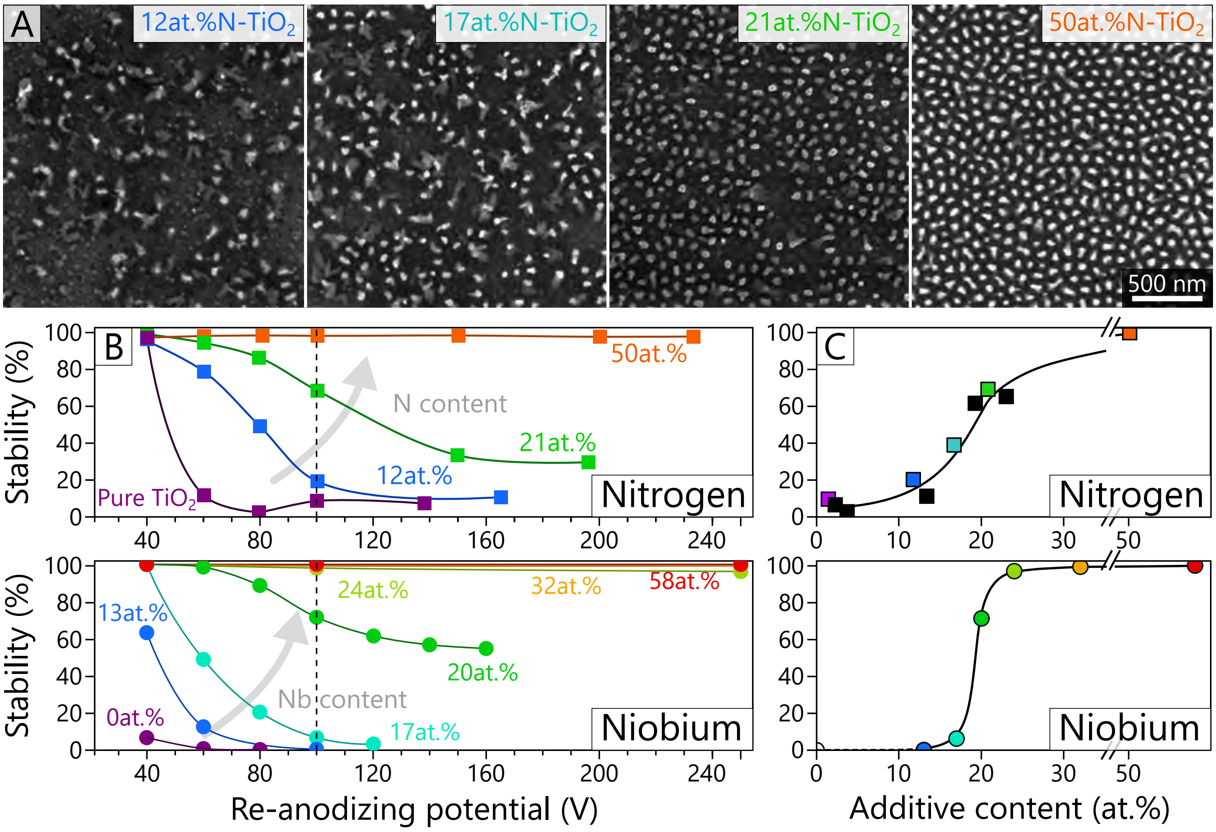

Figure 1.14: (A) SEM images of PAA-free N-doped TiO_2 nanocolumns derived from PAA-assisted anodising of TiN_x substrates of various nitrogen content re-anodised to 100 V. (B) The stability vs re-anodising potential for nitrogen and niobium doped Ti substrates with various doping concentrations. The dashed line marks a cut at 100 V re-anodising potential that is plotted separately in (C) for better illustration. These results for nitrogen and niobium doped samples were obtained at different conditions (refer to original studies). Reproduced and adapted with permission from ref. [119, 138].

statistical sample. Therefore, the stability of the whole array can be estimated as the fraction of free-standing columns to all columns. The evaluation is performed from the SEM images (Figure 1.14:A), where free-standing columns are seen as bright spots while broken columns are usually washed away, leaving a much darker root base.

Graphs in Figure 1.14:B, C show the estimated stability of nanocolumn arrays formed on Ti-based substrates of various nitrogen or niobium content and re-anodised to selected potentials. The most important conclusion is that the stability decreases considerably with the increased re-anodising potential, limiting the attainable length of nanocolumns. The studies show that a significant improvement can be achieved by adding nitrogen or niobium into the titanium layer, thus changing the substrate composition. These admixtures improve the stability, and even longer nanocolumns can be obtained for a selected re-anodising potential (Figure 1.13:D).

1.7 Motivation and aims of the work

In recent years, TiO_2 nanostructures became a hot topic to benefit from increased surface area and decreased bulk volume. Among other techniques (e.g., hydrothermal, sol-gel, physical/chemical vapour deposition), the synthesis of nanotubes/nanopores by anodic oxidation of titanium, an analogy to the PAA fabrication, became the most popular and deeply studied.[7, 9, 139] Despite its popularity, the synthesis requires an aggressive fluorine-based solution that contaminates the titanium nanotubes by fluorine ions and represents an additional safety hazard during the fabrication process. In these regards, the PAA-assisted anodisation (discussed in the previous section) presents a more convenient and environmentally friendly alternative for fabricating TiO_2 nanostructures.

However, compared to the titanium nanotubes (TNTs), this area is barely explored, as can be evident by no reports studying the electrical or photoelectrical properties of these TiO_2 nanocolumns (except for one conference paper [140] from our group). One of the reasons may originate from the difficulty of forming stable and reasonably high nanocolumn arrays. Such an unexplored and challenging area greatly motivates this work to investigate further the fabrication process and properties of TiO_2 nanocolumns formed by this unconventional anodising technique.

As for most TiO_2-based nanomaterials, the ultimate goal is to develop a photo-anode material that can be utilised in solar energy harvesting and water splitting applications. The photocatalytic performance of nanocolumns should be enhanced by minimising the drawbacks of TiO_2, which are the relatively wide bandgap and poor electrical properties. In the literature, two approaches are frequently used to decrease the bandgap of TiO_2 and change its photocatalytic activity towards visible light absorption: i) doping TiO_2 with different elements (e.g., Nb, Ta, N, C); and ii) thermal treatment of TiO_2 in various environments.

Therefore, the objective is split into several tasks:

(i) The investigation of the electrochemical properties of nanocolumn arrays formed from various compositions of substrate demonstrates the effect of doping, while different thermal treatments prove a positive effect of the phase transition and possible formation of oxygen vacancies.

(ii) The main objective of the work is the study of the photoelectrochemical properties of nanocolumn arrays. This study demonstrates the advantages and possible drawbacks of nanocolumn arrays compared to more common TiO_2 surfaces.

(iii) Later, another objective was added due to adverse outcomes from the last part. It was found that poor nanocolumn stability and hollow morphology present severe obstacles on the way to any significant performance. Therefore, the goal was to obtain better stability for a wide range of nanocolumn arrays (substrates, heights). All this was performed by a systematic study of anodising parameters and their effects on the nanocolumn morphology and stability.

2 EXPERIMENTAL, RESULTS AND DISCUSSION

2.1 Fabrication of TiO_2 nanocolumn arrays

Anodisation processes were conducted in two technologically different setups: a flow-through pressing cell and a large-scale fabrication setup. As both setups have different pros and cons, their use varies based on the application. While the pressing cell setup can be advantageous in research and development areas such as finding the right anodising conditions, the large-scale fabrication setup can be utilised for high throughput fabrication where good uniformity in each batch is guaranteed.

2.1.1 Substrates

In this work, the titanium oxide nanocolumn arrays were fabricated by the PAA-assisted anodisation of bilayers of superimposed aluminium on a substrate layer based on titanium (oxidised to some degree) with an admixture of nitrogen or niobium. Table 2.1 summarises the bilayers used in this work (the labels representing the fraction of admixture are used for reference in the further text).

Table 2.1: Parameters of bilayers, used in this study, of superimposed aluminium over substrate layer.

Label	Substrate layer	Thickness [nm]		Atomic concentration [%]				
		Al	Substrate	Ti	O	N	C	Nb
Ti	Ti	500	200	not available				
⅕N	TiO_xN_y	500	$380^\dagger$	50.6	32.6	9.5	7.4	
¼N	TiO_xN_y	600	200	71.5	0.9	18.2	2.4	
⅓N	TiO_xN_y	600	$210^\dagger$	49.8	28.2	16.3	5.8	
1⁄1N	TiO_xN_y	600	$405^\dagger$	40.1	15.4	40.3	4.2	
¼Nb	TiO_xNb_y	600	150	42.1	32.4	3.3	7.1	10.5

† Value estimated from a SEM measurement. Otherwise estimated from deposition parameters.

All bilayers except ¼Nb were sputter-deposited (by Dr Imrich Gablech) on 4 inches oxidised Si wafers using an ion-beam sputtering apparatus (Bestec) equipped with a radio frequency inductively coupled plasma (RFICP) Kaufman ion-beam source.[119, 141] ¼N with the admixture of niobium was sputter-deposited (by Dr Jan Prášek) in the magnetron sputtering system (Bestec, reference) co-sputtering from Ti and Nb targets.

Compositions of substrate layers, tabulated in Table 2.1, were estimated by XPS (section A.4). Before the analysis, the samples were immersed in an aqueous 0.1 M sodium hydroxide solution to remove the superimposed Al layer. Afterwards, they were cleaned in deionised water (MiliPore, 18.2 MΩ) and dried by a nitrogen stream. Compositions of substrates were then estimated by XPS analysis. The quantification was performed from broad XPS spectra obtained after several sputtering cycles (Ar^+, 5 keV).

2.1.2 Anodisation in the flow-through pressing cell setup

The flow-through pressing cell (illustrated in Figure 2.1:A) consists of a cylindrical polytetrafluoroethylene (PTFE) body with a silicon o-ring seal (inner diameter of 7 mm) that confines the anodising area. A gold wire coiled around a glass inlet tube is used in this setup as a counter electrode (CE) and a horizontally placed sample as a working electrode (WE). Both electrodes are connected to a source meter by 4-wire sensing (with a current limit of 21 mA, Keithley 2410) controlled through a home-made software interface (Labview). An electrolyte exchange is secured by a membrane pump (KNF SIMDOS 10) with a flow rate of 70 cm min^{-2}.

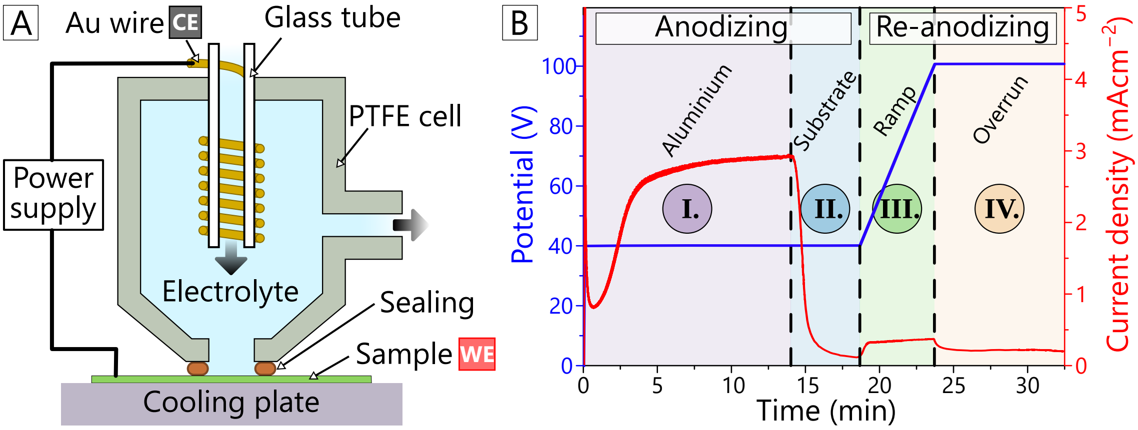

Figure 2.1: (A) Schematic illustration of the flow-through pressing cell during anodisation. (B) A representative example of current density vs time response (red line) during potential-controlled (blue line) anodisation of aluminium/titanium bilayers (Table 2.1: ¼N) in the pressing cell setup.

For this setup, bilayers were processed as received without any additional cleaning or area masking. The wafer was cut to square samples with a side length of at least 10 mm. All anodising processes were performed in a potential controlled regime in a 0.3 M aqueous solution of oxalic acid (Sigma-Aldrich) placed in a reservoir of 500 ml volume and cooled to the desired temperature. Before each anodisation process, the setup (the cell, silicon tubes, and sample) was tempered for at least 5 minutes by electrolyte circulation.

As an advantage of the pressing cell setup, no advanced sample preparation is necessary, which dramatically speeds up the R&D process. Additionally, the WE is well defined, ensuring a reasonable control over the current flowing through the sample and a more straightforward comparison between various anodising methods. In general, disadvantages of the setup include a small WE, non-ideal control of temperature or electrolyte flow, and the CE geometry.

Figure 2.1:B shows the classical behaviour of process parameters (used in this work) during the PAA-assisted anodisation. This process can be divided based on ongoing events (schematically illustrated in Figure 1.12) into four stages: I.) aluminium anodising, II.) substrate anodising, III.) re-anodising ramp and IV.) re-anodising overrun.

First (Figure 2.1:B stage I), the top aluminium layer is porously anodised (Figure 1.12:B). This process is typically done in a potentiostatic mode at 40 V and in 0.3 M oxalic acid to ensure one of the best pore self-ordering (section 1.5). Stage I lasts until the PAA reaches the bottom substrate layer while consuming almost the whole aluminium layer. When stage I ends and stage II starts, a sudden decrease in the current density occurs.

During stage II, two simultaneous events occur; finalisation of the PAA growth causes a significant current density decrease and anodisation of the substrate layer forming initial nanocolumn nuclei at the bottom of pores (Figure 1.12:B stage II). Exponential decay of current density is typical for this stage.

The most probable reason for this slow decay instead of an abrupt drop is the geometry of the PAA bottom consisting of hemispherical pores with a radius of 50 nm. This value approximately matches the estimated consumption of Al, 37 nm, during the first steeper period of substrate anodising (≈ 1 min). The Al consumption rate was estimated based on the initial thickness of Al film and the period of aluminium anodising, which is $0.6\,\mathrm{nm\,s^{-1}}$ in this case (Figure 2.1:B) for anodising at 7 °C. Another contributing factor may be the initial roughness of Al film, an uneven anodising across the sample area, and the growth of nanocolumn nuclei.

Afterwards , nanocolumn nuclei can be lengthened by a so-called re-anodising process (stage III and IV) characterised by a higher anodising potential. This process is divided into a potentiodynamic and a potentiostatic part. The potentiodynamic regime (stage III) represents a rising linear sweep (ramp) of anodising potential, starting at the PAA formation potential and finishing at the so-called re-anodising potential. Here, nuclei grow in length with the increasing potential accompanied by an increase of the current density. In the next stage (stage IV), the growth of nanocolumns halts when a constant re-anodising potential is applied, which gives a current density decay. During this stage, no further morphological changes are expected; however, findings show this stage may influence the chemical composition or crystal structure within the roots of nanocolumns (as will be discussed in later section 2.2).

2.1.3 Anodisation in the large-scale processing setup

In contrast to the individual processing limited by the small diameter of the pressing cell (Figure 2.1:A), the large-scale fabrication process was developed to enable the production of large-scale samples as well as to improve the uniformity control over a large sample area. This setup, illustrated in Figure 2.2:A, uses the same large reservoir of the cooled electrolyte, but instead of delivering it through a circulating system to the sample, the sample is directly immersed into it. The setup includes a two-electrode cell with the partly immersed sample as the anode and a stainless-steel mesh (100 cm) as the cathode. Anodisation experiments in this part were conducted in the same electrolyte (0.3 M oxalic acid) cooled to 10 °C and gently stirred by a magnetic stirrer.

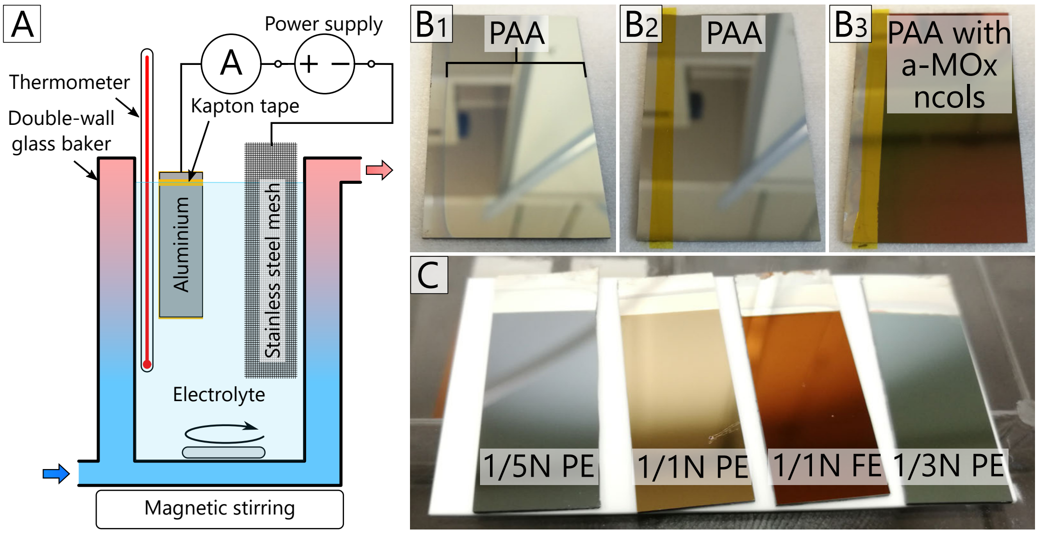

Figure 2.2: (A) Schematic illustration of the large-scale processing setup. (B1–3) Photographs of individual steps of sample processing by the large-scale fabrication process. (B1) A pre-anodised sample partially covered by a PAA layer. (B2) A Kapton strip application on the sample before the second step (left – part for electrical contact, right – anodised part). (B3) Sample after the whole anodisation process. (C) Anodised layers after partial etching (PE) and full etching (FE) of PAA as discussed in the next section (SEM images shown in Figure 2.5).

This setup allows larger samples with up to 50 cm compared to 0.4 cm for the pressing cell setup. It is beneficial mainly in experiments, which require a perfect uniformity of the batch. A large piece can be anodised all at one and then split into several smaller identical samples, which can undergo various post-anodising processing such as PAA etching or thermal annealing. However, this technique has a few drawbacks. The major one is that the sample needs special processing by splitting the anodisation into two parts. Due to common parallel parasitic currents through the sample edges or complicated sample area, the anodisation is better suited for potentiostatic control instead of galvanostatic one.

Before anodisation, the wafer with the deposited layers was cut into 40 mm×25 mm pieces (Figure 2.2:B1), which were backside laser-grooved into four strips of 10-mm width for later dicing.

On the contrary to the previous processing, the anodisation of Al is divided into two steps. The first step (pre-anodising) was conducted with the initial ramp of $5\,\mathrm{V\,s^{-1}}$ from 0 to 40 V and the current limit of 100 mA, followed by a constant 40 V anodising for 200 s (the obtained curves are shown in Figure 2.3:A). Afterwards, the samples were thoroughly washed in deionised water and dried by an air stream . This purely technological step creates a thin PAA layer that, with an additional strip of Kapton tape (Figure 2.2:B2), prevents further undesirable soaking of the sample due to wetting with electrowetting and secures a stable processing area (20 mm×10 mm). Naturally, the Kapton strip has to be aligned with the water level, as illustrated in Figure 2.2:A. The second step (Figure 2.3:B) continues with the Al anodisation at the same potential (40 V). Then, it is followed by substrate anodising starting around the tenth minute (600 s). The re-anodising ramp of 0.2 V s^{-1} to 100 V starts after 5 minutes of substrate anodising, followed by a 5-minute re-anodising overrun. These conditions were the same for all samples of various substrates (1/5N, 1/3N, two pieces of 1/1N) used for the photoelectrochemical experiments.

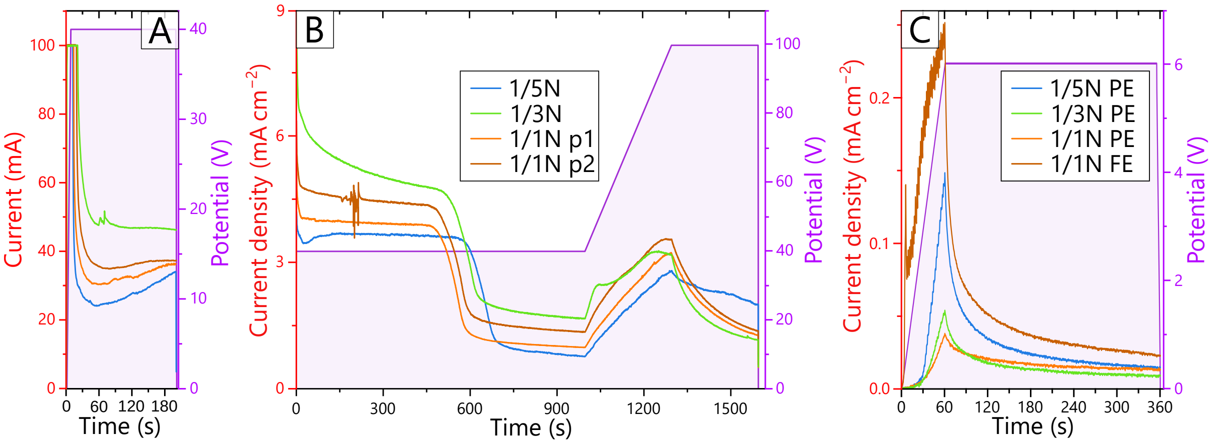

Figure 2.3: Anodising curves of samples prepared by the large-scale fabrication anodising process. (A) Pre-anodising with the initial ramp of 5 V s^{-1} to 40 V. The Y-axis does not show the current density because the area of the immersed sample changes due to wetting. (B) Continuing with Al and subsequently substrate anodising followed by the re-anodising ramp (0.2 V s^{-1}) performed at 1000 s after the start. (C) Post-anodising of etched samples with the initial slope of 0.1 V s^{-1} to 6 V and 5-minute overrun.

Compared with the flow-through pressing cell anodising, the large-scale process has a few possible drawbacks. In the case of conductive support (e.g., Si wafers), an issue may arise due to the parallel current flow through the sample edges. In practice, this manifests as the constant current density offsets noticeable between individual samples (Figure 2.3:B, C). Compared to the pressing cell setup (Figure 2.1:B), the current densities are offset by 1–2 mA cm^{-1}; however, the formed layers are identical (morphology and stability). Moreover, small current spikes appear for 1/3N (Figure 2.3:A) and 1/1N p2 (Figure 2.3:B). These features are typical for micro delamination of the layers, which can occur at the sample edges. Another very minor drawback is the splitting of the aluminium anodising process. However, except for a slightly modified technological aspect, it has a negligible impact on PAA formation, especially the nanocolumn structure. The splitting occurs much before the PAA containing nanocolumns is formed. From the PAA thickness perspective, the split happens around 550 nm height from the bilayer interface while the nanocolumn length is only 180 nm (for 100 V re-anodising of 1/1N, Figure 2.5:C2).

2.1.4 Wet etching of PAA

The PAA-assisted anodisation creates an array of anodic metal oxide (a-MO$_x$) nanostructures still embedded within the PAA template. Such embedded arrays were also the subject of this study (as discussed in the next section 2.3), although many applications require removing the passive PAA template and revealing the whole active surface of nanocolumns. The increase in the accessible surface is significant. For cylindrical geometry, it is at least 5× and 40× increase for columns with the aspect ratio of 1 and 10, respectively.

After the anodising process, the samples were thoroughly washed in deionised water and dried by a nitrogen stream. The PAA was removed by chemical wet etching in an aqueous solution of 0.42 M phosphoric acid (H_3PO_4) and 0.2 M chromium trioxide (CrO_3) at 65 °C (based on the etching process in ref. [142]). The extent of the PAA removal was controlled by the etching time, after which the samples were quickly washed in water and dried again.

Figure 2.4 reveals various stages of the selective PAA removal around the a-MO$_x$ nanocolumns. The PAA surface (Figure 2.4:A) reveals an imperfect hexagonal arrangement of pores overlapped by a grainy texture inherited from the sputter-deposited initial Al layer. The etching first removes the part of PAA placed above the nanocolumns as it is easily accessible through the open pores. This step reveals the nanocolumn array still within the PAA matrix (Figure 2.4:B). Notably, numerous overetched sites occur as the etching solution finds its way into the defects formed at PAA cell boundaries, e.g., triple-junctions. An additional etching leads to a partial (Figure 2.4:C) or complete (Figure 2.4:D) removal of the surrounding PAA, and thus a reveal of the underlying substrate layer. Figure 2.4:D shows freestanding a-MO$_x$ nanocolumns that appear as bright spots surrounded by a darker area of larger perimeter representing the anodised substrate at the bottom of nanocolumns – the root area. Depending on the anodising conditions and the substrate composition, it is possible to obtain a perfectly stable, partly stable, or even completely unstable column layer. Unstable columns usually break in the root part, leaving just the bottom root area that appears much darker in the SEM (Figure 2.4:C, D). Fallen nanocolumns can also be observed in Figure 2.4:D.

Better control over the PAA removal was achieved with larger samples made in the large-scale processing setup (see Figure 2.3). The main reason was the decrease of the etching temperature to 60 °C and a larger volume (500 ml) of etching solution with steady magnetic stirring (500 RPM). Figure 2.5 shows successful partial removal of the PAA layer, so the nanocolumn arrays of various heights are equally exposed. However, still, numerous overetched sites occur in the PAA. These sites expose the underlying substrate layer to a degree related to the thickness of the remaining PAA and nanocolumn lengths. When the columns get longer, and thus the remaining PAA gets thicker (in the order $^1/_5$N $<$ $^1/_3$N $<$ $^1/_1$N), the overetching cannot dig through the whole layer for given conditions. In addition to SEM images (Figure 2.5:A, B, C1), this is also proven by the

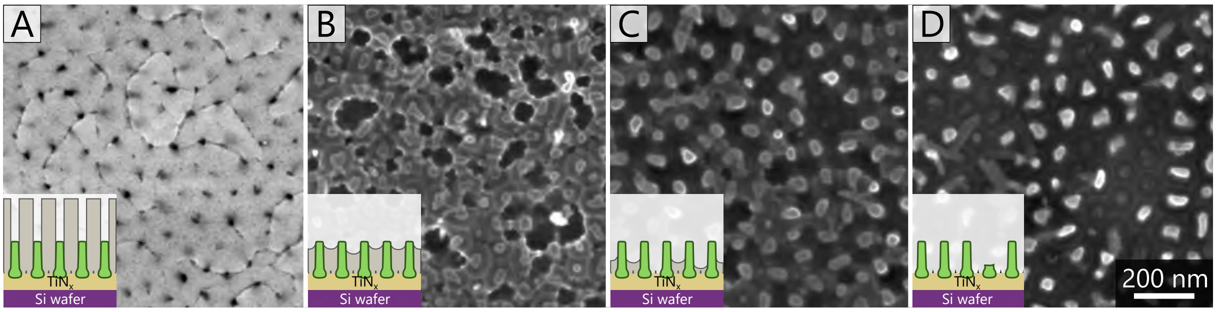

Figure 2.4: Top view SEM images with schematic illustrations of as-anodised (Figure 2.1:B) ¼N bilayer structures: (A) no etching, (B) 6 min, (C) 9 min, and (D) 15 min etched.

increased current consumption during the anodisation of these layers, labelled here as the post-anodising (Figure 2.3:C). The cross-section of Figure 2.5:C1 (right) captures the depth of an overetched site showing almost complete penetration through the PAA. These overetching sites create a characteristic clover-like feature in the top view of SEM (Figure 2.5:C1).

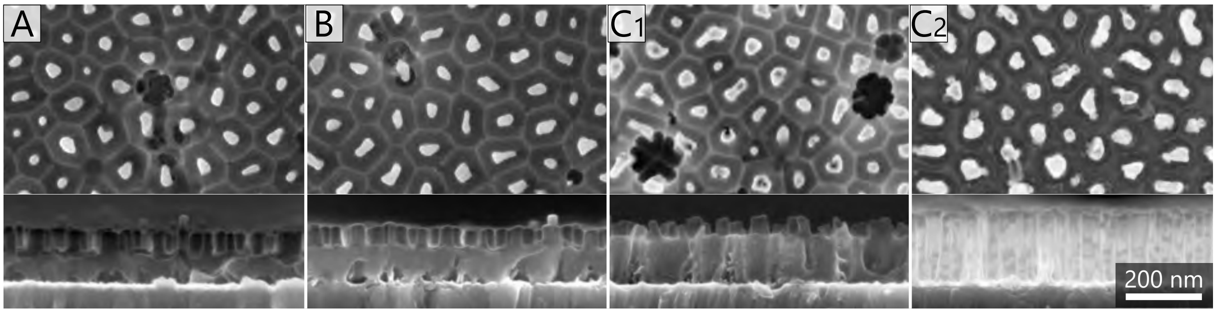

Figure 2.5: SEM images of partly etched (PE) (A) ⅕N, (B) ⅓N, (C1) 1⁄1N, and (C2) fully etched (FE) 1⁄1N nanocolumn layers (Figure 2.3). Samples were etched for 23 and 80 min, in the case of PE and FE, respectively. The length of exposed columns is approximately 70 nm for PE ⅕N, ⅓N, and 60 nm for PE 1⁄1N layers. The thickness of remaining alumina layer was estimate to 80, 110, and 140 nm for ⅕N, ⅓N, and 1⁄1N layers, respectively. The length of FE 1⁄1N nanocolumns is approximately 190 nm.

For the complete removal of PAA, it is necessary to prolong the etching time based on the length of nanocolumns. During this work, the etching time of two hours was found sufficient for all cases re-anodised to up to 330 V with the column length of 500 nm (¼Nb).

It is important to note that this selective PAA etching does not attack aluminium. A residual aluminium layer may be found on many samples as it is not fully anodised during the anodisation process (Figure 2.6:A). These Al residues can be further completely removed in an aqueous solution of sodium hydroxide (e.g., 3 minutes in 1 M NaOH), as shown in Figure 2.6:B.

A short PAA etching of 90 s was also utilised to enhance the contrast of SEM cross-sections of some samples with columns still embedded in the PAA (Figure 2.7). This slight

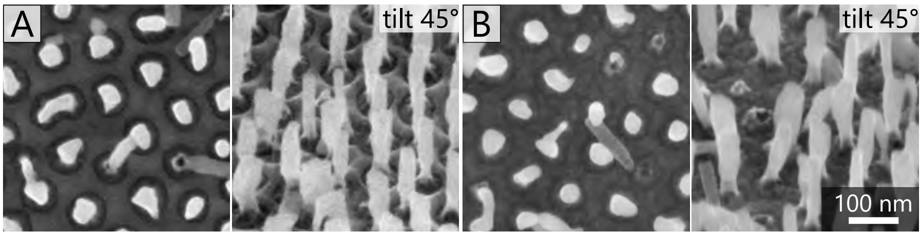

Figure 2.6: SEM images of a FE nanocolumn layer (A) before and (B) after removing residual the Al layer in a NaOH solution.

etching reveals the column morphology and some details of the structure of PAA (cell boundaries). For example, it is possible to observe a detailed structure of PAA cell walls and to see the pure alumina represented by brighter contours at the cell boundaries.[143, 144]

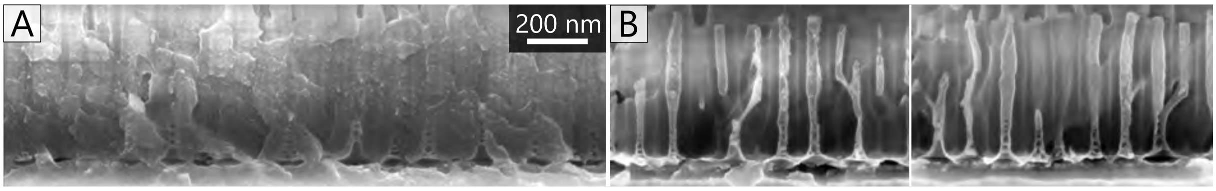

Figure 2.7: SEM cross-section of a nanocolumn layer (1⁄5Nb anodised to 250 V) embedded in PAA (A) before and (B) after short 90 s PAA etching.

Conclusions

This section presents the complete fabrication process of a-MO$_x$ nanocolumns by a PAA-assisted anodising of the listed substrates with a superimposed aluminium layer. Two fabrication setups used in this work were introduced. The pressing cell setup, aimed for research and development, will be mainly used in the following sections to study the anodising parameters and their effect on the stability of columns and a short electrochemical characterisation of nitrogen-doped PAA-embedded a-MO$_x$ nanocolumns. On the other hand, the large-scale fabrication setup was used to prepare samples with various post-treatments such as PAA etching or thermal annealing.

The second half of the section is focused on the PAA removal as it is the only way to achieve free-standing nanocolumns. Despite a few drawbacks, such as overetching leading to defective sites, this process can be well-tuned to achieve the desired column exposure. A short etching was also used prior to SEM cross-section observation to enhance the column contrast within the PAA.

2.2 Morphology and stability of nanostructures

The previous section describes the fabrication process of titanium oxide nanocolumns by the PAA-assisted anodising of an aluminium layer superimposed over a substrate layer. This section further focuses on the vast possibilities of how to influence their morphology, structure, or even their chemical stability. As discussed in the subsection 1.6.3, the stability of a-MO$_x$ nanocolumns depends on the substrate composition and the re-anodising potential at which the columns are formed. The stability drops significantly with increasing titanium purity, thus decreasing the concentration of additives (nitrogen [119], niobium [138]) in the substrate layer (Figure 1.14:C). A similar rapid decrease of stability is observed for the increasing re-anodising potential (Figure 1.14:B) while other parameters are kept constant. Overall, these results demonstrate that the selected anodising conditions will not yield a stable column layer re-anodised to over 100 V for substrate layers with low concentrations of additives (<20 at.% of nitrogen [119] or niobium [138]). Sadly, it limits the potential length of columns, decreases their active surface area, and reduces their competitiveness in possible applications.

These unfavourable findings motivate the following study focused on the effect of anodising parameters on the stability of nanocolumn arrays. The main goal is to achieve a perfect or at least better stability for nanocolumn arrays of various column lengths deriving even from substrates with a low concentration of additives (N, Nb). This section presents a summary of a systematic study conducted to understand the effects of individual anodising parameters.

In this section, all experiments were performed on the titanium substrate layer with 10.5 at.% of niobium (¼Nb, Table 2.1), if not mentioned otherwise. This layer was selected based on its poor stability results, shown in the study of colleagues (mentioned in section 1.6).[138] All anodisation experiments were performed in the flow-through pressing cell setup (Figure 2.1:A) using a 0.3 M aqueous solution of oxalic acid and the flow-rate of 70 mL min^{-1}. The majority of the experiment was performed in the electrolyte tempered at 24 °C, if not stated otherwise. The study varies the temperature and the duration of the individual anodising stages (Figure 2.1:B): aluminium and substrate anodising, re-anodising ramp, and overrun. The first potential ramp of aluminium anodising was kept 5 V s^{-1} for all experiments. It is assumed that this ramp does not influence the column morphology or stability as the columns are too short of reaching the PAA surface, which is formed at the beginning of the anodisation period when the ramp is applied.

Furthermore, it was found that various steep ramps give a similar breakdown potential that can be partly correlated with similar column morphology (subsection 2.2.3). Therefore, only the residual anodising steps (i.e., substrate anodising, re-anodising ramp, and overrun) were investigated. The PAA removal (subsection 2.1.4) was done in the same way for all samples by selective etching in the PAA-dissolving solution for 2 hours at 65 °C.

2.2.1 The effect of temperature

The effect of electrolyte temperature on the morphology and stability of nanocolumns has one of the most complex natures as it influences a series of other anodising parameters, and thus, its impact cannot be fully isolated from other variables. Here, Figure 2.8:B presents nanocolumn arrays formed on the pure Ti substrate at various electrolyte temperatures. These nanocolumns were finished with a substrate anodising for 5 minutes, and thus without any re-anodising stage. The re-anodising stage was skipped to keep as few variables as possible.

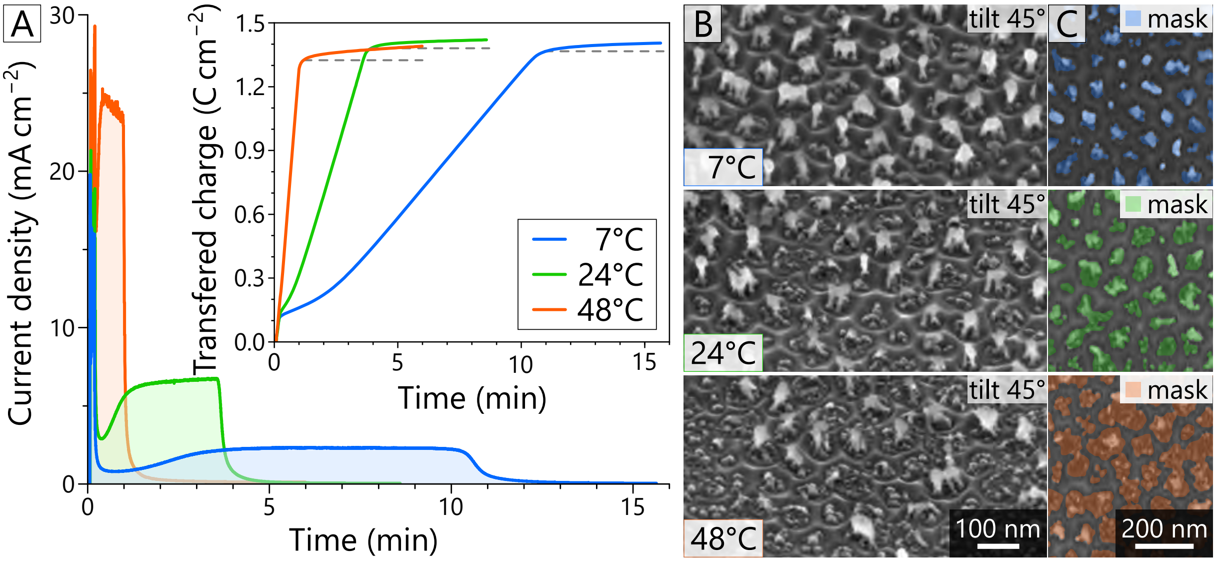

Figure 2.8: (A) Current density response during the potentiostatic anodising at 40 V of Ti samples at various electrolyte temperatures. The substrate anodising was done for 5 min. The inset graph shows the calculated transferred charge. (B) Tilted SEM images of formed columns after the PAA removal and (C) top views with the masked root base area of 20, 30, and 58 % for 7, 24, and 48 °C anodising temperatures, respectively.

Increasing the electrolyte temperature leads to an anticipated boost in the kinetics of reactions. This boost manifests as a shorter anodising period accompanied by an increased anodising current, as shown in Figure 2.8:A. Columns formed in this way vary considerably in morphology as well as stability. The morphology of columns can be explained based on the temperature-induced changes of the PAA morphology, which other researchers have reported.[98, 145–147] In general, higher temperatures lead to faster alumina dissolution during the PAA growth, increasing the pore diameter. This widening was observed in the SEM cross-views of samples before the PAA removal (not presented); with a pore diameter of 48 ± 6, 51 ± 13, and 66 ± 11 nm for 7, 24, and 48 °C anodising temperatures, respectively. An anodising at a low temperature results in narrower pores, giving a majority of columns a relatively small root area with only one or several roots.

On the other hand, higher temperatures leading to wider pores result in the predominant formation of columns with more roots and a broader root base. For a better illustration, the root area is colour-masked in the SEM images shown in Figure 2.8:C, and the calculated relative coverages are noted in the figure caption. Additionally, the enlargement of the root area can be correlated with the slight increase of charge transferred during the substrate anodising phase, as marked in the inset of graph (Figure 2.8:A).

Additionally, the stability of columns across the layer drops noticeably with the increasing temperature. This counter-intuitive result shows that columns with more roots and a wider root base incline to be less stable. Therefore, it is reasonable to assume that stability of columns does not come from their morphology but rather their root structure or chemical composition. A similar observation was made and supported by additional research in the following works ref. [119, 138]. Here, the authors showed that the main reason for the poor chemical stability of columns (to the etchant of aluminium oxide) is an intermixing of titanium oxide with aluminium oxide from the barrier layer of PAA. This reasoning can also be applied in the presented findings as more roots need to penetrate a wider area, and thus the alumina displacement is much more complex, and heavier mixing has to occur.

2.2.2 Duration of anodising stages

The previous section showed that columns derived from a pure Ti substrate formed even at 40 V have inferior stability. As already reported,[138] the presence of doping agents in the substrate layer can sufficiently increase the stability of columns. This doping effect can also be observed when comparing Figure 2.8:B(24 °C) and Figure 2.9:(5 min), representing the same anodising conditions for columns derived from Ti and ¼Nb substrate, respectively. While the Ti substrate gives an array of less than half the survival rate, the 10.5 at% Nb concentration in ¼Nb substrate is already sufficient to give a complete success rate at the formation potential of 40 V.

However, this section focuses on the individual stages of the anodisation process and how their length influences the stability and morphology of columns. Firstly, Figure 2.9 shows the resulting column layers formed without any re-anodising period and thus finished with substrate anodising at 40 V. These layers differ in periods of the substrate anodising (the second stage in Figure 2.1:B), which starts with the characteristic current density decay after the aluminium anodising stage. Extending this period shows no visible differences in the column morphology or stability at first. However, in the most prolonged period, a single detached column can be found, shown in Figure 2.9:(20 min). Based on a broader view field (5.0 µm×3.3 µm, ≈ 2000 columns), a failure rate of 1 % was estimated. On the other hand, shorter anodising times result in defect-free arrays. These findings indicate that prolonging substrate anodising may slightly decrease the stability of the column.

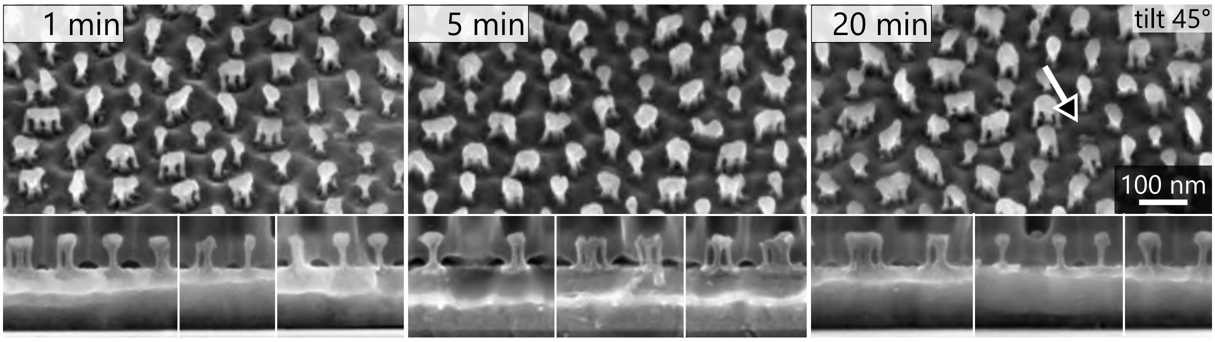

Figure 2.9: Tilted (45°) and cross-view SEM images of (tilted) PAA-free and (cross-view) PAA-embedded nanocolumn arrays formed by PAA-assisted anodising of ¼Nb substrate at **40 V** with **substrate anodising** period: 1 min, 5 min, and 20 min. The re-anodising was not applied. The arrow marks the spot of a detached column (failure rate of 1 %).

A similar experiment was performed with an additional re-anodising to 100 V with a linear ramp of 0.5 V s^{-1} and a 1-minute overrun period (Figure 2.10). Here, the varying substrate anodising period determines the time between the end of aluminium anodising and the start of the re-anodising ramp. As can be seen, prolonging this period dramatically impacts the stability of the final array. From SEM top views (Figure 2.10), survival rates of 84, 82, 60, and 45 % for the 0, 1, 5, and 20-minute substrate anodising period were estimated. Additionally, all column arrays have SEM-indistinguishable morphology except the sample with the 0 minutes (see later). Therefore, changes in the stability are not shape-dependent but presumably due to process-induced variations in the chemical composition.

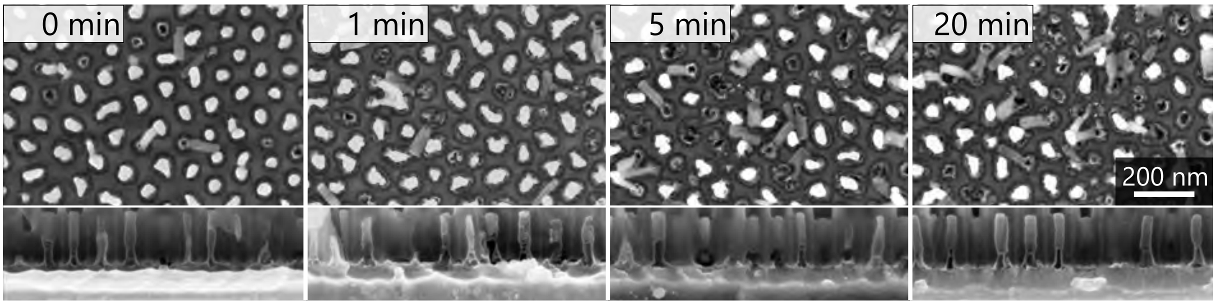

Figure 2.10: Top and cross-view SEM images of (top) PAA-free and (cross-view) PAA-embedded nanocolumn arrays formed by PAA-assisted anodising of ¼Nb substrate. After **substrate anodising** for 0, 1, 5, and 20 min, the sample was re-anodised to **100 V** with **0.5 V$\mathbf{s^{-1}}$** ramp sweep and a 1-minute overrun period.

The sample with the 0 minute of substrate anodising (Figure 2.10:(0 min)) cannot be directly compared with the rest of the batch due to significant morphology deviations. These columns have narrower roots with a slightly less pronounced void structure and a smaller root base area. This effect is much more pronounced for a steeper re-anodising ramp, as shown in Figure 2.11. Here, the ramp of $5\,\mathrm{V\,s^{-1}}$ causes more dramatic changes for the zero-period (0 min) of substrate anodising. The reason is that the end of aluminium anodising is not an abrupt process but instead has an exponential decay due to an inhomogeneous anodising or/and the thickness of the Al layer. An increased anodising potential naturally induces structural changes in the bottom part of PAA. Specifically, a higher potential gives a thicker barrier layer, a wider pore diameter, and a further inter-pore distance, influencing the column morphology. The earlier beginning of the re-anodising leads to thinner and more prolonged column roots, which corresponds to higher forming potentials. The comparison can be observed in cross-sectional view of Figure 2.11, where the width/height of the neck area is $18 \pm 1/76 \pm 8$, $20 \pm 1/37 \pm 2$, $35 \pm 15/(\mathrm{N/A})$, and $48 \pm 8/(\mathrm{N/A})$ nm for re-anodising start at -0.8, 0, 1, and 5 minutes from the start of the current decay (end of Al anodising), respectively. The width was measured in the narrowest point (middle) – the neck of the column. The conically shaped necks (1- and 5-minute samples) were measured at 35 nm height instead.

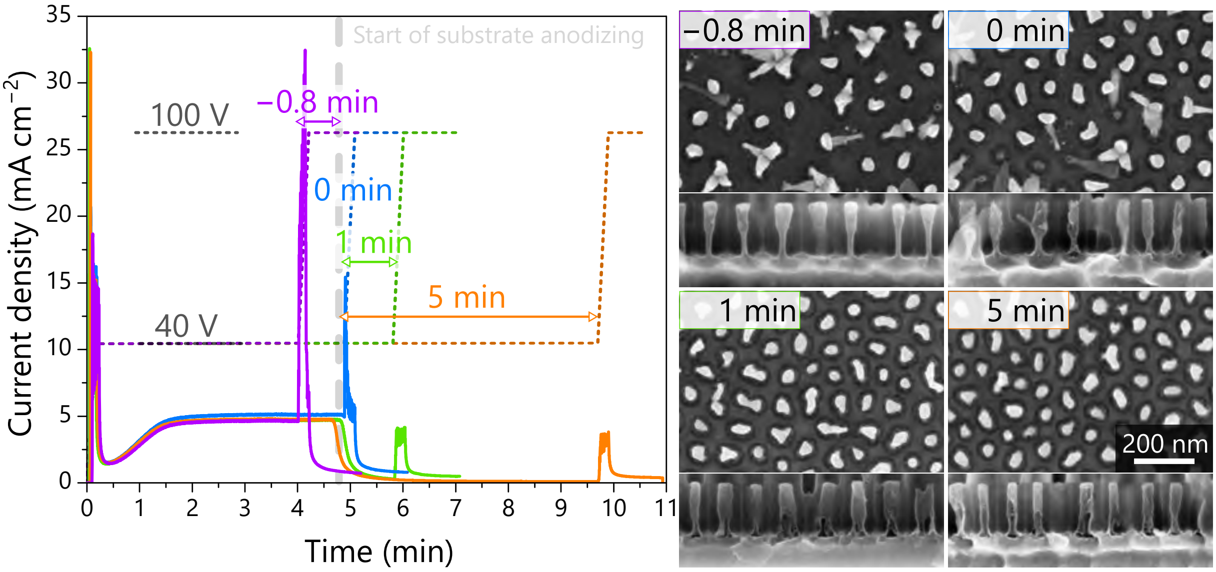

Figure 2.11: Anodising curves showing various periods of the substrate anodising stage with corresponding top and cross-view SEM images of the formed nanocolumn arrays. The re-anodising ramp of $\mathbf{5\,Vs^{-1}}$ to **100 V** with 1-minute overrun is applied -0.8, 0, 1, and 5 minutes (**substrate anodising**) after the end of aluminium anodising. For the sample with the negative value (-0.8 min), the ramp was applied 0.8 minutes before the expected current decay (marked by the dashed line), which has been estimated based on previous anodisation processes.

The poor stability of columns formed by the earlier ramp starts (-0.8 and 0 min) can be associated with narrower column roots, which could weaken the integrity of the structure. On the other hand, a change in chemical composition cannot be omitted since the void structure differs significantly, suggesting deviations in the column growth process. A strong dependence of stability on the chemical structure is also supported by an almost threefold increase of damage for additional etching in a NaOH solution, shown in Figure 2.6. The column survival rate for the sample (Figure 2.10:(0 min)) decreases from 95.5 % after the standard etching in phosphoric acid and chromium oxide solution to 88.4 % after the additional immersion in 1 M NaOH.

Nevertheless, the main finding is that a steeper ramp enormously improves the column stability without any changes in their morphology, as can be seen comparing 1- and 5-minute samples for the 0.5 and 5 $\mathrm{V\,s^{-1}}$ ramps shown in Figure 2.10 and Figure 2.11, respectively. The steeper re-anodising ramp leads to a conspicuous increase of stability from 60 to 99.1 % and 45 to 98.2 % for 1- and 5-minute substrate anodising, respectively. In both cases, the ramps start sufficiently after the Al anodising is finished, not to influence the column morphology, but still, the more extended period of substrate anodising leads to slightly decreased stability.

In addition to the enhanced stability, a faster re-anodising ramp leads to the formation of slightly higher columns (>7 %), as shown in Table 2.2.

Table 2.2: The length of columns (obtain from cross-view SEM images) re-anodised to 100 V with various re-anodising ramps and periods of substrate anodisation.

Re-anodising ramp [$\mathrm{V\,s^{-1}}$]	Nanocolumn length [nm]				
	−0.8 min	0 min	1 min	5 min	20 min
0.5		$176.0 \pm 4.7^{\dagger}$	164.0 ± 6.1	162.7 ± 6.0	166.7 ± 5.0
5.0	$178.3 \pm 3.7^{\dagger}$	$181.8 \pm 4.1^{\dagger}$	175.7 ± 4.5	172.9 ± 7.5	

† A change in the column morphology due to an early start of re-anodising ramp.

An increase of the re-anodising potential to 250 V while preserving other parameters gives relatively stable (>95 %) column arrays (data not presented). However, an undesired breakdown occurred during these anodisation processes (as discussed in detail later). Although it does not influence the column stability, it damages the macroscopic areas of the column array.

One way to shift the breakdown process to a higher potential and avoid it completely during the entire anodisation is to increase the re-anodising ramp. An increase to 50 $\mathrm{V\,s^{-1}}$ sweeping up to 250 V re-anodising voltage results in columns (shown in Figure 2.12) with the height of 422.5 ± 11.0 nm and 406.4 ± 4.5 nm for 0- and 1-minute substrate anodising period, respectively. Surprisingly, almost no detached columns would give these samples 100 % stability. However, it is evident that the stability is not perfect due to many columns supporting and leaning towards each other. Therefore, this situation can be better described by the single-standing columns. For the 0- and 1-minute samples, this number was estimated to be only 24 and 14 % of the total columns, respectively. Again, the prolonged substrate anodising results in worse properties. However, this time it is assumed that the main reason is the mechanical weakness caused by defects/voids within the root area, as marked in the top view of Figure 2.12:(1 min). Again, the prolonged substrate anodising period leads to significantly broader roots (68 vs 101 nm) with fewer aluminium residues. On the other hand, a major role can be played by the height of the columns, which are more than twice higher than columns re-anodised to 100 V. Naturally, columns of this height incline more towards clustering, which is caused by capillary forces during the sample drying or even electrostatic forces (an example is shown in Figure A.4).

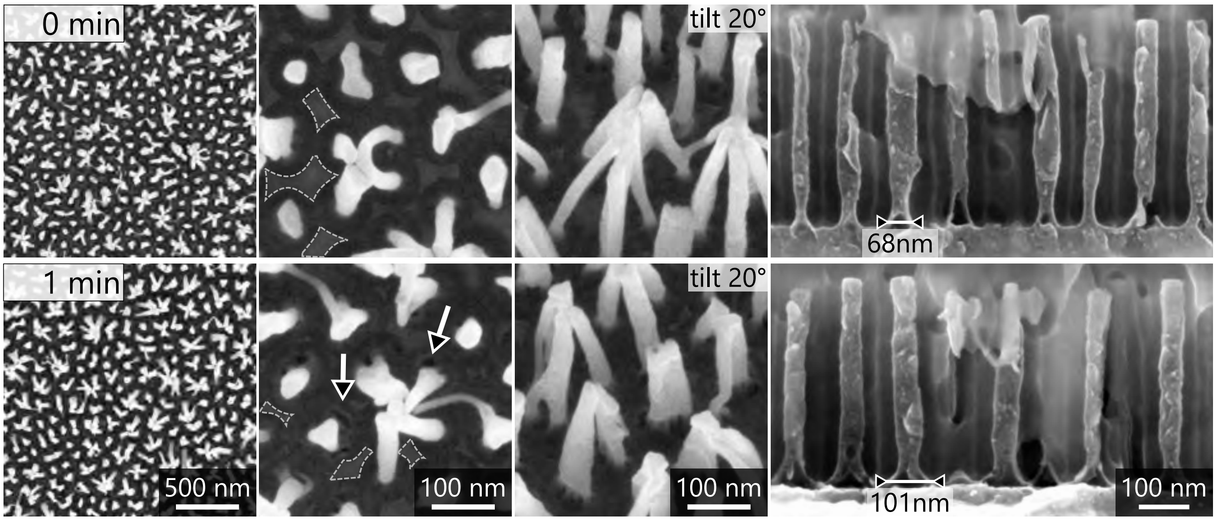

Figure 2.12: SEM images of PAA-free and (cross-view) PAA-embedded nanocolumn arrays formed by PAA-assisted anodising of ¼Nb substrate with 0- and 1-minute **substrate anodising** followed by **50 Vs^{-1}** re-anodising ramp to **250 V** with no overrun stage. Defects within the root area (arrows) and residual aluminium (highlighted area) are marked.

The second way how to shift the breakdown process is by decreasing the temperature of the electrolyte. The temperature-dependent kinetics of reactions can roughly explain this. When the temperature decreases, it slows down the reaction rate and presumably also the anodising development. Furthermore, a slow change of the potential relative to the slow anodising rate can have the same effect as the faster combination. Therefore, the re-anodising ramp is not a single parameter function because it relates to a complex anodising development that depends on the time, temperature, and concentration of additives in the substrate. A simple illustration is a breakdown potential shift from 280 V (24 °C) to 328 V (7 °C) for the re-anodising ramp at 5 V s^{-1} and 0-minute substrate anodising.

The last free parameter in terms of anodising time is the overrun period. This period is the last stage before the cell is disconnected from the power source. A potentiostatic regime characterizes the overrun at the final and highest applied potential. A trend can be observed in Figure 2.9 with no re-anodising ramp that leads to overlap of the substrate anodising and the overrun stage. A more distinguished trend is shown in Figure 2.13, between a relatively stable and mostly damaged array for 1- and 20-minute overrun periods, respectively. In both cases, the columns are of a similar height and morphology of the column body. However, the root area differs. Again, the more extended period

(20-minute) leads to broader roots of 106 ± 15 nm versus 95 ± 15 nm (1-minute), similarly as shown in Figure 2.11. Similarly, this can also be noticed by the decrease of aluminium residues.

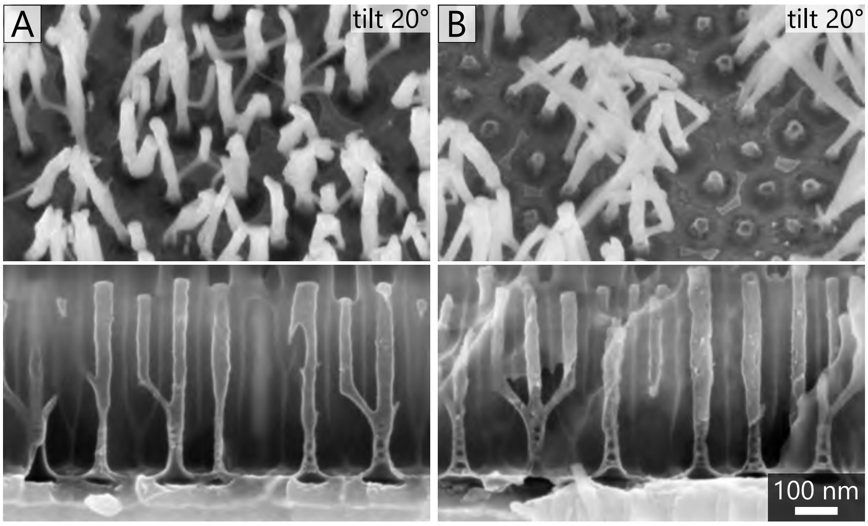

Figure 2.13: SEM images of (top) PAA-free and (cross-view) PAA-embedded nanocolumn arrays formed by PAA-assisted anodising of ¼Nb substrate with −1 min substrate anodising followed by 5 V s^{-1} re-anodising ramp to 250 V with (A) **1-** and (B) **20-minute overrun** period.

2.2.3 Breakdown

The breakdown (BD) phenomenon usually refers only to the dielectric breakdown characterized by a minimum voltage necessary for a dielectric film to get conductive. Here, for the sake of simplification, the BD refers to an event when the film is macroscopically destroyed during the increase of the anodising potential. This event is usually associated with an abrupt increase in the current density. Therefore, the breakdown phenomenon indirectly limits the maximum anodising potential and thus the achievable length of the columns.

Firstly, it was found that the BD potential is not affected by the slope of the aluminium anodising ramp. An example is shown in Figure 2.14, presenting anodising curves for relatively slow 0.5 V s^{-1} and fast 10 V s^{-1} ramps. In both cases, the anodisation was conducted at 24 °C with the 1-minute substrate anodising period followed by the 0.2 V s^{-1} re-anodising ramp until the BD potential. In both experiments, the BD potential occurred at approximately the same potential of 155 V. The exact value was also found for the aluminium anodising ramp of 1 V s^{-1} (not shown). Abrupt current spikes during the anodising process are typical for the breakdown process.

However, the breakdown process can be influenced by the slope of the re-anodising ramp, as shown in Figure 2.15. For steeper ramps, the breakdown is characterized by a development of micro-arc anodisation (plasma electrolytic oxidation) that leads to a

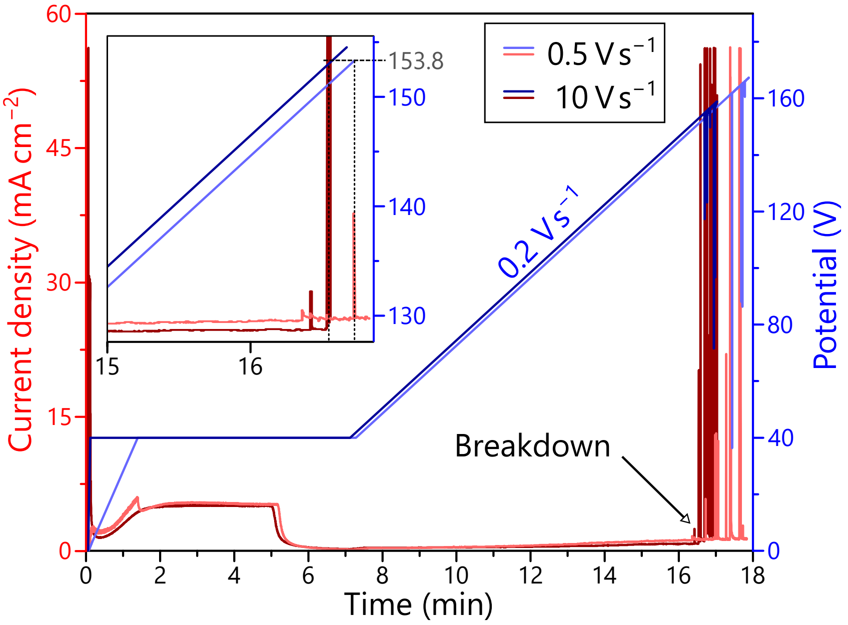

Figure 2.14: Anodising curves for ¼Nb layer anodised in 0.3 M oxalic acid at 24 °C with 0.5 and 10 V s^{-1} aluminium anodising ramp.The substrate was anodised for 2 min before the re-anodising ramp of 0.2 V s^{-1}.

formation of micro-arc anodic oxide (MAO) [148, 149], shown in Figure 2.15:C1. On the other hand, during the slower ramp, the breakdown is accompanied by the delamination of a PAA-embedded a-MO$_x$ layer from the metallic substrate in the form of circles, shown in Figure 2.15:C2. This delamination is believed to be caused by O_2 evolution and trapping below the a-MO$_x$ layer. Liu et al. [150] reported a similar effect of titanium oxide rupture done by the oxygen evolution during the transformation from amorphous to crystalline oxide. The separation of the layers and the damaged area between them can be seen in Figure 2.15:B2. While the micro-arc anodisation breakdown gives a higher BD potential (330 V), usually much lower BD potentials can be achieved when a delamination BD occurs. In both cases, the breakdown develops within a small area and spreads with time over the whole surface of the sample. However, the columns formed by both processes in the BD-free areas for micro-arc BD (5 and 1 V s^{-1} in Figure 2.15:B1, B2) show no morphology variation except their height, which is associated with the BD potential difference.

The breakdown process also depends on the time when the re-anodising ramp starts (i.e., the substrate anodising period). Experiments show that earlier starts tend to lead to a pure micro-arc anodising outcome. The micro-arc BD process was observed for re-anodising starts at −2, 0, and 1 min with 5 V s^{-1} at 7 °C. The BD potential of 330 V was achieved for the −2 min sample, while both later starts (0 and 1 min) give almost the exact value (330 V) of BD potential. The much later re-anodising start of 5 min results in a combined effect of micro-arc anodising and layer delamination with BD potential of 330 V. Images of column arrays formed in the BD-free areas are shown in Figure 2.16.

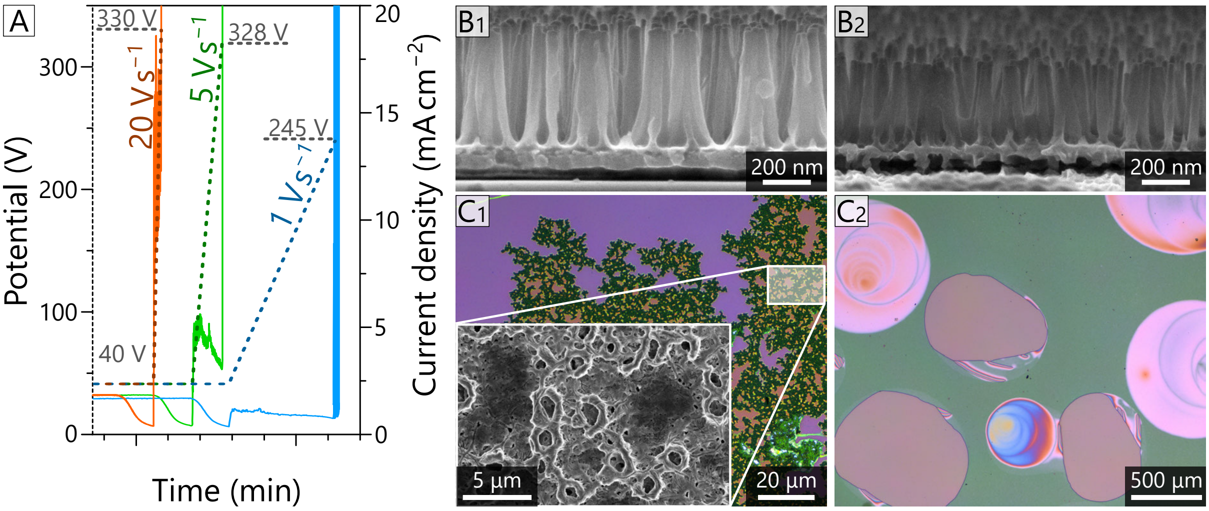

Figure 2.15: (A) Anodising curves for ¼Nb layer anodised in 0.3 M oxalic acid at 7 °C with 1 min substrate anodising period followed by a re-anodising ramp of 1, 5, and 20 V s^{-1}. (B) SEM cross-view images of the resulting nanocolumn arrays for (B1) 5 or 20 V s^{-1} and (B2) 1 V s^{-1} re-anodising ramp. (C) Optical images of the resulting features damaged by the breakdown process: (C1) micro-arc anodic oxide, (C2) film delamination in the form of bubbles caused by O_2 gas evolution and trapping at the interface.

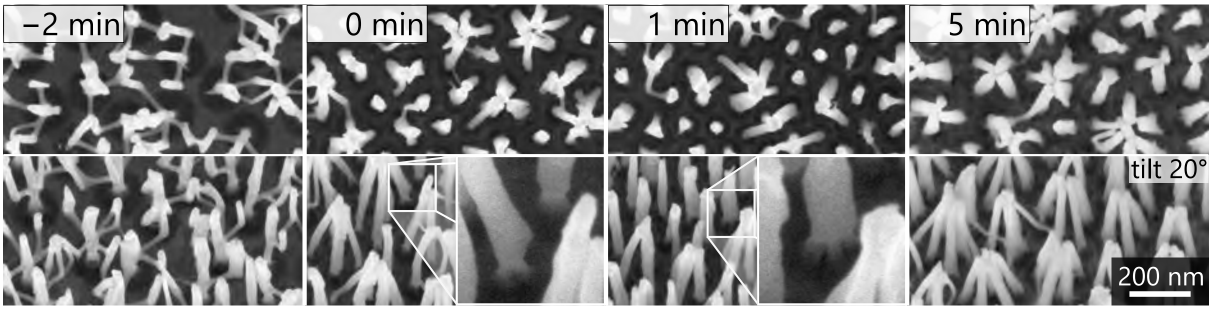

Figure 2.16: Top and tilted (20°) view SEM images of PAA-free nanocolumn arrays formed by PAA-assisted anodising of ¼Nb substrate in 0.3 M oxalic acid at 7 °C with various starts of re-anodising. The re-anodising was performed with a ramp of 5 V s^{-1} till the breakdown, which occurred at potential of 331, 328, 328, and 300 V for −2, 0, 1, and 5 min substrate anodising period. The number of single-standing columns was estimated to be 6, 28, and 5 % for 0-, 1-, and 5-minute samples.

From these findings, it is possible to assume that the transition from one behaviour to another is a gradual process. The breakdown process does not influence the column morphology except limiting the maximum length and damaging the related area. On the contrary, it is assumed that the column morphology is the decisive parameter for the BD process since both depend on the start of the re-anodising and the re-anodising ramp sweep. Prolonging the substrate anodising period leads to enlarging the root base and vice versa, shrinking the unprocessed substrate still covered by thin Al residues (shown in the enlarged insets of Figure 2.16: 0 and 1 min). This effect can also be observed by comparing 0- and 1-minute substrate anodising in Figure 2.12.

2.2.4 The influence of substrate composition

The finding observed with PAA-assisted anodising of ¼Nb substrate were also applied on other substrates to prove their versatility. Figure 2.17 shows the arrays of columns resulting from the PAA-assisted anodising of the Ti substrate at various conditions. Figure 2.17:A1–3 illustrate a series with a varying sweep rate of the re-anodising ramp up to 250 V, starting at the end of Al anodising (0 min) and no overrun. Surprisingly, the 1 V s^{-1} (Figure 2.17:A1) re-anodising ramp gives significantly underdeveloped columns of a much thinner diameter and a noticeably shorter length. The root area is also far more spread with a rough morphology. The other re-anodising ramps give similar results as the ¼Nb substrate. Relatively stable columns were achieved for 5 V s^{-1}, and the faster 20 V s^{-1} ramp formed columns with a single thin root leading to their bending.

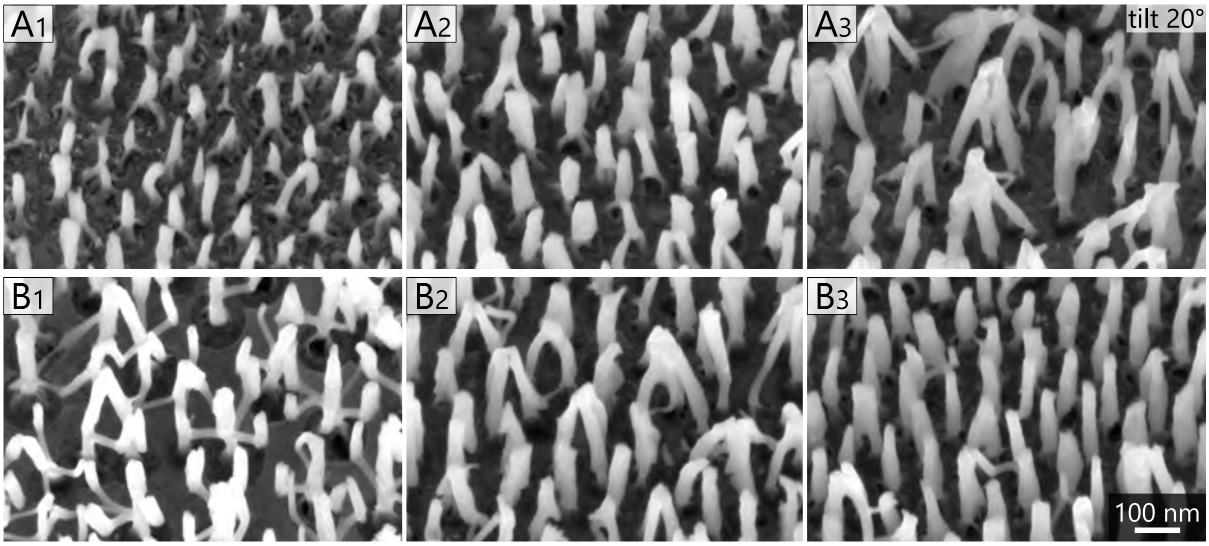

Figure 2.17: Tilted (20°) view SEM images of PAA-free nanocolumn arrays formed by PAA-assisted anodising of the Ti substrate in 0.3 M oxalic acid at 7 °C with (A) various re-anodising ramps up to 250 V and 0 min overrun period: (A1) 1 V s^{-1}, (A2) 5 V s^{-1},(A3) 20 V s^{-1}; and (B) with various starts of the re-anodising sweep of 20 V s^{-1} up to the BD potential (≈300 V): (B1) −2 min, (B2) 0 min, (B3) 0.5 min.

Figure 2.17:B1–3 show a series of various re-anodising starts of a 20 V s^{-1} ramp up to the breakdown potential. Here, the situation exactly reproduces the previous results (Figure 2.16). The earlier start (−2 min) gives very stable columns with saguaro-like (*Carnegiea gigantea*) morphology and a micro-arc BD process at 305 V. The later starts result in the second type of BD process associated with gas evolution and delamination of layers at 300 V. The re-anodising start at 0 min produces a weak, thin rooted column

morphology that suffers from bending like in the previous case (Figure 2.17:B2). Less bent columns were achieved just by postponing the re-anodising start by 30 s (Figure 2.17:B3). This delay formed a broader and stronger root morphology sufficient to support the whole column.

With no surprise, similar results were also achieved with the ⅕N and ¼N substrate layers (data not presented). When compared to the anodising procedure with the more extended substrate anodising period and slower re-anodising ramp (described in section 2.1) that leads to poor stability and hollow morphology of the nanocolumns, these anodising conditions lead to fully stable and fully solid (in the SEM observation) nanocolumns even at 250 V.

2.2.5 Conclusions

This section demonstrates the effect of individual anodising parameters on the morphology and stability of the structures. The main objective of this work was to find process parameters to form as stable columns as possible, even for high re-anodising potentials and low concentrations of additives in the substrate.

The most crucial improvements of stability were achieved by lowering the electrolyte temperature and shortening the re-anodising period. A general rule to form stable TiO_2-based a-MO_x columns by the PAA-assisted anodisation is to promote fast changes of potential, and thus fast kinetics of anodising. Vice versa, this may be interpreted as to avoid idling at any given formation state, such as too long substrate anodising, slow re-anodising, or even prolonging the redundant overrun period.

Significant attention was paid to the morphology of nanostructures depending on the anodising conditions as it plays a significant role in the overall stability of columns together with the chemical composition of their roots. Two features are correlated with their relatively poor stability: a narrow root formed by the early starts of potential sweep and a large root area associated with a prolonged period of the anodising stage. The anodising periods such as re-anodising ramp and overrun can be reduced to a minimum without any profound impact on the columns. However, in the case of the substrate anodising period, the situation is more complex. Short periods result in narrow roots or even more dramatic morphology changes of the whole column into the saguaro-like shape, while too long periods yield the undesirable root broadening. Nevertheless, these edge conditions still give a reasonable operating window, which may be broadened by lowering the temperature.

Surprisingly, the saguaro-like shape columns have superior stability compare to normal (cylindrical) ones formed under similar conditions. Possible drawbacks are some loss of the active surface due to merging in the trunk and getting a more complex shape.

These improvements were applied successfully to nitrogen-doped substrates (¼N, ⅕N) and even the titanium substrate without any additives. The most remarkable result was the formation of a stable (almost 100 %) column array formed from the Ti substrate re-anodised even up to 300 V. This demonstrates a considerable leap from published reports [119, 138], being able to achieve less than 20 % stability for re-anodising potentials over 60 V.

In addition to the studies mentioned above, the breakdown process was investigated in detail. The breakdown of the film has the utmost importance as it limits the maximum value of anodising potential and thus the length of the nanocolumns. Two distinguished BD processes were observed: 1) layer delamination due to gas evolution and 2) micro-arc anodisation. In general, layer delamination can be correlated with extended anodising periods that result in a growth of the root area. The gas evolution can also be why the overly expanded roots have a rough morphology with many defects.

On the other hand, micro-arc anodising is achieved predominantly for short anodising periods, such as quick re-anodising starts (even during Al anodising) and steep re-anodising sweeps. Compared to the first case, the micro-arc BD process is more favourable as it occurs at much higher anodising potentials. However, it still needs to be noted that the stability of columns cannot be fully predicted based only on the BD potential value for the given formation parameters.

2.3 Electrochemical characterizations

In this part of the thesis, electrochemical characterization of PAA-embedded samples was done by cyclic voltammetry (CV), electrochemical impedance spectroscopy (EIS), and Mott–Schottky (M–S) analysis. In this case, the purpose of the CV is to demonstrate the electrochemical stability given by an aversion of the sample towards redox reactions. The EIS and M–S analyses were used to characterize and quantify the electrical properties of the system. These results were published and presented at the international conferences (chapter C).

2.3.1 Sample fabrication

Samples were prepared from the Ti and ¼N layer (Table 2.1) in the pressing cell setup. All samples were identically anodised according to Figure 2.1:B, with a 40 V aluminium anodising, a subsequent 5-minute substrate anodising, followed by a 0.2 V s^{-1} re-anodising ramp to 100 V, and a 10-minute overrun. Cross-section views of the formed composite layers are shown in Figure 2.18. Despite the poor contrast, the Ti sample shows columns sitting over rather large voids (Figure 2.18:A1). This morphology is expected due to a very slow re-anodising ramp leading to excessive oxygen. In contrast, the ¼N substrate (Figure 2.18:B) gives higher columns (180 vs 145 nm) with a distinct root structure.

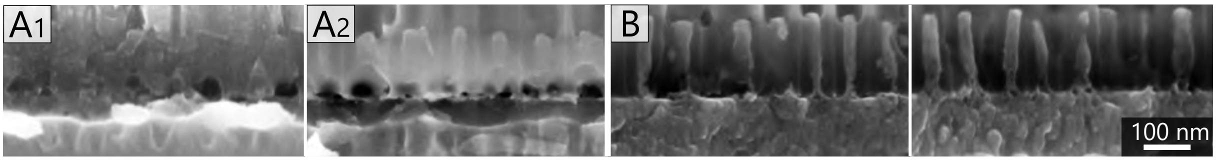

Figure 2.18: SEM cross-section views of PAA-embedded nanocolumns formed from (A1–2) N-free (Ti) and (B) N-doped (¼N) substrate layers (Table 2.1). Samples (A1) before and (A2,B) after the PAA etching for 90 s to enhance the contrast.

Afterwards, the samples were cut into quarters to be separately annealed. Part of the samples was annealed in the ambient atmosphere at 600 °C for 2 hours. This air-annealing was performed with a heating ramp of 10 °C min^{-1} and a natural cooldown. Another part was annealed in a vacuum chamber with pressure less than 10^{-4} Pa for the same period and ramp parameters. For the electrochemical measurements, all samples were masked by a PMMA-based film (nail polish), so only an area of nanocolumns was exposed to the electrolyte when immersed.

Overall, six different samples were characterized, which could be divided by two substrates: N-free (Ti) and N-doped (¼N); and three different post-processing types: as-anodised, air-annealed, and vacuum-annealed. This variety allowed us to study the effect of nitrogen concentration within the substrate layer and determine whether the oxygen concentration (oxygen vacancies) influences the electrochemical properties.

2.3.2 CV and EIS measurements

The CV and EIS were carried out in a borate buffer (0.5 M H_3BO_3 and 0.5 M $Na_2B_4O_7$ aqueous solution, pH 7.4) at 22 °C in the dark. A µAutolab III/FRA2 Metrohm Autolab Potentiostat/Galvanostat was used as the potentiostat and impedance analyser. A three-electrode setup was employed with the sample connected as a working electrode (WE), an Ag/AgCl reference electrode (RE), and a gold sheet as a counter electrode (CE). The current response was measured by cyclic voltammetry in a potential range from −1 to 1 V vs RHE, with a scan rate of 50 mV s^{-1} starting from open-circuit potential. The EIS measurements were performed from 1.44 to −0.56 V vs RHE over a frequency range from 10 kHz to 0.1 Hz with the 10-mV excitation amplitude. The impedance data were analysed by computer simulation and fitting software Autolab Nova 1.10.

Cyclic voltammograms obtained at low potentials for all samples are shown in Figure 2.19:A, B. Several trends are noticed: 1) For both substrates, the current density (and the conductivity) depends on the annealing conditions, and it increases in the order: as-anodised < air-annealed < vacuum-annealed processing; 2) The conductivity is systematically higher for the N-doped samples when compared to the N-free ones; 3) I–V curves are asymmetric with lower anodic and higher cathodic currents.

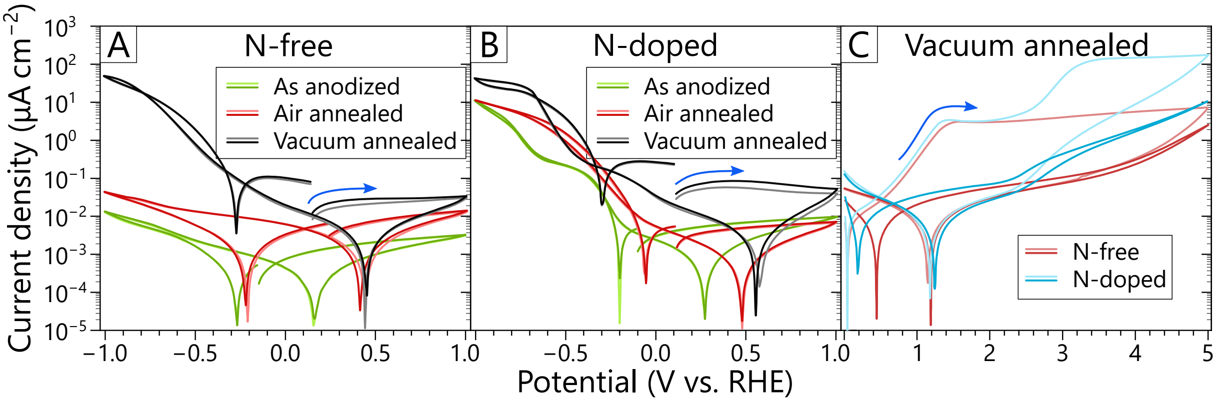

Figure 2.19: Cyclic voltammograms for as-anodized, air- and vacuum-annealed (A) N-free and (B) N-doped TiO_2 nanocolumn arrays. (C) Cyclic voltammograms of the vacuum-annealed N-free and N-doped arrays obtained at higher anodic potentials. A pale colour shows the first measured cycle of each sample, and blue arrows mark the scan direction. The current density is in absolute value and log scale.

Only the vacuum-annealed samples for both N-free and N-doped substrates show substantially higher anodic currents in the first cycle (Figure 2.19:C pale colour) than in the consecutive ones (Figure 2.19:C saturated colour). They both reach a plateau at 1.7 V vs RHE of 3 µA cm^{-1}, while the N-doped sample has another one at 3.5 V vs RHE of 150 µA cm^{-1}. These plateaus are not present in consecutive cycles; however, the N-doped sample still reveals a substantial current density rise at about 3.5 V vs RHE that corresponds to the second plateau. Similar behaviour was also observed by Milošev et al. for anodic oxidation of TiN layers in a phthalate buffer.[151] On the other hand, these features are not present in the case of the remaining samples (as-anodised or air-annealed), which have current densities of 1–2 orders of magnitude lower in this anodic region (approximately $0.1\,\mu\mathrm{A\,cm^{-1}}$ at 5.5 V vs RHE, not shown).

Voltage-dependent EIS measurements were performed for all array types to gain insight into their semiconducting properties. Two sets of measured EIS data for air-annealed samples (N-free and N-doped) are presented in Figure 2.20 in the form of Bode plots. All EIS data were fit in the whole frequency range using an equivalent electrical circuit composed of one or two capacitive layers in series (shown as insets of Figure 2.20). The best fit for the N-free sample was found by one capacitive layer (DL), presumably corresponding to a dielectric layer. On the other side, the N-doped EIS was fitted by two capacitive layers. One of the capacitances usually corresponds to the space charge layer of the semiconductor formed at the top of the columns. Another one, with the higher capacitance and lower resistance, is attributed to the Helmholtz layer.[152] A constant phase element (CPE) is used to account for the non-ideal behaviour of the space charge layer.

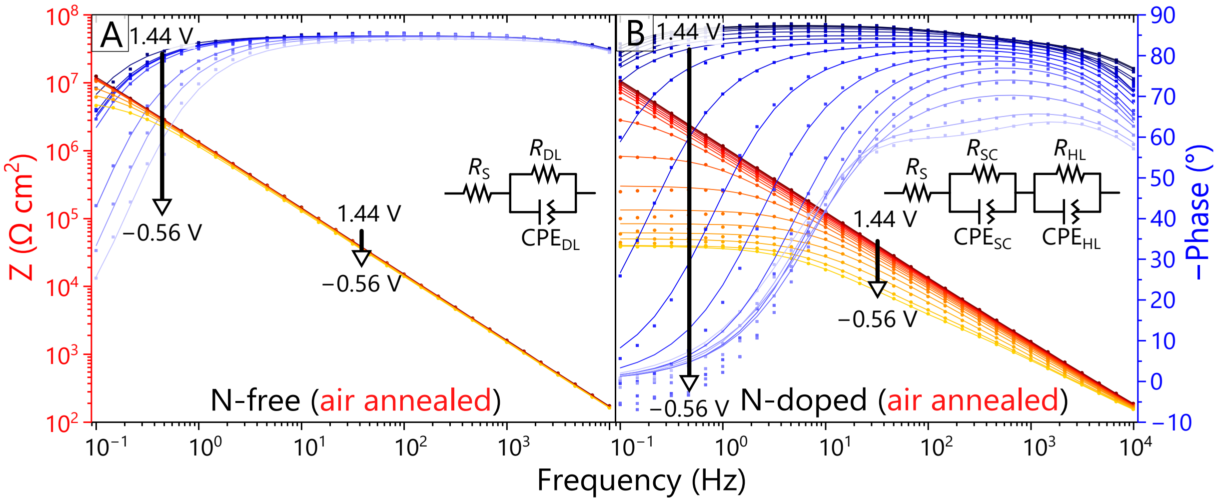

Figure 2.20: Bode plot representation of EIS measurements of the (A) N-free and (B) N-doped air-annealed nanoarrays obtained in the borate buffer at DC voltages from 1.44 to −0.56 V vs RHE. The measured data are represented by dots, whereas the solid lines are fitted equivalent electrical circuits shown as insets (SC = space charge layer, HL = Helmholtz layer, DL = dielectric layer).

M–S plots for all samples are obtained by plotting ${C_{\mathrm{SCL}}}^{-2}$ versus potential, where the donor density N_{d} is estimated from the slope of the linear part according to the M–S relation for n-type semiconductors (see Figure 2.21):

$$\left(\frac{C_{\mathrm{SCL}}}{A}\right)^{-2} = \left(\frac{2}{\varepsilon_{\mathrm{r}}\varepsilon_0 N_{\mathrm{d}} e}\right)\left(E - E_{\mathrm{fb}} - \frac{k_{\mathrm{B}}T}{e}\right) \tag{2.1}$$

where C_{SCL}/A is the capacitance of the space charge layer per area, ε_{r} is the relative permittivity of TiO_2 ($\varepsilon_r = 70$) [153], E is the applied potential, E_{fb} is the flat-band potential, k_B is the Boltzman constant, and T is the temperature.

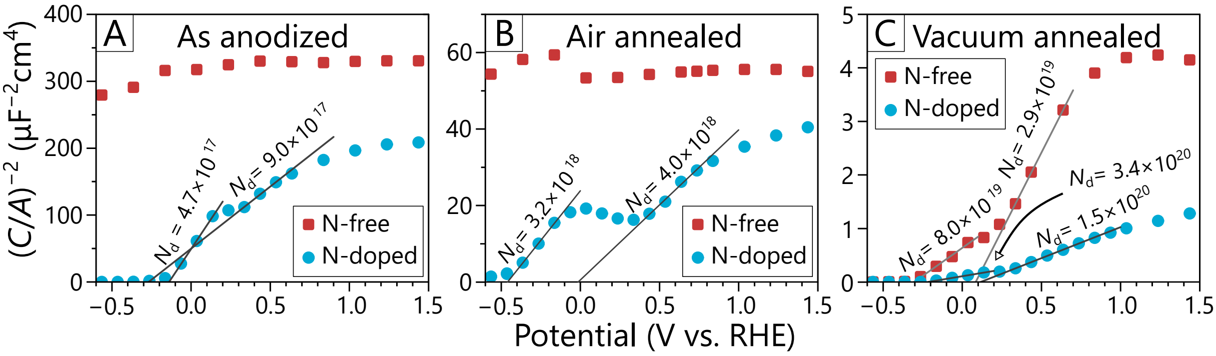

Figure 2.21: Mott–Schottky plots calculated from fits of the potential-dependent EIS measurements. The donor density (N_d) is given per cm^3.

Two types of behaviour can be distinguished. First, a relatively constant capacitance, independent of the potential, is revealed for the N-free as-anodised and air-annealed samples (M–S plots in Figure 2.21:A, B). The same can be seen in the corresponding Bode plots (Figure 2.20:A), where the impedance modulus and phase curves overlap for all potentials. This kind of behaviour is typical for a dielectric material. The second type is observed for all N-doped arrays, and the vacuum-annealed N-free sample, with a positive slope and saturated marginal regions in the M–S plots (Figure 2.21), typical for n-type semiconductors. The corresponding Bode plot (Figure 2.20:B) shows clearly that both the impedance modulus and phase shift change substantially with the potential .

Additionally, the slope in the M–S plots is divided by a plateau that can be easily distinguished from the M–S relation for N-doped air-annealed sample (Figure 2.21:B). This behaviour points to the presence of surface states. When there is a high density of surface states, the Fermi level can become pinned within the potential range in which the surface states lie. For the monoenergetic surface state, the intersect of the Mott–Schottky plot is shifted from its actual flat band potential value, as illustrated in Figure 2.22.[154]

The donor density (N_d) is calculated for the arrays, which revealed an n-type semiconducting behaviour (Figure 2.23:A). This is done according to Equation 2.1, i.e., from the slope of the corresponding M–S plot as marked in Figure 2.21 (the slope of the cathodic potential is used). The PAA matrix is neglected due to its high resistance, and thus only the electrochemically active area of the column top (11 % of a WE area) is being counted. This calculation was simplified using the same dielectric constant, $\varepsilon_r = 70$, for both N-free and N-doped substrate layers. Also, a depletion layer thickness (eventually the dielectric layer thickness) is calculated from the capacitance obtained from the EIS at 1.44 V vs RHE, while using the same active area, ε_r and neglecting the influence of the PAA (see Figure 2.23:B). The M–S analysis shows that N-doped samples reveal an explicit n-type semiconducting behaviour with N_d increasing in the order: as-anodised < air-annealed

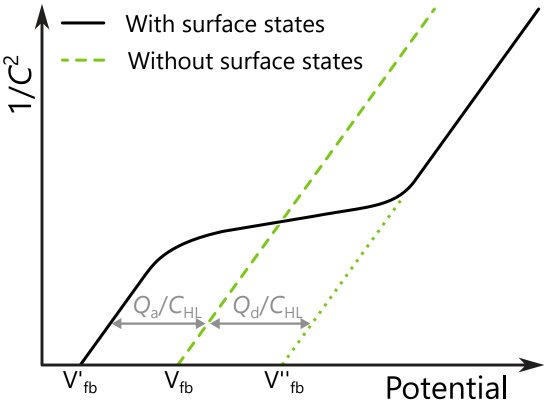

Figure 2.22: Diagram clarifies surface state-imposed changes on the shape and flat band position in a Mott–Schottky plot. Surface states can pin the Fermi level. In this case, all or part of the applied potential is dropped across the Helmholtz layer, as the surface states are ionised without changing the capacity according to the Mott–Schottky relation.[155] Where Q_d is the positive charge when the donor surface states are empty, Q_a is the negative charge when the acceptor surface states are fully occupied, and C_HL is the Helmholtz capacitance.

$<$ vacuum-annealed (Figure 2.23:A). On the other hand, except for the vacuum-annealed films, all other N-free samples show predominantly dielectric behaviour as the value of $(C/A)^{-2}$ is almost constant.

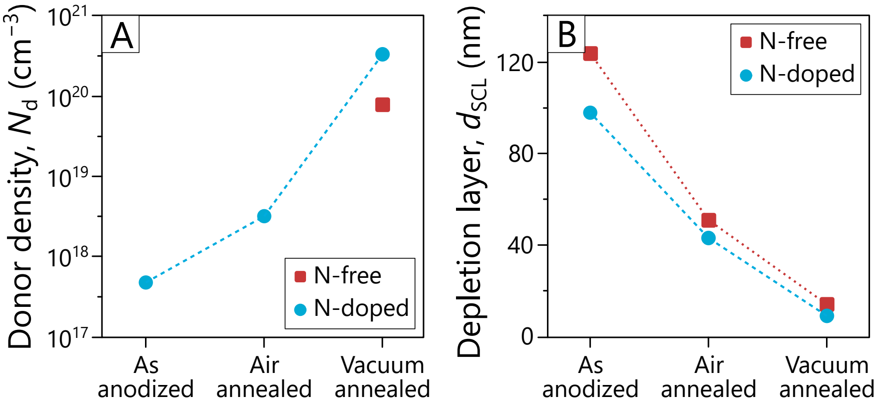

Figure 2.23: (A) Donor density N_d calculated for the different types of $\mathrm{TiO_2}$ nanocolumn arrays from the Mott–Schottky plots. (b) Depletion layer thickness calculated from the capacitance obtained by EIS measurements at 1.44 V vs RHE.

2.3.3 Conclusions

Based on the cyclic voltammograms and voltage-dependent EIS, a rough insight into the electrochemical properties of the samples was obtained. Both the annealing treatment and the nitrogen doping of the initial substrate affect the measured donor density of the samples together with their conductivity. These findings can be categorized into two topics: the influence of the substrate and the post-anodising treatment.

The thermal treatments increase the donor density (N_d) for the N-doped series in the order: as-anodised < air-annealed < vacuum-annealed samples. This finding is in good agreement with the cyclic voltammetry results, where the current density (conductivity) shows similar trends, even for both substrate types (Figure 2.19:A, B). These observations are consistent with literature reports demonstrating that thermal treatment leads to a phase transformation, in this case, from an initial amorphous anodic titanium oxide to the anatase phase.[45, 46, 156–159] Increasing the crystallinity of the materials results in higher conductivity, which was demonstrated by the CV. On the other hand, a thermal treatment may cause oxidation/reduction and thus changes in the chemical composition. For example, annealing in an oxygen-deficient environment leads to creating oxygen vacancies (VO) in the material, which act as shallow donors and lead to enhancement of the n-type semiconducting behaviour.[48, 49] This effect depends mainly on the annealing temperature, the initial VO concentration in the sample, and the partial pressure of O_2 in the gas phase.[48] Therefore, the loss of oxygen is more pronounced after the annealing in a vacuum than in the ambient atmosphere. Besides, the vacuum annealing seems to lead to a substantial reduction of the columns, as was proven by their reoxidation during the cyclic voltammetry at higher anodic potentials (Figure 2.19:C).

The presence of nitrogen in the substrate layer increases the measured donor density and conductivity for all annealing treatments. N-doping is known to narrow the bandgap of TiO_2 or form impurity states, leading to enhanced light absorption.[160, 161] M–S analysis of the N-doped arrays performed in this work shows a distinct plateau (Figure 2.21:B), which may be attributed to Fermi level pinning due to surface/trap states.[162] This may be an indication of the prevailing N-doping mechanism. Additionally, the CV of the vacuum-annealed N-doped samples shows a characteristic behaviour for TiN anodising that may hold some information about the presence of nitrogen in the columns.[151] For more information about the chemical composition (TEM EDX and XPS analysis) of the as-anodised pure TiO_2 and N-doped TiO_2 nanocolumns, please refer to the collaborative publication.[119]

To summarize, the electrochemical properties of N-free and N-doped TiO_2 nanocolumns prepared by using PAA-assisted anodising, and post-anodising annealing in different atmospheres have been studied. Cyclic voltammetry and Mott–Schottky analysis has revealed that the incorporation of nitrogen and annealing in oxygen-deficient conditions lead to a significant rise of n-type donor concentration in the titanium-oxide-based nanocolumns. This demonstrates that the donor density, as well as the space charge layer of the columns, can be easily adjusted by these treatments.

The present findings are of vast importance for future utilization of the TiO_2-based nanocolumn arrays for photoelectrochemical water splitting to obtain nanocolumns with good electrical conductivity and a space charge layer localized at the column surface.

Improving these properties will substantially enhance the photogenerated charge carrier separation in these nanoarrays.

2.4 Photoelectrochemical characterizations

The central objective of this work is to investigate the photoactivity of the prepared TiO_2-based nanostructures for their possible application as photo-anodes for the water splitting reaction. This task has been simplified to photocurrent measurements (cyclic voltammetry with chopped illumination at various wavelengths and incident photon-to-current efficiency (IPCE) measurements) of selected MO_x nanocolumn layers, focusing on N-doped TiO_2 films. Even though the samples were extensively characterized, the interpretation of some results is out of the scope of this work due to their complex nature. Therefore, for the sake of avoiding uncertain conclusions and speculations and for keeping a clear focus, only the most relevant outcomes are discussed. Despite this, the motivation is to present and objectively compare a comprehensive set of MO_x nanostructured layers with less sophisticated analogies like compact MO_x layers prepared by thermal or anodic oxidation.

The performance of photoactive materials can be compared by their external quantum efficiency (EQE), also referred to as the incident photon-to-current efficiency. In the case of photoelectrodes, the IPCE is defined as the ratio of the number of charge carriers (electrons/holes) collected by the photoelectrode to the number of incident photons of given energy:

$$\mathrm{IPCE}(\lambda)\,[\%] = \frac{J_{\mathrm{ph}}\,[\mathrm{mA\,cm^2}]}{I_{\mathrm{light}}\,[\mathrm{mW\,cm^2}]} \cdot \frac{1239.8\,[\mathrm{V\,nm}]}{\lambda\,[\mathrm{nm}]} \cdot 100\% \tag{2.2}$$

where J_{ph} is the photocurrent density, I_{light} is the intensity of the incident (monochromatic) light, and λ is the wavelength of the monochromatic light. IPCE is affected by the efficiencies of three fundamental processes involved in PEC as illustrated by Equation 2.3, including charge generation ($\eta_{\mathrm{e^-/h^+}}$), charge transport within the material ($\eta_{\mathrm{transport}}$), and charge collection (transfer) at the electrode/electrolyte interface ($\eta_{\mathrm{collection}}$).[163]

$$\mathrm{IPCE} = \left(\eta_{\mathrm{e^-/h^+}}\right)\left(\eta_{\mathrm{transport}}\right)\left(\eta_{\mathrm{collection}}\right) \tag{2.3}$$

2.4.1 Sample fabrication

Samples studied in this subsection are exclusively made from nitrogen-doped substrate layers, specifically $^{1}/_{5}$N, $^{1}/_{3}$N, and $^{1}/_{1}$N (see Table 2.1). Samples were anodised in the large-scale setup with parameters chosen to match the previous study (Figure 2.3).[119] For the complete fabrication procedure, please refer to subsection 2.1.3. Afterwards, the surrounding PAA was partially (PE) or fully (FE) etched away (Figure 2.5) as described in subsection 2.1.4. The complete removal of PAA was applied only to the $^{1}/_{1}$N nanocolumn layer (Figure 2.5:C2) as it is the only one that forms a fully stable nanocolumn layer for the given anodising conditions. Because the PAA etching may lead to a partial exposure of the metallic substrate (or aluminium residues), all samples were subsequently anodised one more time to a lower potential of 6 V (post-anodisation shown in Figure 2.3) to oxidize this layer. Samples were broken into smaller strips according to laser pre-engraved grooves (10 mm×20 mm).

Similarly to the samples prepared for the electrochemical investigations (section 2.3), part of the samples was annealed at 500 °C for 2 hours in the ambient atmosphere (AA), a vacuum (VA), or a hydrogen atmosphere (HA). Overall, 16 different samples were characterized, divided into two morphologies (with and without PAA, i.e., partially and fully etched, respectively), three substrates, and four different post-processing techniques. This series allows us to study the effect of nitrogen concentration within the substrate layer and study the effect of oxidizing or reducing thermal treatment. Lastly, in the case of the ¹⁄₁N substrate, the influence of the surrounding PAA can be discussed when the PE sample is compared with the fully exposed nanocolumns.

Additionally to the nanostructured layers, flat titanium oxide layers were prepared by thermal and anodic oxidation. A titanium sheet (1.5 mm thick) of high purity (99.999 %) was used as the starting material. The sheet was cut into 10 mm×30 mm strips, which were mechanically polished to a mirror-like finish. One sample was thermally oxidized in an ambient atmosphere for 5 hours at 550 °C. Other samples were potentiostatically anodised in 1 M H_2SO_4 aqueous solution at room temperature at 10 and 20 V for 15 minutes without any further annealing. The 10 V anodised sample gives a gold look (20 nm) while the 20 V anodised and air-annealed samples have a blue tint (50–70 nm).[156, 164]

2.4.2 Experimental setups and measurement procedures

Photoelectrochemical scanning droplet cell microscopy (PE-SDCM) setup

Photoelectrochemical properties of selected MO_x nanocolumn layers were studied by an experimental photoelectrochemical scanning droplet cell microscopy (PE-SDCM) setup at Institute for Chemical Technology of Inorganic Materials, Johannes Kepler University Linz, where I did an internship in the group of Univ.-Prof. Dr Achim Walter Hassel.

A PE-SDCM is an advanced tool specifically designed to perform automatized mapping of photoelectrochemical properties over a specimen with a spatially varying composition.[165–167] A basic diagram of PE-SDCM is shown in Figure 2.24:A with a simple operation concept shown in Figure 2.24:B.

The most crucial and complex part of PE-SDCM is an SDCM probe represented by a flow-through 3-electrode photoelectrochemical cell (PEC), as will be discussed later. The 3D movement of the cell was provided by 3-axis motorized translation stages controlled by home-made controllers and software (done by Dr Andrei Ionut Mardare). While a sample was fixed to an x/y-stage, the cell was mounted through a tension meter to a z-stage to control and monitor the applied pressure. A home-made peristaltic pump ensured an electrolyte exchange with the flow rate of 0.5 ml min^{-1} and 50 ml reservoir (at room temperature). A Faraday cage was built around the PEC to suppress electrical interferences during the impedance measurements.

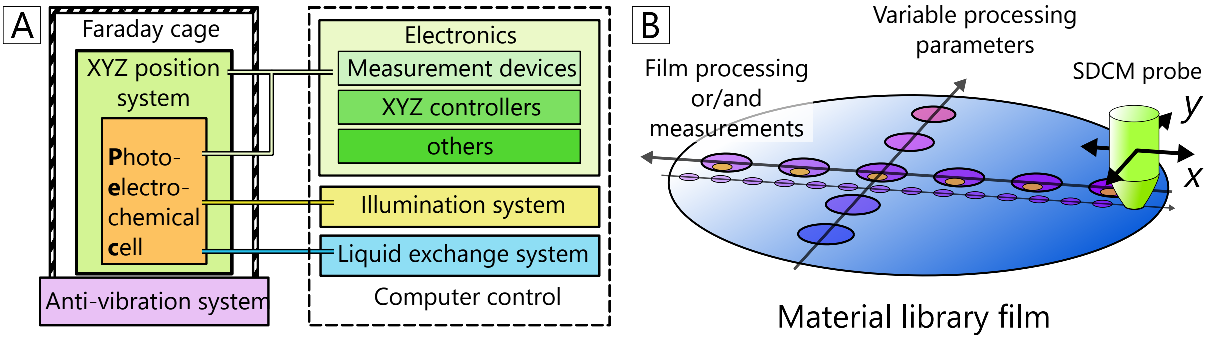

Figure 2.24: (A) Schematic diagram of PE-SDCM setup and (B) illustration of the systematic investigation of library materials by PE-SDCM as future proof of concept.

The PE-SDCM probe was a 3D printed flow-through 3-electrode cell (shown in Figure 2.25:A and designed by Dr Jan Philipp Kollender) that consisted of an electrolyte inlet and outlet, a gold wire counter electrode (CE), a home-made silver chloride reference electrode (RE) shown in Figure 2.25:B, optical fibre and a silicon o-ring seal. The original electrode configuration shown in Figure 2.25:A1, where the CE is placed in the opposite channel as the RE, led to artefacts in the impedance measurements, presumably caused by the narrow geometry of the channels with high resistance and thus the potential screening. This issue was solved by placing the CE near the RE (Figure 2.25:A2, B). The stability and potential of the home-made RE (Figure 2.25:B) were measured ($E = E_0 + 5\,\text{mV}$) against a commercial Ag/AgCl in 3 M NaCl RE ($E_0 = 195\,\text{mV}$ vs RHE at 25 °C, RE-1B, ALS Co., Ltd). The 3-electrode cell was connected to a potentiostat (Compactstat IVIUM) and controlled by PC software (IviumSoft 2.794).

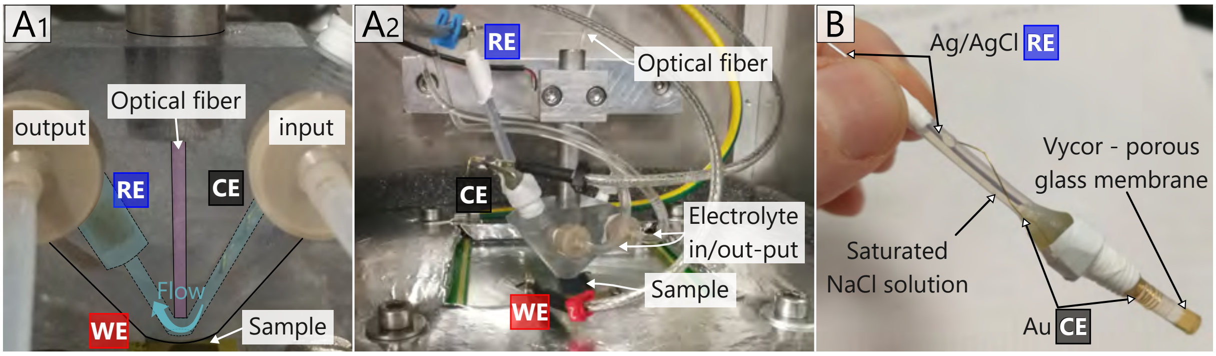

Figure 2.25: Photographs of (A1) PE-SDCM cell with the original separate electrode configuration and (A2) with the improved united configuration. (B) Detailed photograph of the home-made Ag/AgCl RE with a gold wire as CE.

The last component of PE-SDCM is the illumination system (Figure 2.26) that was specially designed and built for this application. The main requirement was to ensure a high illumination intensity of the sample area within the PE-SDCM cell for eventual photo-corrosion experiments. Six discrete light-emitting diodes (LEDs) were chosen to cover the UV–VIS range for this purpose (Table 2.3). Two LED groups can be noticed in Figure 2.26:3. The reason is that the VIS LEDs were already implemented within the heatsinks, while the UV LEDs were bought bare on metal-core printed circuit boards (PCBs) for easier exchange.

Table 2.3: LED sources used in the setup and their measured output illumination intensity.

Wavelength [nm]	Part Number	FWHM [nm]	Illumination intensity [mW]
365	M365D1	7.5	0.34
395	M395D3	16	0.36
420	H2A1-H420†	20	0.93
470	M470F3	20	3.13
530	M530F2	30	1.29
625	M625F2	15	1.31

Supplier: Thorlabs
† Supplier: Roithner LaserTechnik

All LEDs were powered by LED drivers (LEDD1B, Thorlabs), which are controlled by a microcontroller (Arduino Uno) pulse width modulation (PWM) through a custom low-pass filter circuit board. A broad-band stabilized tungsten-halogen light source (SLS201L/M, Thorlabs) was added to imitate the sunlight illumination. All light sources are fibre-coupled by a 1-to-7 fan-out bundle with 600 µm core diameter (BF76HS01, Thorlabs).

The power of illumination was measured by an optical power metre—microscope slide thermal sensor (S175C, Thorlabs), shown in Figure 2.27:A. This was performed in a pseudo black box at room temperature using the PE-SDCM cell filled with a buffer solution to imitate the electrochemical experiments. The power density is estimated as the measured power divided by the working electrode (WE) area—the area in contact with an electrolyte. This rough simplification was done only due to the solely comparative nature of this work. Meanwhile, the theoretical estimation of the illuminated area is approximately 70 % of the WE area based on the geometry, the numerical aperture (NA) of the fibre and excluding the refraction.

Our wish was that the illumination system should be able to perform at chopped illumination. This feature was realized by adding a fast switching mechanical shutter into the system, requiring additional optical elements (Figure 2.27:B). The optics for this system was designed in the Zemax software to minimalize the intensity losses. The input light is decoupled from the bundle fibre then focused by two aspheric condensers into an output fibre with 1500 µm core diameter (not shown in figures).

The shutter was made out of a hard drive disk (HDD) reading mechanism. This idea was inspired by report of Scholten [168], which utilizes a fast-moving HDD reading arm

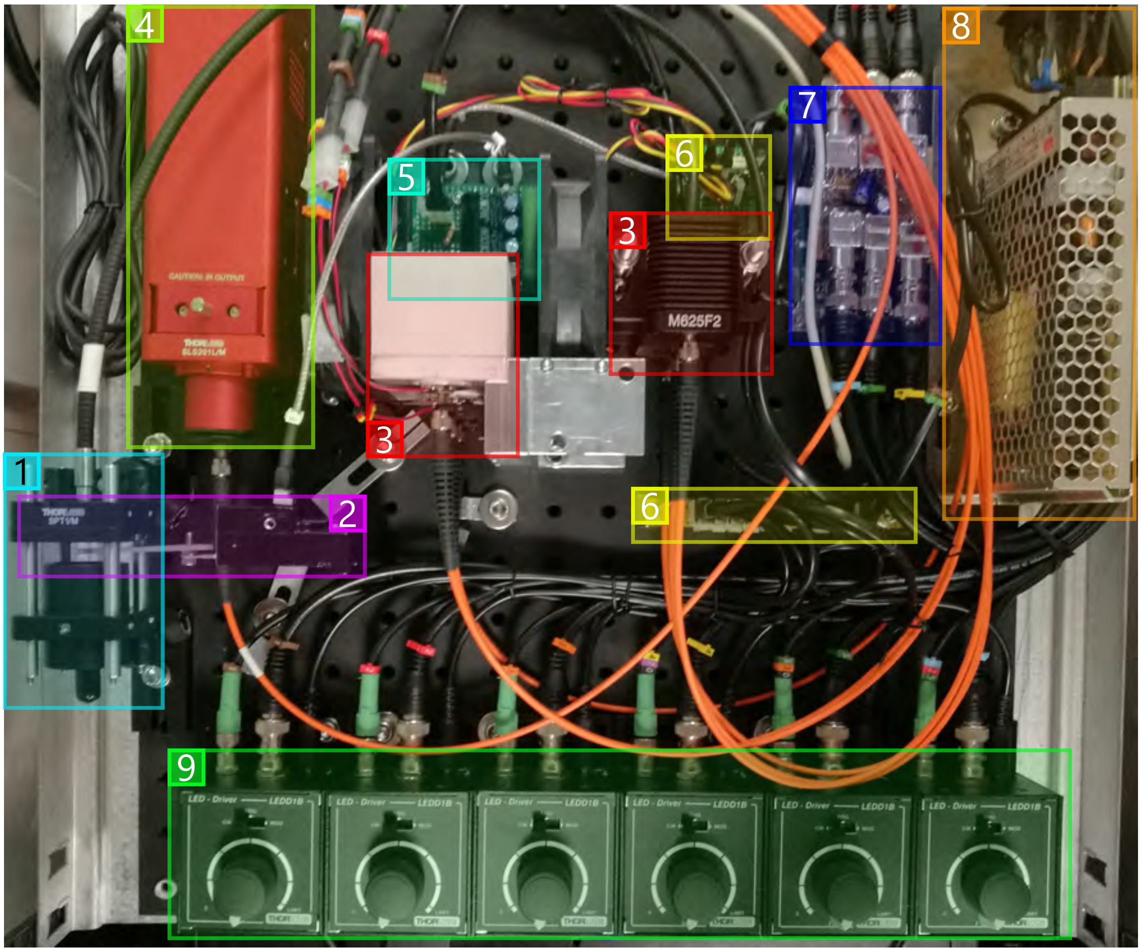

Figure 2.26: Photograph of the illumination system: (1) The mechanical shutter optics. (2) The mechanical shutter made out of an HDD reading mechanism. (3) Six fibre-coupled LEDs with heatsinks. (4) Fibre-coupled stabilized Tungsten-halogen light source. (5) The shutter driver. (6) Electric power distribution and voltage regulator. (7) Arduino Uno with the custom circuit board for LED drivers. (8) Power supply. (9) LED drivers.

as a laser beam shutter. The movement of the arm was induced by a current flow in the voice coil, for which a custom driver was built and controlled by the microcontroller board (Arduino Uno). This driver, LED drivers, and the microcontroller board are powered by a 150 W power supply (15 V DC). The shutter performance was measured using a silicon photodiode (FDS100, Thorlabs) on a testing circuit (Figure 2.27:C1). The speed of both state changes was estimated under 1.3 ms (Figure 2.27:C2). Noteworthy, this value is far slower than 450 ns in the referred report [168], where the design of the arm was optimized for fast laser pulses, being lighter, with shorted travel distance and V-shaped notch. Still, this performance is sufficient for the planned chopped illumination experiments.

Lastly, a program was developed in the LabView environment, ensuring communication with Arduino microcontroller that controls the output of LEDs and the shutter position.

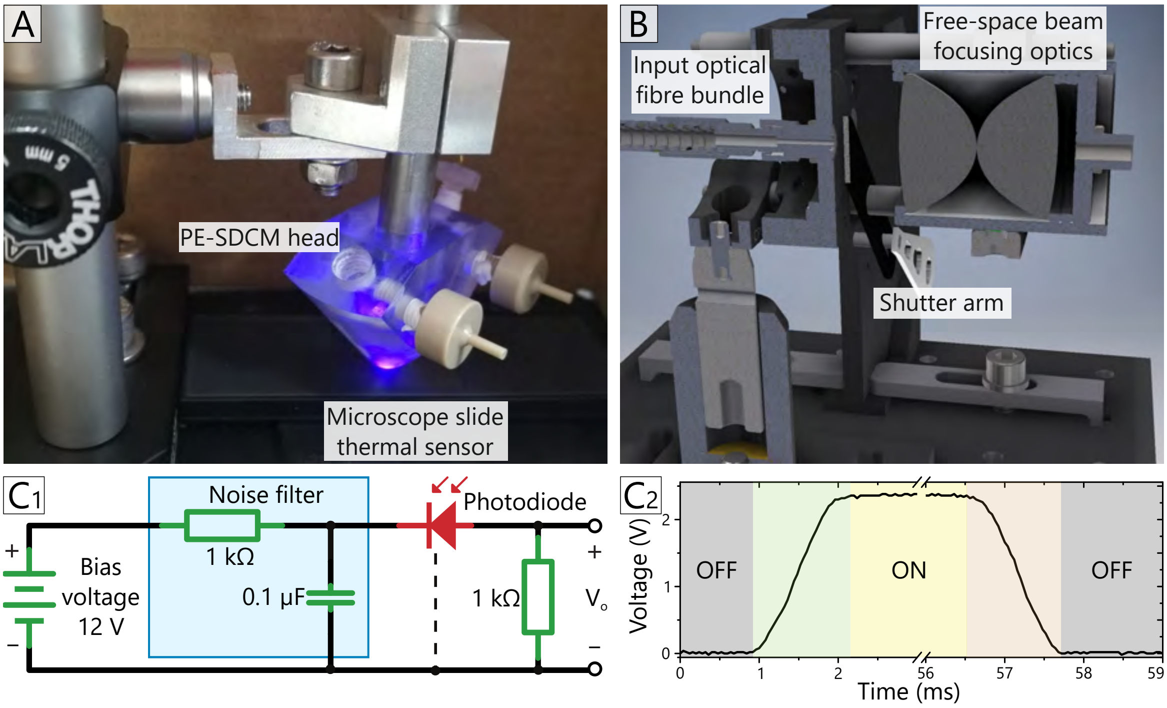

Figure 2.27: (A) Photograph of illumination intensity measurements within the PE-SDCM cell by a thermal sensor (measured intensities are tabulated in Table 2.3). (B) Cross-section of a 3D model of the shutter and its optics. (C1) Circuit for performance measurement of shutter and (C2) the measured data. The estimated rise time is 1.24 ms and fall time is 1.20 ms.

Photoelectric spectrometer setup

The majority of photocurrent measurements on the selected MO_x layers were performed by the aforementioned experimental PE-SDCM setup at ICTIM, JKU. To add to the credibility, these results are supplemented by additional independent testing performed on a different setup. This setup is situated at the Center of Materials and Nanotechnologies (CEMNAT) at the Faculty of Chemical Technology of the University of Pardubice. In this case, Dr Miloš Krbal, headed by Dr Jan Macák, performed all experiments and processed the data. When compared to the PE-SDCM, the setup used in CEMNAT consists of a photoelectric spectrometer (Instytut Fotonowy) with a 150 W Xenon lamp and a monochromator with a bandwidth of 10 nm connected with the modular electrochemical system AUTOLAB (PGSTAT 204, Metrohm Autolab B·V., Nova 1.10 software). Table 2.4 summarizes the key differences between these two setups.

Measurement procedures

All measurements were done in 0.1 M phosphate buffer (pH 6) at room temperature. The standard 0.1 M Na_2SO_4 solution [169, 170] was purposely avoided because it caused a significant PAA dissolution during the electrochemical measurements damaging the layer. This corrosion is still a surprising outcome because the 0.1 M Na_2SO_4 solution has a pH

Table 2.4: Parameters of photocurrent measurement setups.

	PE-SDCM (ICTIM, JKU)	Photoelectric spectrometer (CEMNAT, UPCE)
Light source	6×LED + Tung.-hal. lamp	Xe lamp→monochromator
Electrolyte	0.1 M phosphate buffer (pH 6)	
Flow-rate	0.5 ml s^{-1}	none
CE	Au wire	Pt wire
RE	home-made Ag/AgCl	commercial Ag/AgCl
Size of WE	⌀2.7 mm	⌀6 mm

of 6.7–6.8, which is still in the passivation range (pH 5–8) of the aluminium Pourbaix diagram,[171] and thus, the alumina should be immune. One of the most reasonable explanations is a local change of pH caused by the electric field. A popular sodium hydroxide (NaOH) solution was not considered because it is a highly aggressive PAA etchant.

The procedure for every sample measured by PE-SDCM consists of open circuit potential (OCP) measurement/stabilization for at least one hour. Afterwards, an EIS at OCP in the dark (10^4 to 10^{-1} Hz, 10 mV amplitude) was performed to check the sample before a series of CVs (−0.5 to 1.5 V vs Ag/AgCl) that could modify the sample surface. At first, a series of three CV cycles (50 mV s^{-1}) in the dark was performed, followed by a series of variable scan rate (10, 20, 40, 80 mV s^{-1}). The chopped illumination CVs were performed at the scan rate of 10 mV s^{-1} and each LED (Table 2.4) illumination. Finally, EIS in the range of −0.7 to 0.2 V vs Ag/AgCl (for Mott–Schottky analysis, starting from the anodic potential) was performed in the dark and under the illumination of the 365 nm LED. Unfortunately, only the chopped illumination CVs are presented as the rest of the results are inconclusive.

The measurement procedure using the photoelectric spectrometer for selected samples (mainly air-annealed nanostructured samples and flat Ti films) was simplified to only three CV cycles in the dark in the same potential window (−0.5 to 1.5 V vs Ag/AgCl). Photocurrent measurements followed this at 0.5 and 1.5 V versus Ag/AgCl within a spectral range of 300–500 nm (step size of 5 nm) to obtain the IPCE spectra.

2.4.3 Chopped light linear sweep voltammetry and IPCE measurements

Chopper light linear sweep voltammetry

Figure 2.28 shows the current density vs potential curves under chopped illumination of the 365 nm LED using the PE-SDCM setup for all samples. The photocurrent density (J_{ph})

can be easily extracted as the difference between the total current (J_{total}) and the dark current (J_{dark}), as illustrated in Figure 2.28:C. The photocurrent density of all samples increases with the anodic potential, which indicates the standard n-type nature of the electrode material. This growth is in good agreement with expectations and the previous M–S analysis (see section 2.3).

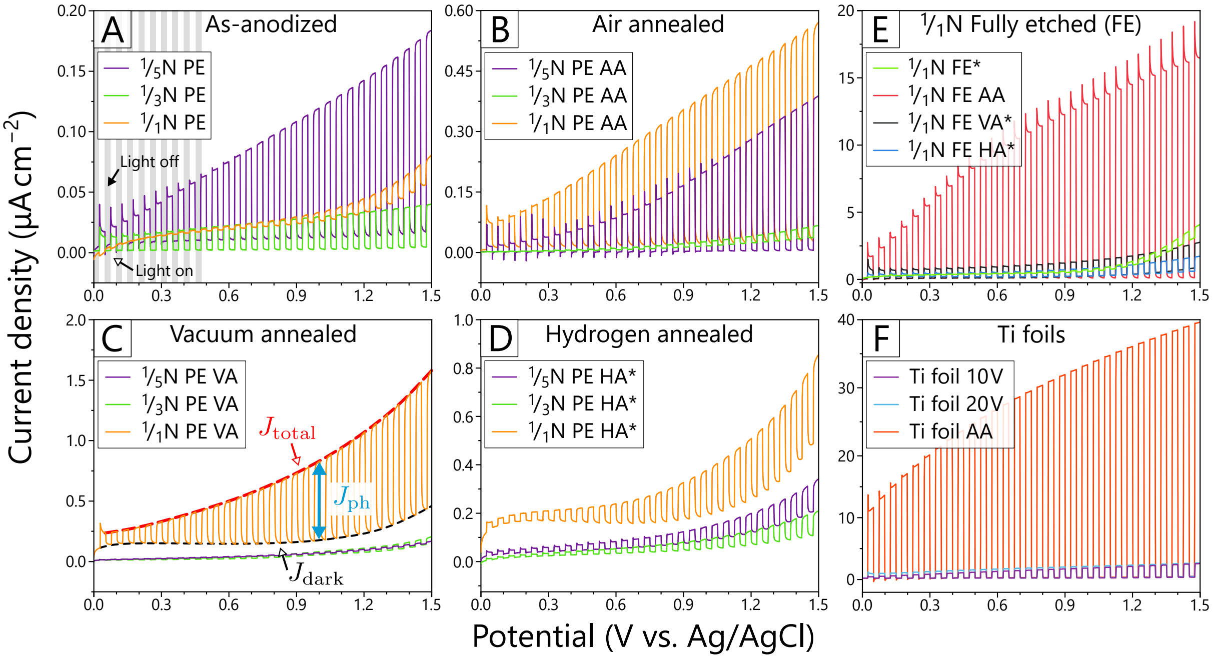

Figure 2.28: Photoelectrochemical properties of (A–E) nanostructured layers formed on nitrogen-doped substrates (Table 2.1) and (F) oxidized titanium foils. The chopped J–V curves were obtained under the 365 nm LED and illumination cycle of 5 s (frequency 0.2 Hz and cycle duty of 50 %, illustrated in (A)). Measurements were performed using the PE-SDCM in 0.1 M phosphate buffer and a scan rate of $10\,\mathrm{mV\,s^{-1}}$. Samples marked by an asterisk (*) have been anodised to 4 V versus Ag/AgCl before measurement (as discussed in the following text).

Dark currents and additional anodising

The CV helps identify samples with relatively low electrical resistivity that show high dark currents (Figure 2.29 in pale colour). In this group belongs all hydrogen annealed (HA) and fully etched (FE) samples except the air-annealed (AA FE) one. In the case of hydrogen annealing, it may be simply explained as oxidation of the reduced TiO_2. TiO_2 is reduced by thermal treatment in a hydrogen environment, which increases the oxygen vacancies as shown in the following equation:

$$\mathrm{O_O^{\times}} + \mathrm{H_2} \longrightarrow \mathrm{V_O^{\bullet\bullet}} + 2\,\mathrm{e'} + \mathrm{H_2O} \tag{2.4}$$

where O_O is the O^{2-} ion in the oxygen lattice site, V_O is the oxygen vacancy with a double positive charge, and e′ is the conduction electron.[45] In this case, the conductivity of the layer grows with the increased density of charge carriers, resulting in an unwanted rise of dark currents.

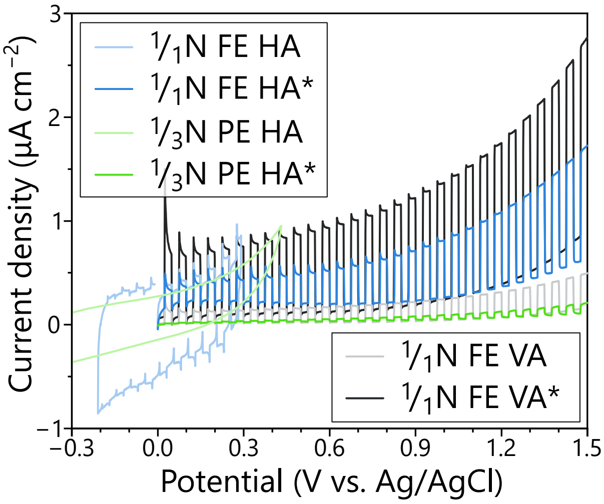

Figure 2.29: Comparison of voltammograms under chopped LED illumination (365 nm, ≈6 mW cm^{-1}, Table 2.3) for samples before and after (marked by asterisk (*)) anodisation by CV (−0.5 V to 4 V versus Ag/AgCl).

From the technological aspect, these samples behave like metals, which undergo another oxidation when an anodic potential is applied during the first cycle of the CV procedure. This unstable behaviour during the characterization, as well as relatively high dark currents, is undesirable. Therefore, the affected samples were additionally anodised to form a thin oxide layer to get more useful photocurrent information. This time, the anodisation was done right before the characterization inside the PE-SDCM cell using the same electrolyte (0.1 M phosphate buffer of pH 6) and three CV cycles in the range from −0.5 V to 4 V vs Ag/AgCl and scan rate of 50 mV s^{-1}.

Surprisingly, this additional anodising also improves the response of the FE samples. This outcome may appear predictable as removing the PAA layer exposes the underlying metallic substrate. However, these samples were post-anodised up to 6 V in 0.3 M oxalic acid right after the PAA etching. Therefore, analogically to the aluminium anodisation, the anodisation of titanium in the phosphate buffer probably gives a more compact oxide layer than in the oxalic acid. A similar conclusion was made by Sul et al. in their comprehensive study of titanium anodising,[172] where they conclude that less concentrated and more neutral electrolytes make more dielectrically stable oxides. On the other hand, the air-annealed fully etched sample (1/1N FE AA) gives the lowest dark current values in the FE series (Figure 2.28:E), demonstrating the superiority of the thermal oxidation on air. This observation elegantly concludes the topic, proving that proper oxidation is essential for fabricating a working photoelectrode.

The samples anodised before the PEC characterization in this way are for further reference labelled by an asterisk (*) and cannot be directly compared with the other samples, which were not processed as such, without caution.

IPCE measurements

By extracting the photocurrent density from voltammograms measured under chopped illumination of the remaining LEDs (not presented), rough IPCE spectra can be plotted as shown in Figure 2.30 by dashed lines for the air-annealed samples. For comparison, the graph is supplemented by the IPCE spectra of the same samples measured by the photoelectric spectrometer setup. Here, the differences between both measurements of air-annealed samples can be observed. Unfortunately, these values are not linearly dependent, which excludes a singular systematic error caused by a sample or measurement variation. Nevertheless, the IPCE trends match for both machines, and thus it is believed that even the experimental PE-SDCM setup provides sufficiently relevant information, especially in the case of comparative interpretations.

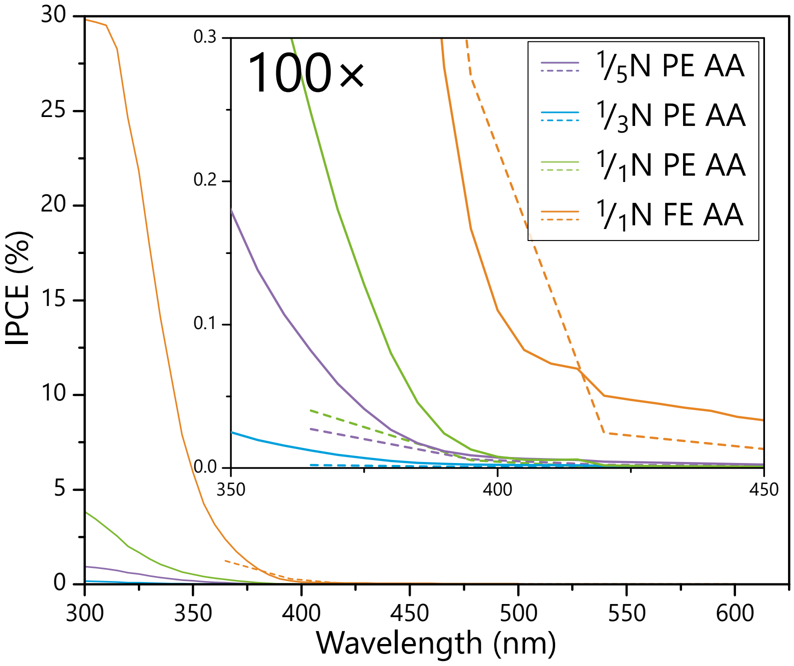

Figure 2.30: A comparison of the IPCE spectra measured by both setups: (full line) the photoelectric spectrometer setup and (dashed line) the PE-SDCM setup. Photocurrents were measured at an applied bias of 1 V versus Ag/AgCl.

For a better illustration, Figure 2.31 presents a summarized comparison of IPCE obtained by PE-SDCM under 365 nm LED illumination for the various nanocolumn layers and compact oxide layers formed on a titanium sheet (used as a reference). These IPCE values were calculated from the photocurrents measured at 1 V versus Ag/AgCl. Several important trends can be observed here. The most significant outcome is that the highest IPCE of almost 3 % has been found for the thermally oxidized Ti sheet used as the reference. This value matches the reported values between 2–3 % for thermally oxidized

Ti foils at 500–700 °C for 10–60 min.[173] The second-highest IPCE with a value of less than half of the AA Ti sheet was obtained for the PAA-free air-annealed layer (1/1N FE AA). The two anodic layers (10 V and 20 V) on the Ti sheet and the PAA-free vacuum-annealed layers (1/1N FE VA) are in the middle, close to but still over the 0.1 % level of the second-highest IPCE. The rest of the MO_x nanostructured layers are left far behind with relatively poor performance.

The shape of the IPCE spectra (Figure 2.30) is almost identical for all air-annealed partly etched samples with relative very low efficiencies at wavelengths above 400 nm (3.1 eV). This indicates that these layers have similar properties (indirect bandgap), yet they may differ in the active surface area (not the macroscopic WE area). The same also applies to the fully etched sample except for a small plateau at low wavelengths at the 300–315 nm region. Surprisingly, this feature is observed only for the fully etched nanostructured 1/1N layers (with or without nanocolumns) shown in Figure 2.33. Meanwhile, the partly etched nanostructured layers (Figure 2.30) and the planar thermal oxide formed over the 1/1N substrate (Figure 2.31:A) give a sharp slope. This plateau is only interesting because it usually indicates the maximum value of the IPCE peak.[46] Therefore, it is possible that half of the IPCE peak (1/1N FE AA) is already visible in the observed range.

The observations mentioned above indicate that, in the case of the studied TiO_2-based nanocolumns, the planar MO_x layer grown below the nanocolumns has a crucial impact on the IPCE values and the a-MO_x nanocolumns do not bring a significant improvement. This hypothesis is confirmed by the following conclusions:

(i) The IPCE of the 1/1N FE AA sample is over 20× higher than that of the same film but PE, even though the difference in the active area (the surface of the columns and the substrate) is only up to 4× larger. Therefore, this extensive increase must be attributed to the layer of thermal oxide grown on the substrate during air annealing.

(ii) The structure of the formed nanocolumns contains voids (hollow parts). In the case of 1/5N and 1/3N layers, usually, a singular void is located under the root. In contrast, the 1/1N columns form a predominantly hollow structure seen in the cross-view in Figure 2.32:A. However, Bendová et al.,[119] reported that these interior parts of the 1/1N nanocolumns are filled by a hydrated N-doped TiO_2–Al_2O_3. This claim, predominantly based on the XPS analysis of Ar sputtered layers, is believed to be wrong due to a possible misinterpretation of the XPS results. Surprisingly, neither the included TEM (EDX) analysis does support this claim. Moreover, similar features in the columns formed from substrates with less nitrogen content are claimed to be voids or bubbles. To prove whether the inside of the column (1/1N) is solid or hollow, a cross-section of the 1/1N PE sample (Figure 2.32:B1) was coated by a thin gold layer, shown in Figure 2.32:B2. Here, the Au layer tightly envelops the inner part of columns, clearly showing a concave interior that is anticipated for hollow columns. Unfortunately, the hollow profile is assumed to be less advantageous to the solid column due to low light absorption, electrical conductivity, and charge

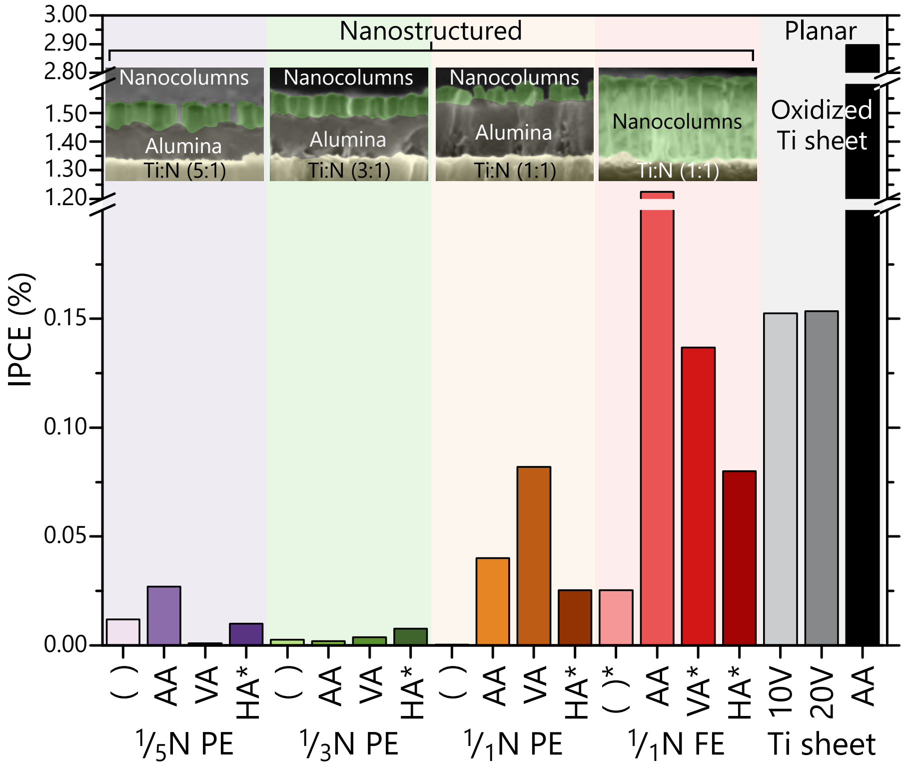

Figure 2.31: A comparison of the IPCE values measured in the PE-SDCM setup under the 365 nm LED illumination (3.4 eV) at the applied bias of 1 V versus Ag/AgCl (the corresponding voltammograms are shown in Figure 2.28). The labels are consistent with the fabrication section (section 2.1): partly etched (PE), fully etched (FE), as-anodised ( ), and annealed in the air (AA), vacuum (VA), or hydrogen (HA) atmosphere. Two layers formed by anodic oxidation of the Ti sheet in a sulphuric acid electrolyte are added, marked by their anodising potentials: 10 V and 20 V. Insets show false colour SEM cross views of the nanostructured layers (green – nanocolumns, grey – alumina, yellow – substrate). High-resolution SEM images of and further information about the nanocolumn samples are shown in Figure 2.5.

separation.

(iii) The performance of the 1/1N FE AA layer with or without nanocolumns is almost identical, as shown in Figure 2.33:D. The observed difference in the lower wavelengths is presumably caused by the nanocolumn residues after their removal by a cloth cleaning swab stick (Figure 2.33:C). Therefore, the contribution of nanocolumns to the IPCE is either negligible or zero.

(iv) Among the PE series, just the 1/5N gives the highest IPCE values for the AA layer. The reason is that the 1/5N PE samples suffer from the largest exposure of the underlying substrate caused by alumina defects (discussed in subsection 2.1.4). The subsequent air annealing leads to its additional oxidation and formation of a localized thermal oxide film that probably carries most IPCE. This effect is analogous to the 1/1N FE AA but much weaker due to a partial exposure of the substrate.

(v) Like in the previous point, a correlation between the exposed substrate area and the IPCE value of the as-anodised samples can be observed in the increasing order from $^{1}/_{1}$N PE < $^{1}/_{3}$N PE < $^{1}/_{5}$N PE < $^{1}/_{1}$N FE. Same as in the case of air annealing, the exposed area is oxidized by the post-anodising process. However, the IPCE enhancement caused by the additional anodic oxide is much smaller compared to the thermal one. An analogy can be noted for anodised and thermally annealed Ti sheets.

(vi) Lastly, the thermally oxidized planar sample (Figure 2.33:A) has approximately 2× higher performance than the nanocolumn version (Figure 2.33:B), as illustrated on the $^{1}/_{1}$N substrate shown in Figure 2.33:D. This difference suggests that nanocolumns not only have a poor additional value to the IPCE of the system (as discussed in point iii)) but also somehow hinder the possible performance of the thermal oxide. This shadowing can be roughly supported by the geometry of the system, where the nanocolumns take up to 25 % of the 2D projection, and the root takes an additional 30–35 % of the oxide surface, giving together approximately 50 % of the missing performance. Even though the poor performance of nanocolumns was indirectly proven, the similar behaviour of the root area is just a speculation, as it is not possible to separate it from the substrate oxide.

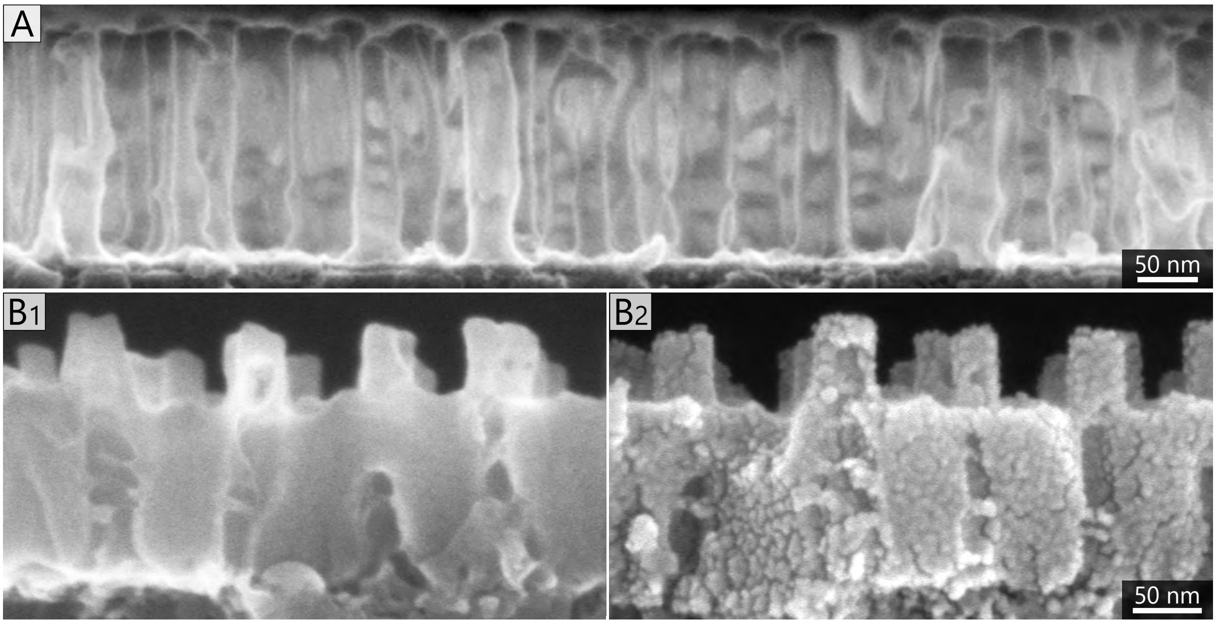

Figure 2.32: SEM cross-section views showing the hollow structure of nanocolumn layers of (A) $^{1}/_{1}$N FE and $^{1}/_{1}$N PE (B1) before and (B2) after being coated by 8 nm thin gold layer (sputter deposited in the Leica setup, see subsection 5.3.1).

Furthermore, the performance of the as-anodised layers is, in most cases, notably low. It can be seen for the $^{1}/_{3}$N, $^{1}/_{1}$N substrates, and especially for the anodised titanium sheet (Figure 2.31). Although the air annealing of the Ti sheet and its anodising at 20 V produces oxide films of similar thickness (50–70 nm; estimated from the colour and

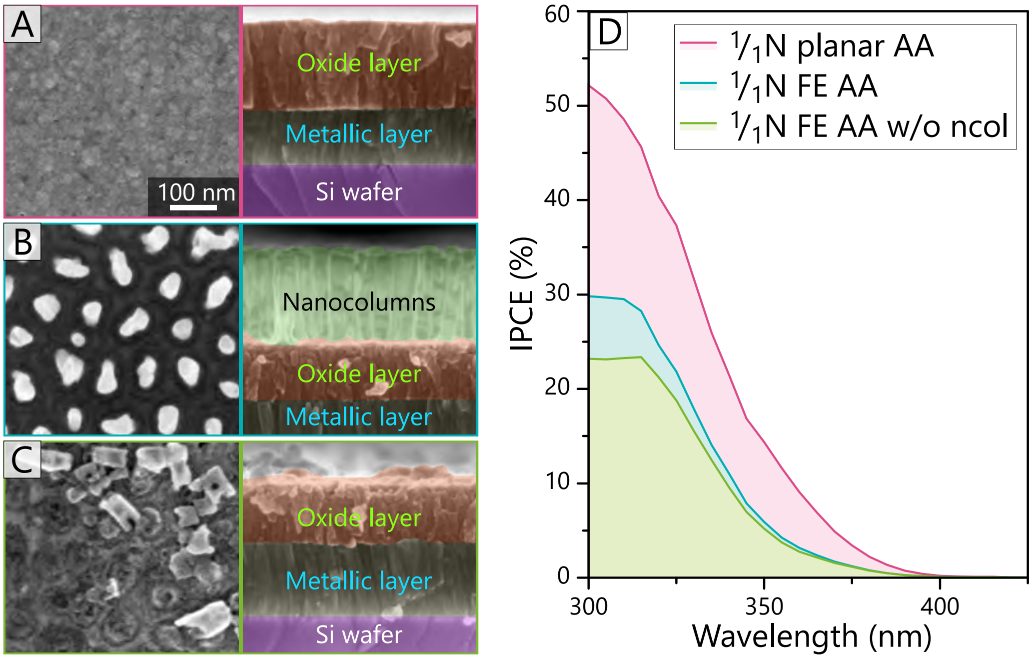

Figure 2.33: SEM top and cross-section views of (A) a compact MO_x layer (185 nm) formed by thermal oxidation (same as for the air-annealed nanostructured samples, 550 °C for 2 h in the ambient atmosphere) of the ¹⁄₁N substrate layer. Before annealing, the superimposed aluminium layer was removed by a 1 M NaOH aqueous solution. The ¹⁄₁N FE air-annealed nanocolumn array with 128 nm thick oxidized substrate layer (B) before and (C) after column removal. (D) IPCE spectra of these layers measured by the photoelectric spectrometer setup at the applied bias of 1.5 V versus Ag/AgCl.

literature)[156], their performances are apart by order of magnitude. This performance gap originates from the different crystal structure of the oxide formed by the anodisation (amorphous), and the thermal oxidation (anatase or rutile), as will be discussed in later texts. This difference between as-anodised and air-annealed oxides also supports point v).

Point vi) assumes the equivalence between MO_x layers formed on the planar substrate with the 185 nm thickness (Figure 2.33:A) and the one formed through the nanocolumn layer (Figure 2.33:B, C) with the thickness of 128 nm. Although these layers differ in their thickness, it is assumed that it does not play a significant role. The reason for neglecting this apparent difference is based on the IPCE comparison of a much thinner (25 nm, Figure 2.34:A) layer that performs better than the 128-nm layer. Therefore, the thickness cannot be a dominant cause for the 128-nm layer formed under nanocolumns to perform worse than the 185-nm layer formed over a free surface.

Figure 2.34 shows a comparison of air-annealed MO_x layers grown on all three nitrogen-doped substrates. The annealing parameters were the same as for the air-annealed nanocolumn samples, i.e., 550 °C for 2 h in the ambient atmosphere. The microstructure of the deposited metallic films changes with the nitrogen content from a dense to a more columnar structure (already seen in the ¹⁄₁N substrate) typical for TiN films.[174] It

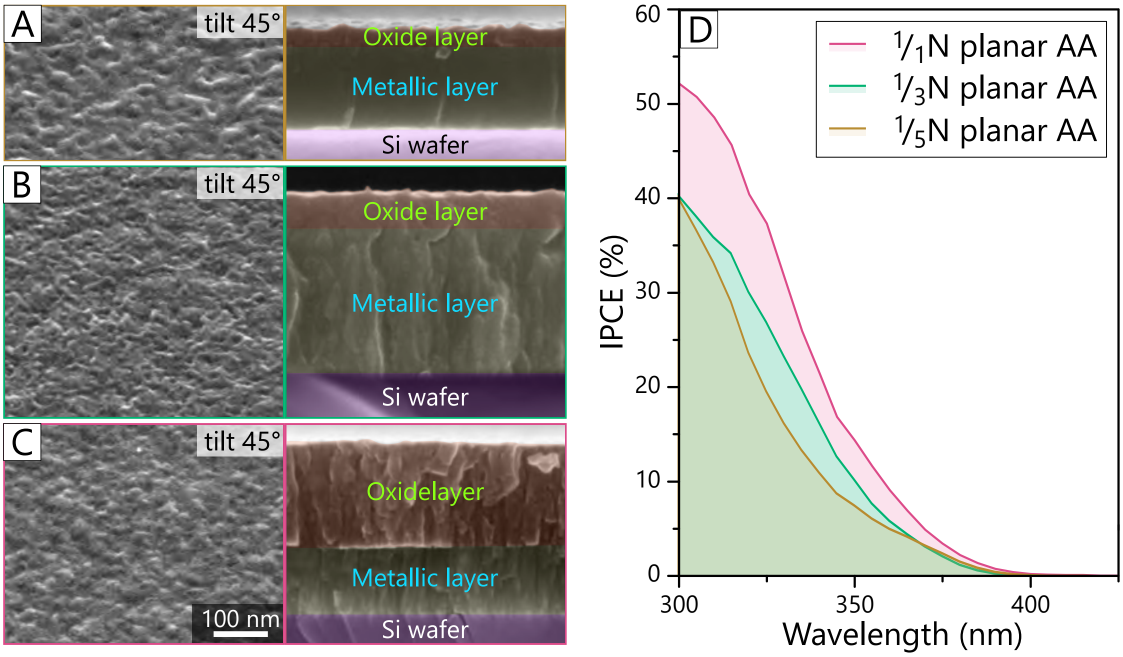

Figure 2.34: SEM tilt and cross-section views of air-annealed (same as for the air-annealed nanostructured samples, 550 °C for 2 h in the ambient atmosphere) nitrogen-doped substrates (after Al removal): (A) ⅕N with 25 nm oxide and 160 nm metallic layer, (B) ⅓N with 50 nm oxide and 270 nm metallic layer, and (C) 1⁄1N with 185 nm oxide and 125 nm metallic layer. (D) IPCE spectra of these layers measured by the photoelectric spectrometer setup at the applied bias of 1.5 V versus Ag/AgCl.

is well documented that the microstructure of the films can influence the thickness of the thermal oxide.[158, 174, 175] The same is observed here. The substrates of lower nitrogen concentration (⅕N, ⅓N) result in much thinner oxide layers with fewer morphological features than the 1⁄1N substrate.

More surprising is that these oxide layers have an almost identical chemical composition with a zero nitrogen content, as estimated by XPS and shown in Table 2.5. These findings demonstrate that the thermally grown oxide has stoichiometry very close to a pure TiO_2. Surprisingly, the oxygen ratio increases slightly with the nitrogen content in the initial substrate. A similar observation was made by Hinode et al.,[175] who showed that thermal oxidation of TiN leads to a bilayer structure composed of TiO_2 on TiN without any intermixing layer. The comparative IPCE spectra (Figure 2.34:D) show up to a 15 % higher response for the oxide layer formed over the 1⁄1N substrate. As discussed before, such an increase cannot be associated solely with the oxide thickness. The morphology of the oxide might have significant effects as well as the crystallinity, which can vary based on the microstructure of the initial substrate and still needs to be proven in future work.

In all cases, the thermal TiO_2 layers should be composed of the anatase phase, according to numerous reports.[46, 157, 164, 173] These annealing parameters (550 °C for

Table 2.5: Relative atomic concentrations of elements present in the planar oxide layer grown on the nitrogen-doped substrates by thermal oxidation (shown in Figure 2.34). Concentrations are estimated from the wide XPS spectra of Ar^+ beam sputtered spots.

Label	Stoichiometry	Atomic concentration [%]						
		Ti	O	N	C	Si	F	P
1/5N flat AA	$TiO_{1.93}$	31.7	61.2	0.1	5.5	1.1	0.3	0.1
1/3N flat AA	$TiO_{1.96}$	31.2	61.0	0.1	5.6	1.7	0.4	0.1
1/1N flat AA	$TiO_{2.01}$	30.6	61.6	0.1	5.4	1.3	0.6	0.6

2 h in the ambient atmosphere) were chosen as they were reported to give the highest ratio of anatase phase, which results in large photocurrents and IPCE values.[46, 176] A higher temperature treatment leads to the formation of the rutile phase, which has a lower bang gap (3.0 eV) than anatase (3.2 eV) but, in general, gives a worse photocatalytic activity.[46] This is no surprise since anatase has a lighter effective mass and longer lifetime of photoexcited electrons and holes.[177] This is nicely shown on the IPCE spectra of the 1/1N substrate air-annealed at 600 °C (Figure 2.35:B black curve). Here, the IPCE maximum is shifted to higher wavelengths as a result of the rutile smaller bandgap. Meanwhile, the overall IPCE decreases significantly. The same transition effect during the air annealing is expected also for nanocolumns having their composition close to pure TiO_2 in the anatase phase. However, further excessive study (TEM analysis) still needs to be made to better understand their composition and microstructure after various treatments. For more information about the composition of the as-anodised nanocolumns, please refer to our collaborative publication.[119]

Lastly, Figure 2.35:A, B shows a trial to reproduce the results of Licklederer et al.,[178] who reported that a gold nanoparticle (AuNP) layer formed by the dewetting of a thin Au film (described in detail in section 5.3) over a rutile TiO_2 film increases the IPCE in the visible region (≈600 nm). A similar result was reported by Krysiak et al.,[179] who used photodeposited gold nanoparticles on the rutile and anatase phase of TiO_2. Sadly, no detectable increase of photocurrents was observed in the 400–800 nm region (of plasmonic resonance) for any of the deposited AuNPs layers (data not shown). Nevertheless, AuNP layers of various distributions were successfully deposited over the oxidized substrate, and a similar trend of IPCE was measured, as observed by Licklederer. Based on the current knowledge, it is assumed that the problem might be in a low dewetting temperature that may be high enough for the nanoparticle formation, but it may not be sufficient to create a proper bond between AuNPs and the substrate oxide. Substrate contamination by carbon can have the same effect, preventing direct contact between Au and TiO_2 (see subsection 5.3.3 for the Au deposition on a carbon layer). Therefore, more extensive and systematic research should be conducted in the future to find the best working parame-

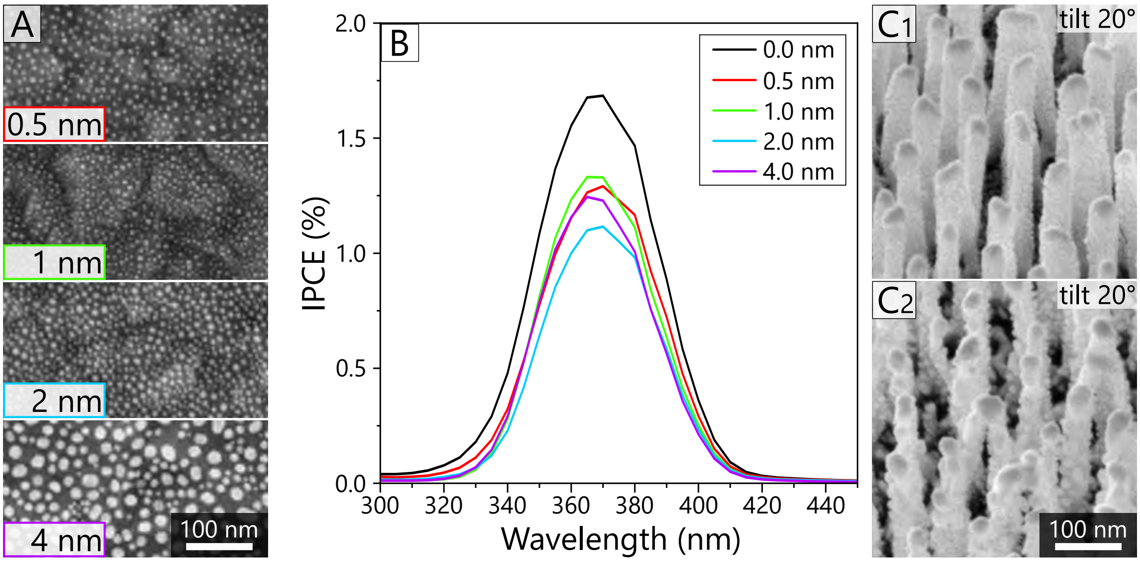

Figure 2.35: (A) SEM images of dewetted (350 °C, 5 min) Au thin films of various thicknesses on the air-annealed (600 °C, 10 h) ¹⁄₁N substrate layer. (B) Graph showing IPCE of these layers measured at 0.4 V in 0.1 M phosphate buffer (pH 6) with 5 nm step. (C1–2) Tilted SEM images of nanocolumn substrate sputter-deposited by a 10-nm gold layer (C1) before and (C2) after the dewetting process.

ters to utilize the plasmonic effect of AuNPs. Figure 2.35:C1–2 shows a preview of the nanocolumn a-MO$_x$ layer decorated by a very dense and homogenous layer of AuNPs. This sample was fabricated as a proof of concept to show a possibility to uniformly cover even these columns with a high aspect ratio.

2.4.4 Conclusions

This section investigates the photoelectrochemical properties of the selected nanocolumn layers formed by PAA-assisted anodising of titanium substrates of various nitrogen contents. Here, the anodising parameters were chosen to obtain the same column morphology as studied in our previous work.[119] Unfortunately, using these parameters (a long substrate anodising with the slow re-anodising ramp) resulted in very unstable columns (section 2.2), except for the ¹⁄₁N substrate. Therefore, the PAA has to be only partially removed to reveal only the tops of the columns while still leaving a sufficient layer for their support.

Although this solved one problem and allowed us to compare the effect of various nitrogen concentrations in the substrate for nanocolumn layers, it also has created a new problem caused by the inhomogeneous etching of the PAA. This process revealed the underlying substrate layer to varying degrees depending on the thickness of the partly etched PAA layer related to the substrate composition (column length). Therefore, the layers were anodised (post-anodising) after etching to oxidize all metallic surfaces accessible to the electrolyte. Furthermore, the samples were thermally annealed in various oxidizing or reducing atmospheres to study the effect of the created oxygen vacancies. The presence of the supporting PAA layer creates an additional issue because it is incompatible with common and well-performing electrolytes used for photoelectrochemical characterization of TiO_2, such as $NaSO_4$ or NaOH. To avoid the undesirable etching of the PAA, phosphate buffer was chosen for all experiments.

All samples were measured in the experimental PE-SDCM at ICTIM JKU, with a custom-built LED illumination system, which is in detail discussed in subsection 2.4.2. For further validation of the results, the IPCE of the selected samples was also measured by Dr Miloš Krbal using the photoelectric spectrometer at CEMNAT UPCE.

Based on all findings, the most significant conclusion is that the prepared nanocolumns have negligible IPCE performance and thus are not feasible as a photoelectrode material. The most convincing argument is the IPCE comparison between a nanocolumn layer before and after columns being wiped, showing a minor difference. Even though, this decrease cannot be unambiguously associate only with the removal of nanocolumns. A more reasonable explanation can be simple shadowing of the surrounding more active thermal oxide by nanocolumn residues. This outcome is even more highlighted when the nanostructured surfaces show just a fraction of performance compared to the flat oxide layers, which are considerably less demanding in terms of the fabrication requirements.

This poor performance is assumed to be primarily related to the morphology of the selected nanocolumns. The formed nanocolumns consist of defects in the form of voids located near the root for substrates of lower nitrogen concentrations ($^1/_5$N, $^1/_3$N), while for the highest nitrogen concentration ($^1/_1$N), the nanocolumns have the characteristic hollow structure. The voids are surrounded by a very thin TiO_2-based shell, presumably not a great electrical conductor, light absorber, or electron–hole separator.

The chemical composition is another factor that can play a significant role. This can especially be related to the less stable nanocolumns ($^1/_5$N, $^1/_3$N), in which the roots consist of a mixture of titanium and aluminium oxides that makes them chemically unstable and less conductive.

3 CONCLUSIONS AND FUTURE OUTLOOK

This part of the thesis studied the morphology and electrochemical and photoelectrochemical properties of titanium oxide nanocolumn arrays formed by the porous anodic alumina-assisted anodising of a superimposed aluminium layer over titanium-based substrates. The general goal of this work was to fabricate and analyse nanostructured TiO_2-based layers, which could possibly be used as a photoanode for photoelectrochemical water splitting, otherwise termed as the production of solar hydrogen.

The fabrication section demonstrates two anodising setups successfully used to prepare a variety of samples:

1. The flow-through pressing cell that can be used with significant advantages in R&D applications where a broad variability of anodising parameters is required.
2. The large-scale setup that can be, on the other hand, utilized for applications requiring large sample areas and homogeneous processing.

The etching of PAA was optimized to achieve the same exposure for various heights of the nanocolumn arrays. However, it was found that it leads to the formation of defective sites, which have a crucial impact on further evaluating PEC properties of partly etched samples.

The electrochemical characterization of the PAA embedded nanocolumns (section 2.3) confirmed most of the expectations. A significant difference between the behaviour of the layers formed on pure (N-free) and nitrogen-enriched (N-doped) titanium substrates was identified. The N-free nanocolumns showed classical dielectric properties for the as-prepared and air-annealed samples, while the N-doped layers gave a desirable (n-type) semiconducting behaviour for all post-processing conditions as confirmed by Mott–Schottky analysis. It was also revealed that the selected parameters of the vacuum annealing treatment lead to a substantial increase in the dopant concentration, presumably in the form of oxygen vacancies. These findings agree with the literature. Even though these results did not deliver any significant novelty to the field, they are of vast importance for future utilization of the TiO_2-based nanocolumn arrays for photoelectrochemical water splitting. They describe how to obtain nanocolumns with good electrical conductivity and a space charge layer localized at the column surface and how to enhance the photogenerated charge carrier separation in these nanoarrays substantially.

The photoelectrochemical properties of nanocolumn layers (section 2.4) were investigated during an internship at JKU in Austria. For this purpose, a custom-built illumination system was constructed and added to the experimental PE-SDCM setup. Additionally, the results obtained by this setup were validated by IPCE measurements performed on a photoelectric spectrometer by Dr Miloš Krbal (University of Pardubice). In summary, the prepared nanocolumn layers showed only minor photoelectrochemical performance based on the IPCE results. The nanostructured layers were greatly overperformed by flat thermal or anodic oxides formed by technologically more straightforward methods. The reason is probably the characteristic hollow morphology of the nanocolumns formed by the chosen substrate composition and anodising parameters. This influences not only the morphology of the nanocolumns but also their chemical stability to withstand the PAA etching. Due to this reason, the comparison between the nanocolumns formed on substrates of different nitrogen contents could be performed only between arrays still partly embedded in the alumina layer.

This issue was later addressed by a systematic study of the effect of anodising conditions on the morphology and stability of the formed nanocolumns (section 2.2). The most critical outcome demonstrates the possibility to fabricate a perfectly stable nanocolumn array re-anodised to up to 300 V even from the pure Ti substrate. This is an overwhelming advancement compared to the previous reports on achieving stable arrays only to re-anodised potential up to 40 V. Besides the increase of stability, the improved anodising conditions also lead to a more compact/solid column structure without undesirable voids.

Unfortunately, further photoelectrochemical investigation of these novel layers was not conducted within the time scope of this thesis. However, the current findings present solid foundations for a future comprehensive study comparing both effects of the substrate composition and the nanocolumn morphology. All of this without any complications with the stability of the nanocolumns, and thus wholly avoiding the supporting alumina layer. Therefore, it is believed that these improved nanocolumn layers may provide a much higher IPCE when compared to the ones presented in this work. On the other hand, it is questionable whether they can rival other materials in PEC water splitting, where other methods can easily achieve a larger surface area and higher light absorption. The objective reason for this is that the PAA-assisted anodisation cannot deliver the same flexibility in the prepared structures hand in hand with a simple fabrication process. On the other hand, currently, there is no utilization of the nanostructured prepared by PAA and the ability to achieve a high order for the PEC. Therefore, it is advised that future studies also focus on the unique advantage of this technique that can be utilized in optical sensing.

Part II

Template-based fabrication of gold nanoparticles

'And now for something completely different.'

Monthy Python

Introduction

The interest in gold nanoparticles (AuNPs) dates to the 4th century Lycurgus Cup (shown in Figure 3.1), which changes colour depending on the location of the light source. However, the first rigorous and scientific study was done in 1857 by M. Faraday when he delivered his Bakerian Lecture to the Royal Society entitled 'Experimental Relations of Gold (and other Metals) to Light'.[180] He described the preparation of (colloidal) gold nanoparticles for the first time as well as their intense red-violet colour as a function of the particles.[181] Today, it is known that the underlying phenomenon is attributed to the collective electron oscillation excited by optical frequency electromagnetic wave known as the localized surface plasmon resonances (LSPR). It is well known that localized surface plasmons (LSPs) can focus light to a nanometre scale and strongly enhance the electric field near nanometals, which is called the antenna effect.[182] The research field dealing with such plasmon characteristics is called 'plasmonics' and has been extensively investigated for its wide application area in, e.g., optical sensing, light generation, biomedicine, electronics, and data storage.[183] Among other plasmonic NP candidates (Ag, Cu) having their LSPR in the visible region, AuNPs are preferred especially for biological applications due to their inert nature and biocompatibility,[183] and easy functionalization provided by the thiol-gold association.[184] The increased utilization of AuNPs in recent decades quickly reflects the growing demand for their application-tailored production.

Figure 3.1: The Lycurgus cup: (A) The glass appears green when illuminated from the outside and (B) purple-red when illuminated from the inside.[185]

This part of the thesis will demonstrate one of the AuNPs fabrication methods. AuNPs are synthesized by a solid-state dewetting (SSD) of a thin gold film deposited on nanobowled aluminium (Al) templates. The Al templates are prepared by controlled anodic oxidation of the Al sheet and subsequent removal of the formed porous anodic alumina (PAA). Thus, similarly to the previous part, this fabrication technique utilizes the PAA morphology that forms the bottom Al template. In contrast to the PAA-assisted anodisation (section 1.6), this time, the focus is on the self-ordering phenomenon of the PAA (section 1.5), resulting in an almost uniform hexagonal alignment. This way, it is possible to prepare a 2D array of highly ordered AuNPs with tunable properties, e.g., size and spacing. This AuNP array was further transferred to various transparent substrates to obtain the LSPR element.

This work was conducted in close collaboration with Dr Attila Bonyár (Department of Electronics Technology at Budapest University of Technology and Economics, Hungary), who demonstrated a label-free DNA biosensing on these AuNP layers. This real application proved that these plasmonic nanostructures could be used as a versatile optical sensing platform (illustrated in Figure 3.2) for the detection of a large variety of receptor–target molecular interactions (e.g. nucleotide sensors or immunosensors). This biosensing part can be found already in the published joint study [186], or as the attachment (in the appendices chapter B) at the end of this thesis.

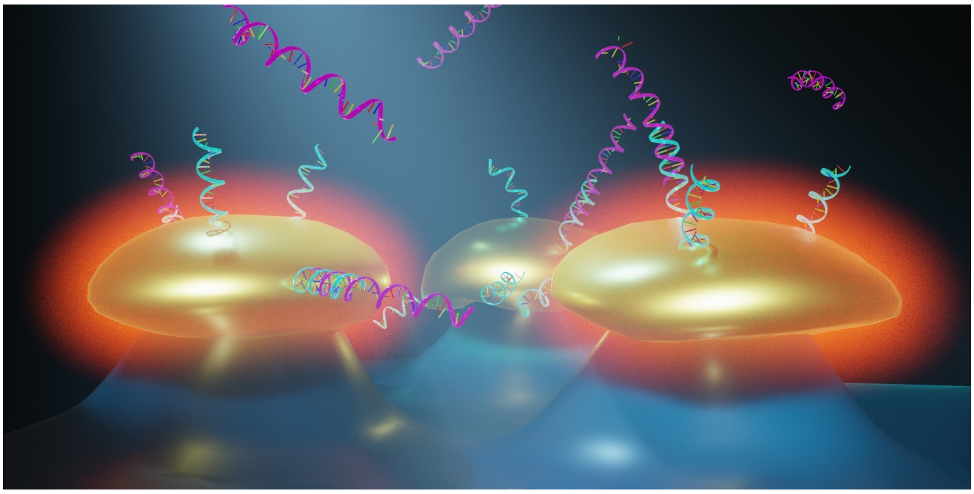

Figure 3.2: Graphical illustration of mushroom-like plasmonic structures functionalized by single-stranded DNA (ssDNA) probes (cyan) for the detection of target ssDNA (magenta).

This part of the thesis is like the first part, divided into two thematical chapters: theoretical/review and experimental. The introduction of the PAA is skipped because it is already presented in the Part I, and thus the first chapter starts with a short introduction of the solid-state dewetting of thin films and localized surface plasmons. This topic smoothly shifts into the applications of localized surface plasmon resonance (LSPR) and the current state of the art on the fabrication method of plasmonic structures and their utilization, specifically focused on label-free DNA detection. The broad overview is supposed to help the reader identify the vast amount of contemporary technological challenges related to this work. This part was adopted with minor modifications (and approval) from Dr Attila Bonyár that was partially published in the joint article [186] and further extended in the full review [187]. This chapter is concluded with the motivation, combined with a brief history and a review of very similar techniques.

The second experimental chapter is organized by the fabrication process. It starts with the preparation of aluminium and the fabrication of aluminium templates. Then, the fabrication of AuNP layers is described, their transfer to transparent substrates, and further substrate modifications. Because this chapter describes the development of a fabrication method, each fabrication step is supplemented by characterizations to clearly illustrate the role of individual process parameters.

4 THEORY & REVIEW

This chapter provides a brief theoretical introduction to a handful of literature reviews. Since the porous anodic alumina (PAA) has been introduced in the previous part (Part I, section 1.5), the fabrication of aluminium templates is already well covered. This chapter will therefore jump straight to the topic of the solid-state dewetting formation of nanoparticles, followed up by the condensed topic of nanoparticles utilization in plasmonics. This chapter is concluded by the literature review of the current progress in label-free LSPR-based DNA sensors, which serves as a stepping stone for the motivation of this work.

4.1 Solid-state dewetting of thin metal films

Thin films are in general metastable in the as-deposited state and will dewet (agglomerate) to make arrays of islands when heated (schematics and examples are shown in Figure 4.1). This transformation can happen at a temperature that is well below the melting point of the material. This temperature also decreases with the film thickness (shown in Figure 4.1), for example, for thin Au films (<10 nm), dewetting occurs already at 150 °C.[188]

The driving force behind SSD is to achieve the minimization of the free energy of the system by the change in geometry. In general, it leads to a reduction of the surface area of the thin film and the interface area between the film and the substrate. The energy minimization for a fixed volume (island) gives the Young-Laplace equation

$$\gamma_\mathrm{s} = \gamma_\mathrm{i} + \gamma_\mathrm{f} \cos\theta \tag{4.1}$$

where γ_s and γ_f are the substrate and island (film) surface energies per area, respectively. γ_i is the energy per area of the island-substrate interface, and θ is the equilibrium contact angle (schematically illustrated in Figure 4.2). If $\gamma_\mathrm{s} > \gamma_\mathrm{i} + \gamma_\mathrm{f}$, the film is stable and will not dewet. If this condition is not satisfied, the film will dewet when the rates of the necessary kinetic processes are sufficiently high (the rate of dewetting strongly depends on temperature). In other words, a thin Au film will dewet more easily on substrates with lower free surface energy.

While the dewetting of liquids can be characterized by hydrodynamic mass transfer in the film, SSD proceeds by capillary-driven surface diffusion via a flux J_s of material A.[190] For isotropic materials, it is the local surface curvature that drives the atomic flux (schematically shown in Figure 4.3) that may be written as

$$J_\mathrm{s} = -B\nabla_\mathrm{s}\kappa \quad \text{with} \quad B = \frac{D_\mathrm{s}\gamma_\mathrm{f}\mathit{\Omega}^2 n}{k_\mathrm{B}T} \tag{4.2}$$

where $\nabla_\mathrm{s}\kappa$ is the surface gradient of the film curvature κ, D_s is the surface diffusion constant, n is the number of diffusing adatoms per unit area, $\mathit{\Omega}$ is the atomic volume, k_B is the Boltzman constant, and T is the absolute temperature.

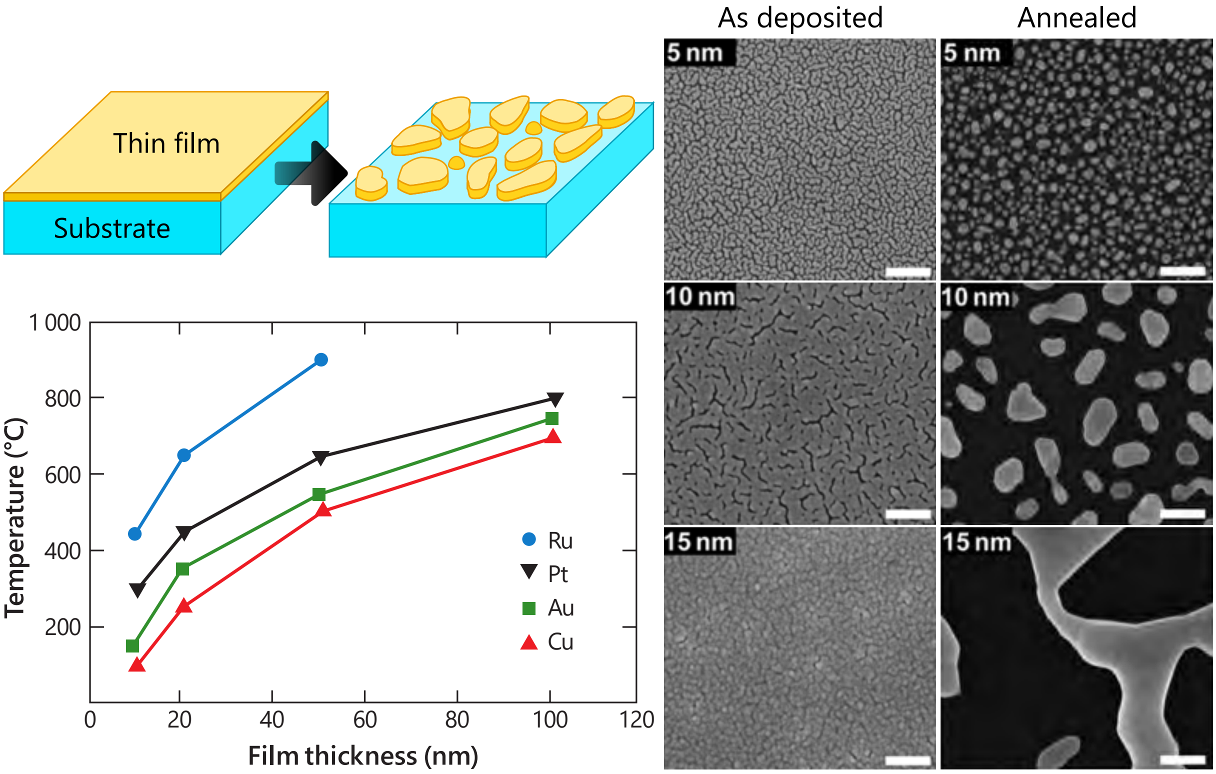

Figure 4.1: Schematic illustration of the formation of isolated islands from a thin film by SSD. This transition still occurs during solid-state. The graph shows the film thickness at which dewetting is observed as a function of annealing temperature for four different metals. Reproduced from ref. [188]. SEM images of the as-deposited thin Au layers (5, 10, and 15 nm) on 60 nm SiO_2 and resulting dewetted layers after annealing at 300 °C for 2 h in ambient atmosphere. The scale bar is 200 nm. Reproduce from ref. [189].

Morphological evolution of the thin film usually occurs via surface self-diffusion and generally progresses through at least three distinct stages: hole formation, hole growth and impingement, and ligament breakup. The overall process is complex with Rayleigh-like and fingering instabilities, grain boundaries, substrate morphology, and surface energy anisotropy.[188, 191]

In this work, the focus will be primarily on the effect of film morphology and substrate topography. The SSD typically initiates from film defects such as holes or cracks in the film (examples shown on 5 and 10 nm as-deposited film in Figure 4.1), local depletions (visible on 15 nm thick deposited film in Figure 4.1) or in the case of polycrystalline films, the grain boundary, especially triple junctions. From those defects, the hole growth nucleates and continues while the diffused material forms a thick rim in the perimeter of holes that breaks into beads or islands in the last stage. Even though this effect offers some way to control SSD of the thin metal film by artificially introducing defects [192], and/or confining the film area [188, 193–195], there are not many studies showing its utilization in a fabrication procedure. One of the reasons may be that this method does

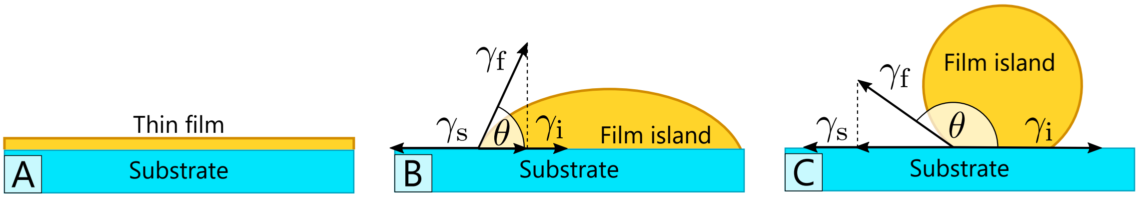

Figure 4.2: Schematic illustration of the thermodynamic equilibrium on the triple junction. (A) The substrate is perfectly wetted (no dewetting), (B) the film forms islands (partial wetting), (C) droplet formation (poor wetting). The equilibrium shape of a film island on a rigid substrate is represented by the contact angle determined from the Young-Laplace equation (Equation 4.1).[188]

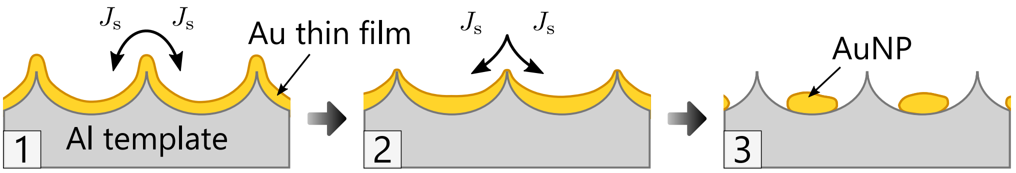

Figure 4.3: Schematic cross-sectional view of an ideal thin Au film dewetting on a nanobowled Al template and formation of AuNPs. J_s is the curvature-driven self-diffusion on the surface. Redesign according to ref. [188].

not offer considerable advantages (for example, a better spatial resolution) compared to the requirements on substrate and surface micro-machining.

On the other hand, there is a vast amount of reports using substrate surface topography to control the SSD process to fabricate nanostructures. When a conformal coating is deposited over a topographically structured substrate, it inherits its topographic features (example shown in Figure 4.3, stage 1). When heated, the film protrusions are smoothed by curvature-driven self-diffusion, leading to flattening the surface (Figure 4.3, stage 2). However, for the film thinner than a specific thickness, this can lead to the exposure of substrate protrusions that create holes/cracks in the film. The process continues as a standard SSD process, resulting in the formation of particles at the sides of the protrusions. If the substrate topography consists of pits and the film thickness is in a certain range, one particle (NP) formation per pit may occur (Figure 4.3, stage 3).[196] Then the size of NP is proportional to the volume of the thin film within the pit area. Therefore, a monodisperse NP layer can be achieved by SSD of a thin film over a periodic array of uniform pits (without trenches, an example is shown Figure 4.3). This behaviour gives a powerful tool to control the size of NPs and displacement by substrate topography and film thickness.

This phenomenon has impressed many researchers, resulting in numerous novel fabrication methods combining various periodically structured substrates. In this work, the predominant interest is on the self-assembled or so-called 'natural' substrates for their high efficiency, high throughput, and low cost compared to artificial substrates generally formed by methods such as optical/electron lithography or focus ion milling. Many systems show self-assembly character forming a periodic structure, but only a few have been used as dewetting templates, for instance: monoatomic steps or microfaces [197]; copolymer templates [198]; self-organized bowled substrate prepared by colloidal lithography [199], titanium nanotubes [200], or substrates prepared by PAA growth [201–203].

In summary, the SSD is an impressive and accessible tool to fabricate well-controlled NP layers from a thin film. Especially in combination with predesigned substrates, it is possible to precisely control the alignment of NPs and size over a large area of the templated substrate.

The most critical parameters include:

- film morphology,
- film thickness,
- substrate topography,
- film material,
- annealing temperature.

4.2 Localized surface plasmons

This section provides a very brief theoretical framework for plasmonics,focusing on localized surface plasmon resonance (LSPR) of gold nanoparticles. It aims to provide a fundamental background to the applications described in the experimental chapter (**??**). For a more in-depth description, see related review articles [204, 205], books [206–210], and theses [211, 212], which were used as sources for this section.

4.2.1 Introduction

Surface plasmon resonance (SPR) refers to the electromagnetic wave-induced collective oscillation of charge carriers (delocalized electrons) at the interface between materials with positive and negative permittivities, typically dielectric and metal. Concerning geometry, those electron oscillations can propagate along with a planar interface as the surface plasmon polariton (SPP) illustrated in Figure 4.4:A, or be confined to a subwavelength structure resulting in localized surface plasmons (LSPs) illustrated in Figure 4.4:B.[213]

4.2.2 Localized surface plasmons

In the case of metallic nanoparticles (NPs), i.e., with a size much smaller than the wavelength of light ($R \ll \lambda$), the resulting plasmon oscillation is distributed over the whole particle. Such a coherent accumulated displacement of electrons on one side of the NP creates a positive charge in the opposite part, creating an electric dipole. This dipole creates an electric field inside the NP opposite to that of the incident light, which pulls the polarized electrons back to the lattice, restoring the equilibrium position, i.e., the NP

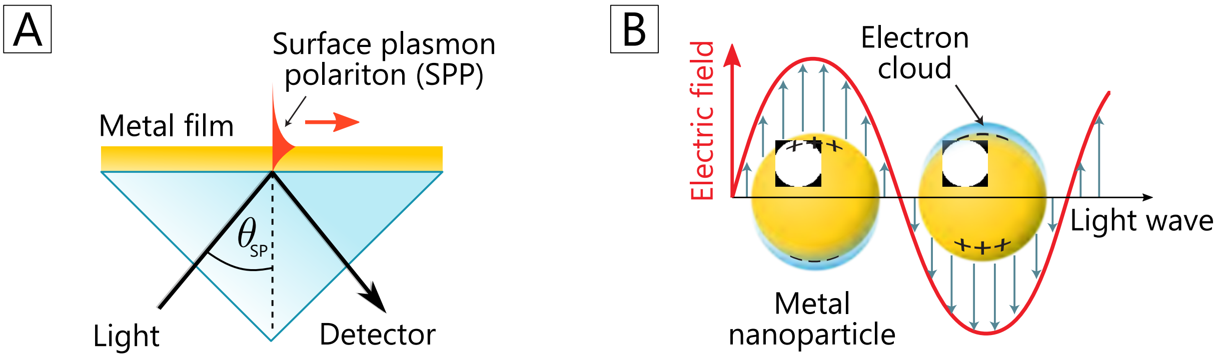

Figure 4.4: Schematic illustration of (A) SPP excitation at a thin metal film interface (Kretschmann configuration)[214] and (B) LSPs at metal nanoparticles within a propagating light wave.

acts much like a 'nanoantenna'.[215] Hence, the plasmon in an NP can be considered a mass-spring harmonic oscillator, where the electron cloud oscillates like a simple dipole in a parallel direction to the electric field of the electromagnetic radiation (Figure 4.4:B). This induced dipole moment inside the spherical particle with dielectric function $\varepsilon(\omega)$ and radius R located in a uniform static electric field $\mathbf{E}$ can be expressed as:

$$\mathbf{p} = 4\pi\varepsilon_0\varepsilon_\mathrm{m}R^3\frac{\varepsilon(\omega)-\varepsilon_\mathrm{m}}{\varepsilon(\omega)+2\varepsilon_\mathrm{m}}\mathbf{E} = \varepsilon_0\varepsilon_\mathrm{m}\alpha\mathbf{E} \tag{4.3}$$

where ε_0 is the dielectric constant of vacuum, ε_m is the dielectric constant of the surrounding medium, and α is the proportional constant called polarizability defined via $\mathbf{p} = \varepsilon_0\varepsilon_\mathrm{m}\alpha\mathbf{E}$. The polarization α is resonantly enhanced whenever the denominator term of the Equation (4.3) $\varepsilon(\omega)+2\varepsilon_\mathrm{m}$ goes to zero, which in the case of small and slowly varying $\mathrm{Im}\left[\varepsilon(\omega)\right]$ simplifies to Fröhlich condition [208]:

$$\mathrm{Re}\left[\varepsilon(\omega)\right] = -2\varepsilon_\mathrm{m}. \tag{4.4}$$

For a metallic nanoparticle located in the air, this condition is met at the resonant frequency $\omega_0 = \omega_\mathrm{p}/\sqrt{3}$, while the plasmon frequency (ω_p) is given by $\omega_\mathrm{p} = \sqrt{n_e e^2/m_e\varepsilon_0}$ [208], where e is the absolute value of the electron charge, n_e is the electron density, m_e is the effective electron mass. The Fröhlich condition (Equation (4.4)) further expresses a strong dependence of the resonance frequency on the dielectric constant of the environment. The most fundamental outcome is the resonance red-shifts as ε_m is increased. This response makes metal nanoparticles an ideal platform for optical sensing of changes in the refractive index ($n^2 = \varepsilon_\mathrm{m}$ for nonmagnetic materials with relative permeability $\mu \approx 1$). To compare the performance of various plasmonic systems, the bulk refractive index sensitivity (S) can be defined as the shift of the extinction peak (λ) per unit change in the bulk refractive index of the surrounding medium ($n_2 > n_1$) [216]:

$$S = \frac{\Delta\lambda}{\Delta n} = \frac{\lambda_{n_2} - \lambda_{n_1}}{n_2 - n_1}. \tag{4.5}$$

Its value can be experimentally obtained by a standard calibration procedure using aqueous sucrose solutions at different concentrations (0–50 % w/w, RI of 1.333–1.420) as the surrounding medium.[217] Using the bulk sensitivity value, a comparable signal—change of the effective refractive index $\Delta n_{\text{eff}}\left(t_\ell, n_\ell, n\right) \equiv \Delta\lambda/S$. The effective refractive index defined as an average of the refractive index of the medium integrated by the evanescent field can be derived for a thin layer adsorbed on the particle as:

$$\Delta n_{\text{eff}} = \left(n_\ell - n\right)\left[1 - \left(1 + \frac{t_\ell}{R}\right)^{-(2p+1)}\right], \tag{4.6}$$

where n_ℓ is the refractive index of the layer, t_ℓ is the layer thickness, and p is the order of the plasmon mode.[218] The possibility to detect such a small local change of the refractive index on the surface of a particle emerged in many exciting applications.[183, 219–221] One of them, label-free detection of DNA, is illustrated in Figure 4.5. The absorption spectrum red-shifts with NP functionalization by a DNA probe and once more with the binding of target DNA.

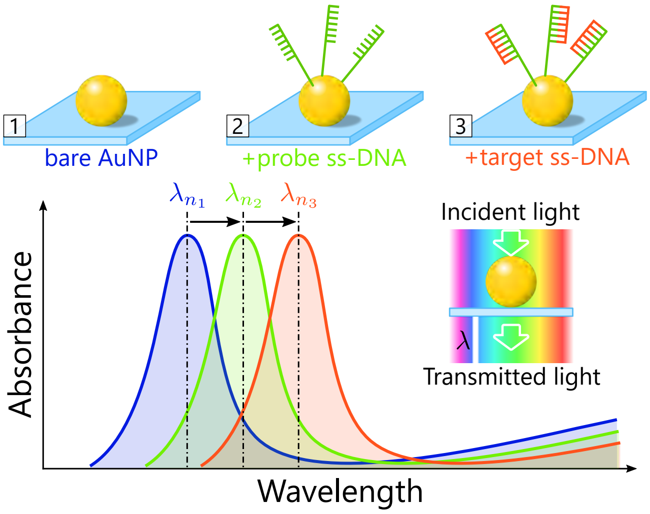

Figure 4.5: Schematic illustration of LSPR red-shift caused by DNA binding to detect targeted DNA strings.

Furthermore, the electric field distribution $\mathbf{E} = -\nabla\Phi$, can be calculated using the solution of the Laplace equation for the potential, $\nabla^2\Phi = 0$ with the electrostatic approximation [208, 222]:

$$\mathbf{E_{in}} = \frac{3\varepsilon_{\text{m}}}{\varepsilon + 2\varepsilon_{\text{m}}}\mathbf{E}, \tag{4.7a}$$

$$\mathbf{E_{out}} = \mathbf{E} + \frac{3\mathbf{n}\left(\mathbf{n}\cdot\mathbf{p}\right) - \mathbf{p}}{4\pi\varepsilon_0\varepsilon_{\text{m}}}\frac{1}{r^3}, \tag{4.7b}$$

where $\mathbf{n}$ is the unit vector in the direction of the point of interest and r is the distance between the point of interest and the centre of the metallic sphere. The fields, both inside the ($\mathbf{E_{in}}$) and outside ($\mathbf{E_{out}}$) the sphere, are enhanced due to the dipole resonance. This field enhancement of the plasmon resonance is the crucial factor on which rely many of the prominent plasmonic applications of metal NPs.

Bohren and Huffman [223] also provided the expression for scattering and absorption cross-section $C_{\mathrm{sca/abs}}$, which can be defined as the fraction of the total power $P_{\mathrm{sca/abs}}$ [W] scattered or absorbed by a particle and the incident source intensity I_{inc} [Wm^{-2}]:

$$C_{\mathrm{sca}} \equiv \frac{P_{\mathrm{sca}}}{I_{\mathrm{inc}}} = \frac{k^4}{6\pi}|\alpha|^2 = \frac{8\pi}{3}k^3R^6\left|\frac{\varepsilon(\omega)-\varepsilon_{\mathrm{m}}}{\varepsilon(\omega)+2\varepsilon_{\mathrm{m}}}\right|^2, \tag{4.8a}$$

$$C_{\mathrm{abs}} \equiv \frac{P_{\mathrm{abs}}}{I_{\mathrm{inc}}} = k\mathrm{Im}\,(\alpha) = 4\pi kR^3\mathrm{Im}\left|\frac{\varepsilon(\omega)-\varepsilon_{\mathrm{m}}}{\varepsilon(\omega)+2\varepsilon_{\mathrm{m}}}\right|. \tag{4.8b}$$

As these equations demonstrate, both scattering and absorption (also summarized as extinction $C_{\mathrm{ext}} = C_{\mathrm{sca}} + C_{\mathrm{abs}}$) are resonantly enhanced when the Fröhlich condition (Equation (4.4)) is met. Besides, as can be noted for small nanoparticles, the efficiency of absorption ($C_{\mathrm{abs}} \propto R^3$) dominates over the scattering efficiency ($C_{\mathrm{abs}} \propto R^6$) and vice versa for larger particles.

Up to this point, it was shown that nanoparticle behaviour could be defined as an electric dipole that resonantly absorbs and scatters electromagnetic fields. Even though this approximation is valid only for vanishingly small particles ($R \ll \lambda$), in practice, the calculation above provides a reasonable approximation for spherical or ellipsoidal particles with $R < 100\,\mathrm{nm}$ illuminated by visible (VIS) or near-infrared (NIR) radiation.[208] Nevertheless, according to Lingmajer's thesis [211], localised surface plasmons have some critical aspects that this model does not capture. One example is that the central position of the dipole resonance red shifts and broadens with increasing particle size. The second is the deformation of dipole fields in the direction of wave propagation caused by the non-negligible retardation of the incident wave. Therefore, a rigorous electrodynamic approach solving Maxwell's equations in spherical geometry is required for particles of larger dimensions. The exact analytical solution is nowadays attributed to Mie [224], who first applied it to the problem of understanding the colour of colloidal gold particles in a solution. His approach, known as the *Mie theory*, expands the internal and scattered fields into a set of normal modes described by vector harmonics.[208] The difference between the quasi-static and Mie approach is illustrated on the graphs of the extinction cross-section (C_{ext}) in Figure 4.6 of AuNPs with varying diameters.

Because the results of this work are not perfectly spherical particles but more closely reminiscent of oblates, it is worth shortly discussing the shape effect of particle on its optical properties. As with the spheres, the band position red shifts with increasing dimensions of the ellipsoidal particle (Figure 4.7:A). Due to the asymmetry of the particle, the absorption strongly depends on the direction of propagation and polarization of the incident electromagnetic wave, as shown in Figure 4.7:B. Compared to a simple spherical

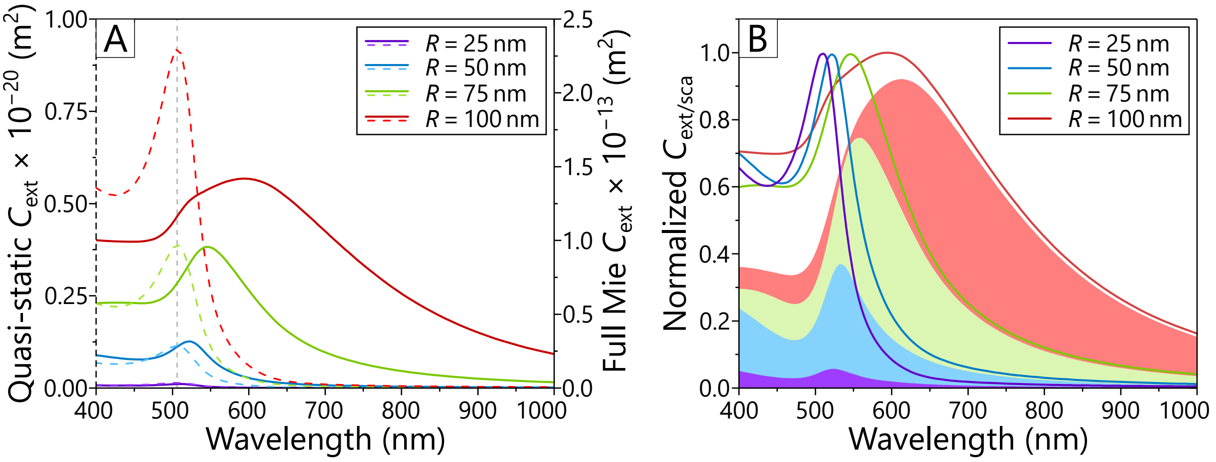

Figure 4.6: (A) Extinction coefficient C_{ext} for gold spherical NPs of various radius R calculated within quasi-static approximation (dashed lines) and using the Mie solution (solid lines). The vertical grey line indicates the quasi-static LSPR wavelength. (B) Normalized Mie theory extinction coefficient C_{ext} (lines) together with corresponding scattering contribution (filled area). Reproduced from Ligmajer's thesis [211].

particle, ellipsoids may give even better bulk refractive index sensitivity when the right parameters are found with higher flexibility for tuning the LSPR by changing the aspect ratio.[225–227]

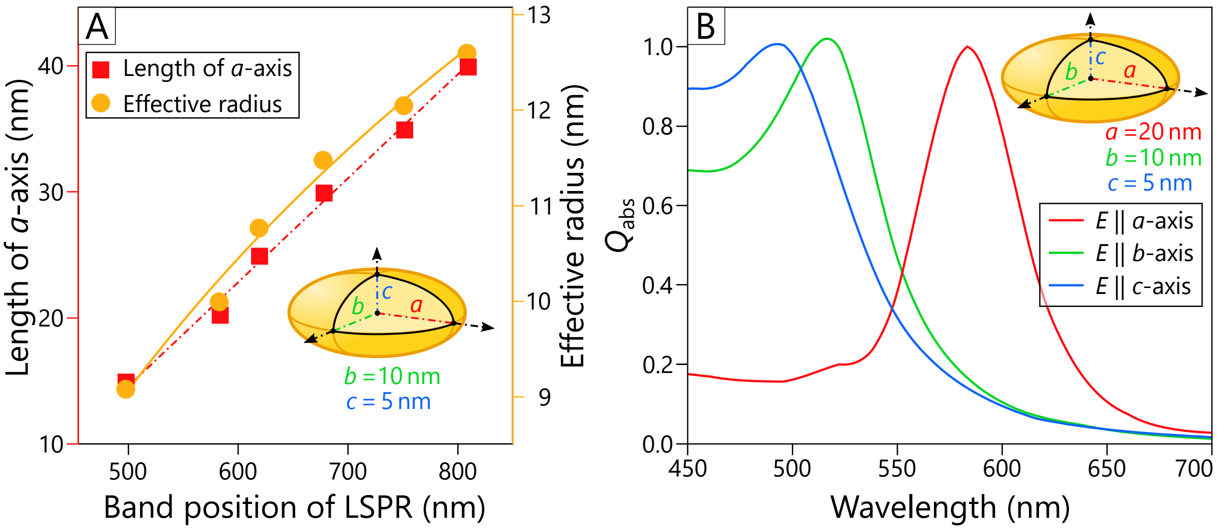

Figure 4.7: (A) Band position for the longitudinal mode versus length of the a-axis and as a function of the gold ellipsoid effective radius, $r_{\text{eff}} = (abc)^{1/3}$. (B) Normalized absorption coefficient Q_{abs} spectra for the incident electric field parallel to main axes of ellipsoids. Adapted and reproduced from ref. [228].

4.2.3 Surface plasmon coupling effect

Until now, the focus was solely on a single particle and its exclusive optical properties. However, the quality factor of the resonance Q ($Q = \lambda_{\mathrm{res}}/\lambda_{\mathrm{fwhm}}$) typical for most LSPRs of metal nanoparticles ($\approx$ 10–20) is found to be well below that desired for many applications. As Kravets et al.[204] stated 'Fortunately, and at first sight rather surprisingly, the limitations on the Q-factor LSPs associated with individual nanostructures discussed above can be largely overcome when nanostructures are arranged in arrays. The electromagnetic fields related to the LSP mode of one nanoparticle may then act to influence the response of neighbouring nanoparticles. This electromagnetic coupling can take several forms: via near-fields and via far-fields.' The near-field coupling dominates in densely packed arrays leading to hybridization of plasmonic modes that may result in slightly narrower resonances (fwhm $\approx 50\,\mathrm{nm}$). On the other side, the far-field coupling (diffractive coupled LSPR) can lead to a remarkable narrowing of the resonance width (down to a few nanometres). However, this requires specially engineered periodic arrays of nanostructures to the conditions of incident light.

As is the case with the dipole approach for isolated particles, it is possible to get a solution for the extinction cross-section of a particle in an array by calculating the dipole sum (S). The dipole sum depends on the array parameters (e.g., period, orientation, size and shape of particle) and provides an additional degree of freedom to improve the quality of lattice coupled SPR compared to the LSPR of a single particle. This approach is called coupled/discrete dipole approximation (CDA/DDA) and is discussed in more detail in ref. [204, 229]. Other approaches usually have to resort to a numerical solution of Maxwell's equations by finite element methods (FEM) or finite-difference time-domain (FDTD).

The effect of the array on the extinction cross-section can be illustrated on the comparison between an isolated particle and particles in a 2D array shown in Figure 4.8:A. Here, SPR is greatly enhanced, giving a narrower and stronger extinction spectrum. Similarly, the inset of Figure 4.8:A shows the increasing Q-factor with the growing size of the array. As shown in Figure 4.8:B, the lattice geometry does not play a significant role compared to the particle spacing illustrated in Figure 4.9.

Besides far-field bulk properties (C_{ext}), the coupled resonant excitation of the plasmon can provide a significant field enhancement in the vicinity to the particle surface (Equation 4.7b), also known as hotspots. These may provide a dramatic increase in the detected signal for adsorbed molecules on the particle surface utilized by techniques of surface-enhanced spectroscopy (SES).[215, 233, 234]

Although, in theory, the enhancement increases with decreasing the gap between particles (Figure 4.10:B), finding the best particle arrangement and size for practical application is still a challenging task. One of the hindrances is an inverse relation of hotspot size compared to the field enhancement (shown in Figure 4.10:B). Additionally, decreasing the gap can lead to a drastic decrease of analysed molecule access to the hotspot, especially for larger molecules such as long RNA/DNA chains.

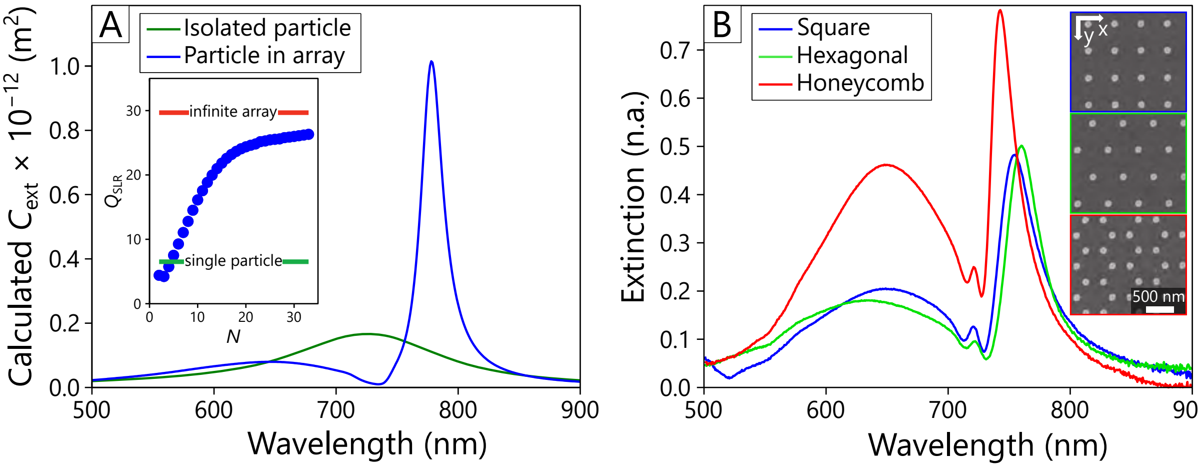

Figure 4.8: (A) Calculated extinction cross-sections C_{ext} per particle for isolated particle (silver disc with a radius of 60 nm and height of 30 nm) and the same particle in a hexagonal array with 555 nm pitch between the nearest discs (shown in the inset of graph B). (B) Measured extinction spectra of same discs in the square, hexagonal, and honeycomb lattices with corresponding SEM images as inset. The particle array is illuminated with linear polarized light at normal incidence with the electric field parallel to the y axis of the array. Reproduced from ref. [230]. The inset in the graph (A) shows the calculated quality factor for surface lattice resonances (Q_{SLR}) as a function of the number of particles (N) along each dimension of the 2D gold nanodiscs array (a height of 50 nm, a diameter of 120 nm, and a rectangular arrangement with lattice constants $a_x = 500\,\text{nm}$ and $a_y = 300\,\text{nm}$). Reproduced from ref. [231].

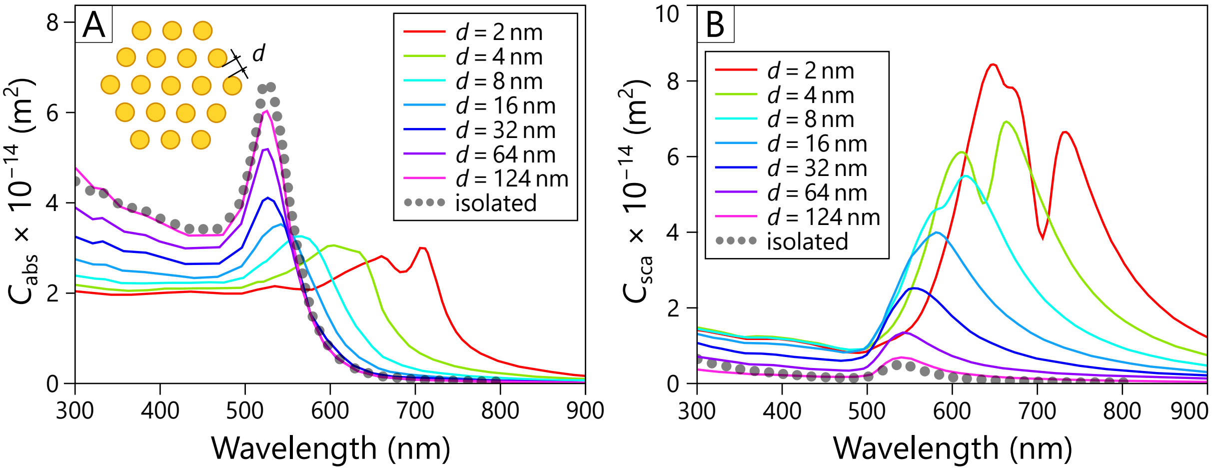

Figure 4.9: Variation of (A) absorption C_{abs} and (B) scattering C_{sca} cross-section of the 19-nanoparticle cluster (inset of A) in a hexagonal lattice with inter-particle distance d for particles of 40 nm diameter. Reproduced from ref. [232].

As shown in Figure 4.10:A the electric field needs to be parallel to the dimer axis to excite a constructive interference of plasmon coupling. This orientation dependence further applies to the 2D arrays of particles when the light propagation should be perpendicular to the array plane.[235–237]

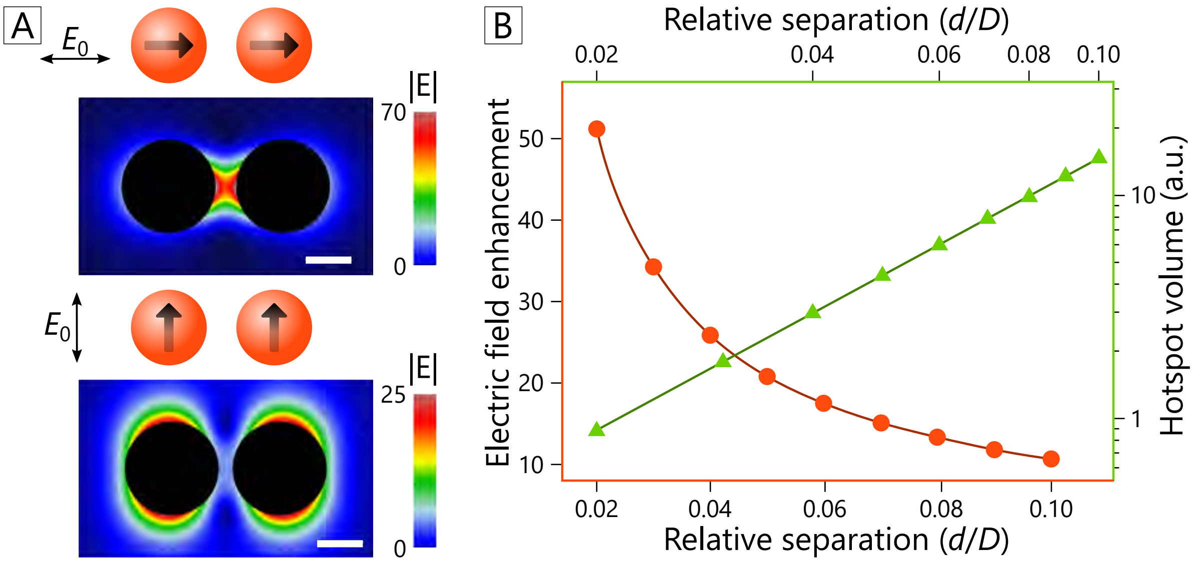

Figure 4.10: (A) Example of plasmon coupling in spherical dimers ($D = 20\,\text{nm}$) with a small gap ($d = 5\,\text{nm}$). The scale bar is 10 nm. (Top) Constructive and (bottom) destructive interference between dipoles. Reproduced and adapted from ref. [237]. (B) Maximum electric field enhancement factor $\eta = E_{\text{max}}/E_0$ and hotspot volume V_{H} as a function of separation d/D for a 2D array of spheres. The hotspot relation (green) is plotted on a log-log scale, and the slope is $V_{\text{H,sphere}} \propto (d/D)^{1.742}$. Adapted from ref. [235].

Conclusions

This section briefly described the fundamental theory behind the unique optical properties of plasmonic structures supporting LSPR. Various aspects of plasmonic structures have gained significant scientific attention for their application in different areas. These manifest when resonant conditions are met, providing resonance enhancement to the light scattering, light absorption, and electric field intensity near the particle surface.

The critical result of analytical solutions is the relation between LSPR and the dielectric constant of the medium that manifests as a red shift of absorption with the increase of the refractive index of the surrounding medium. This effect, which can be even seen by the naked eye, is used in the experimental part of this work. The second effect, still not addressed in this work, is a near-field enhancement, which plays a significant role in sensing (SERS, SIERA), photocatalysis, and solar energy devices.

Since this thesis deals with the fabrication of a gold nanoparticle array, this section demonstrated the strong influence of the size and geometrical aspects of nanoparticles on the collective plasmonic behaviour. Their relevant aspects, such as the polarization dependence, near-field enhancement, and the effect of interparticle distance, were already analysed in several existing studies.[229, 235–237] One important aspect of multiparticle systems is the interaction between the radiative modes that results in constructive and destructive interference.

The takeaway is that the plasmonic properties of structures depend on their geometry, size, and array parameters. Therefore, one of the experimental work goals was to find a way to control the size of nanoparticles, and their spacing.

4.3 State-of-the-art

The phenomenon of localized surface plasmon resonance on nanostructures can be effectively utilized to measure changes in the refractive index of the surrounding media, thus enabling its application in the fields of gas sensing, chemical sensing or biosensing. Since their first application for sensing purposes in the early 1980s [238], surface plasmon resonance (SPR) based instruments became one of the most widely used tools of our time for the label-free characterization of biomolecular interactions.[239] The major advantages of SPR based chemical-/bio-sensors are their excellent sensitivity (even in the range of 10^{-7} RIU)[240], and the fact that they are only sensitive to the changes in the refractive index of the medium a few hundred nanometers close to the metal-dielectric interface. Besides, SPR can provide real-time information regarding molecular interactions or even sensing of a large area in the form of SPR imaging (SPRi).[241] Besides the apparent success and the widespread distribution of SPRi instruments, a disadvantage of the configuration is that the classical Kretschmann-type reflective optical setup is hard to be integrated into small, handheld point-of-care (PoC) devices, which is the main reason for the comparatively limited success of integrated SPR constructions [242–245], and for the lack of handheld SPRi devices on the market.

On the other hand, the sensitivity and limit of detection of LSPR sensor elements strongly depend on the size, shape, and distribution of the applied nanostructures and can vary a lot.[246] Hence, with proper nanostructures, the detection limit of LSPR can even reach one of the Kretschmann-configuration based SPR devices on the market (considering molecular or biosensing applications). At the same time, LSPR on nanoparticles is more easily excitable, and thus, a simpler measurement configuration can be used.[207] There are various configurations in which nanoparticles can be used as sensor transducers, such as in colloidal form [246], used as coatings on optical fibres [246, 247] or used on the surface of a transparent substrate.[248] The latter is called a chip-based LSPR setup, and considering its rather simple transmissive optical configuration, it could enable the integration of this principle into small, handheld point-of-care LSPR imaging devices.[219, 249]

Several recent reviews focus on the advances of plasmonic nanoparticles [205, 250] and nano-array [251] based LSPR sensors and their application for bio-sensing purposes. Out of these applications, label-free DNA sensing is one of the most challenging due to the inherently small size of target molecules. Table 4.1 collects and compares the reported label-free LSPR-based DNA sensors.

The types of the plasmonic nanostructures are shown in the collection of Figure 4.11, the fabrication technology of the sensor and the measurement methods are indicated in the table. To compare the performance of these solutions, the bulk refractive index sensitivity and the absolute wavelength shift caused by the presence of the target ssDNA molecule (during the saturation at maximum target concentration) are given. Although

Table 4.1: An overview of the LSPR-based label-free DNA sensors. Images of the structures are shown in Figure.

ref.	Structures	Fabrication technology	Characterization	Bulk RI Sensitiv. [nm RIU^{-1}]	Redshift to sat. target DNA [nm]	Signal/target length [nm/base]
Roether (2019)[252]	AuNPs on SiO_2 pillars [$d_p = 22$ nm, $d_{gapp} = 20$ nm]	SiO_2 template + thin film technology + annealing + SiO_2 etching	VIS spectrosc., refl. mode	54	3	0.10
Thamm (2018)[253]	AuNP on glass (not coupled) [$d_p = 80$ nm]	Colloid.prep. + surface functional. (APTES) on glass	VIS spectrosc., transmittance	108[a]	3	0.12
Huang (2012)[254]	Au nanorings on glass [$d_{in} = 100$ nm, $d_{out} = 130$ nm, $d_{gap} = 200$ nm]	Nanosphere litho. with PS beads + vacuum depos. of thin film + ion milling	VIS spectrosc., transmittance	350	3	0.12
Schneider (2013)[255]	AuNP on glass (not coupled) [d_p =77–85 nm]	Colloid. prep. + surface functional. (APTES) on glass	Single particle optical spectrosc.	108[a]	3	0.15
Nguyen (2015)[239]	AuNP on glass (not coupled) [$d_p = 50$ nm]	Colloid. prep. + surface functional. (MPTES) on glass	Single particle optical spectrosc.	80[a]	12	0.17
Qi (2019)[256]	AuNP array on glass [$d_p = 300$ nm, $d_{gap} = 1000$ nm]	PS monolayer colloid. crystal formation + thin film dewetting	VIS spectrosc., refl. mode	120	6	0.2–0.3[b]
Su (2018)[257]	Au nanofingers on a 2D photonic crystal surface [size: 230 nm]	Mold prep. with EBL and nickel electrocasting + nanoimprint litho. + polymer coating	VIS spectrosc., refl./abs. mode	N.A.[c]	7	0.30
This work[LeBo20]	**Au NP array on epoxy [$d_p = 100$ nm, $d_{gap} = 10$ nm]**	**Nanobowled template + Au thin film dewetting + transfer**	**VIS spectrosc., transmittance**	**83–108**	**6.6**	**0.33**
Soares (2014)[258]	Au nanotriangles (not coupled) [side: 91 nm, height: 17 nm]	VIS spectrosc., transmittance	Single particle micro spectrosc.	468	33	0.66
Kaye (2017)[259]	Au nanodisk array [$d_p = 180$ nm, $d_{gap} = 200$ nm]	EBL + thin film depos. + lift off + transfer (+ optical fiber prep.)	Fiber-optic sensor, particle backward scatter.	230	26	1.30
Zhu (2018)[260]	3D multilayer nanostructure (Au film on SU-8 nanopillars) [size: 200–280 nm, gap: 538 nm]	Reversal nanoimprint lithography (RNIL): multi-steps litho., etching, vacuum depos., lift-off	VIS spectrosc., refl. mode	442	82	1.64
Gartia (2013)[261]	NanoLCA, Ag particles in nanocups [height: 500 nm, $d = 180$ nm]	Nanocone pattern. on glass with interf. litho. + transfer to PET + vacuum depos.	VIS spectrosc., trans./refl. mode	8066	32	1.78

[*] The references are organized based on max. signal (red shift) measured on target DNA binding per target length (nm/base). d_p is the nanoparticle diameter (when applicable), d_{gap} is the interparticle distance (when applicable).

[a] Not given, estimated based on Mie theory for spherical particles.

[b] Not given, estimated.

[c] Not available.

higher bulk RI sensitivity generally means higher sensitivity to target molecules, the relationship between the RI sensitivity and molecular sensitivity is not trivial in LSPR (as confirmed by Table 4.1).

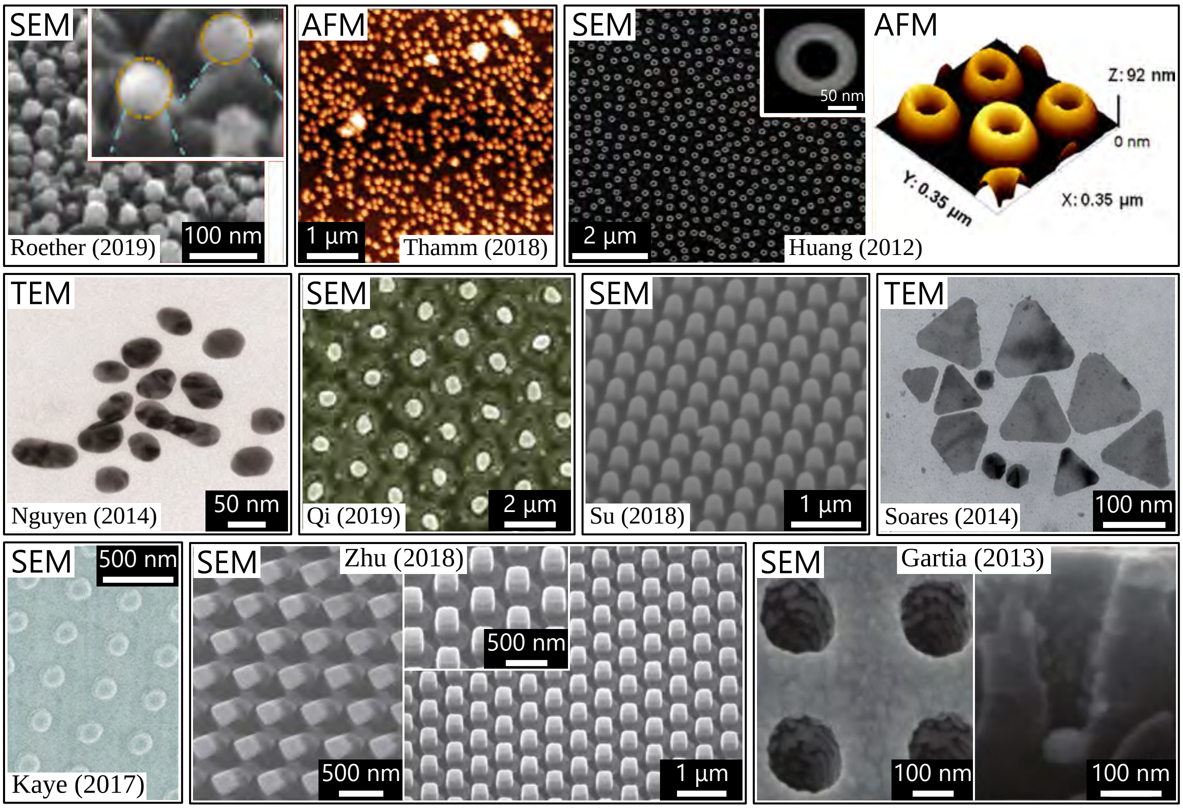

Figure 4.11: Various type of plasmonic nanostructures used for label-free LSPR-based DNA sensors. Images adapted from corresponding references. For more information, see Table 4.1.

In 2014, Tu et al.[247] collected the reported LSPR bulk sensitivity values for various nanostructures, and they showed substantial variation: From the simplest colloidal gold spheres ($71\,\mathrm{nm\,RIU^{-1}}$) to the more exotic gold nanocages (783–$1933\,\mathrm{nm\,RIU^{-1}}$), the difference can be more than one order of magnitude. Nevertheless, it can still be considered low compared to the equivalent bulk refractive index sensitivity of thin film-based classical SPR instruments (which can be above $3300\,\mathrm{nm\,RIU^{-1}}$).[262] Concerning molecular sensitivity, LSPR can match the standard thin film-based SPR instruments.[262, 263] Xu et al. studied the plasmonic behaviour of gold nanoparticles (AuNPs) fixed to glass substrates and found that the decay of the excited near field is depending on the particle size.[264] The proposed $(r_0/r)^6$ decay length (where r_0 is the radius of the spherical nanoparticle and r is the distance from the particle) is at least one order of magnitude smaller than the exponentially decaying evanescent field length in the thin film SPR. In other words, LSPR is more focused on the changes, which occur in the near vicinity of the particle surface, and molecular-scale interactions occur in the region. The near field intensity and its decay around the particles depend on the size, shape, and material properties of the nanostructures.[265, 266] Coupling and interparticle distances also play a major role in near field intensity and thus sensitivity enhancement.[217, 267]

Generally, selecting a nanofabrication method for LSPR sensor construction requires compromise. Control over the particle size, shape, and distribution in a sufficiently large surface area (several cm^2), preferably with cheap and reproducible technology, could be considered optimal. With electron beam lithography (EBL)[268] or focused ion beam (FIB) lithography [269], it is possible to control the size and distribution of the nanostructures (with around 10 nm resolution), but patterning large surface areas is too expensive with these methods. This issue is also true for nanoimprint lithography (NIL), where hard masks are usually prepared with these technologies.[257, 270, 271] Their advantage is high sensitivity ((Kaye 2019)[259] in Table 4.1). Colloidal lithography [272] and hole-mask colloidal lithography (HCL)[219] are often used to pattern larger surface areas. There are, however, some limitations regarding the size/shape of the fabricated structures, resulting in mediocre/small surface coverage leading to low sensitivity ((Huang 2012, and Qi 2019)[254, 256] in Table 4.1). Perhaps the most precise control over the size and shape could be achieved through the colloidal synthesis of nanoparticles.[273] Here, the challenge is the subsequent binding of the nanoparticles to a substrate, which is most commonly achieved by silanization [274] or through thiol chemistry.[275] In both of these cases, the control over the resulting distribution of the nanoparticle array is limited, and the uncoupled spherical nanoparticles usually have low molecular sensitivity ((Schneider 2013, Nguyen 2015, and Thamm 2018)[239, 253, 255] in Figure 4.11). Thermal annealing of a previously deposited thin film on glass or silicon is a simple technique to produce nanoislands [276], also combined with the substrate's etching to produce nano-mushrooms.[252, 277] However, the control over the arrangement is limited (along with the sensitivities, (Roether 2019)[252] in Table 4.1). Furthermore, since gold does not adhere well to SiO_2, fluidic environments can remove the NPs from the surface. As shown in Table 4.1, our proposed sensor offers reasonably good performance with a significantly simpler, robust, and large-scale fabrication technology. Drawbacks of the listed technologies which enable extra high sensitivity are either the small fabrication area (EBL, (Kaye 2017)[259]) or the inhomogeneous surface. For example, the extra high sensitivity of the nano-Lycurgus cup arrays of Gartia et al.[261] enables even a naked eye colourimetric detection of DNA binding, but the surface of their sensors is not homogeneous enough for LSPRi applications. The only fabrication technology in the table excelling in all these requirements is the reversal nanoimprint lithography of Zhu et al.[260] It has to be noted that their extreme sensitivity was measured in the NIR range (at 1001 nm), but their response is significantly smaller in the VIS range (15 nm shift to target binding at 600 nm).

It has to be noted that Table 4.1 only collects label-free LSPR-based DNA sensors. Plasmonic nanoparticles can be used as labels conjugated to DNA molecules to increase the signal upon binding to an LSPR sensor [278], either in a core-satellite particle arrangement [279], or through nanoparticle aggregation [280], to enable colourimetric detection of binding on a surface [281], or used as plasmon-enhanced fluorescence biosensing.[282] These labelled methods, however, are not considered in this study.

4.4 Motivation and aims of the work

In recent decades, a phenomenon called localized surface plasmon resonance (LSPR) on metal nanoparticles has attracted much attention due to its many favourable properties such as the high sensitivity of resonance conditions to the dielectric properties of the ambient medium; confinement of light within a nanometer region, or a large electromagnetic field enhancement around the particles. Nowadays, LSPR flourishes above all in optical sensing, where it pushes the boundaries of the sensitivity of molecular detection. It has naturally created a vast demand for application-tailored and affordable plasmonic nanostructures.

The fabrication method proposed in this work (illustrated in Figure 5.1) is based on the controlled, template-assisted SSD synthesis of AuNPs and their transfer to a transparent substrate. The motivation for this work is the technology has distinct advantages in comparison to other methods, such as:

(i) Controlled synthesis: the particle size and interparticle distance can be well controlled in a sub-100 nm hexagonal distribution, and thus the plasmonic absorption peak (and sensitivity) in VIS range can be fine-tuned for individual applications. Besides plasmonic sensing, the absorption peak should be tuned for surface-enhanced Raman scattering (SERS) applications as well, where the relation between the resonance peak of the substrate and the excitation wavelength defined by the laser affects the SERS enhancement.[276, 283]

(ii) Large-scale fabrication: the lateral size of the substrate is not limited, sensors with several cm^2 surface area can be easily prepared, and the nanoparticle size/distribution is homogenous on the whole surface. Such large sensor areas are required for LSPR imaging (LSPRi) applications [249] and beneficial for SERS.[284, 285]

(iii) Robustness: the prepared nanocomposite—gold nanoparticle arrangement fixed on substrate pillars—is stable to a great extent; no particle removal exposed to fluidic environments. The surface of the gold can be cleaned multiple times with low-power O_2 plasma without any significant drop in sensitivity.

Like many other inventions, this fabrication technique has been discovered a way before it found its application. The origin dates to 2014, when this concept—AuNPs fabrication by utilizing well-ordered nanobowled aluminium as a substrate for template-assisted SSD of the thin gold film—was published in the author's master thesis [286]. To our knowledge, this is the first report of this technique.

A similar method was published in 2011 by Yang et al.[199], where they used a self-organized monolayer colloidal crystal (MCC) composed of polystyrene spheres (diameter of 0.5, 1 and 2 µm) to form a bowled template for SSD of the thin metal film. One of the first attempts utilizing the self-ordered PAA for SSD of gold film and pushing AuNP diameter into sub-100 nm range were in 2013 by Yingwei et al.[287] and in 2014 by Jo et al.[288] In both cases, the authors used PAA with broader pores as the template for SSD. Compared to the inconclusive results of Yingwei et al., Jo et al. show a high-quality work focusing on SERS application. Similarly, in 2016, Altomare, Nguyen and Schmuki [200] used SSD of various Au/Ag layers on TiO_2 nanotube arrays showing improvement in their photocatalytic activity.

In the same year (2016), a part of this work was published in a conference proceeding.[202] Here, the fabrication method was extended by the AuNP size control and, for the first time was demonstrate the sensing properties of this AuNP array thanks to its transfer from Al template to simple polydimethylsiloxane (PDMS) microfluidic cell. Later, in 2017 Fan et al.[203] and in 2019, Ikeda et al.[201] published their results of AuNPs formed by the same technique. In both cases, they focused only on the fabrication method, showing the effect of template dimensions, the thickness of the deposited layer, or annealing parameters. Even though these works conducted a very similar study, there are a few deviations in the results, which will be in more detail discussed in the experimental chapter 5. In the most recent work published in 2020 [186], we show a comprehensive fabrication method of AuNP layers, their transfer on the epoxy substrate, and utilization for label-free DNA detection.

This work aims to demonstrate the fabrication of the AuNP array as a feasible LSPR sensor. Through the development process of this technique, many issues have been overcome, which may represent individual objectives:

1. Achieve a high uniformity in the distribution and alignment of AuNPs within the array.
2. Develop a method to control the dimensions of AuNP arrays, especially the diameter and spacing of the AuNPs.
3. Utilized the AuNP array as an LSPR-based sensor, and thus its transfer to an appropriate transparent substrate.
4. The final micromachining of the nanocomposite to enhance its performance.

5 EXPERIMENTAL, RESULTS & DISCUSSION

This experimental section is structured according to the scheme shown in Figure 5.1, where the fabrication method is divided into three thematic parts: fabrication of nanobowled aluminium template (processes 1–3), furthermore split into the aluminium preparation and formation of self-ordered PAA; formation of AuNPs on the template by solid-state dewetting of a gold thin-film (processes 3–5); and transfer of AuNP layer to another substrate, its modifications (process 5–8) and characterization of prepared nanocomposite material.

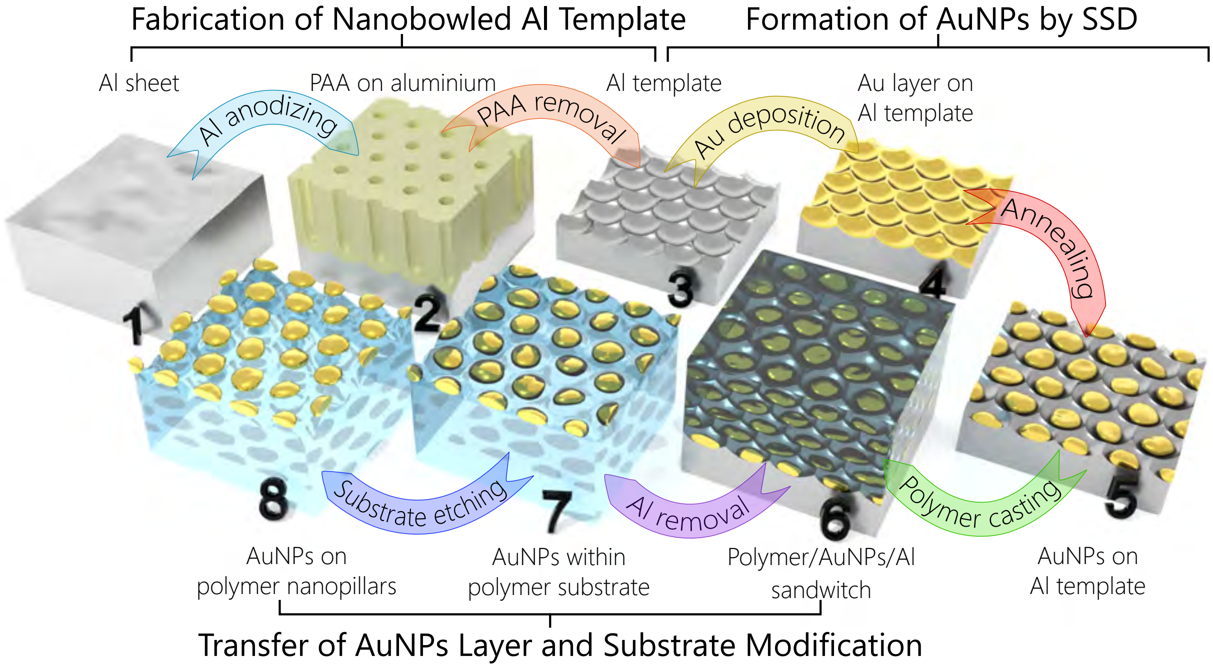

Figure 5.1: Comprehensive 3D illustration of the technology to fabricate ordered gold nanoparticle arrangements on transparent (polymer) substrates. The main steps of the process are the following: (1) Preparations (cleaning, annealing, mechanical and electrochemical polishing) of the aluminium sheet. (2) Formation of PAA on aluminium through controlled anodic oxidation. (3) PAA selective removal and the reveal of a nanobowl Al template. (4) Thin gold film deposition on the Al template. (5) Formation of AuNP layer by solid-state dewetting of the Au film. (6) Transparent substrate (polymer) casting and curing on top of the AuNP layer. (7) Removal of the Al sheet to reveal transferred AuNP layer on the transparent substrate. (8) Substrate etching to boost up the performance by enhancing the surface accessibility of AuNPs.

5.1 Aluminium preparation

Aluminium foil with high purity of 99.999 % was chosen as the starting material, temper: as rolled, with the size of 100 mm × 100 mm and thickness of 250 µm from Goodfellow Ltd.

It is noteworthy that the high purity of aluminium was found to be crucial for our application. It was experimentally found that anodisation of aluminium with a higher amount of impurities (for example, 99.95 %) leads to worse pore ordering, more defects, and in some cases, even formation of a sponge-like layer on top of PAA consisting of precipitated impurities. Similar observations were conducted by other researchers, anodising pure and alloyed (AA1050) aluminium.[289, 290] The thickness of the foil was chosen considering the cost and handling during fabrication processes. Thinner foils (≤100 µm) are much more prone to bending, especially after annealing or mechanical polishing. On the other hand, thicker foils (> 500 µm) cannot be fully utilized, and they are significantly more expensive.

Before cleaning, the aluminium foil was cut to 50 mm×25 mm samples, and any bending was flattened by rolling. Samples were then ultra-sonicated in acetone, washed in isopropyl alcohol (IPA) and deionized water (MiliPore, 18.2 MΩ). To increase the aluminium grain size and relax materials, samples were annealed at 550 °C for 15 hours (heating ramp of 10 °C min^{-1} with natural cooling). Vacuum (pressure less than 10^{-4} Pa) annealing was performed to avoid thermal oxidation. The result of annealing is shown by a comparison of electron backscatter diffraction (EBSD) maps and size distribution (Figure 5.2) between the received and annealed foils. Received foil is formed by a higher number of grains smaller than 100 µm with a much diverse crystallographic orientation. On the other hand, the grain orientation spread is narrower around the [001] orientation after annealing. Overall, the main advantages are reducing the length of grain boundaries that behave as defect initiators and relaxing grains close to the [001] orientation that produces the best pore ordering when compared to [101] or [111].[96, 99, 291]

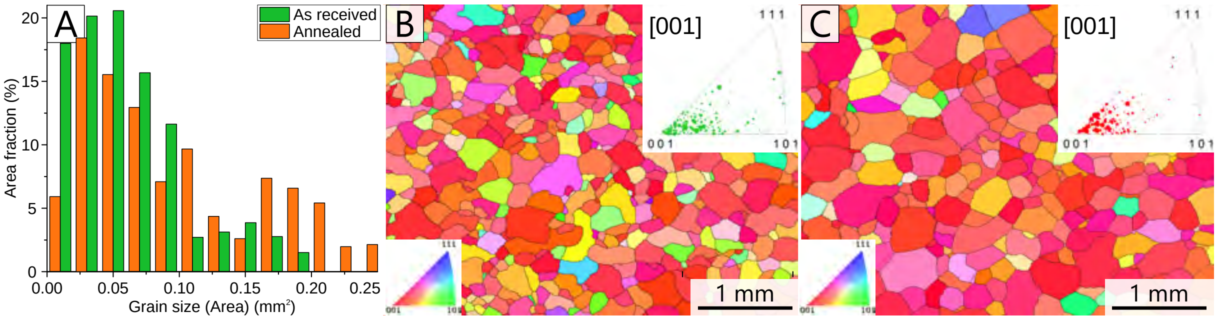

Figure 5.2: The grain size distribution (A) and Inverse Pole Figure (IPF) map of the received (B) and annealed (C) aluminium foils. The bottom left inset shows the colour coded map type IPF [001]. The top right inset shows the corresponding grain orientation based on size.

After annealing, the samples were mechanically polished to decrease the surface roughness and create a mirror-like finish. It was found that mechanically polished samples give in general better results. For example, the occurrence of pitting during subsequent electrochemical polishing is lower than in unpolished foils, probably due to the removal of impurities introduced by foil processing.[292] Furthermore, the nanostructure layers prepared on smoother surfaces have more negligible light diffusion, which is beneficial for optical measurements. However, the mechanical polishing of large thin foils is considerably challenging handwork. Before grinding, samples were fixed on a 0.5 mm thick corundum ceramic plate of the same size by a temporary adhesive (Crystalbond 509). This step is crucial for a better manipulation. The grinding and polishing were done in manual mode on a 300 mm rotating disk (Tegramin 30, Struers). The best results were obtained, starting on SiC paper grit 1200 and finishing with 1 µm diamond suspension (all steps are described in Table 5.1). After each step, the sample was ultra-sonicated in a water bath for 3 min to remove any residuals and abrasive particles from previous processing. Finally, the foil was carefully removed from the corundum plate by melting the Crystalbond adhesive on a hot plate at 150 °C and washed in acetone to remove the adhesive residuals.

Table 5.1: Summary of parameters used for mechanical grinding and polishing steps.

Grinding			Polishing	
SiC paper 1200	SiC paper 2000	MD-Largo	MD-Nap	MD-Nap
+ water	+ water	+ 9 µm†	+ 3 µm †	+ 1 µm†
50 RPM	100 RPM	300 RPM	200 RPM	200 RPM
< 1 min	> 2 min	> 3 min	≈ 3 min	> 3 min

† MD-Largo is a composite disc, MD-Nap is a polishing cloth disc, 9 µm to 1 µm are diamond suspensions (Struers).

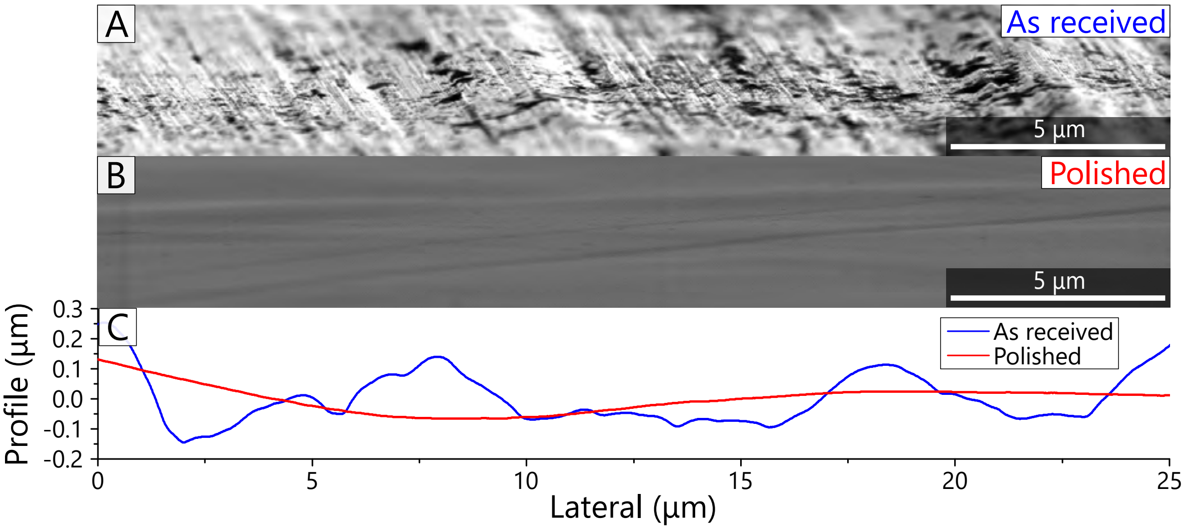

Figure 5.3: Surface roughness comparison between (A) received and (B) electrochemically polished Al foils. SEM images of surface morphology at low grazing angle (A, B) and profilometric measurements (C).

The last step of preparation was electrochemical polishing of the Al foil. Electrochemical polishing not only smoothed the surface (an example is shown in Figure 5.3), but it also removed a thin top layer that was mechanically deformed due to previous mechanical polishing (for example, it is a requirement for EBSD analysis).

Samples were electropolished on one side in standard 1:4 (v:v) perchloric acid (70 %) and ethanol (99.8 %) solution. Before polishing, the whole backside and a corner strip at the front side (placed between the contact and immersed area, where the solution level is located) was covered by a low tack self-adhesion PVE tape. This protection film decreases the overall current requirements (current density can reach over 300 µA cm^{-2}) and avoids the air/solution/solid interface where polishing is dramatically accelerated. The electropolishing is performed in a simple two-electrode setup (shown in Figure 5.4). Here, the sample is connected to a controlled power supply as an anode (working electrode, WE) and a stainless steel mesh as a cathode (counter electrode, CE). Both are immersed in the solution cooled to 0 °C in a double glass baker (500 ml) connected to an external temperature control system with a mineral oil exchanger (Huber Petite Fluer). Additionally, the setup includes a thermometer and magnetic stirring. The polishing was done potentiostatically at a potential of 20 V for 90 s. It was found out that increased pitting occurs when the solution is not stirred, while strong stirring leads to enhanced grain etching located at the sample edges where a higher electrolyte exchange occurs. Therefore, stirring was not used at the beginning of the process until a dark layer formed over the surface (20 s). After that, strong stirring was applied for a moment to wash away this layer and again turned off until the end of the process. Finally, the sample was thoroughly washed with deionized water, dried by a nitrogen stream, and the protective tape was carefully peeled off.

5.2 Formation of self-ordered nanobowled templates

This section presents the fabrication of well-ordered nanobowled aluminium templates, as illustrated in Figure 5.5. This simple fabrication method exploits the effect of PAA self-ordering that produces its signature honeycomb-like morphology. Pore cells are aligned in a hexagonal lattice with a single circular central pore per cell. However, as discussed in section 5.1, this self-ordering regime can be only achieved for a narrow range of anodising conditions. After the formation of the PAA, this layer is sacrificed to reveal its imprinted morphology in the underlying Al substrate in the form of well-ordered nanobowls.

Two well-known anodising approaches using anodising in sulphuric acid at 25 V and oxalic acid at 40 V, with anodising conditions tabulated in Table 5.2, were adopted for this work. The process using phosphoric acid was not considered since it requires the anodising potential of 195 V, resulting in a cell size of 500 nm that is out of the VIS range for LSPR and competes with optical lithography.

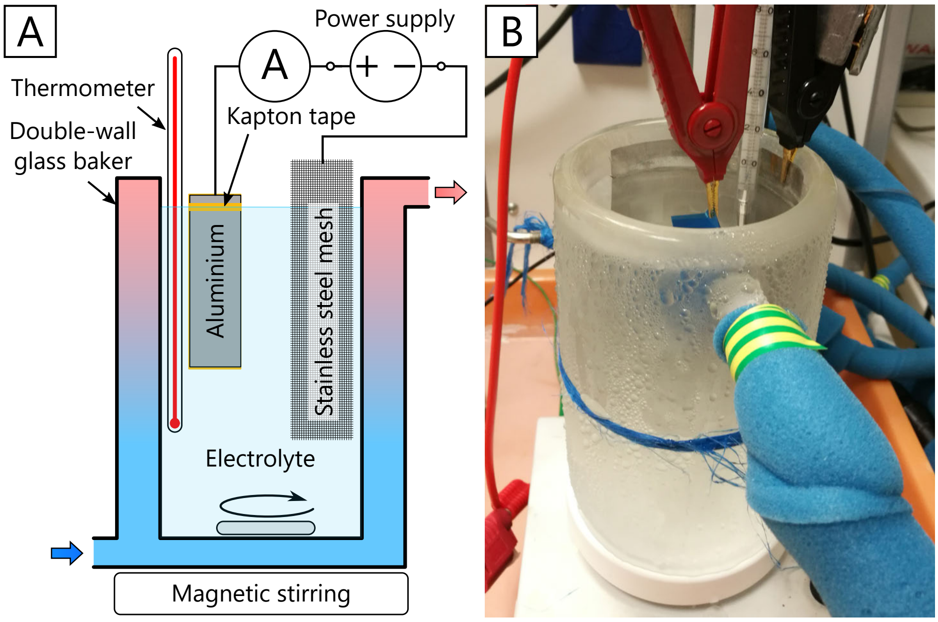

Figure 5.4: (A) Schematic and (B) photo showing the polishing/anodising two-electrode electro-chemical cell setup used for large-scale (cm^2) sample processing. The volume of the double-glass beaker is 500 ml.

Table 5.2: anodisation parameters used for template fabrication.

anodising potential*	Electrolyte	Temperature	anodising time
25 V	0.3 M sulphuric acid	2 °C	18 h
40 V	0.3 M oxalic acid	5 °C	20–25 h

* Values are used as the notation for anodising processes and type of templates in the following text.

Aluminium foils (50 mm×25 mm) prepared by previous processing (annealing, polishing, and cleaning) were processed by one-step anodising performed potentiostatically in the same two-electrode setup used for electrochemical polishing (Figure 5.4). To avoid unnecessary consumption of Al from the unpolished back side of the sample, the anodisation was interrupted after the first 20 minutes. The sample was then washed in deionized water and dried. Then, a Kapton tape was applied on the whole backside and to a small area on the front side to separate the immersed part of the sample from the electrically contacted area. This taping prevents the masked areas from further anodising. The tape adhesion is significantly promoted using a few micrometres thick PAA layer, which formed during the first 20 min (example for 40 V shown in Figure 5.6) significantly promotes the tape adhesion during anodising. Masking an aluminium with only thin native oxide frequently results in the mask peeling off during anodising due to the PAA volume expansion. After masking, anodising continues under the same conditions for a predetermined time.

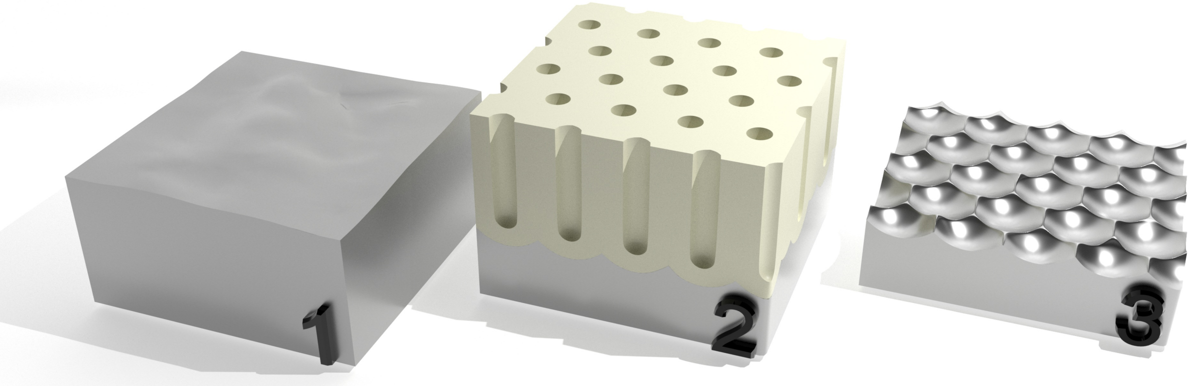

Figure 5.5: Schematic illustration of the fabrication of the self-ordered nanobowled aluminium templates by PAA-assisted anodising process. (1) Mechanically and electrochemically polished Al sheet. (2) Formation of self-ordered PAA on Al by anodic oxidation. (3) Selective etching of PAA and reveal of nanobowled Al template.

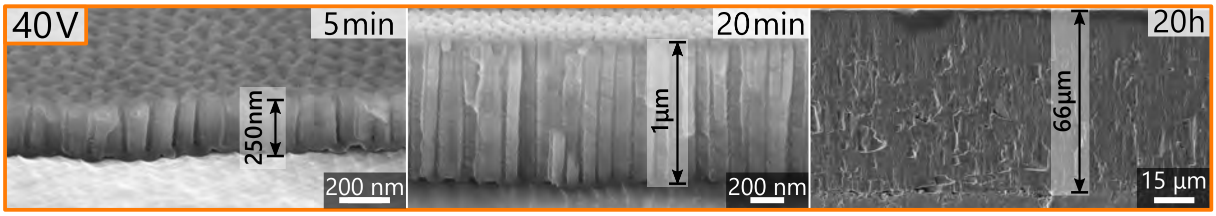

Figure 5.6: SEM images of PAA grown on the Al sheet by 40 V anodising for 5, 20, and 1200 minutes. The 5 and 20 min cross-section samples were taken by bending the Al sheet and breaking the top PAA. The 20 h cross-section was glued (dark area on top shows residual glue) between supporting ceramic plates, cut-off by a precision saw (Accutom 100, cutting speed of $5\,\mu m\,s^{-1}$), and 10 nm thick Au layer was deposited over (Coater Leica EM ACE600) for SEM observation. The growth rate can be estimated to $\approx 55\,nm\,min^{-1}$.

After anodisation, the samples were washed in deionized water, and the masking Kapton tape was slowly mechanically removed in an isopropyl alcohol bath. The exposure of the nanobowled aluminium structure was done by selective removal of the formed PAA. This removal was done in a water solution of 0.42 M phosphoric acid (H_3PO_4) and 0.2 M chromium trioxide (CrO_3) at 65 °C for at least 2 h (based on the etching process from ref. [142]), followed by thorough washing and ultra-sonication in deionized water. The mixture of H_3PO_4 and CrO_3 effectively dissolved ($\approx 10\,nm\,min^{-1}$) the anodic alumina (or native oxide), leaving the residual aluminium intact.

The resulting nanobowled aluminium structures (SEM images are shown in Figure 5.7, and AFM measurements are shown in Figure 5.8) were subsequently used as a template for solid-state dewetting of the thin gold layer. The depth of nanobowls for the 40 V process (22.5 nm) is twice as deep as the 25 V (10.9 nm). The cell size of each bowl is estimated to 65 and 106 nm for 25 V and 40 V process, respectively. A slight deviation between SEM and AFM measurements were observed but remained within the error of measurements. Values match the linear relation to anodising potential ($D_c = kU$), where U is the anodising potential and k is the proportional constant of approximately $k \approx 2.5\,\mathrm{nm\,V^{-1}}$.[74]

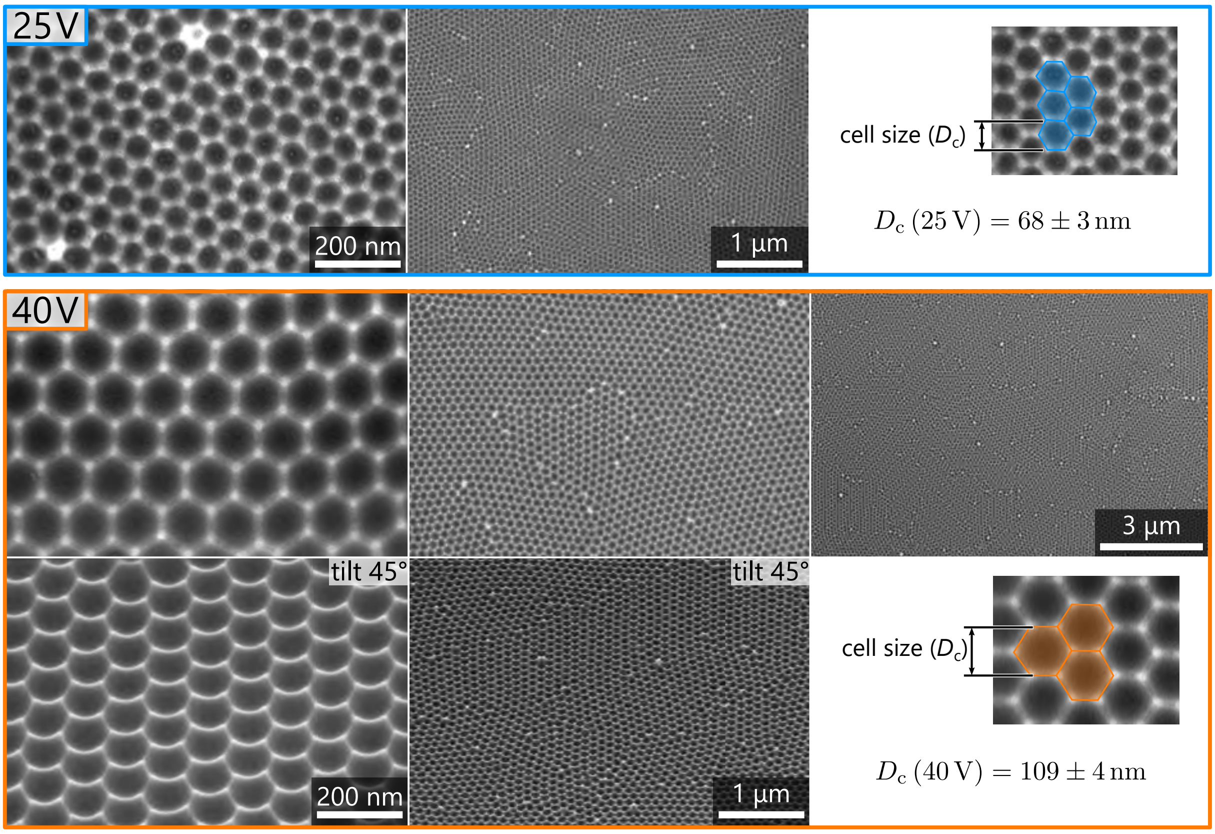

Figure 5.7: SEM images of Al template topography prepared by 25 V and 40 V process. Measured cell sizes are 68 ± 3 and $109 \pm 4\,\mathrm{nm}$ for the 25 V and 40 V process, respectively.

Conclusions

A relatively straightforward fabrication of the nanobowled Al template is presented. The SEM measurements show a high order in domains with the size of a few micrometres. To further increase the long-range order, several trials were performed to reproduce the experiment from ref. [90]. Here, the authors show a positive effect on pore order with increasing cycles of PAA growth followed by its delamination. However, the process of delamination results in visible damage (etching) of the underlying Al substrate that is not suitable for target applications. Nowadays, the long-range order is acquired only by relatively expensive techniques or their combinations such as FIB patterning [293, 294], EBL [104, 295], interference lithography [102, 296] and NIL [103, 297], while a cost-effective and large-scale method was not found, yet.

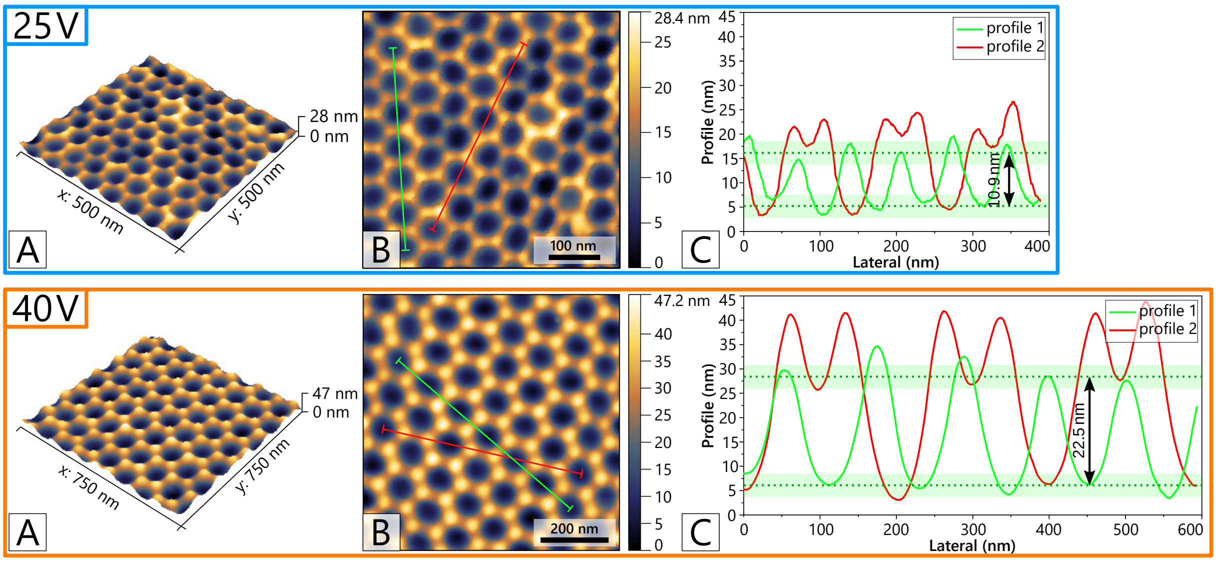

Figure 5.8: (A) AFM 3D and (B) 2D images of Al templates prepared by 25 V and 40 V process. (C) The extracted profiles show the height of protrusions and the depth of nanobowls. Measured cell sizes are 65 ± 3 and 106 ± 4 nm for the 25 V and 40 V process, respectively.

5.3 AuNPs fabrication

The fabrication of gold nanoparticle (AuNP) layers by utilizing solid-state dewetting (SSD) of a thin gold film over the nanobowled aluminium templates is presented in this section and schematically illustrated in Figure 5.9. When a gold-coated Al template undergoes thermal treatment, it produces a gold nanoparticle layer where the nanoparticle alignment is directly inherited from the Al template topography. Therefore, as shown in the previous section (section 5.2), good care needs to be taken to produce templates with the smallest number of defects possible.

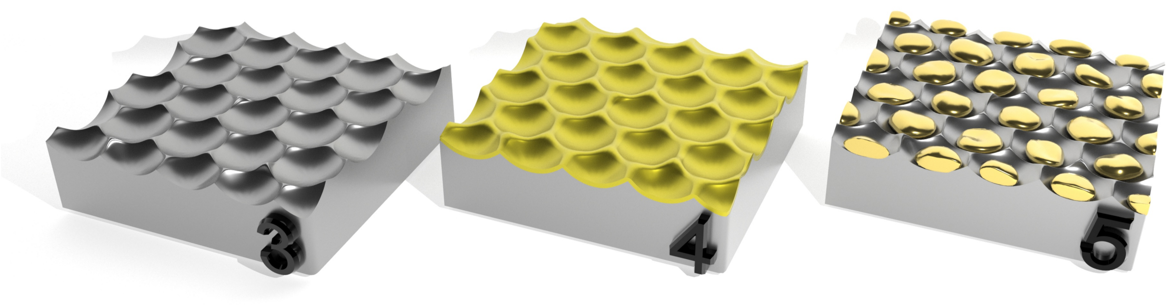

Figure 5.9: Schematic illustration of the fabrication of ordered AuNPs over Al template by a controlled SSD process. (3) Al nanobowled template. (4) Deposition of thin Au film. (5) Formation of AuNPs caused by thermal treatment (dewetting).

While this technique is based on the SSD of thin metal films, a concise theoretical part is presented to support the following experimental part. A more extensive theory beyond this work scope can be found in several review articles covering this topic, given in references [188, 190, 298]. The theoretical part then transitions to a brief state-of-the-art focused primarily on AuNPs fabrication by SSD.

The experimental part is devoted to optimization the deposition and annealing parameters concerning SSD outcomes. All experimental work was performed with Al nanobowled templates of 25 V and 40 V types as a starting material (discussed in section 5.2).

5.3.1 Thin-film deposition techniques

The deposition of thin gold films was done by Physical Vapour Deposition (PVD) techniques, which use the vapour phase to deposit layers of atoms/molecules onto a solid substrate. In general, those processes are done in a vacuum chamber (schematically shown in Figure 5.10) that, among other things, ensures a good purity of the deposited layers. In this work, two PVD types were compared: Magnetron Sputtering and Electron Beam Evaporation. The magnetron sputtering was performed in two setups: Coater Leica EM ACE600 and BESTEC Magnetron sputtering system, further noted as Leica and Magnetron, respectively. The evaporation deposition was performed in BESTEC E-beam Evaporator system, further noted as Evaporator.

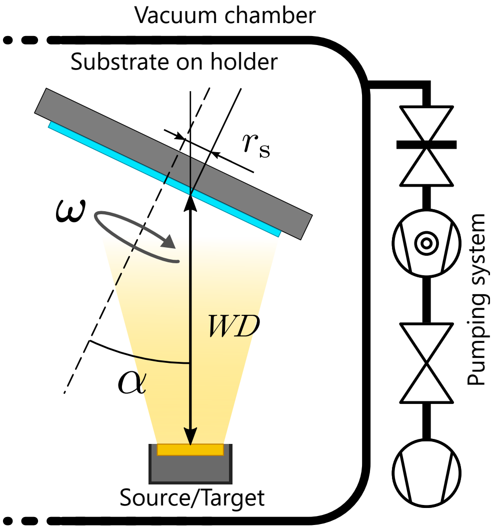

Figure 5.10: Schematic illustration of simplified PVD deposition setup. WD is the working distance between source and substrate, α is the angle between substrate and source axis, r_s is the distance between substrate centre and the intersection of substrate plane and source axis, and ω is the rotation speed. Magnetron gun with a gold cathode (target) is used as a source for sputter deposition, while a crucible filled with gold is used for evaporation deposition.

The Leica setup consists of a relatively small vacuum chamber with a rotating stage with a tilt option and two positions for sources: a magnetron with a gold target (99.99 %, Lesker) and a unit for carbon sublimation deposition. Table 5.3 presents the tuned parameters used for film deposition in the Leica setup.

Table 5.3: Leica setup deposition parameters, where P_{init} is the predeposition pressure, P_{dep} is the sputtering pressure (controlled by argon flow), and R_{dep} is the deposition rate. If not stated otherwise, these deposition parameters were used for the following samples prepared in the Leica setup.

WD	α	r_s	P_{init}	P_{dep}	ω	R_{dep}
80 mm	0°	≈ 30 mm	10^{-2} Pa	1.5 Pa	60 RPM	$\approx 9 \times 10^{-1}\,\text{nm}\,\text{s}^{-1}$

The studied variables were the type of stage, deposition rate, and film thickness. The film thickness was in-situ monitored by a quartz crystal microbalance (QCM) and checked by mechanical profilometry (Bruker DektaktXT®) of a calibration sample (deposited film with grooves). Glass slide with Au film thickness of 48.74 nm according to QCM was used as the calibration sample. The measured film thickness by profilometer was 48.4 ± 4.7 nm.

It was found out that the type of stage plays an essential role in the deposited film morphology. For the stationary stage, where the samples rotate around the stage axis, the film thickness is preferentially inhomogeneous in one direction. This inhomogeneity can be seen in the magnified inset of SEM images in Figure 5.11, where the thinner parts on the left slope areas are discontinuous, forming tiny separated NPs during SSD, while on the other hand, the thicker parts are compact without voids. A planetary stage, which rotates samples along the stage axis and simultaneously along their normal, eliminated this effect, as shown by the as-deposited layers of Figure 5.11.

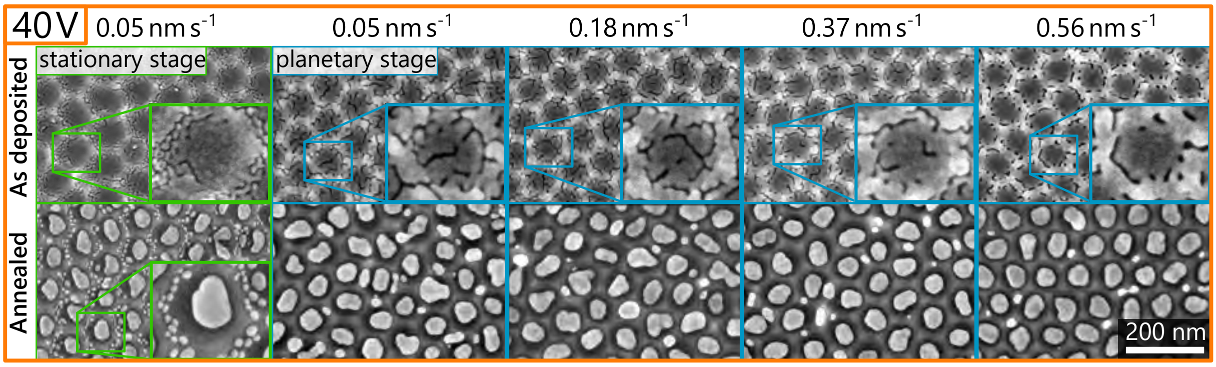

Figure 5.11: SEM images of resulting Al layer (thickness of ≈8 nm) deposited in the Leica setup and annealed (on a hotplate, 300 °C for 5 min). The comparison shows the difference between the use of the stationary and planetary stage as well as deposition rates.

Even though voids in the film are still present, they do not have a preferred location and thus are more homogeneous. Furthermore, it was observed that the film quality could be significantly improved by increasing the deposition rate (shown in Figure 5.11). Similar behaviour was observed by Syed [299], studying gold deposition on flat SiO_2 substrate, and by Wu et al.[300] sputtering titanium on a Si substrate. Both studies support this finding that higher deposition rates result in smoother films with fewer defects/voids. As shown by the annealed results, it is evident that film voids lead to an undesired dewetting mechanism forming numerous NPs per bowl. Without question, good quality such as homogeneity and integrity of the deposited layer is necessary for the best results of SSD.

A further study was conducted to find an ideal film thickness forming one NP per bowl based on previous findings. Figure 5.12 shows varying thickness series on both templates (25 and 40 V). The 40 V series nicely illustrates the trend of increasing deposited film thickness on its morphology and dewetting outcome. The thinnest as-deposited film (2 nm) consists of small islands that form individual NPs. The volume is preserved for each NP as the annealing temperature is too low to drive any material migration between them. With increasing thickness, deposited islands start to grow and merge into larger agglomerations, as shown in Figure 5.12:4.2 nm. During the annealing, these agglomerates dewet into a single proportionally large NP or split into a few NPs. In this case, the splitting happens due to the film topology – defects in the form of grooves. Film defects and substrate curvature govern the film splitting, as mentioned in Section (SSD). Their combined effect leads to larger NPs in the middle of nanobowl that is smooth and convex. While smaller NPs are formed on the sharp protrusion at the perimeter. that is sharply concave.

Further increasing the deposited thickness, those agglomerates continue to grow and merge until they form a continuous layer (Figure 5.12:5.3 nm) with numerous voids and holes. As shown, those voids are gradually closing with increased film thickness, but the slowest curing occurs on slopes under protrusions. This effect may be concluded as an effect related to the template topography to the geometry of the deposition setup. Since the rims of the nanobowls are almost perpendicular to the sputtering direction ($\alpha = 0°$), the material deposition rate here is significantly reduced. Surprisingly, changing the deposition angle to 20° or the working distance by 20 mm had no noticeable effect on the film morphology (examples shown in Figure 5.13). Therefore, it is believed that the self-shadowing effect may play a significant role here. The shadowing may occur when the material is firstly deposited on the top site of protrusion, forming a rim that furthermore shields the slope areas underneath it.

With the increasing rigidity of the deposited film and the decrease of film defects, substrate morphology became the predominant factor governing the film splitting. As can be already seen in Figure 5.12:10.5 nm, a well template-assisted SSD occurred despite minor hole-like defects in the film. Further increase of thickness beyond this ideal point leads to poor separation of NPs across the nanobowls. As discussed in the previous subsection (section 4.1), the reason for this effect is either the template screening with an overly thick layer or a high amount of abundant material per bowl.

Noticeably, the quality of the AuNP layer formed over 25 V templates is worse when compared to the larger 40 V templates. There are several reasons for this. The film defects are larger relative to the template dimensions. The quality of the 25 V template is usually worse in comparison to the 40 V templates. Lastly, the effect of various defects or contaminations plays a more significant role for smaller dimensions. For these reasons, the dominant part of the experiments was primarily conducted with 40 V templates on purpose, and the behaviours for 25 V templates were either directly related or deduced from those findings, if possible. The general trend for both templates is very similar, schematically shown in the inset of Figure 5.15.

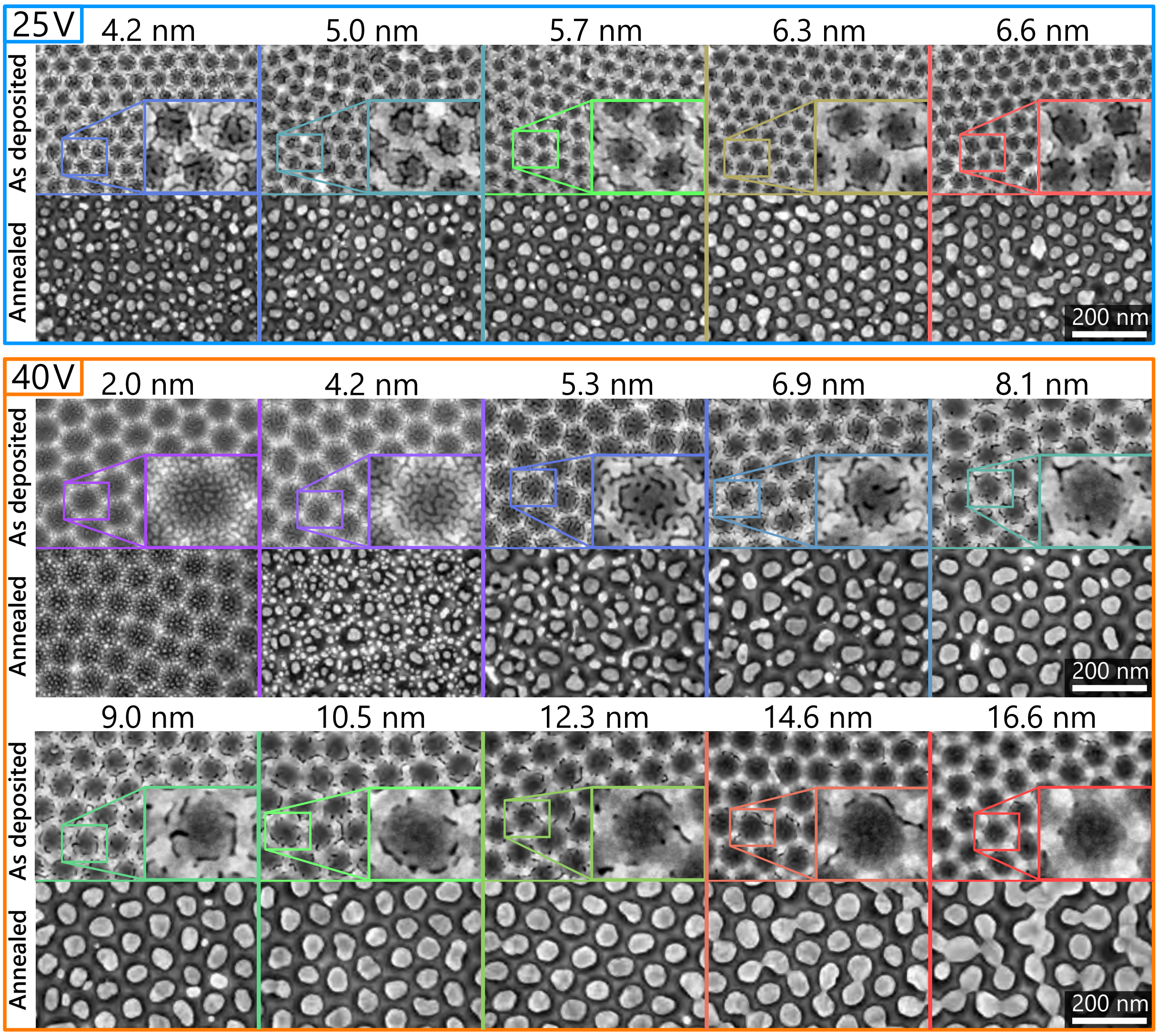

Figure 5.12: Collection (SEM images) of the as-deposited and annealed Au film of various thicknesses (monitored by QCM) deposited on 25 V and 40 V templates in the Leica setup. Depositions were carried out with parameters noted in Table 5.3, using planetary stage and deposition speed of 0.67 nm s^{-1}. Sample annealing was done on a hotplate at 300 °C for 5 min.

Even though the Leica setup is easy to use and has good reproducibility, it has a few significant drawbacks. First is the control of deposited thickness is rough. It can

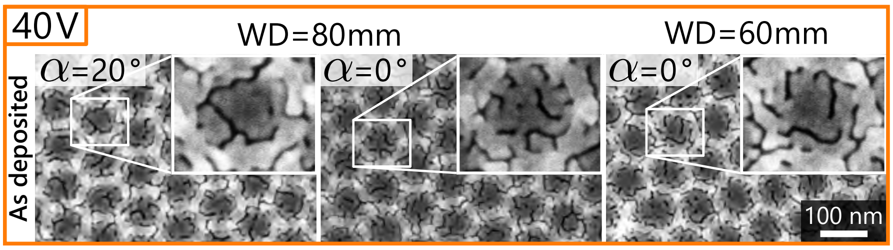

Figure 5.13: Comparison (SEM images) of the as-deposited Au thin-films showing effect of the deposition angle (α) and the distance between substrate and target (WD). The remaining deposition parameters were fixed to a deposited film thickness of 8.1 nm for all samples.

be monitored by QCM that is limited by the slow readout of 1 Hz or controlled by the deposition time that is yet software limited to 1-second steps. Additionally, the deposition rate cannot be directly controlled. However, the most limiting is the maximum sample size of only 25 mm×25 mm for the planetary. Due to these limitations, this setup was used only for test samples rather than a large-scale batch fabrication.

The evaporator setup consists of a relatively large vacuum chamber with eight crucibles filled with materials. During the deposition, one of them is heated by an electron beam (e.g., 8 keV) to the point when the material evaporation starts. During the evaporation, the deposition rate is in-situ monitored by QCM. The used deposition parameters are tabulated in Table 5.4.

Table 5.4: Deposition parameters of the evaporator setup. These deposition parameters were used for the samples prepared in the Evaporator setup, if not stated otherwise.

WD	α	r_s	P_{init}	P_{dep}	ω	R_{dep}
425 mm	0°	0 mm	2×10^{-5} Pa	7×10^{-5} Pa	10 RPM	$0.1\,\mathrm{nm\,s^{-1}}$

The effect of the deposition rate is shown in Figure 5.14. The higher deposition rate leads to a more continuous layer on the 40 V template. Meanwhile, it leads to material aggregation on the top side of the protrusions for much smaller 25 V templates. This outcome is undesirable because inhomogeneous film thickness leads to poor template-assisted SSD in general. SSD often leads to poor NP separation, which can even manifest in Au overflow from one bowl to another, merging with the neighbouring material, or forming unequal NPs (as shown in Figure 5.15:25 V).

The thickness relation follows a similar trend as shown in the previous case (Leica setup). However, the ideal thickness for the 40 V template shifted from 10.5 to 8 nm. The deposited material thickness should be correct in both cases since it was monitored by QCM and confirmed by profilometry. Moreover, the measurement of the diameter of AuNPs shows a difference, too. The film (8 nm) deposited by the Evaporator setup gives by 5 nm smaller NPs than the one (10.5 nm) done in the Leica setup. However, the values are shifted only for 40 V templates, while for 25 V templates, the thickness values of both setups match. Therefore, it is assumed that the cause of the shift may be a difference in the film morphologies, systematic error in the Leica depositions on 40 V templates or some neglected effect.

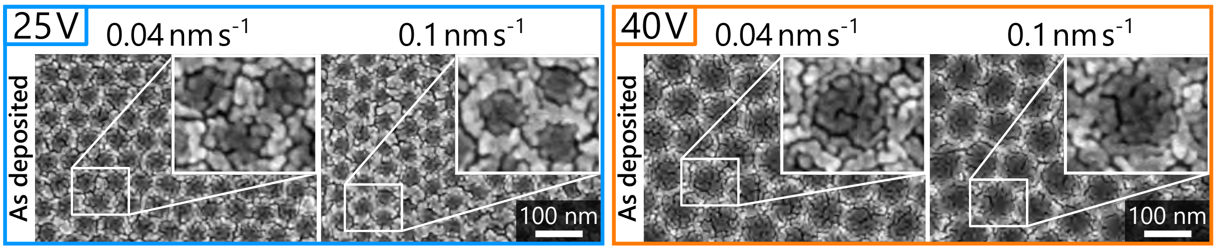

Figure 5.14: Comparison (SEM images) of the as-deposited Au film morphologies prepared in the Evaporator setup by various deposition rates on the 25 V and 45 V templates. Deposition parameters according to Table 5.4 and film thickness of 6 nm were retained for all samples.

The magnetron sputtering system is similar to the Leica setup, but it consists of a much bigger vacuum chamber with an additional seven separated magnetron guns. Deposition parameters tuned for homogenous deposition over 100 mm samples are defined in Table 5.5. The deposited rate was monitored before each deposition by QCM. Additionally, it was controlled by mechanical profilometry and XRR.

Table 5.5: Deposition parameters of the evaporator setup. These deposition parameters were used for the samples prepared in the Evaporator setup, if not stated otherwise.

WD	α	r_s	P_init	P_dep	ω	R_dep
200 mm	29°	25.4 mm	10^{-6} Pa	10^{-1} Pa	10 RPM	3.5×10^{-2} nm s^{-1}

The Magnetron setup gives the best results among the tested equipment. Deposited films have the smoothest morphology with fewer defects (comparison with the evaporator resulting layers shown in Figure 5.16). Thus, it was possible to achieve AuNP layers of better quality, even for smaller 25 V templates. Based on previous results, narrower ranges of thickness values were investigated, as shown in Figure 5.17.

5.3.2 Effect of annealing conditions

Temperature plays a significant role during annealing because SSD kinetics is thermodynamically dependent (equation Equation 4.2). Surprisingly, very satisfactory results can be achieved in a broad range of temperatures and a relatively short annealing time of 5 minutes (shown in Figure 5.18). At lower temperatures (200 and 250 °C), the diffusion is

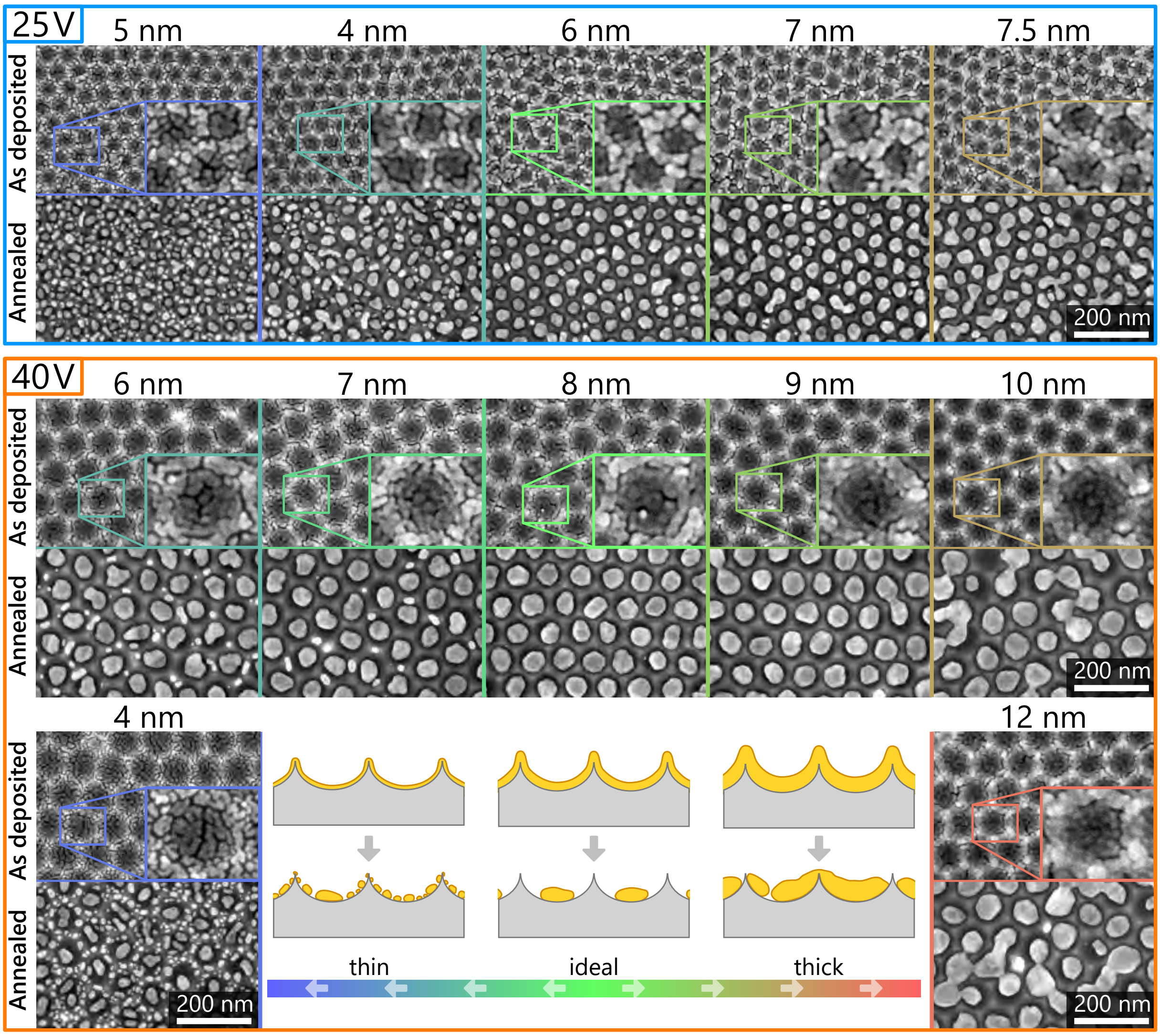

Figure 5.15: Collection (SEM images) of the as-deposited and annealed Au film of varying thickness deposited on the 25 V and 45 V templates in the Evaporator setup. Depositions were carried out with parameters noted in Table 5.4. Samples were then annealed on a hotplate at 300 °C for 5 min.

not fast enough, producing only partially separated or shape-deformed Au islands. Ikeda et al.[201] show similar results for SSD of various Au thicknesses at 200 °C. A good round shape can be already observed at 300 °C, while a further increase in temperature does not contribute to any noticeable changes. Additionally, a comparison with another procedure applying a higher temperature and longer annealing time are shown in Figure 5.18. Notably, Fan et al.[203] published results of very similar samples processed with this procedure. However, no difference was observed for the selected film thicknesses, except for slightly better separation and smaller islands for the 10 nm film. Similar results are presented by Ikeda et al.[201] using annealing temperature of 500 °C for 1 hour. While the increased temperatures and prolonged annealing time do not improve the dewetting

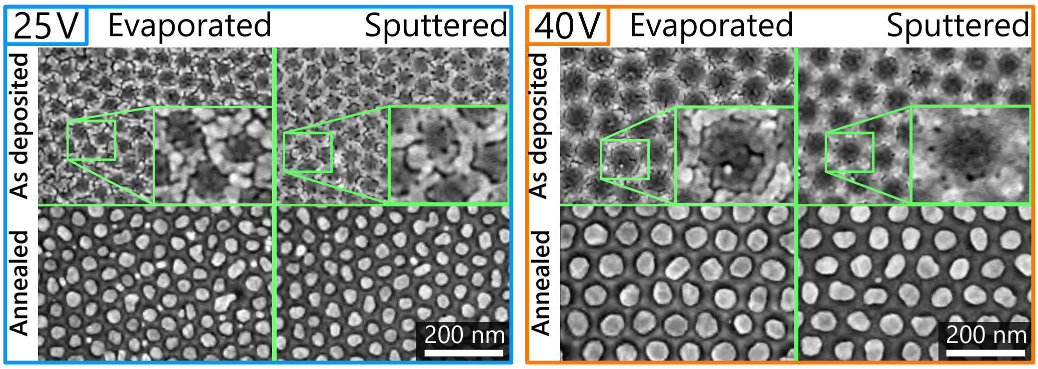

Figure 5.16: Comparison between layers prepared by evaporation and sputtering (Magnetron setup). The deposited thickness (same for both techniques) is 6 and 8 nm for 25 V and 40 V templates, respectively.

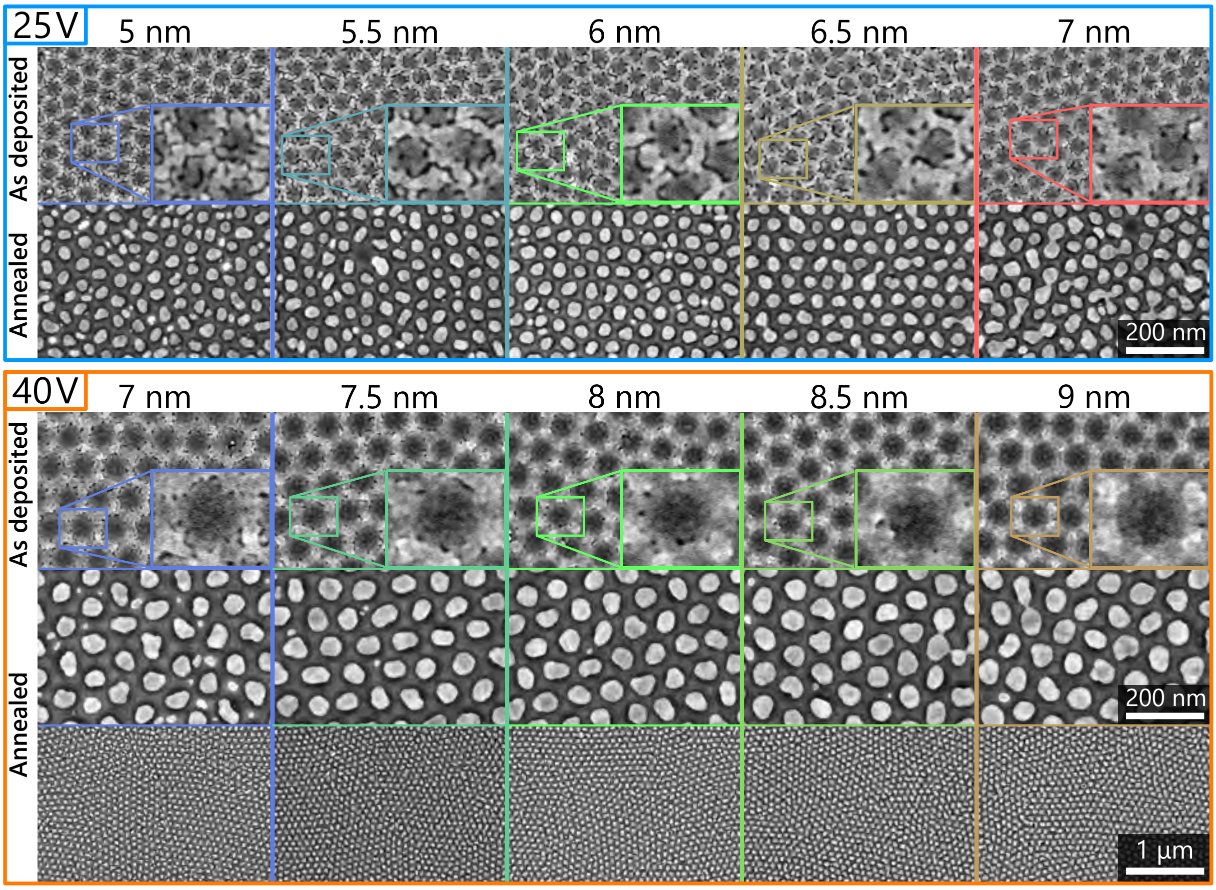

Figure 5.17: Collection (SEM images) of the as-deposited Au films deposited in the Magnetron setup and resulting dewetted AuNP layers on the 25 V and 40 V templates. Deposition parameters are noted in Table 5.5.

on the templates but still increase the chance of undesirable aluminium thermal oxidation, these procedures were avoided. Therefore, the annealing at 300 °C on a hotplate for 5 minutes was used for all SSD in this work.

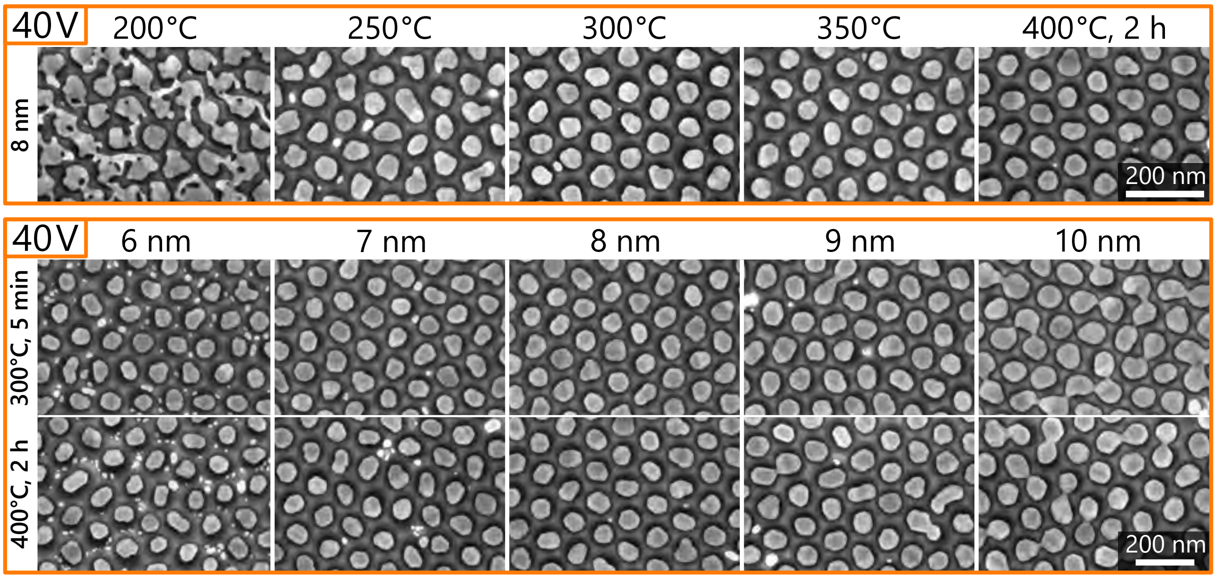

Figure 5.18: (Top) Effect of annealing temperature on SSD of 8 nm Au film on 40 V templates. Annealing at 200–350 °C was performed on a hotplate for 5 minutes. (Bottom) The relation of film thickness on dewetting results for two thermal treatments on a hotplate.

5.3.3 Effect of substrate material

The influence of the substrate material was neglected for a long time because aluminium templates worked relatively well. However, after more detailed data evaluation, a few minor deviations in the morphology of the as-deposited Au layer and AuNP shape were discovered between freshly prepared and few weeks old Al templates. In this work, two possible reasons were investigated: aluminium oxidation and surface hydrocarbon contamination.

Native oxide. The effect of native oxide is indirectly shown in Figure 5.19. Since native oxide forms almost immediately over the Al surface in the presence of atmospheric oxygen, it is not trivial to eradicate it. The growth rate is time-dependent, with an exponential decay that is mainly influenced by the temperature and partial oxygen pressure. The thickness of a freshly grown (under 1 hour) native oxide is expected to be approximately 1.2 nm according to several reports (denoted as thin native oxide in Figure 5.19).[301, 302] The maximum thickness of native oxide grown in ambient conditions is reported to be approximately 3–5 nm (denoted as a thick native oxide in Figure 5.19).[303] As-deposited Au film on the template with thin oxide is much more compact than a film formed over the aged template with a presumably thicker oxide layer. This native oxide layer can be seen in the transmission electron microscopy (TEM) images, shown in Figure 5.20, where the slightly thicker oxide thickness of 6.5 nm may be attributed to the observation technique (thickness of the lamella) and additional thermal annealing in comparison to the ambient conditions referred in the previous reports.

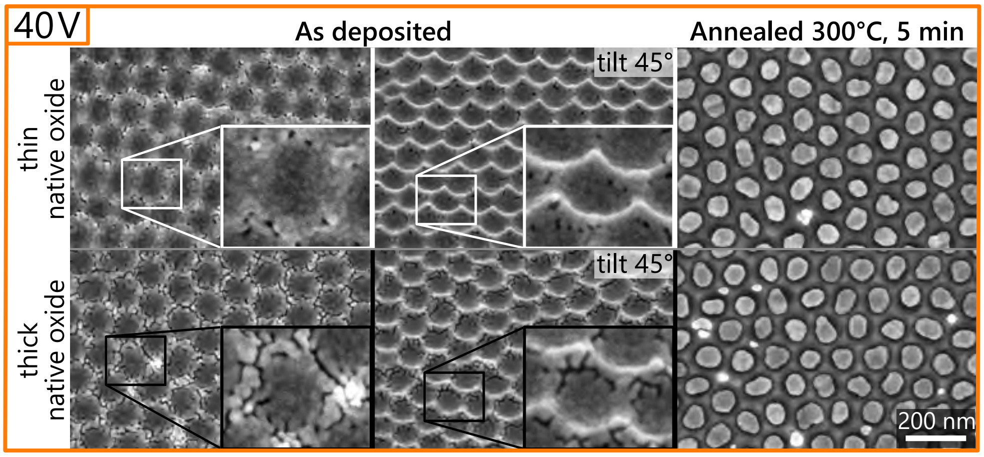

Figure 5.19: Comparison of deposited Au film morphologies on 40 V Al templates with thin and thick native oxide layer. In the first case, the oxide was removed by the PAA selective etchant (CrO_3 and H_3PO_4 solution) before gold deposition (maximum of 1 hour), while in the second case, the Au film was deposited over a few weeks old sample.

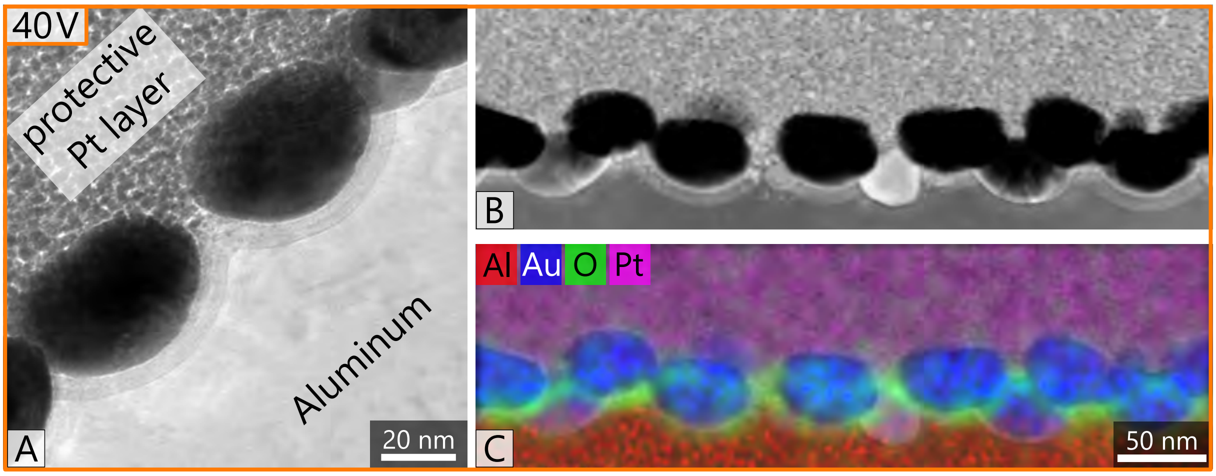

Figure 5.20: (A) TEM image, (B) STEM image, and (C) Energy-dispersive X-ray spectroscopy (EDX) analysis of AuNPs on 40 V Al template showing the oxide layer. The lamella for TEM was fabricated with a platinum protective cap. The lamella preparation and analysis were done by Jan Michalička (CEITEC BUT) performed with a Carl Zeiss LIBRA200FE (with Bruker Quantax 200, 30 mm^2 EDS detector).

It should be noted that vacuum annealing was tested but abandoned as it does not improve SSD and increases time and instrument demand. However, with the development of control over AuNP size by multiple depositions and dewetting cycles in later stages, vacuum annealing is now strongly considered to avoid unnecessary thermal oxidation of the aluminium template.[304, 305]

Carbon layer. Surface hydrocarbon contamination is a time-dependent process like aluminium oxidation, which also strongly depends on the fabrication process and storing conditions of the sample. Seah and Spencer showed that the thickness of the adventitious carbon layer on an as-received silicon wafer is 0.6 nm and can be increased by the wrong handling to up to 2 nm.[306] Forrest et al.[307], showed that the wettability of the surface decreases with the thickness of carbon contamination that is also in agreement with metal dewetting proposed by Eustathopoulos [308]. To remove this contamination in a similar way to native oxide, samples were cleaned by oxygen plasma before the Au deposition. However, no substantial differences were observed between plasma treated and untreated samples. It may be explained either by an insufficient carbon thickness that would manifest into a recognizable outcome or a cross-effect of additional Al oxidation (or other modification) during the plasma treatment.

The effect of natural hydrocarbon contamination was simulated and overcompensated by the carbon deposition. The carbon deposition was done in the Leica setup by flashing carbon thread method that uses the desorption process of heated carbon filaments. As shown in Figure 5.21, a carbon layer has very little influence on the as-deposited Au film morphology, while it significantly influences the dewetting results, especially the AuNP shape. This change in morphology is apparent in the evaluated dimensions (Table 5.6). The AuNPs formed over the 5 nm carbon layer are more spherical with a smaller diameter and larger circularity, shown in SEM images (Figure 5.21). Moreover, this carbon layer has a positive effect on the NP size distribution. On the other hand, the thicker (10 nm) carbon layer gives NPs with broader size distribution and lower circularity, presumably due to worse dewetting over the smoothen surface.

Table 5.6: Dimensional characteristics of AuNPs formed on the carbon layer modified 40 V Al templates (shown in Figure 5.21).

The thickness of carbon layer [nm]	Mean diameter [nm]	Particle perimeter [nm]	Circularity[†]
0	68.7 ± 1.8	247.2 ± 8.2	0.851
5	63.4 ± 1.6	223.2 ± 6.8	0.886
10	63.6 ± 2.2	228.0 ± 8.4	0.856

[†] Centre of distribution.

Although the role of the carbon layer was not further studied in the scope of this work, it may have several advantages. A carbon layer may act as a buffer layer, decreasing the wettability of the substrate. Adding a carbon layer can be convenient and easy to implement for advanced AuNP tuning or even a novel way for new nanostructure fabrication. The dewetting conditions are too mild to dissolve any carbon in gold and form a eutectic system.[309] It presumably withstands the annealing process, as can be seen in SEM images, as additional texture with high contrast to AuNPs. It may also rapidly decrease AuNP adhesion and thus improve their transfer (further discussed in the next section 5.4), while it can be easily cleaned in oxygen plasma.

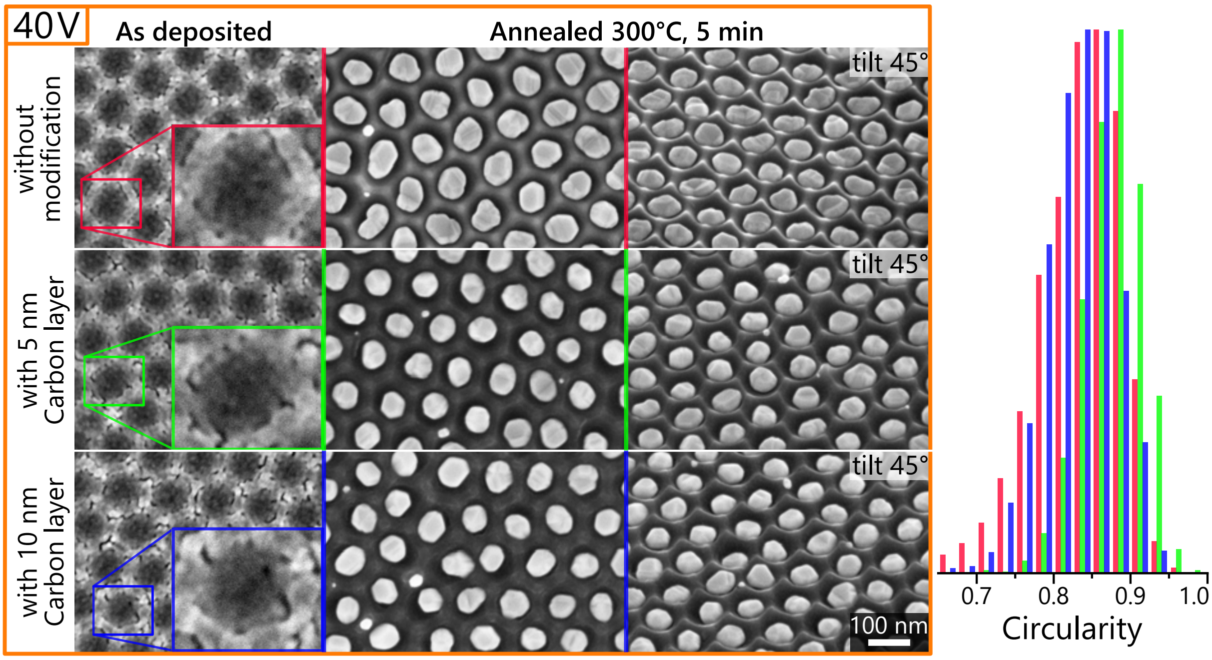

Figure 5.21: Comparison of deposited Au film (8 nm) morphologies and dewetting outcome on 40 V Al templates with and without additional carbon layer (5 and 10 nm). The inset graph presents calculated circularity distribution (maxima in Table 5.6).

5.3.4 AuNPs controlled enlargement

AuNP size control is one of the main objectives of this work. As it directly influences the LSPR, it opens new possibilities for utilization in various applications (e.g., LSPR, SERS, SIERA). Naturally, the size of AuNPs depends on the amount of deposited material—Au film thickness. Unfortunately, it is restricted to a narrow window of values, as discussed in the previous subsection (subsection 5.3.1). To overcome this limitation, a repeated deposition and dewetting process were applied to increase the size of AuNPs (illustrated in the inset of Figure 5.22).[310, 311] It is important to point out that this process is still governed by the same principles as the first deposition and dewetting cycle when the best result can be achieved only in a narrow window of deposited film thicknesses. Figure 5.22 shows examples of various thicknesses of the deposited film for three cycles on 40 V templates. Again, not optimal thickness leads to poor template-assisted dewetting; NPs merging for too thick films and small satellite NPs for too thin films. The best outcomes, the main line, were achieved by 8 + 7 + 5.5 nm and 6 + 5 nm for 40 V and 25 V templates, respectively (shown in Figure 5.23). Since the thickness decreases with the cycle to retain a good NP separation, it becomes challenging to keep a compact film and avoiding undesirable splitting. These boundary conditions naturally limit the number of cycles to three and two for 40 V and 25 V templates, respectively.

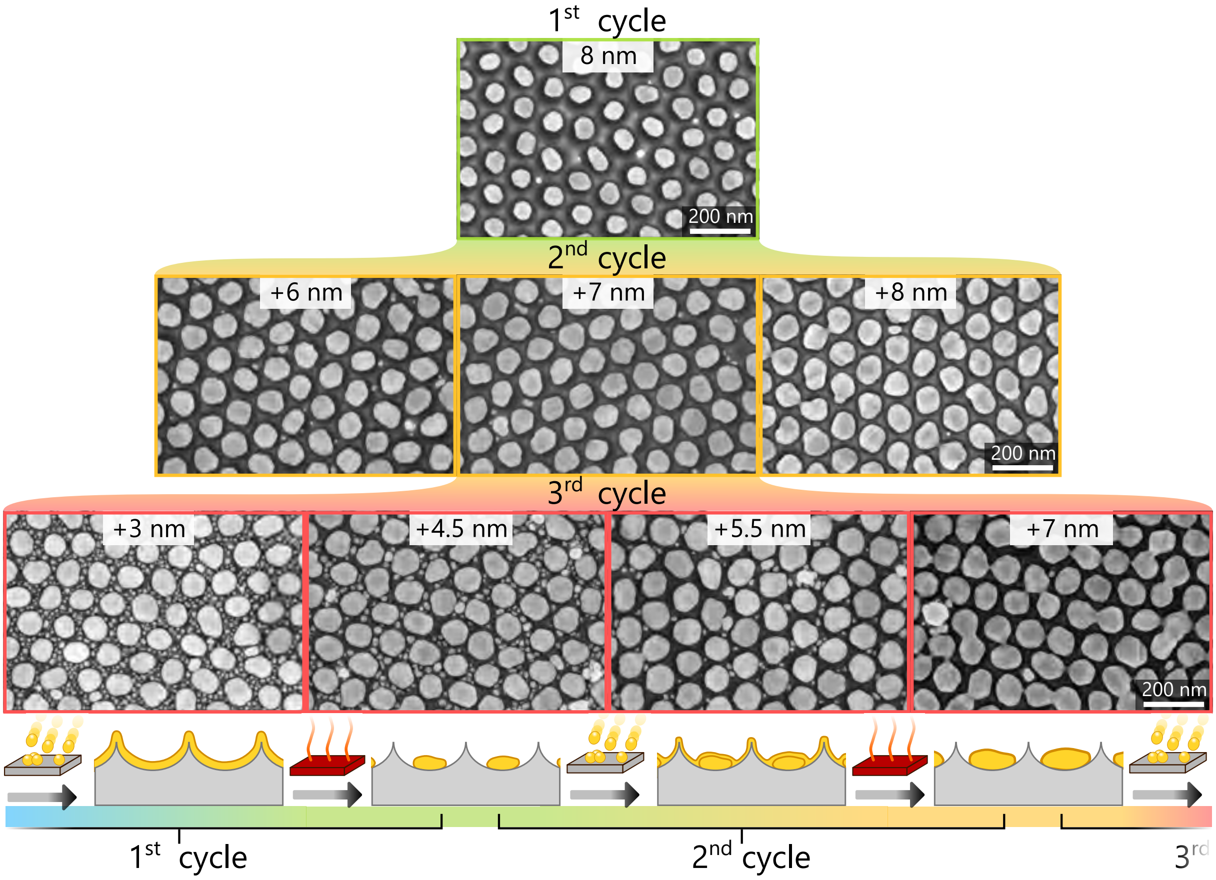

Figure 5.22: SEM images showing various cycle stages of repeated deposition and annealing over 40 V template with the schematic illustration of fabrication cycles.

As can be noted, the AuNP growth in lateral dimensions is predominant primarily during the first two cycles, between which the size increases by 27 %. After the 3rd cycle, the lateral size increases only by less than 4 %. The tilted SEM images (Figure 5.23) show that AuNPs have a very flat shape resembling blood cells or oblates. After the 2nd and 3rd cycle, the AuNPs grow preferentially in a horizontal direction due to their lateral confinement by the high curvature of the nanobowls, resulting in more spherical NPs. A cross-section of AuNPs can be observed in Figure 5.24 of the lamella STEM images.

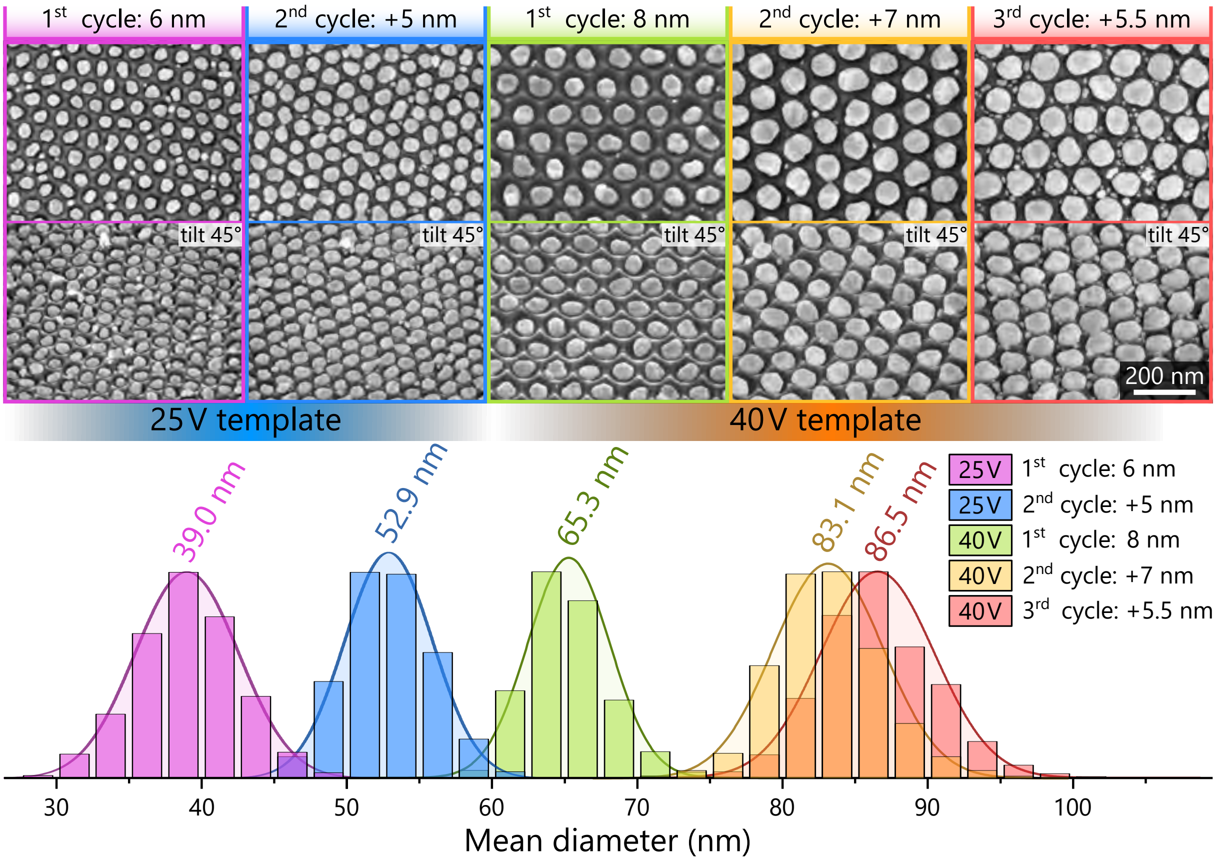

Figure 5.23: SEM images of the main lines of AuNPs formed over 25 V and 40 V Al templates with the corresponding size distribution (mean diameter) fitted by a Gaussian function. Mean diameters for 25 V are 39.0±1.8, 52.9±1.5 nm, and for 40 V are 65.3±1.4, 83.1±1.9, 86.5±2.0 nm.

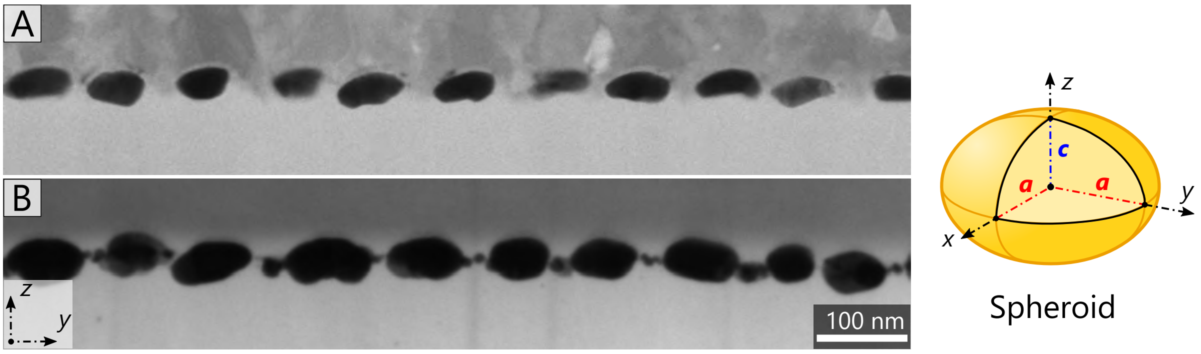

Figure 5.24: STEM images of AuNPs of (A) 1st cycle and (B) 2nd cycle. The AuNP shape resembles an oblate (schematically illustrated in the inset). The AuNPs of the 1st cycle are flatter with $a/c = 1.90 \pm 0.26$ compared to the 2nd cycle ones with $a/c = 1.73 \pm 0.21$. The lamellas were prepared from AuNPs: (A) on an epoxy substrate covered by an Al layer, (B) on PDMS substrate covered by a carbon layer.

5.3.5 Conclusions

This section was devoted to the large-scale fabrication of AuNPs by utilizing the SSD process over nanobowled Al templates. An emphasis was t placed on the demonstration that the AuNP layer depends primarily on the initial morphology of the Au film governed by the film thickness and deposition technique. The best results were achieved by the magnetron sputtering system and thicknesses of 6 and 8 nm for 25 V ($D_c = 65$ nm) and 40 V ($D_c = 106$ nm) templates, respectively. Additionally, an increase of AuNP size was performed by repeated deposition and SSD cycles, where satisfactory results were achieved for 6 + 5 nm and 8 + 7 + 5.5 nm cycles in the case of 25 V and 40 V templates, respectively.

It was also shown that the annealing temperature of 300 °C for 5 min is sufficient for this system. Presented experiments also proved that the native oxide thickness plays a significant role in the morphology of the deposited Au film. Even though a detailed systematic study was not conducted, it is believed that suppression of aluminium oxidation may further improve the quality of the deposited films (even for thinner thicknesses). It can be done by shortening the storage time and avoiding thermal oxidation (vacuum annealing) in repeated cycles.

Moreover, the additional thin carbon layer improves the AuNPs sphericity and size distribution. Besides these improvements, it is suggested that it may lower the adhesion of AuNPs and protect aluminium from extended oxidation.

Lastly, based on current results, the morphology of the deposited layer plays a crucial role. Therefore, improving it can significantly shift the current limitations. This may be possibly achieved by other more advanced deposition techniques, such as High-power impulse magnetron sputtering (HiPIMS) or Ion-beam sputter deposition by Kaufman source.

5.4 Transfer of AuNPs layers

To utilize the fabricated AuNP layers as an LSPR sensor element, they were transferred to an electrically non-conductive and optically transparent substrate. During this process, a new substrate is cast over the AuNP layer, and the Al substrate is removed by chemical etching, as shown in Figure 5.25.

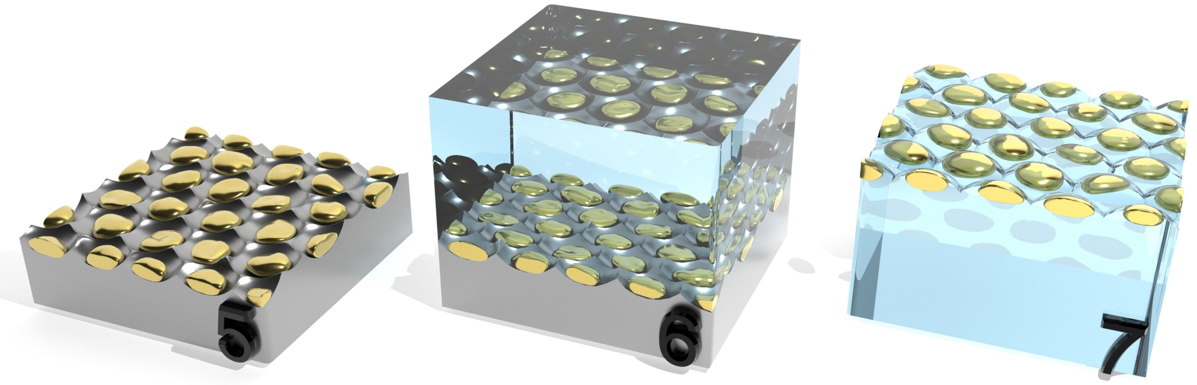

Figure 5.25: Schematic illustration of the transfer process of AuNP layer from the Al template to another substrate. (5) AuNP layer prepared on the Al template. (6) Casting a new substrate material over the structures. (7) Selective removal of Al template leaving AuNPs embedded in a new substrate.

The ideal substrate should be optically transparent in the region of plasmon resonance (VIS) with low diffusion. Additionally, it has to be compatible with fabrication processes, including good chemical stability to acids, bases, and organic solvents and has sufficient thermal stability to withstand wet or dry etching processes. Other critical property such as good adhesion to AuNPs, durability, and cleanability will also be evaluated.

In the course of this work, four main types of substrate materials were tested: polydimethylsiloxane (PDMS), polymethyl methacrylate (PMMA), epoxy resin, and sandwich structure of the top evaporated thin SiO_2 layer with epoxy support.

PDMS was chosen as the first candidate for the substrate for its wide application in the fabrication and prototyping of microfluidic chips. Additionally, it has desired properties such as excellent optical transparency in the visible region, high flexibility, and chemical stability.[312]

PDMS casting was done over the sample in a mould.[313] PDMS was prepared from a two-component elastomer kit SYLGARD 184 (Dow) with a weight ratio of 1:10 (curing agent to base). These compounds were thoroughly mixed, and then the solution was degassed either in vacuum or by centrifugation based on the processed volume.

At the early stages of development, a unique mould (shown in Figure 5.26:A, B) was used to cast PDMS over a small AuNPs sample. The advantage of this was that cast

PDMS form a simple element of a microfluidic cell with an NP layer on the side of interest after Al removal (Figure 5.26:C). Even though this method produces an almost finished sample ready for application, it was later replaced by a simplified procedure with a much higher throughput. This procedure uses a dural rectangular frame of various dimensions concerning the sample size as a mould. Frames have the same height of 3 mm and a border thickness of 5 mm. One-sided adhesive Kapton tape was stretched over the frame forming the bottom of the mould. Then the sample was placed in the middle of the mould facing upwards with the AuNP layer and firmly adhered to the tape. The PDMS solution was then slowly poured over a filling frame up the top. To speed up hardening, the mould was baked for at least 20 min at 80 °C; however, at least 12-hour baking is recommended. After baking and cooling down, the PDMS block with the embedded sample was carefully peeled off from the frame. Note that any extended manipulation with samples still embedded in the PDMS block might lead to Al sheet detachment and incomplete AuNP transfer between substrates. This peeling can be avoided by etching the aluminium substrate before peeling the substrate block from the mould. One way to do this is to make the mould frame from a compatible material regarding chemical etching, for example, 3D printed acrylonitrile butadiene styrene (ABS). The drawback is a lower baking temperature to avoid frame bending and extend the baking time. The Al substrate was removed by selective chemical etching, as is described in the following procedure. This procedure was used in all transfer methods.

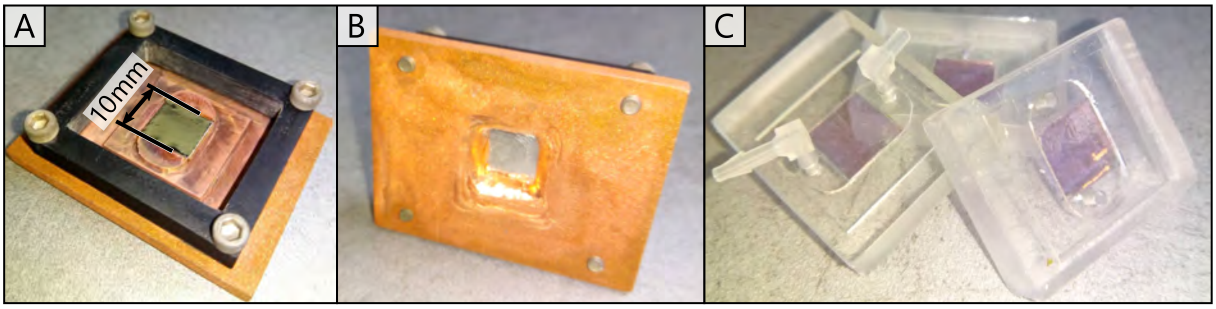

Figure 5.26: Photo of a simple microfluidic mould for PDMS casting composed of a copper base with plastic rim and a glued AuNPs sample (10 mm × 10 mm). (A) Top-view, (B) bottom-view and (C) final PDMS microfluidic elements with transferred NP layers (pink area).

Standard Al removal procedure: Right before Al etching, the backside of the Al substrate was gently scratched by sandpaper to damage the oxide layer. This treatment dramatically enhances the chemical etching and speed up Al removal. The Al substrate was immersed in hydrochloric acid (HCl, 35 % w/w) and 1 M copper(II) chloride ($CuCl_2$) water solution. The dissolution of Al is a very vigorous exothermic reaction accompanied by a rapid chlorine gas evolution; therefore, appropriate precautions need to be taken. It is also suitable to properly place the sample to avoid trapping gas bubbles during the etching. Otherwise, it may damage the AuNP layer. When the gas evolution stops, the etching is finished, and the sample is pulled out and thoroughly rinsed in tap water, followed by washing in deionized water. Afterwards, it was subsequently immersed into 1 M iron(III) chloride ($FeCl_3$) water solution and 1 M sodium hydroxide (NaOH) water solution for 10 min to remove copper and aluminium oxide residues, respectively. After the etching procedure, the sample was thoroughly washed in deionized water and dried by nitrogen stream.

PMMA has similar optical properties as PDMS in the VIS region. The PMMA was chosen primarily due to its simpler micromachining (selective ion etching) and better adhesion to the AuNP layer. However, the PMMA lacks in terms of chemical stability to various organic solvents and has worse thermal stability (thermoplastic with $T_g = 105\,°C$) compared to the PDMS that can withstand over 200 °C.

The casting of PMMA was done in a slightly different way since the casting is solvent-based. The sample was glued by PMMA on the top side of a microscopic slide or a piece of plexiglass plate. A solution of PMMA dissolved in anisole with maple syrup viscosity (100–200 Pa s) was used as glue. After putting the sample and glass together, the PMMA solution was left to cure (dry) for two days. Then, the Al substrate was removed by the standard procedure.

Epoxy resin has a much better thermal stability (thermoset), exceptional adhesion to AuNPs, and good chemical resistance. Like PMMA, its high rigidity is inconvenient for mechanical machining; however, the biggest drawback is a weak resistance to oxygen plasma cleaning, resulting in a limited cleanability of AuNPs.

Epoxy casting was done similarly to PDMS casting. Two compound epoxy resin Elantron® EC 570 and W 363 with a weight ratio of 100:33 was used as a base material. After mixing, the solution was quickly degassed by centrifugation for 1 min at 2500 RPM. The application over AuNP samples is the same as for PDMS. The epoxy resin was cast in a frame over the AuNP sample to a thickness of a few millimetres and cured for 12 h at 50 °C in an oven. After casting, Kapton tape was applied on the top side of the epoxy against the sample to protect it from chemical damage during the Al removal. Then, the Al substrate was removed.

SiO_2 has ideal properties, including perfect chemical stability as well as resistance to O_2 plasma. The setback is just more advanced requirements for the deposition.

A SiO_2 layer of 500 nm was deposited over the AuNP layer in the evaporator setup. The deposition rate was gradually increased, starting with 0.1–0.2 $nm\,s^{-1}$ for the first 50 nm and then up to 2 $nm\,s^{-1}$ for the rest of the deposition. Since the SiO_2 layer is too thin to act as a free-standing support for the AuNP layer, a thick epoxy layer was cast over it (as described in the epoxy paragraph). Afterwards, the Al substrate was removed.

After transfer, samples were usually cut to smaller pieces with an AuNP layer area of at least 10 mm×10 mm. PDMS samples were cut by a razor, while epoxy samples were cut off by a precision saw (Accutom 100) and then washed by ultra-sonication in deionized water for 2 min. The resulting samples (examples shown in Figure 5.27) have blue colour indirect transmission from the LSPR absorbance peak of AuNPs at 580–600 nm. In refraction, they show a metallic gloss similar to a compact gold film.

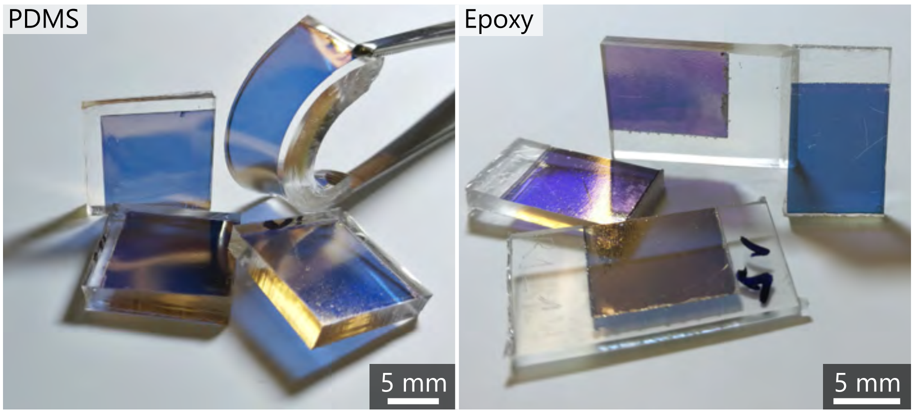

Figure 5.27: Photographs of transferred AuNP layers on PDMS and epoxy substrates.

The transfer efficiency was monitored simply by colour saturation and coverage across the sample area after etching. From experience, the transfer efficiency was the lowest for PDMS when compared to almost perfect for PMMA, epoxy, and SiO_2 substrates. Poor transfer frequently results in macroscopic blank spots in the AuNP layer or even washing out during water rinsing. This poor adhesion to PDMS may be observed in SEM (Figure 5.28:A) as vacant spots, usually caused by particle movement due to PDMS bending. The reason for this can be a weak adhesion of PDMS to AuNPs or possible poor wetting due to high viscosity (PMMA 100–200 Pa s, epoxy 120–180 Pa s, PDMS 350 Pa s).

The poor AuNP adhesion to PDMS was solved by AuNP modification by (3-Mercaptopropyl)trimethoxysilane (MPTMS), which can create a chemical bond between gold and PDMS (illustrated in Figure 5.28).[314] The application of MPTMS was made before PDMS casting. The sample was placed into a Petri dish with the AuNP layer upwards and immersed in ethanol (99.8 %) to an approximate volume of 20 ml or a height of 10 mm. MPTMS (95 %, Sigma-Aldrich) was drop-cast over the sample with a density of $0.5\,\mu l\,cm^{-2}$. The sample was kept in the mixture for 1 hour with irregular stirring to allow MPTMS molecules to spread and make a monolayer coverage over AuNPs. After that, the sample was washed by ethanol and dried under a nitrogen stream.

The adhesion difference is shown by SEM images and a simple scotch tape adhesion test demonstrated in Figure 5.28. In SEM images, unmodified AuNPs form blank areas, which are believed to be caused by sample bending with poor adhesion of AuNPs to

PDMS substrate. The poor adhesion is also confirmed by the scotch tape test, where the unmodified layer is almost entirely transferred to the tape while no visible transfer is observed in the case of modified AuNPs.

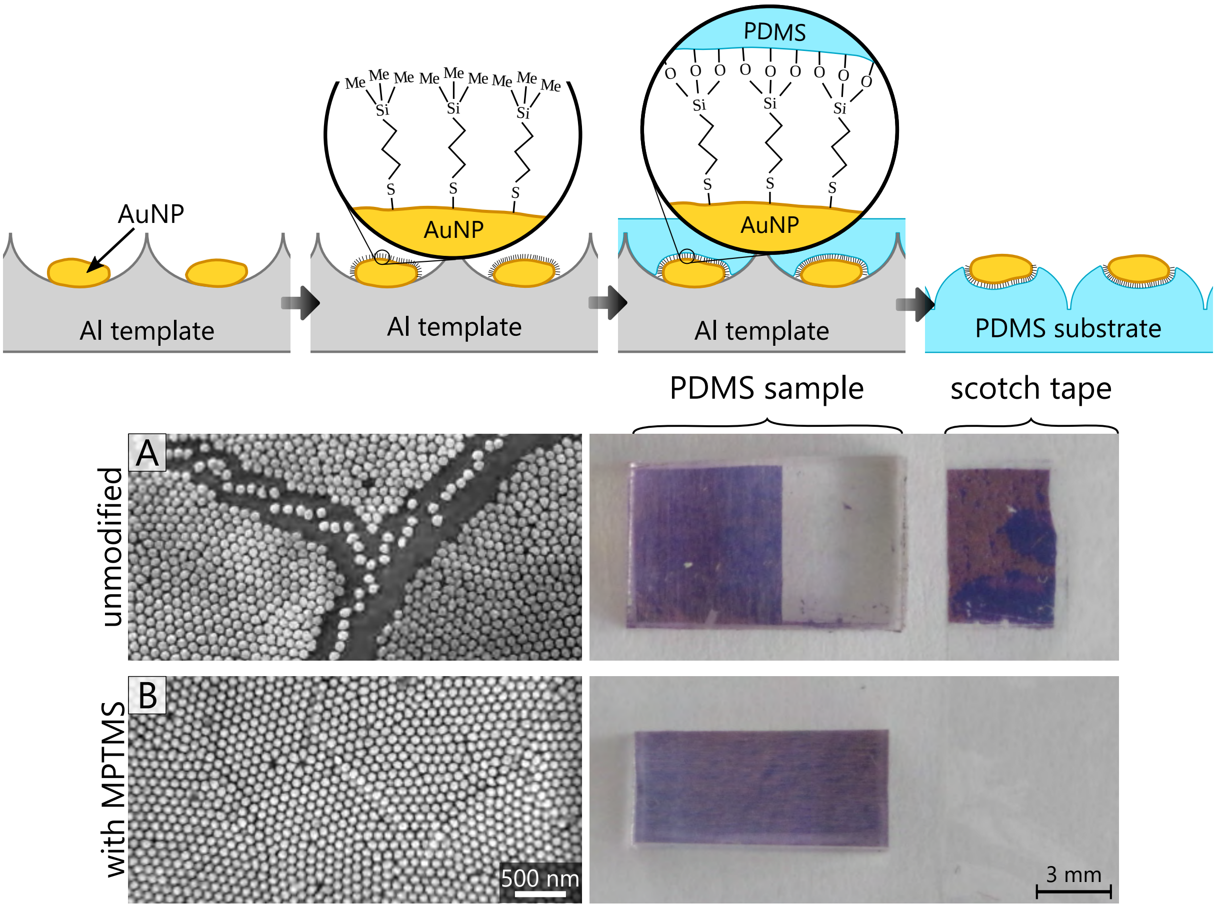

Figure 5.28: (Top) Schematic illustration of the MPTMS application as a covalent bond between AuNPs and PDMS substrate. The SEM images show comparisons between AuNPs on PDMS (A) with and (B) without modification by MPTMS, while the photos show transfer results of the adhesion test by a scotch tape.

Figure 5.29 shows examples of transferred AuNP layers. In general, the resulting morphology consists of AuNPs on top of the substrate, more or less embedded in hemispherical domes. For PMMA, epoxy, and SiO_2 substrates, embedding is almost perfect, forming very sharp boundaries between the domes. Meanwhile, in the case of PDMS, a smooth wave-like surface is observed. This smoothing may result from either poor wetting performance, migration of PDMS oligomers (discussed later), or an effect of the observation technique (SEM).

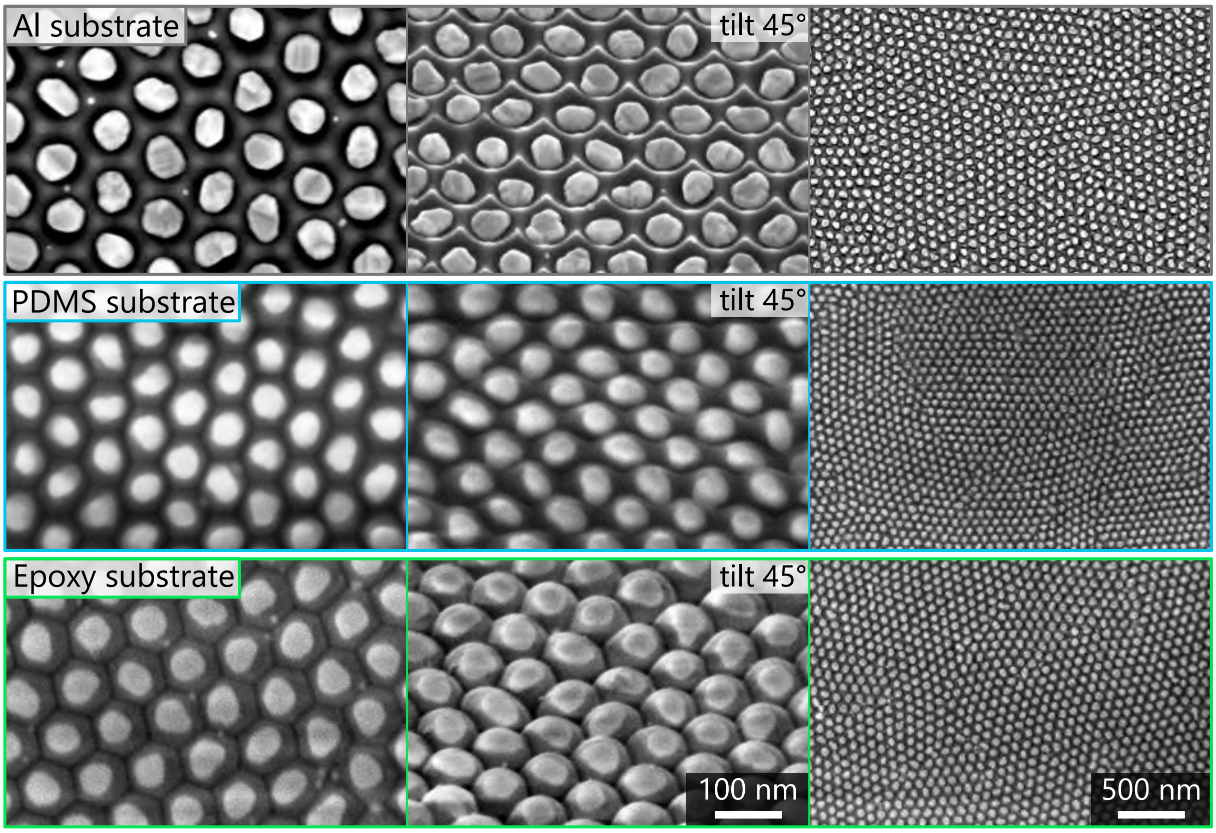

Figure 5.29: SEM images of the AuNP layer before and after transfer on the PDMS and epoxy substrate.

Conclusions

This section presents a simple transport method of AuNP layers from an Al substrate to another transparent substrate while keeping their initial alignment. Additionally, this method provides good scalability, high throughput, good repeatability, and cost-effectiveness.

Overall, a possible drawback of this method may be the requirement to sacrifice the initial Al substrate. This sacrificing waste the material ($\approx 0.4\,€\,\mathrm{cm}^{-2}$), which is acceptable; however, it requires an individual template for each AuNPs layer that is time-consuming. Unfortunately, other methods utilizing various peel-off techniques [314–316] failed due to the strong adhesion of the AuNPs to the Al substrate. Another limitation may be the compatibility of the new substrate with the wet-etching of aluminium.

5.5 AuNPs substrate etching and characterization

As presented in the previous section (section 5.4), the AuNP layers can be successfully transferred to various substrates while preserving their initial arrangement. However, due to the technological aspects of the transfer, AuNPs are by large part immersed in their new substrate. The drawback of this configuration is that the surrounding substrate significantly obstructs another medium to access the surface or space between AuNPs, inhibiting the bulk RI sensitivity and DNA hybridization. This section demonstrates a solution in the form of controlled substrate removal around AuNPs (illustrated in Figure 5.30) that results in a massive increase of sensitivity and the accessibility of AuNP surface for potential modification.

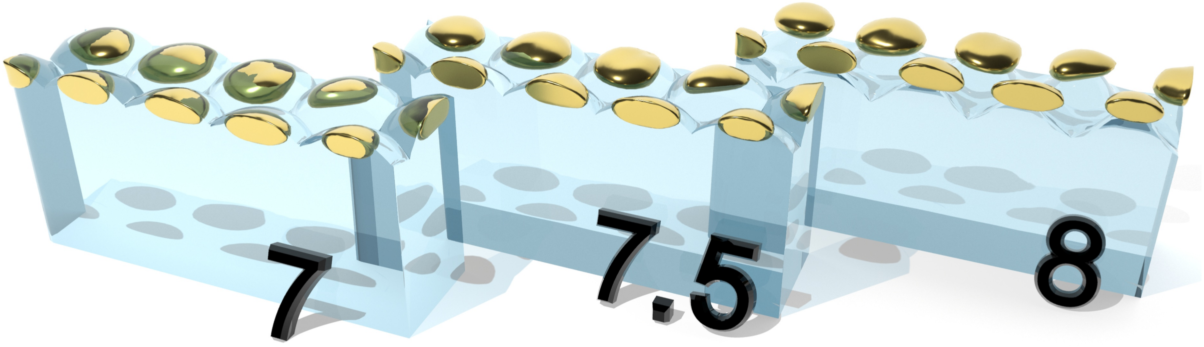

Figure 5.30: Schematic 3D representation of the etching effect on the substrate morphology. (7) As-transferred AuNPs, (7.5) mildly and (8) fully etched.

The removal of all substrates was done by plasma reactive ion etching to ensure reasonable control and homogeneity of the process. Additionally, the properties of the selected samples are characterized using SEM/STEM, AFM, XPS, and VIS spectroscopy. The LSPR sensors were successfully used for the label-free detection of a 20 bp long DNA molecule. The DNA detection was done in collaboration with Dr Attila Bonyár, and the results can be found in the attached collaborative article (section B).

This section describes the final fabrication step and summarizes the whole development of the LSPR sensor and its fabrication. Four substrate materials (PDMS, PMMA, epoxy, and SiO_2) are compared regarding the sensor's bulk RI sensitivity and durability. The comparison is predominantly shown on the AuNP layer formed over 40 V templates by 1st cycle dewetting with a diameter of 65 nm (if not mentioned otherwise).

5.5.1 Reactive ion etching (RIE)

Reactive ion etching (RIE) was performed in a PlasmaPro 80 RIE chamber (Oxford Instruments Plasma Technology), which uses capacitively coupled plasma (CCP).[317]

The process chamber is schematically illustrated in Figure 5.31. The plasma can be tuned by process parameters such as chamber pressure, gas composition (e.g., Ar, O_2, SF_6, CHF_3), gas flow, source power, and process time. In CCP, the ion energy can reach several hundred eV, but a stable plasma can be maintained only at pressures between 2.5 and 40 Pa. The resulting plasma density is lower than inductively coupled plasma (ICP), between 109 to 1010 electron/cm^3. However, increasing the power increases not only the plasma density but also the self-bias voltage and thus the ion energy.

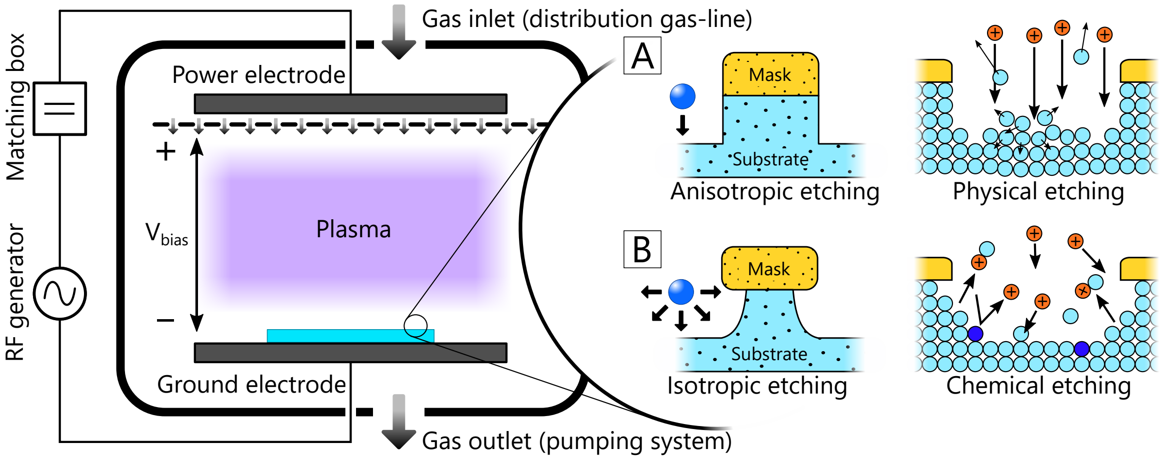

Figure 5.31: Schematic of the CCP chamber configuration. Inset images illustrate the categorization of etching processes by etching orientation and character of material removal.

Removal of the substrate material is performed by two fundamental principles (illustrated in the inset of Figure 5.31):

1. Physical etching is characterized by a transfer of momentum from an incident species to the atoms of the substrate that can eventually escape the surface. The etching occurs only in the ion flux direction that is perpendicular to the sample surface (electrode surface). Therefore, this process is highly anisotropic.[318]
2. Chemical etching usually occurs when surface atoms react with reactive radicals from the plasma (O^*, F^*, $SF_5{}^*$).[319] For this, products of reactions have to be volatile (surface temperature and plasma pressure) to desorb from the surface. Plasma chemical etching is very similar to wet etching, resulting in isotropic etching.

Whether physical or chemical etching is primarily predominant depends on the plasma composition. For example, to achieve pure physical etching, only an argon atmosphere can be used. However, chemical etching will be still accompanied by partial physical etching, while the source power and plasma pressure can control their contribution. In general, increasing the source power produces a more dissociated plasma with a higher density and ion flux. Simultaneously, it increases the ion energy, which favours process anisotropy but decreases the selectivity between the mask and the substrate layer. Changing the pressure impacts the electron temperature and neutral density, but it is not straightforward since it also influences dissociation and plasma density.[318] In the majority of cases, the increase of pressure favours isotropic (chemical) etching.

5.5.2 RIE calibration and process parameters

RIE etching was first performed over flat PDMS samples to estimate the etching rate. For this purpose, samples of spin-coated PDMS over a silicon wafer were prepared since the typically cast PDMS surface is too rough for precise profilometric measurements. The samples were prepared by pouring the degassed PDMS prepolymer (curing agent with PDMS base, wt:wt = 1:10) over a 4-inch silicon wafer to cover the whole top side. In a spin-coater, the speed of 500 RPM was applied for the first 10 s, and then it was increased to 2000 RPM for 26.5 µm thick PDMS layers (4000 RPM for 13 µm). Note that a thin layer down to ≈ 2 µm can be prepared by adjusting the spin-coating speed or the viscosity of PDMS (through diluting PDMS prepolymer with hexane).[320]

PDMS was then cured on a hot plate for 20 min at 130 °C. Afterwards, a metal mask with structure (dimensions of ≈ 0.5 mm) was applied over the surface. The experiments showed that slim strips of Kapton tape are sufficient for this purpose and can be used with less effort compared to a metallic mask fabrication that also includes metal deposition, resist lithography, and wet etching of the metal layers. However, the surface has to be cleaned with acetone or IPA to remove glue residues from the Kapton tape and be thoroughly dried to avoid PDMS swelling.[321]

The process of fabrication and estimation of the etching rate is illustrated in Figure 5.32:A. The process parameters (tabulated in Table 5.7) were experimentally tuned according to ref. [320, 322–324] to achieve reasonable control, short etching time, and good selectivity. The etch rate was estimated to be 1.23 nm s^{-1} (plotted in Figure 5.32) with preferentially isotropic etching. Plasma etching with CHF_3 and O_2 of various concentrations (from 1:1 to 5:1), plasma pressure (50–100 mTorr / 6.7–13 Pa) or power (100–300 W) gives inconclusive results mostly leading to the opposite process—depositing a thin polymeric film over the substrate.

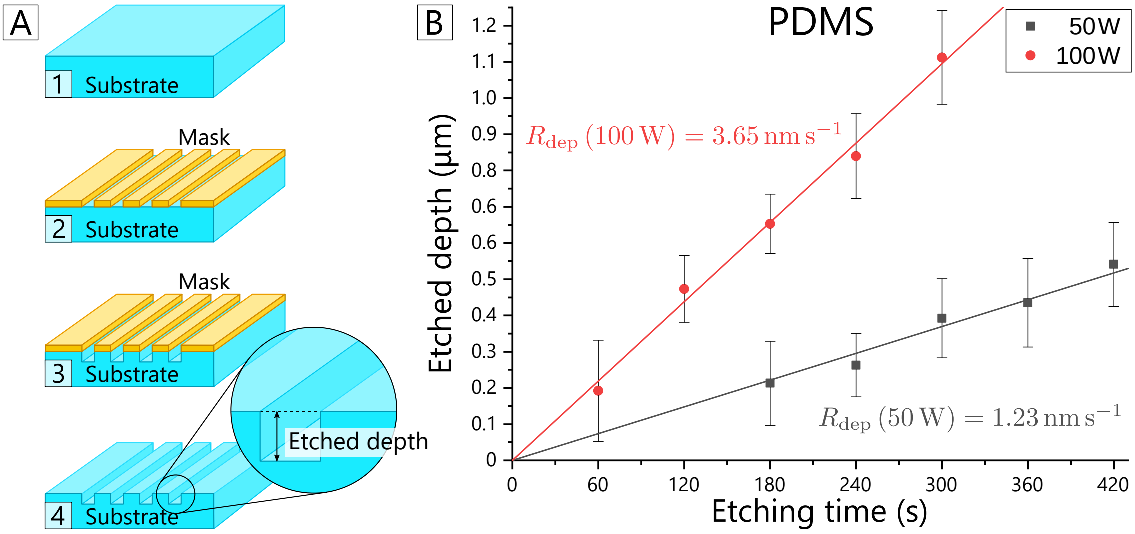

Figure 5.32: Etching rate estimation for a PDMS substrate in RIE with process parameters from Table 5.7. (A) Illustrates the method where a patterned mask (1–2) is applied over the substrate (PDMS), and the substrate is etched through it (3). In the end, the mask is removed, and a profilometer measures etched steps to estimate the depth of the etched material (4). (B) Graph of plotted values for various times representing etching rates (R_{etch}) for source power of 50 and 100 W.

Table 5.7: RIE process parameters for substrate etching of AuNP layers on PDMS, PMMA, epoxy, SiO_2 performed in PlasmaPro 80 RIE chamber (Oxford Instruments Plasma Technology).

Material	Power [W]	Pressure [Pa]	Gas composition	Gas flow [sccm]	DC bias* [V]	Etch rate [$\mathrm{nm\,s^{-1}}$]
PDMS	50	6.7	$SF_6 : O_2$ (5 : 1)	60	60–70	1.23
PMMA	50	5.3	O_2	20	250	3†
Epoxy	50	6.7	O_2	50	360	1.6‡
SiO_2	100	4.0	Ar : $CHF_3 : O_2$ (6 : 3 : 1)	50	400	N.A.‡†

* Not an independent variables.

† According to ref. [325].

‡ Estimate from AFM measurements of etched AuNPs-epoxy composite.

‡† Anisotropic etching.

5.5.3 RIE of the substrate through AuNP layers

Conveniently, the etching progress of all substrates over the AuNP layer can be observed by a visible change of the sample colour. In general, the embedded AuNP layers have strong absorbance peak maxima around 600 nm, which gives them a bluish look in transmitted white light. This effect is illustrated in Figure 5.33, showing the absorption spectra of various etched epoxy samples. With the removal of the surrounding material, the effective bulk RI of the AuNP medium decreases, resulting in a blue shift of AuNP plasmonic resonance with the corresponding change of the sample colour from blue through purple to pink (insets of Figure 5.33).

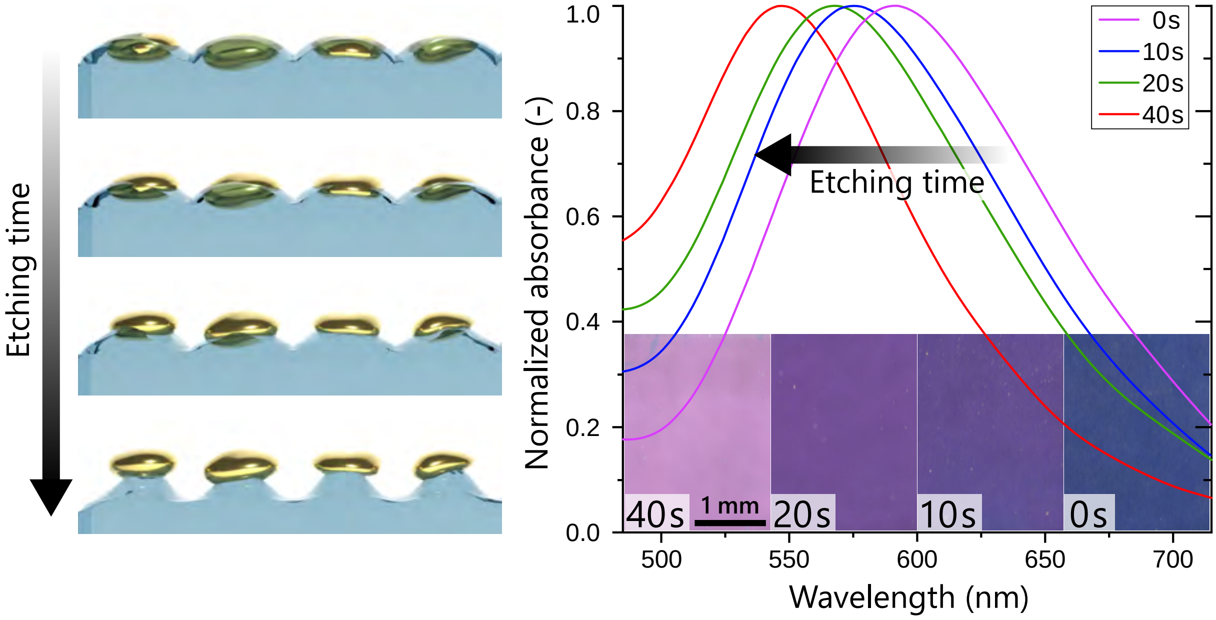

Figure 5.33: 3D illustration and effect of selective substrate etching and normalized absorption spectra of AuNP layers on the epoxy substrate after the different number of repetitions of selective epoxy etching with O_2 plasma measured in air with the inset containing optical microscopy images (transmission) of corresponding samples.

This fundamental principle of SPR sensing elements can also be used to monitor sample sensitivity by simple colour change observation by immersing part of the sample into a liquid (Figure 5.34). With RI of liquid higher than air and close to the substrate, the colour change reverses back to a bluish one.

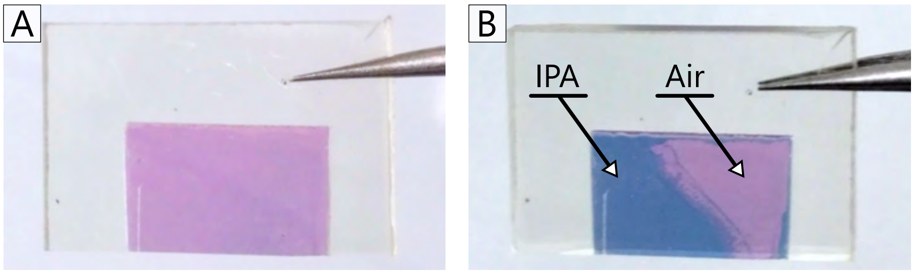

Figure 5.34: Photographs of AuNP layer on SiO_2 substrate (A) after 2 min of RIE and (B) its change of colour caused by IPA droplet.

This behaviour was used as a method for the detection of the so-called substrate overetching. This behaviour was used as a method for the estimation of the time limits for the etching process. The strong isotropic nature of polymers' etching (SiO_2 etching is predominantly anisotropic) leads to a significant underetching that can be described as the removal of the supporting substrate below AuNPs. Weakening those pillars (underetching) leads to poor AuNP adhesion that may even manifest in AuNP peeling off and flushing away in a liquid solution—overetching. When the overetched layer is introduced to a liquid solution, a substantial colour change may be observed. However, it will not return to the initial colour after drying. This behaviour usually corresponds to the washing of AuNPs from their initial positions and their agglomeration into clusters due to poor adhesion, shown in Figure 5.35. This process is irreversible, resulting in a rapid performance drop and sample degradation. Despite this fact, the isotropic nature of the RIE is not a significant hindrance because deep etching is not the primary goal. On top of that, a controlled underetching can even enlarge the accessible AuNP surface.

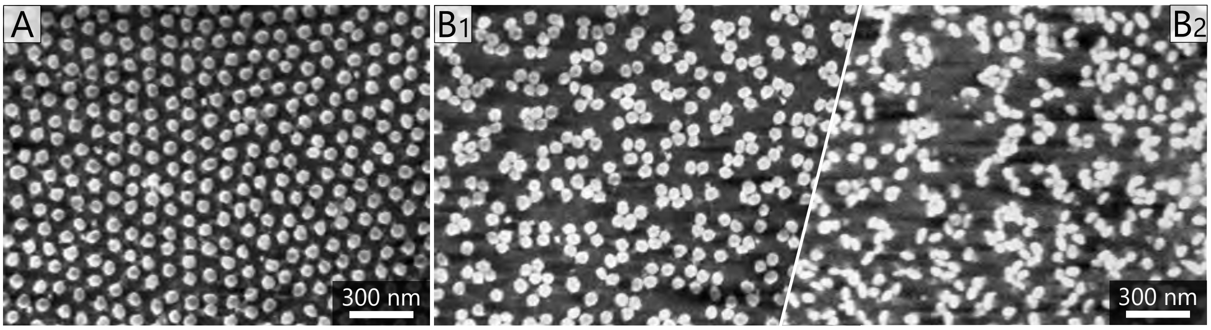

Figure 5.35: SEM images of AuNPs on an overetched epoxy substrate (A) before and (B1) after being introduced to a solution (IPA).

PDMS etching over AuNP layers (Table 5.7) gives good results already after several tens of seconds. The overetching time was estimated to be around 100 seconds. Etching between 40–80 s produces a sensitivity of up to 40 nm RIU^{-1}. However, it was found that this sensitivity drops rapidly to zero in 14 days. Compared to other substrates (epoxy, SiO_2), this sensitivity decrease was associated with both natural carbon contamination [326] and contamination by PDMS. The reason for this may be a migration of free oligomers contained within PDMS from the bulk to the surface where they coat AuNPs. The effect of oligomer migration outside the bulk PDMS was also reported in imprint lithography [327] and microfluidics [328].

The sole carbon contamination and related hydrophobic behaviour of PDMS were disproved by the impossibility to restore the sensitivity of aged samples by O_2 plasma. On the other hand, regeneration of aged samples was only possible with more aggressive etchants performed by additional RIE (SF_6 and O_2). This presents a great obstruction for further implementation since RIE is not a common nor a standard cleaning procedure for sensor surfaces.

PMMA etching was performed directly on AuNP layers with process parameters (in Table 5.7) adapted from ref. [325]. During the first trial to etch PMMA, no colour change was observed even when etching was over 10 min (in steps). Despite additional etching for 4 min at an increased power of 100 W (360 V), the sample did not indicate any PMMA etching—no colour changes due to etching or bulk RI testing. Samples after 20 s of etching and all etchings are shown in Figure 5.36:B1 and B2, respectively. After an additional 6 min of standard etching, a change was observed to the sensitivity of 75 nm RIU^{-1} (shown in Figure 5.36:C).

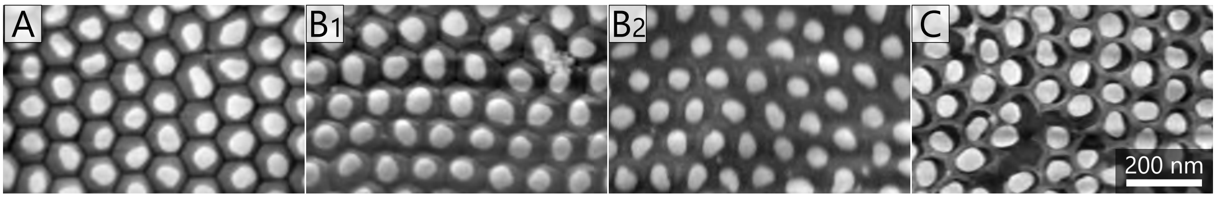

Figure 5.36: AuNPs/PMMA surface SEM image (A) before etching, (B1) after 20 seconds of RIE, (B2) after additional 14 minutes of RIE, and (C) after additional 6 minutes of RIE.

Compared to PDMS, the PMMA etching through the AuNP layer does not correlate with the bulk etching rate of PMMA (3 nm s^{-1}). It is assumed that PMMA etching still occurs during the process; however, AuNPs are sinking into the substrate at the same time. PMMA is a thermoplastic polymer with a relatively low glass transmission temperature of 105 °C. This temperature can be locally reached due to the dielectric heating of AuNPs, caused by microwave irradiation during the etching process. However, this theory based on previous observations was not confirmed in any other way.

Epoxy etching was performed similarly to PMMA etching (process parameters are tabulated in Table 5.7). The overetching time was estimated to be approximately 60 s. Different etch time was selected to investigate the effect of etching in detail by the SEM (Figure 5.37), STEM (Figure 5.38), AFM (Figure 5.39), and XPS (spectra shown in Figure 5.40 and estimated surface atomic concentrations in Table 5.8).

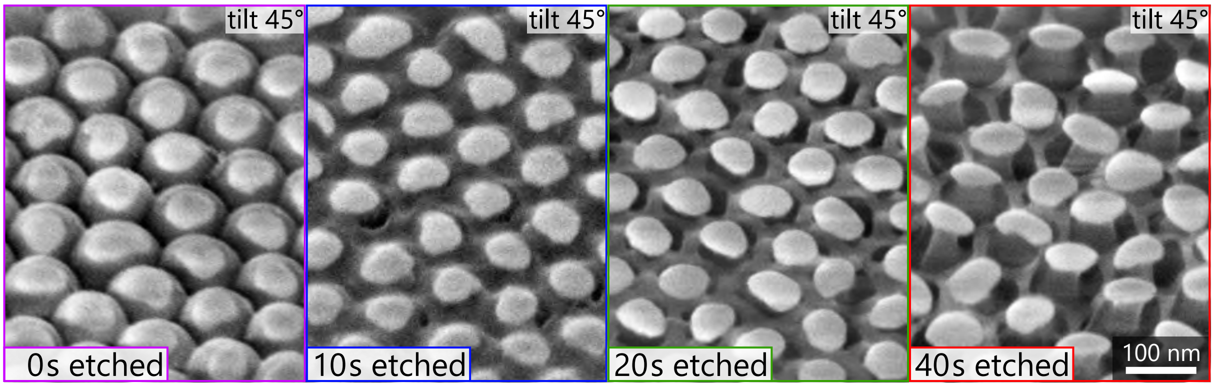

Figure 5.37: SEM images of AuNP layers on epoxy substrate etched for different times in O_2 plasma.

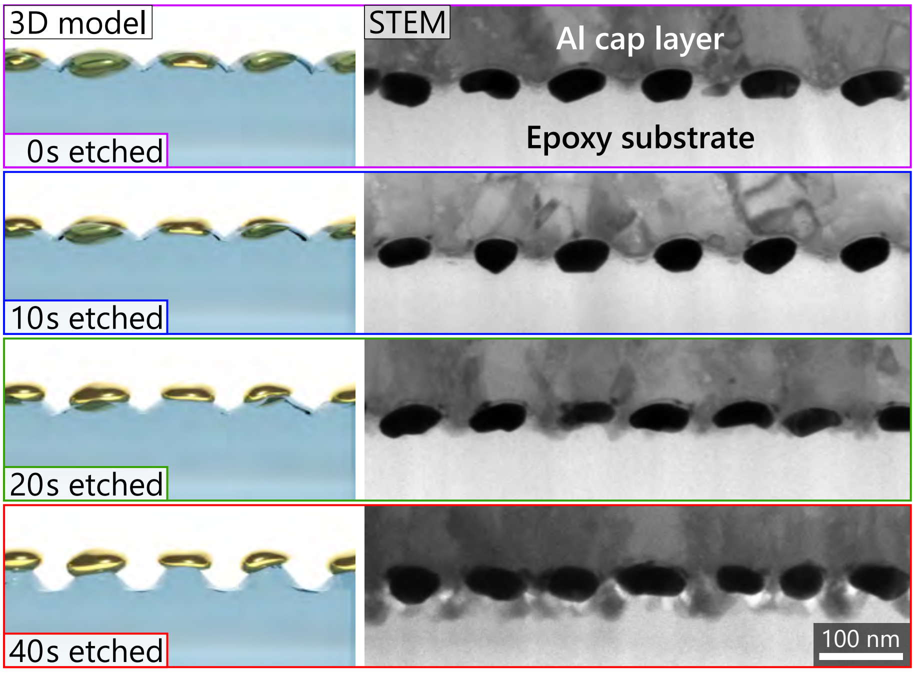

Figure 5.38: STEM images with 3D schematics of lamellas prepared from samples presented in Figure 5.37.

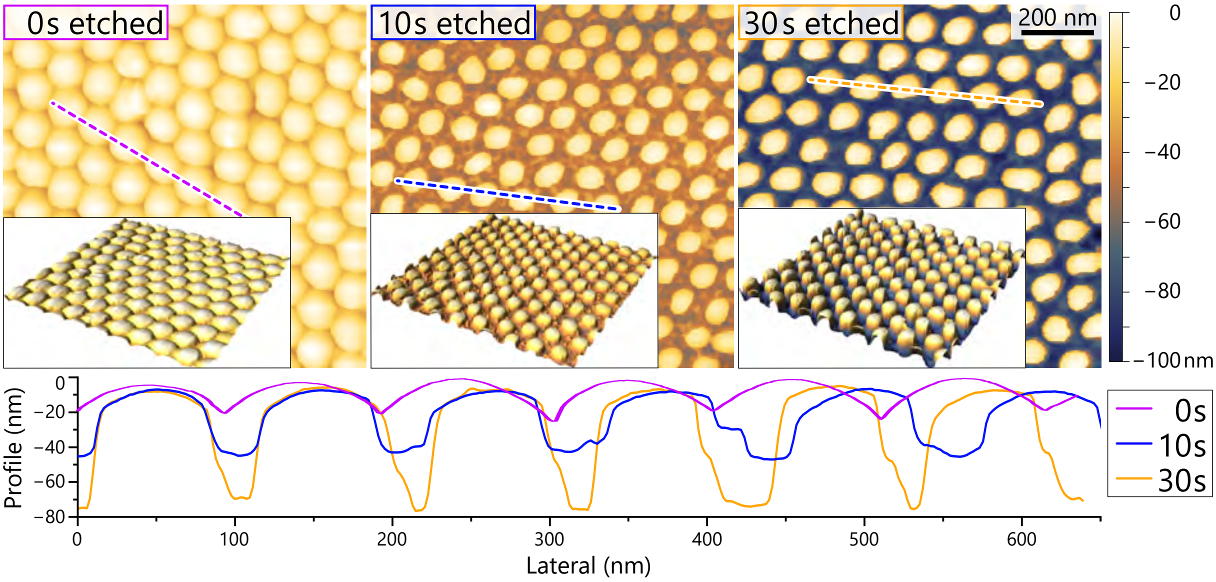

Figure 5.39: Topographical images (AFM) with 3D view insets of AuNP layer etched for (A) 0, (B) 10, and (C) 30 seconds. The graph shows extracted profiles marked by dashed lines. The average height of protruding AuNPs is 16, 33, and 68 nm for 0, 10, and 30 s etched time, respectively.

The sample without any etching shows a recognizable epoxy array of spherical caps with embedded AuNPs (SEM). Embedding is better visualized by STEM cross-sections, while AFM images and profiles give better insight into the topography. As can be noted,

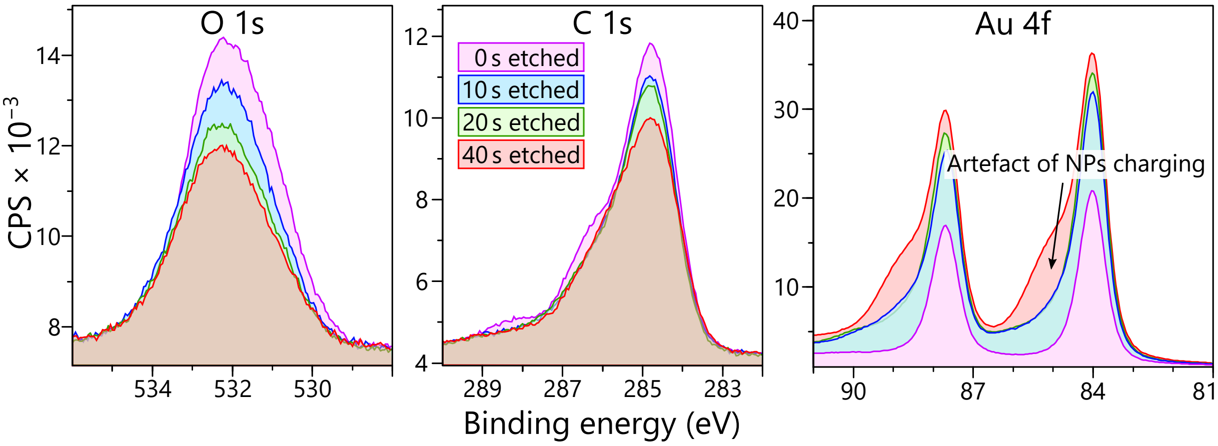

Figure 5.40: Narrow XPS spectra of O 1s, C 1s, and Au 4f peaks measured for differently etched samples (shown in Figure 5.37 and Figure 5.38) at the take-off angle $\theta = 90°$.

Table 5.8: Relative surface atomic concentrations of nanocomposites after different times of selective epoxy etching with O_2 plasma (Figure 5.37 and Figure 5.38) estimated from the narrow XPS spectra shown in Figure 5.40.

Etching time [s]	Surface atomic concentration [%]		
	O	C	Au
0	25.4	66.7	7.9
10	25.9	60.4	13.7
20	23.4	61.4	15.2
40	20.9	62.8	16.3

the height of spherical caps is about 16 nm, which is smaller when compared to the corresponding Al template with a protrusion height of 22 nm. This topological effect is a standard AFM artefact caused by the probe shape (tip radius of 2–12 nm with a tip angle of 40 °C), which cannot perfectly trace over narrow and deep surface features.

After the first 10 s of etching, the substrate is primarily removed from the top sides and periphery of AuNPs. It can be seen on AFM images where the hemispherical topography is lost, revealing protruded AuNPs. The height of the protruding parts is 33 nm, and in this case, approximately the same as the AuNPs height (30.7 ± 3.8 nm). With additional etching, the substrate removal is going into more depth with simultaneous undereching of AuNPs. This process forms the characteristic mushroom-like structure with AuNP on top of a conical epoxy pillar (SEM/STEM: 40 s). The height of the structures for the 30 s etched sample (AFM), and similarly, the 30 s etched sample (STEM) is approximately twice as big as the AuNP thickness. The etching rate can be roughly estimated from AFM measurement to 1.6 nm s^{-1}.

Additionally, narrow XPS spectra (Figure 5.40) were obtained to compare the relative surface element concentrations of samples etched for different times (Table 5.8). After the first (10 s) etching, the gold (Au) concentration significantly increased at the expense of the carbon (C) concentration. This increase is contributed to the removal of the top layer of hydrocarbon contamination and the covering epoxy substrate. The oxygen (O) concentration decreased with further etching, whereas Au and C concentrations slightly grew. While the Au concentration increase follows the complementary results and the idea of AuNPs revealing, the Au concentration (maxima of 16 %) is twice as lower as the expectation from the total projected area of AuNPs (32 %) estimated from SEM measurements. The low surface concentration of Au can be caused by high AuNPs affinity to carbon contamination that forms a thin layer over the Au surface in ambient conditions. Due to the high surface sensitivity of XPS, this layer can very effectively blocks the signal (photoelectrons) from AuNPs.

On the other hand, carbon and oxygen development with increasing etching rate is still not fully understood. In general, O_2 plasma treatment of polymers should lead to oxidation and an increase of O content on the surface.[329] However, reports are showing a decrease in O content by extensive (> 3 minutes) plasma treatment [330] or by exposure to the ambient atmosphere after plasma treatment [331]. Additionally, the morphology of the sample can also play the role or even the degradation of epoxy due to X-ray irradiation. Therefore, the character of these results is primarily for illustrative comparison.

Parallel optical spectrophotometry measurements were done on the same samples. The normalized absorbance spectra (Figure 5.33) confirmed the successful removal of the surrounding epoxy. The absorbance peak maxima measured in the air decreased from the initial 590 nm to 575, 567.5, and 547 nm after 10, 20, and 40 s etchings, respectively. The changes in the colour of the samples upon etching are visible to the naked eye as well (inset of Figure 5.33). As shown in Figure 5.41:B, this change goes hand in hand with the increase of bulk RI sensitivity, from the initial 15 nm $\mathrm{RIU^{-1}}$ to around 80 nm $\mathrm{RIU^{-1}}$, for this particular type of AuNP layer (diameter 65 nm, pitch 105 nm).

The adhesion of AuNPs to the epoxy substrate was also tested by a simple scotch tape test. In contrast to the previous scotch test (Figure 5.28), a standardized tape (8705B, TQC Sheen) for EN ISO 2409: 2003 adhesion tests were used. As shown in the example in Figure 5.42, the tests resulted in no visible transfer of AuNPs for the 40 s etched samples. The same results were also achieved for shorter etching times.

Figure 5.43 shows the selected absorbance spectra of epoxy samples measured in air and water that give the best sensitivity. All samples were etched for the same time of 30 s, which always resulted in stable samples, with reproducible spectra and reversible changes after multiple steps of washing and drying. As shown, the sensitivity of ≈ 100 nm $\mathrm{RIU^{-1}}$ can be easily achieved, while more tailored optimization for different AuNP arrangements may deliver even better performance.

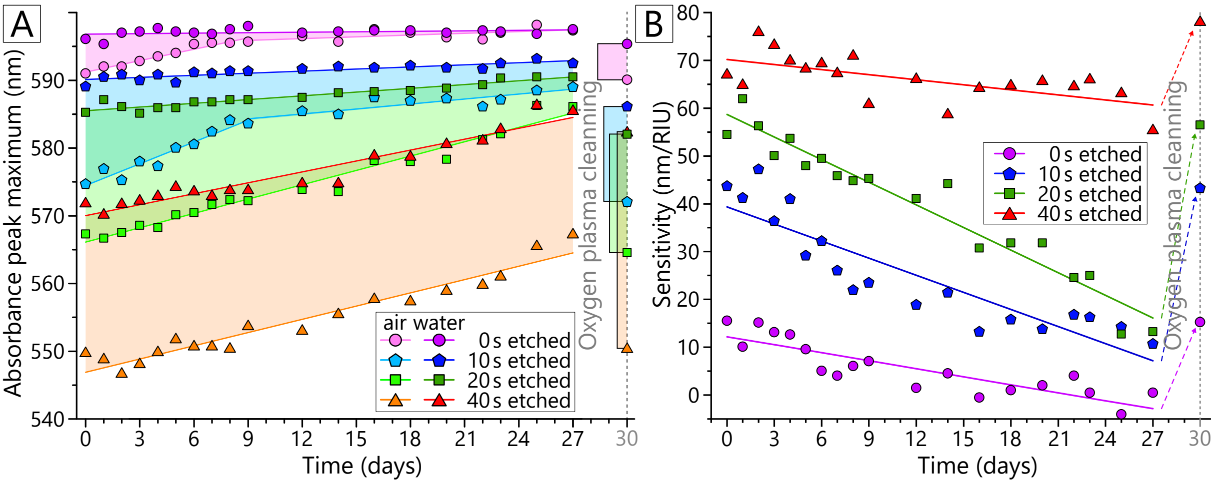

Figure 5.41: (A) Position of the LSPR absorbance peak maxima of the etched nanocomposite samples (Figure 5.37) measured in air ($n = 1$) and water ($n = 1.33$). (B) Calculated bulk RI sensitivities of the same samples. The values on the right side of the graph represent the condition of the samples after cleaning them with low-power O_2 plasma after 30 days. Plasma cleaning was performed in a low-pressure plasma chamber (Tetra 30, Diener) at the pressure of 40 Pa and power of 20 W in an oxygen atmosphere for 15 s.

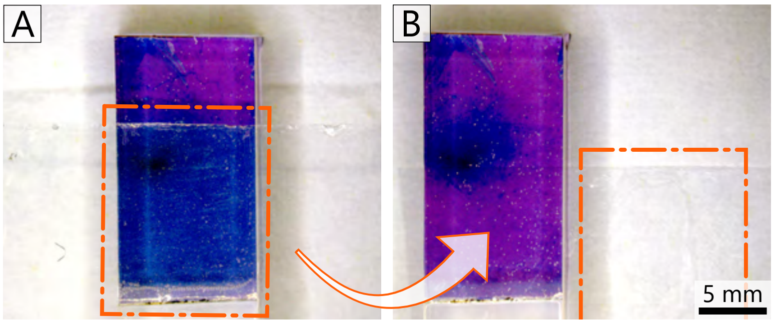

Figure 5.42: Scotch tape adhesion test performed over a sample etched for 40 s (SEM showed in Figure 5.37, XPS in Figure 5.40). (A) Photograph of tape attached to the sample shows a good contact of AuNPs with the glue of the tape, given by visible colour change. (B) Photograph of the sample and the tape after peel-off shows no visible transfer between the sample and the tape (area of contact is marked by an orange square). The coloured spot on the left side of the sample originates from epoxy degradation caused by X-ray irradiation during XPS analysis.

SiO_2 substrate for AuNPs and its application is included in this work as a proof of concept. The possibility to clean samples by oxygen plasma to any extent without damaging the structures right before or even after selective SiO_2 etching is an excellent advantage of this configuration.

The samples were cleaned before selective etching by oxygen plasma for 1 min at 100 W, 13.3 Pa, 20 sccm (O_2) in the same chamber. This cleaning reduces the uncertainty of etching introduced by surface contamination. A standard procedure for SiO_2 etching

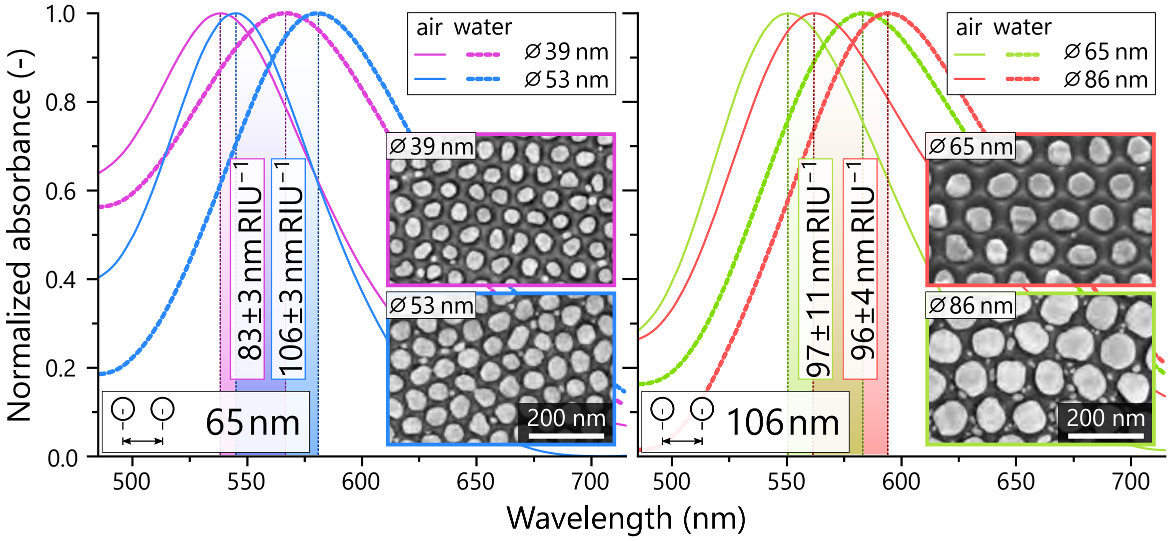

Figure 5.43: Normalized absorbance spectra of the epoxy-based sample after 30 s selective etching measured in air and water with SEM images of corresponding AuNPs arrangement. Spectra measured by Dr Attila Bonyár.

was modified by adding O_2 and reducing the etching rate (Table 5.7). This recipe resulted in preferentially isotropic etching of the structures, as shown in Figure 5.44.

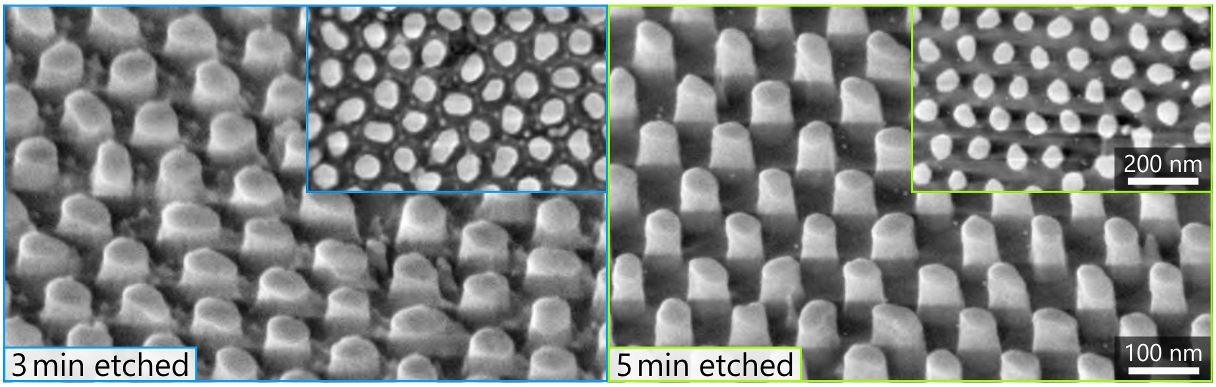

Figure 5.44: SEM images of AuNPs on SiO_2 layer etched for different times.

The reason for this is the use of fluorocarbon (CHF_3) that leads to the deposition of a thin (few nanometres) fluorocarbon layer, which passivates the substrate.[332] However, with sufficient physical etching (Ar ions and potential bias), this layer can be eroded, and further chemical etching may be performed. Since physical etching is the primary driving mechanism, this process is primarily isotropic. The introduction of O_2 helps reduce additional carbon contamination.

The etched samples show great sensitivity (Figure 5.45:C), almost 100 % higher than an epoxy substrate using the same AuNP arrangement. Moreover, the stability of the samples was exceptional without any signs of wear due to NP washing. In contrast to previous substrates, the samples were more discoloured and bluish in the transmission view (Figure 5.45:A). In the reflection, all etched substrates have a greenish metallic look (Figure 5.45:B).

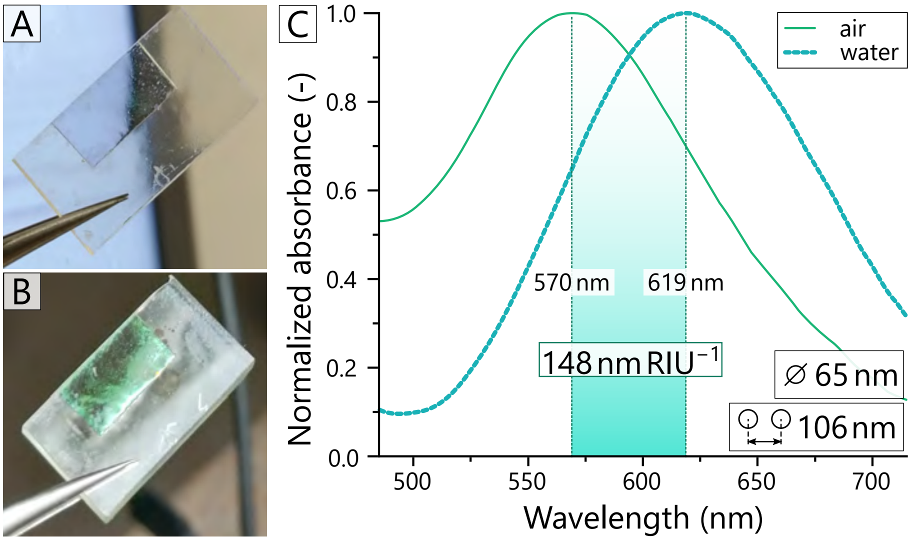

Figure 5.45: Photos of 5 min etched AuNPs on a SiO_2 sample (from Figure 5.44) in the (A) transmission and (B) reflection view with (C) normalized absorption spectra of a 3 min etched sample (from Figure 5.44) measured in air and water.

5.5.4 Chemical analysis

Chemical analysis was performed by XPS (detaily discussed in section A.4) to understand better the impact of various fabrication steps and decrease sample sensitivity regarding various contaminations. Even though XPS is, in general, a non-destructive method,X-ray irradiation (Al Kα, 1486.7 eV) can modify the structure of polymers or even lead to changes in their chemical composition. These changes can be easily observed macroscopically. In the case of epoxy, it is associated with the so-called yellowing [333, 334] shown in Figure 5.46:B, while in the case of PDMS, it can be observed as the hardening of the top layer shown in Figure 5.46:A1–2. Thanks to the present AuNP layer, this change can also be detected as a blue shift of colour. This glassing of the PDMS top layer was observed for the UV/ozone modification leading to a breaking of $Si-CH_3$ bonds, chain scissions (indicated by a decrease of $\equiv Si=O-Si\equiv$ signal) and creation of new $-OH$ bonds. These can be summarized as a decrease of C at the expense of O and Si increase.[335–337] Vacuum modification by UV was reported [338], concluding that even in the absence of oxygen, the breaking of methyl groups still occurs, followed by the formation of $Si-H$ bonds. However, the O/Si ratio increased only by 0.14 compared to 1.18 for UV irradiation in an O_2 atmosphere.

The character of the modification by X-ray irradiation of XPS can be guessed from these reports studying the impact of UV irradiation. Nevertheless, the full scope of the

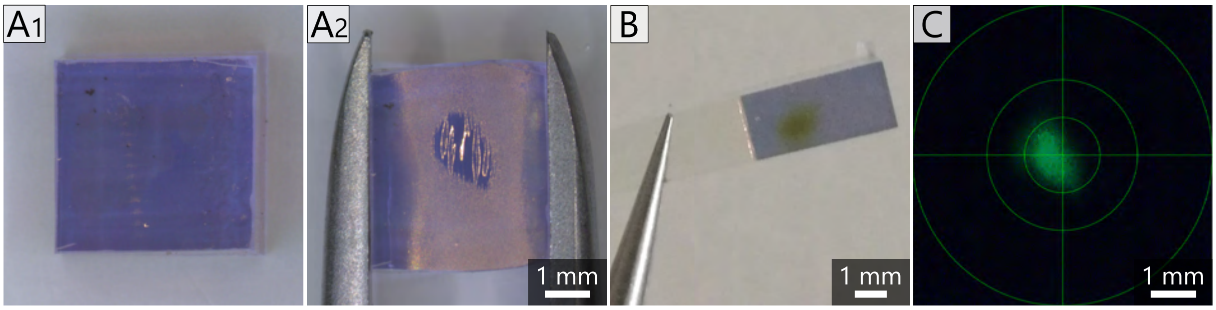

Figure 5.46: Optical images of the XPS analysed spot on (A1–2) PDMS sample, (B) epoxy sample and (C) on fluorescence sample during analysis. To observe the spot size on (A1) the PDMS sample, it was (A2) pressed by tweezers revealing the hardened region of the analysed area.

impact is unknown, and thus the following results are primarily illustrative. Further conclusions consider this, but the chemical compounds in PDMS and epoxy are not evaluated in detail. Therefore, this section is focused mainly on explaining the presence of individual elements and their origin and their possible impact on the sensitivity of AuNP layers.

Figure 5.47 shows a comparison of XPS wide spectra of similar AuNP layers on mildly etched PDMS, epoxy and SiO_2 substrates. Even though the sensitivity of those samples is relatively low, they are perfect examples to illustrate various contaminations. Elements found in the spectra may be divided into material elements, process, and natural contaminants based on their source. Some of the process contaminants (Al, Cu, Na, Cr) can be reduced to a minimum by longer etching steps, such as removing Al/Al_2O_3 or Cu in NaOH or $FeCl_3$ solution, respectively. Complete removal of Al oxide is a prerequisite for controllable substrate etching. Traces of Na and Cr can be avoided by more thorough cleaning (ultra-sonification) in distilled water between fabrication steps.

Fluoride presence can be found in all samples. It originates from RIE process gases for PDMS and SiO_2. RIE of the epoxy does not use fluorine-based gasses; therefore, the origin of fluorine is most probably in the chamber walls, which are sputtered during RIE. The XPS spectra (Figure 5.47 and inset of narrow spectra) conclude that the presence of F presumably does not originate from the fluorocarbon layer, which is most relevant for SiO_2 samples. The narrow spectra do not contain any high fluorinated carbon groups, which can be found in the region from 290 to 294 eV.[339] The presence of the $-\mathrm{CHF}-$ groups in the C 1s spectra is questionable since their peaks (288 and 288.4 eV)[340] can overlap with the ester or carbonic acid ($-\mathrm{O}-\mathrm{C}{=}\mathrm{O}$) groups; however, this would also cause the shift of F 1s to 689.3 eV that is not observed (686.7 eV). Fluorine contamination can also be successfully removed by oxygen plasma (applicable only for SiO_2). Na, Ca, K, Zn traces are usually not present or only in insignificant amounts. They most likely originate from improper handling or storing conditions.

The most critical contaminations are silicone (e.g., 8.3 % in the epoxy sample) and carbon (e.g., 23 % in the SiO_2 sample). Even though silicone is one of the natural contam-

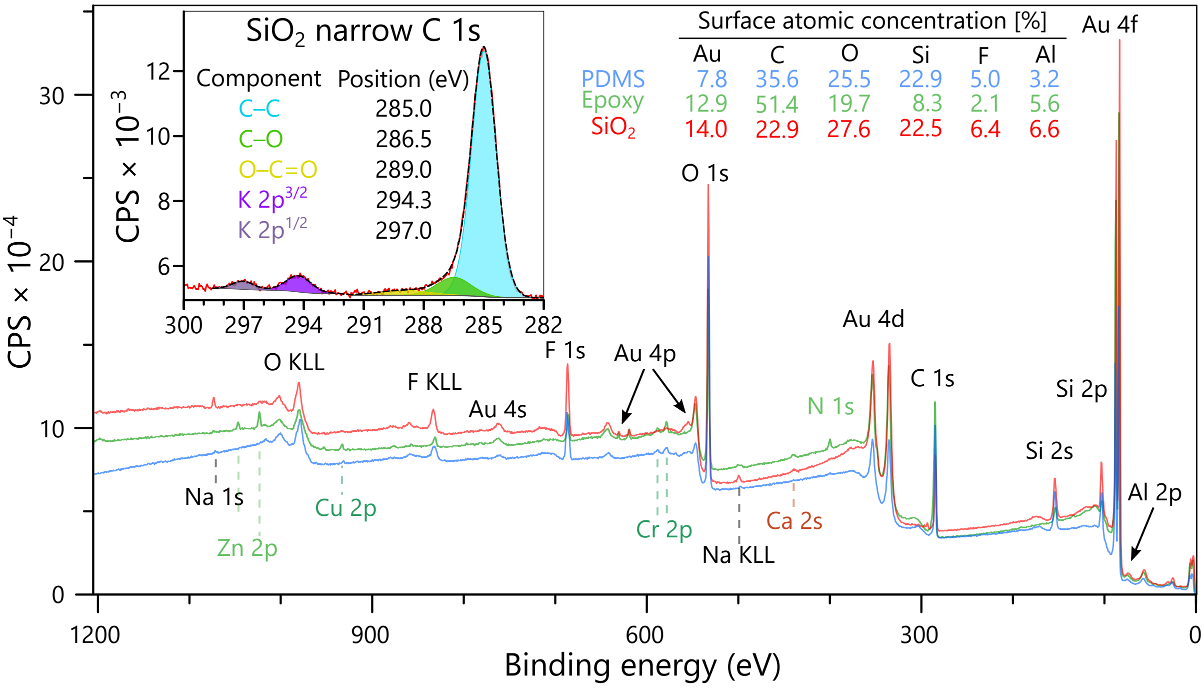

Component	Position (eV)
C–C	285.0
C–O	286.5
O–C=O	289.0
K 2p$^{3/2}$	294.3
K 2p$^{1/2}$	297.0

Surface atomic concentration [%]

	Au	C	O	Si	F	Al
PDMS	7.8	35.6	25.5	22.9	5.0	3.2
Epoxy	12.9	51.4	19.7	8.3	2.1	5.6
SiO$_2$	14.0	22.9	27.6	22.5	6.4	6.6

Figure 5.47: XPS wide spectra of AuNPs on PDMS (20 s etched), epoxy (10 s etched) and SiO$_2$ (1 min etched). The inset figure shows a narrow C 1s spectrum of SiO$_2$ sample with fitter components, and the inset table presents atomic concentration calculated from Au 4f, C 1s, O 1s, Si 2s, F 1s, and Al 2p peaks using Shirley background.

inants, experiments showed that the primary source of the silicone contamination comes from standardly used tapes (Kapton, copper) for the sample fixation, which uses silicone silicone (PDMS) based adhesive. To make a general picture of the diffusion rate, a test sample was measured for a few days. The sample consists of a thin Au layer deposited on a polished Corundum slide on which a piece of Kapton tape was stuck. 0.3 % and 1.0 % concentration increase of silicone and carbon per day was observed on the Au layer (distance 10 mm from the Kapton tape). This diffusion rate depends on the substrate material and is most probably governed by the concentration gradient of those elements since the increase in silicone was observed only on the epoxy samples, while it was stable or even decreased for PDMS and SiO$_2$ samples (Figure 5.48). Likewise, the carbon content increased only for PDMS and SiO$_2$ samples, while it has a decreasing trend for the epoxy substrate. A similar effect was observed with other materials.

An attempt to correlate the long-term XPS data with sensitivity decrease was made by measuring identical samples (same as in Figure 5.47). However, these results are mostly just illustrative since they suffer from the issues above: an unknown impact of the X-rays induced material degradation, silicone and carbon diffusion from Kapton tapes. Moreover, the storage conditions vary between batches measured by XPS (Figure 5.48) and optical spectrophotometry (Figure 5.49).

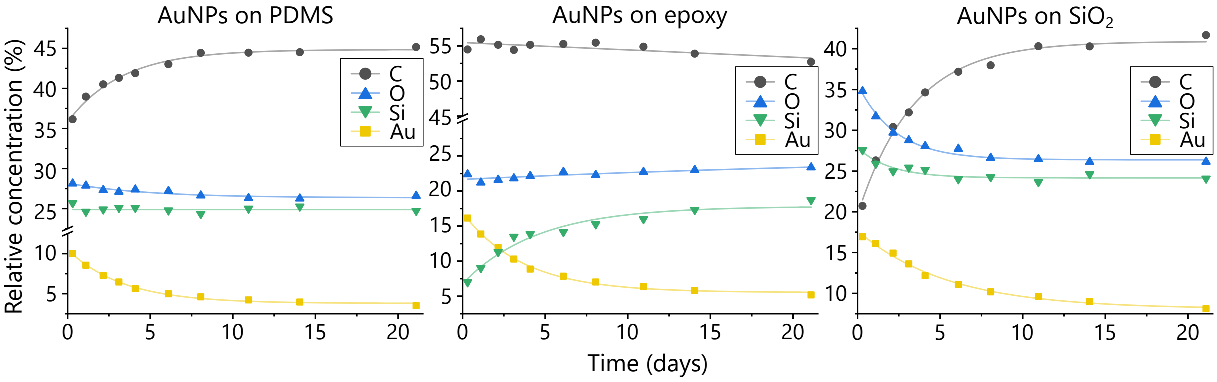

Figure 5.48: Long-term development of surface relative concentrations of AuNPs on various substrates (sample are same as in Figure 5.47). Concentrations were estimated from narrow XPS spectra of Au 4f, C 1s, O 1s and Si 2s peaks using Shirley background. Samples were kept in a vacuum with a Kapton tape (the source of Si and C contamination) for most of the period.

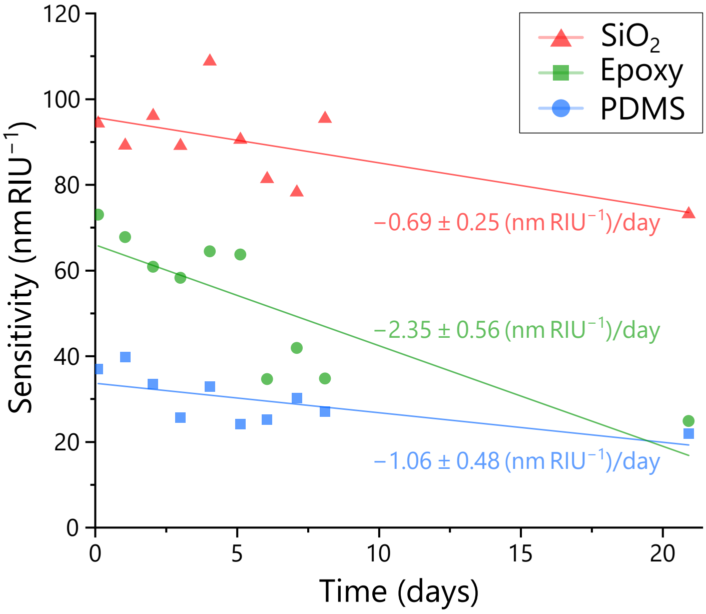

Figure 5.49: Sensitivity development for AuNPs on PDMS, epoxy and SiO_2 substrates. The same samples from Figure 5.47 were used, but they were stored in normal office conditions between measurements.

5.5.5 Conclusions

This section presents selective substrate etchings by RIE to enhance the performance of transferred AuNP layers. RIE represents the final step of the LSPR sensor fabrication. The main technological issues and solutions will be pointed out in this conclusion, while work achievements will be discussed later in the conclusions and future directions (chapter 6).

Working LSPR elements were prepared on PDMS, PMMA, epoxy, and SiO_2 substrates with the maximum reached sensitivities of 40, 75, 106, and 148 $\mathrm{nm\,RIU^{-1}}$, respectively. These sensitivities were achieved with non-optimized AuNP layers, and therefore these results are primarily used to illustrate the effects of the substrate.

Even though PDMS has the most excellent material properties (optical, mechanical, chemical), it was found that AuNP layers on PDMS suffer from 'sturdy' contamination in the long term. What is more, compared to a typical (hydrocarbon) contamination, this one cannot be cleaned by simple means (e.g., O_2 plasma). Unfortunately, this dramatically limits the potential applications of such layers. However, the investigation of PDMS behaviour is still ongoing to utilize it as the substrate in the future. It is therefore necessary to understand the oligomer migration and PDMS aging better to minimize or completely block subsequent AuNP contamination. Efforts were made to better understand the character of the contamination, especially for PDMS samples. A key finding shows that Kapton tapes were one of the main silicon contamination sources. Additionally, the experiments also showed that X-ray irradiation degrades the polymers, compromising the XPS results. These issues will be tackled in our future work by avoiding Kapton tapes and analysing different spots to minimize the induced degradation.

The PMMA does not contain any silicone groups in comparison to PDMS. Therefore, the PDMS contamination issue can be easily avoided. This work demonstrates a successful fabrication of an LSPR element on a PMMA. However, the repeatability of the RIE of the PMMA substrate over an AuNP layer gave an unsatisfactory result. Even though this behaviour was not studied in detail, it is believed that the reason is the low thermal stability of the PMMA that is locally compromised by heating AuNPs during RIE. Additionally, applications are limited by the weak chemical stability of the PMMA against many organic solvents.

With improved thermal stability than the PMMA, the epoxy resin gives stable and reproducible results of the RIE. Furthermore, it was possible to show an increasing RI bulk sensitivity due to the substrate removal. The successful removal of the substrate was illustrated by SEM, STEM, and AFM analyses. Even though the RI bulk sensitivity drops in a long-term period due to natural surface contamination, it can be simply recovered by O_2 plasma cleaning. However, a notable drawback of the epoxy substrate is its vulnerability to O_2 plasma. It limits the reusability of LSPR sensors since an O_2 plasma cleaning is standardly used, e.g., before nanoparticle hybridization. Therefore, extensive cleaning may lead to irreversible damage of the supporting substrate pillars under AuNPs that leads to their detachment.

The last studied material was SiO_2 introduced by a PVD deposition over an AuNP layer right before the epoxy casting. LSPR sensor elements prepared this way showed exceptional stability during an O_2 plasma cleaning without any sign of wear. An increase of the RI bulk sensitivity of almost 100 % was observed compared to the pure epoxy substrate elements.

6 CONCLUSIONS AND FUTURE OUTLOOK

This part of the thesis presented a fabrication technology that uses porous anodic alumina (PAA) to form a well-ordered gold nanoparticle layer transferred to a transparent substrate to be utilized for plasmonic sensor applications.

Experimental results in this thesis are structured according to fabrication technology with mini theoretical sections for the selected techniques. After the fabrication of aluminium templates, the fabrication of gold nanoparticles (AuNPs) is explained, showing the crucial aspects of AuNP formation, displacement and size control. It was extensively demonstrated that with this versatile, nanopatterned template-based fabrication technology, large-scale and relatively cheap production with tunable properties is possible. The main advantage of the proposed fabrication technology is the homogeneity of the nanoparticle size/distribution over a large (several cm^2) surface area.

Afterwards, the AuNP layers were transferred onto transparent dielectric substrates to utilize their properties as a plasmonic sensor fully. A reliable technique that sacrifices the Al template was presented with an additional selective etching of the substrate. This selective etching not only changes the AuNP substrate but also modifies its morphology, giving these nanocomposite layers their characteristic mushroom-like structure with lentil-shaped AuNPs on top of conical substrate pillars.

Through some complications in the development, working LSPR sensors based on an epoxy substrate were successfully prepared and characterized. The nanocomposite layers show exceptional sensitivity in comparison to the previous PDMS concepts. This work demonstrated an increase of sensitivity due to selective etching as well as long-term stability of those layers with successful cleaning, providing reproducible sensitivity. These LSPR sensors were successfully used for the label-free detection of a 20 bp long DNA molecule,[186] performed by Dr Attila Bonyár, making it one of the first NP-polymer surface nanocomposite sensors ever demonstrated for the plasmonic detection of DNA.

Additionally, this work includes the progress that has been made by introducing SiO_2 as a carrier layer for AuNPs. These LSPR sensors offer an almost 100 % increase in sensitivity and improved long-term stability compared to the previous epoxy-based samples. They also do not suffer from degradation during the O_2 plasma cleaning procedures.

In summary, the AuNPs fabrication technique demonstrated in this work represents a robust and scalable technology that allows fine-tuning and optimization of AuNP layer absorption spectra for plasmonic applications such as LSPR and SERS. A significant advantage of this technology is its relatively low cost and that it only includes solid-state processes, while it does not rely on any lithographic processes. Thus, this technique represents a link between randomly arranged nanoparticles formed by, e.g., SSD of thin metallic film or NPs deposited from colloids, and fully controlled arrangements done by, e.g., electron beam lithography (EBL), focused ion beam (FIB), nanoimprint lithography (NIL).

Even though this fabrication method shows remarkable results, it still suffers from a few drawbacks. One of them is the transfer of AuNPs from templates that require the dissolution of the template. Finding a method to separate an AuNP layer and save an underlying template would be the most considerable improvement. It would not be necessary to prepare a fresh Al template for each AuNP layer, and each AuNP layer will be identical. This single step would also make a breakthrough in other methods of AuNPs fabrication. The second drawback is the large-scale order of the defect-free domain size that is limited (to several microns) by the nature of pore nucleation during anodising and PAA growth. Without artificial methods such as lithography, increasing the self-order would be a giant leap proportionate to the first discovery of self-order of PAA.

The future work will include utilizing the recent SiO_2 layer to improve the performance and stability of AuNP layers. Additional performance can also be possibly achieved by optimizing AuNPs that are more focused on specific applications. Additional task will be to understand better the behaviour of PDMS and its possible utilization as a flexible substrate. Besides these, a big challenge will be to find or develop an AuNP transfer technique that will not damage the primary template. The last and probably most challenging to tackle will be improved large-scale self-ordering of PAA formed on an aluminium sheet or even thin deposited layers.

REFERENCES

[1] B. Decourt, B. Lajoie, R. Debarre, and O. Soupa, *Hydrogen based energy-conversion factbook*, A. K. Amgad Elgowainy, Marcel Weeda, Ed. SBC Energy Institute, 2014, p. 280.

[2] L. M. Gandía, G. Arzamendi, and P. M. Diéguez, 'Renewable Hydrogen Energy,' in *Renew. Hydrog. Technol.* Elsevier, 2013, pp. 1–17, ISBN: 9780444563613.

[3] P. Migowski and A. F. Feil, 'Uses of Physical Vapor Deposition Processes in Photoelectrochemical Water Splitting Systems,' *Recycl. Catal.*, vol. 3, no. 1, pp. 1–12, Jan. 2016, ISSN: 2084-7629.

[4] J. C. Alexander, *Surface Modifications and Growth of Titanium Dioxide for Photo-Electrochemical Water Splitting*, ser. Springer Theses November. Cham: Springer International Publishing, 2016, ISBN: 978-3-319-34227-6.

[5] X. Chen and S. S. Mao, 'Titanium Dioxide Nanomaterials: Synthesis, Properties, Modifications, and Applications,' *Chem. Rev.*, vol. 107, no. 7, pp. 2891–2959, Jul. 2007, ISSN: 0009-2665.

[6] M. Dahl, Y. Liu, and Y. Yin, 'Composite Titanium Dioxide Nanomaterials,' *Chem. Rev.*, vol. 114, no. 19, pp. 9853–9889, Oct. 2014, ISSN: 0009-2665.

[7] K. Huo, B. Gao, J. Fu, L. Zhao, and P. K. Chu, 'Fabrication, modification, and biomedical applications of anodized TiO_2 nanotube arrays,' *RSC Adv.*, vol. 4, no. 33, p. 17 300, 2014, ISSN: 2046-2069.

[8] G. Liu, L. Wang, H. G. Yang, H.-M. Cheng, and G. Q. (Max) Lu, 'Titania-based photocatalysts–crystal growth, doping and heterostructuring,' *J. Mater. Chem.*, vol. 20, no. 5, pp. 831–843, 2010, ISSN: 0959-9428.

[9] J. Macak, H. Tsuchiya, A. Ghicov, K. Yasuda, R. Hahn, S. Bauer, and P. Schmuki, 'TiO_2 nanotubes: Self-organized electrochemical formation, properties and applications,' *Curr. Opin. Solid State Mater. Sci.*, vol. 11, no. 1-2, pp. 3–18, Feb. 2007, ISSN: 13590286.

[10] T. Ochiai and A. Fujishima, 'Photoelectrochemical properties of TiO_2 photocatalyst and its applications for environmental purification,' *J. Photochem. Photobiol. C Photochem. Rev.*, vol. 13, no. 4, pp. 247–262, 2012, ISSN: 13895567.

[11] Y. Cai and Y. P. Feng, 'Review on charge transfer and chemical activity of TiO_2: Mechanism and applications,' *Prog. Surf. Sci.*, vol. 91, no. 4, pp. 183–202, Dec. 2016, ISSN: 00796816.

[12] U. Diebold, 'The surface science of titanium dioxide,' *Surf. Sci. Rep.*, vol. 48, no. 5, pp. 53–229, 2003, ISSN: 01675729.

[13] A. Fujishima, T. N. Rao, and D. A. Tryk, 'Titanium dioxide photocatalysis,' *J. Photochem. Photobiol. C Photochem. Rev.*, vol. 1, no. 1, pp. 1–21, Jun. 2000, ISSN: 13895567.

[14] A. L. Linsebigler, G. Lu, and J. T. Yates, 'Photocatalysis on TiO_2 Surfaces: Principles, Mechanisms, and Selected Results,' *Chem. Rev.*, vol. 95, no. 3, pp. 735–758, May 1995, ISSN: 0009-2665.

[15] J. Schneider, M. Matsuoka, M. Takeuchi, J. Zhang, Y. Horiuchi, M. Anpo, and D. W. Bahnemann, 'Understanding TiO_2 Photocatalysis: Mechanisms and Materials,' *Chem. Rev.*, vol. 114, no. 19, pp. 9919–9986, Oct. 2014, ISSN: 0009-2665.

[16] T. Tachikawa, M. Fujitsuka, and T. Majima, 'Mechanistic Insight into the TiO_2 Photocatalytic Reactions: Design of New Photocatalysts,' *J. Phys. Chem. C*, vol. 111, no. 14, pp. 5259–5275, Apr. 2007, ISSN: 1932-7447.

[17] Y. Bai, I. Mora-Seró, F. De Angelis, J. Bisquert, and P. Wang, 'Titanium Dioxide Nanomaterials for Photovoltaic Applications,' *Chem. Rev.*, vol. 114, no. 19, pp. 10 095–10 130, Oct. 2014, ISSN: 0009-2665.

[18] D. Chen and R. A. Caruso, 'Recent Progress in the Synthesis of Spherical Titania Nanostructures and Their Applications,' *Adv. Funct. Mater.*, vol. 23, no. 11, pp. 1356–1374, Mar. 2013, ISSN: 1616301X.

[19] R. Daghrir, P. Drogui, and D. Robert, 'Modified TiO_2 For Environmental Photocatalytic Applications: A Review,' *Ind. Eng. Chem. Res.*, vol. 52, no. 10, pp. 3581–3599, Mar. 2013, ISSN: 0888-5885.

[20] T. Jafari, E. Moharreri, A. Amin, R. Miao, W. Song, and S. Suib, 'Photocatalytic Water Splitting–The Untamed Dream: A Review of Recent Advances,' *Molecules*, vol. 21, no. 7, p. 900, Jul. 2016, ISSN: 1420-3049.

[21] D. Y. C. Leung, X. Fu, C. Wang, M. Ni, M. K. H. Leung, X. Wang, and X. Fu, 'Hydrogen Production over Titania-Based Photocatalysts,' *ChemSusChem*, vol. 3, no. 6, pp. 681–694, Apr. 2010, ISSN: 18645631.

[22] Y. Ma, X. Wang, Y. Jia, X. Chen, H. Han, and C. Li, 'Titanium Dioxide-Based Nanomaterials for Photocatalytic Fuel Generations,' *Chem. Rev.*, vol. 114, no. 19, pp. 9987–10 043, Oct. 2014, ISSN: 0009-2665.

[23] C. McCullagh, J. M. C. Robertson, D. W. Bahnemann, and P. K. J. Robertson, 'The application of TiO_2 photocatalysis for disinfection of water contaminated with pathogenic micro-organisms: a review,' *Res. Chem. Intermed.*, vol. 33, no. 3-5, pp. 359–375, Mar. 2007, ISSN: 0922-6168.

[24] K. Nakata and A. Fujishima, 'TiO_2 photocatalysis: Design and applications,' *J. Photochem. Photobiol. C Photochem. Rev.*, vol. 13, no. 3, pp. 169–189, Sep. 2012, ISSN: 13895567.

[25] K. Shankar, J. I. Basham, N. K. Allam, O. K. Varghese, G. K. Mor, X. Feng, M. Paulose, J. a. Seabold, K.-s. Choi, and C. a. Grimes, ‘Recent Advances in the Use of TiO_2 Nanotube and Nanowire Arrays for Oxidative Photoelectrochemistry,’ *J. Phys. Chem. C*, vol. 113, no. 16, pp. 6327–6359, Apr. 2009, ISSN: 1932-7447.

[26] Y. Zhao, N. Hoivik, and K. Wang, ‘Recent advance on engineering titanium dioxide nanotubes for photochemical and photoelectrochemical water splitting,’ *Nano Energy*, vol. 30, pp. 728–744, Dec. 2016, ISSN: 22112855.

[27] A. J. Nozik and R. Memming, ‘Physical Chemistry of Semiconductor-Liquid Interfaces,’ *J. Phys. Chem.*, vol. 100, no. 31, pp. 13 061–13 078, Jan. 1996, ISSN: 0022-3654.

[28] Krishnan Rajeshwar, ‘Fundamentals of Semiconductor Electrochemistry and Photoelectrochemistry,’ in *Encycl. Electrochem.* Weinheim, Germany: Wiley-VCH Verlag GmbH & Co. KGaA, Dec. 2007, pp. 1–51, ISBN: 978-3-527-30398-4.

[29] W. W. Gärtner, ‘Depletion-Layer Photoeffects in Semiconductors,’ *Phys. Rev.*, vol. 116, no. 1, pp. 84–87, Oct. 1959, ISSN: 0031-899X.

[30] J. J. Kelly and A. van Driel, ‘The Electrochemistry of Porous Semiconductors,’ in *Naturwissenschaften*, ser. Nanostructure Science and Technology 11, P. Schmuki and S. Virtanen, Eds., vol. 69, New York, NY: Springer New York, 2009, pp. 249–278, ISBN: 978-0-387-73581-8.

[31] I. Butterfield, P. Christensen, and a Hamnett, ‘Applied studies on immobilized titanium dioxide films ascatalysts for the photoelectrochemical detoxification of water,’ *J. Appl. Electrochem.*, vol. 27, pp. 385–395, 1997, ISSN: 0021-891X.

[32] P. Salvador, ‘Hole diffusion length in n-TiO_2 single crystals and sintered electrodes: Photoelectrochemical determination and comparative analysis,’ *J. Appl. Phys.*, vol. 55, no. 8, p. 2977, 1984, ISSN: 00218979.

[33] A. J. Nozik, ‘Photoelectrochemistry: Applications to Solar Energy Conversion,’ *Annu. Rev. Phys. Chem.*, vol. 29, no. 1, pp. 189–222, Oct. 1978, ISSN: 0066-426X.

[34] Y. Xu and M. A. Schoonen, ‘The absolute energy positions of conduction and valence bands of selected semiconducting minerals,’ *Am. Mineral.*, vol. 85, no. 3-4, pp. 543–556, Mar. 2000, ISSN: 0003-004X.

[35] W. Wu, C. J. Changzhong Jiang, and V. A. L. Roy, ‘Recent progress in magnetic iron oxide–semiconductor composite nanomaterials as promising photocatalysts,’ *Nanoscale*, vol. 7, no. 1, pp. 38–58, Dec. 2015, ISSN: 2040-3364.

[36] C. Renz, ‘Lichtreaktionen der Oxyde des Titans, Cers und der Erdsäuren,’ *Helv. Chim. Acta*, vol. 4, no. 1, pp. 961–968, 1921, ISSN: 0018019X.

[37] A. Fujishima, X. Zhang, and D. Tryk, ‘TiO_2 photocatalysis and related surface phenomena,’ *Surf. Sci. Rep.*, vol. 63, no. 12, pp. 515–582, Dec. 2008, ISSN: 01675729.

[38] A. Fujishima, K. Honda, and S. Kikuchi, ‘Photosensitized Electrolytic Oxidation on Semiconducting n-Type TiO_2 Electrode,’ *J. Soc. Chem. Ind. Japan*, vol. 72, no. 1, pp. 108–113, 1969, ISSN: 0023-2734.

[39] A. Fujishima and K. Honda, ‘Electrochemical Photolysis of Water at a Semiconductor Electrode,’ *Nature*, vol. 238, no. 5358, pp. 37–38, Jul. 1972, ISSN: 0028-0836.

[40] S. Y. Chae, P. Sudhagar, A. Fujishima, Y. J. Hwang, and O.-S. Joo, ‘Improved photoelectrochemical water oxidation kinetics using a TiO_2 nanorod array photoanode decorated with graphene oxide in a neutral pH solution,’ *Phys. Chem. Chem. Phys.*, vol. 17, no. 12, pp. 7714–7719, 2015, ISSN: 1463-9076.

[41] C. A. Grimes and G. K. Mor, *TiO_2 Nanotube Arrays*, Intergovernmental Panel on Climate Change, Ed., 9. Boston, MA: Springer US, 2009, vol. 1542, pp. 1–30, ISBN: 978-1-4419-0067-8.

[42] V. Zwilling, M. Aucouturier, and E. Darque-Ceretti, ‘Anodic oxidation of titanium and TA6V alloy in chromic media. An electrochemical approach,’ *Electrochim. Acta*, vol. 45, no. 6, pp. 921–929, Dec. 1999, ISSN: 00134686.

[43] G. Liu, K. Wang, N. Hoivik, and H. Jakobsen, ‘Progress on free-standing and flow-through TiO_2 nanotube membranes,’ *Sol. Energy Mater. Sol. Cells*, vol. 98, pp. 24–38, Mar. 2012, ISSN: 09270248.

[44] J. Wang, H. Sun, J. Huang, Q. Li, and J. Yang, ‘Band Structure Tuning of TiO_2 for Enhanced Photoelectrochemical Water Splitting,’ *J. Phys. Chem. C*, vol. 118, no. 14, pp. 7451–7457, Apr. 2014, ISSN: 1932-7447.

[45] F. Amano, ‘Hydrogen Reduced Rutile Titanium Dioxide Photocatalyst,’ in *Titan. Dioxide*, InTech, Jul. 2017.

[46] Y. Liu, F. Ren, G. Cai, M. Hong, W. Li, X. Xiao, W. Wu, and C. Jiang, ‘Fabrication of TiO_2 Nanofilm Photoelectrodes on Ti Foil by Ti Ion Implantation and Subsequent Annealing,’ *Adv. Condens. Matter Phys.*, vol. 2014, pp. 1–7, 2014, ISSN: 1687-8108.

[47] G. Wang, H. Wang, Y. Ling, Y. Tang, X. Yang, R. C. Fitzmorris, C. Wang, J. Z. Zhang, and Y. Li, ‘Hydrogen-Treated TiO_2 Nanowire Arrays for Photoelectrochemical Water Splitting,’ *Nano Lett.*, vol. 11, no. 7, pp. 3026–3033, Jul. 2011, ISSN: 1530-6984.

[48] M. K. Nowotny, T Bak, and J Nowotny, ‘Electrical Properties and Defect Chemistry of TiO_2 Single Crystal. I. Electrical Conductivity,’ *J. Phys. Chem. B*, vol. 110, no. 33, pp. 16 270–16 282, Aug. 2006, ISSN: 1520-6106.

[49] X. Pan, M.-Q. Yang, X. Fu, N. Zhang, and Y.-J. Xu, ‘Defective TiO_2 with oxygen vacancies: synthesis, properties and photocatalytic applications.,’ *Nanoscale*, vol. 5, no. 9, pp. 3601–14, May 2013, ISSN: 2040-3372.

[50] L. Aïnouche, L. Hamadou, A. Kadri, N. Benbrahim, and D. Bradai, 'TI^{3+} STATES INDUCED BAND GAP REDUCTION AND ENHANCED VISIBLE LIGHT ABSORPTION OF TIO_2 NANOTUBE ARRAYS: EFFECT OF THE SURFACE SOLID FRACTION FACTOR,' *Sol. Energy Mater. Sol. Cells*, vol. 151, pp. 179–190, Jul. 2016, ISSN: 09270248.

[51] T. K. Das, P. Ilaiyaraja, P. S. Mocherla, G. Bhalerao, and C. Sudakar, 'Influence of surface disorder, oxygen defects and bandgap in TiO_2 nanostructures on the photovoltaic properties of dye sensitized solar cells,' *Sol. Energy Mater. Sol. Cells*, vol. 144, pp. 194–209, Jan. 2016, ISSN: 09270248.

[52] N. Tatarenko and A. Mozalev, 'Geometry and element composition of a nanoscale field emission array formed by self-organization in porous anodic aluminum oxide,' *Solid. State. Electron.*, vol. 45, no. 6, pp. 1009–1016, Jun. 2001, ISSN: 00381101.

[53] Y.-H. Chang, H.-W. Lin, and C. Chen, 'Growth Mechanism of Self-Assembled TiO_2 Nanorod Arrays on Si Substrates Fabricated by Ti Anodization,' *J. Electrochem. Soc.*, vol. 159, no. 9, pp. D512–D517, Aug. 2012, ISSN: 0013-4651.

[54] D. Di Camillo, F. Ruggieri, S. Santucci, and L. Lozzi, 'N-Doped TiO_2 Nanofibers Deposited by Electrospinning,' *J. Phys. Chem. C*, vol. 116, no. 34, pp. 18 427–18 431, Aug. 2012, ISSN: 1932-7447.

[55] S. Z. Islam, A. Reed, N. Wanninayake, D. Y. Kim, and S. E. Rankin, 'Remarkable Enhancement of Photocatalytic Water Oxidation in N 2 /Ar Plasma Treated, Mesoporous TiO_2 Films,' *J. Phys. Chem. C*, vol. 120, no. 26, pp. 14 069–14 081, Jul. 2016, ISSN: 1932-7447.

[56] H. Melhem, P. Simon, J. Wang, C. Di Bin, B. Ratier, Y. Leconte, N. Herlin-Boime, M. Makowska-Janusik, A. Kassiba, and J. Bouclé, 'Direct photocurrent generation from nitrogen doped TiO_2 electrodes in solid-state dye-sensitized solar cells: Towards optically-active metal oxides for photovoltaic applications,' *Sol. Energy Mater. Sol. Cells*, vol. 117, pp. 624–631, Oct. 2013, ISSN: 09270248.

[57] G. Rajeev, B. Prieto Simon, L. F. Marsal, and N. H. Voelcker, 'Advances in Nanoporous Anodic Alumina-Based Biosensors to Detect Biomarkers of Clinical Significance: A Review,' *Adv. Healthc. Mater.*, vol. 7, no. 5, pp. 1–18, 2018, ISSN: 21922659.

[58] W. Lee and S.-J. Park, 'Porous Anodic Aluminum Oxide: Anodization and Templated Synthesis of Functional Nanostructures,' *Chem. Rev.*, vol. 114, no. 15, pp. 7487–7556, Aug. 2014, ISSN: 0009-2665.

[59] J. W. Diggle, T. C. Downie, and C. W. Goulding, 'Anodic oxide films on aluminum,' *Chem. Rev.*, vol. 69, no. 3, pp. 365–405, Jun. 1969, ISSN: 0009-2665.

[60] H. Zhao, L. Liu, and Y. Lei, ‘A mini review: Functional nanostructuring with perfectly-ordered anodic aluminum oxide template for energy conversion and storage,’ *Front. Chem. Sci. Eng.*, vol. 12, no. 3, pp. 481–493, 2018, ISSN: 20950187.

[61] W. J. Stępniowski and Z. Bojar, ‘Nanoporous Anodic Aluminum Oxide: Fabrication, Characterization, and Applications,’ in *Handb. Nanoelectrochemistry*, Cham: Springer International Publishing, 2015, pp. 1–47.

[62] G. Sriram, P. Patil, M. P. Bhat, R. M. Hegde, K. V. Ajeya, I. Udachyan, M. B. Bhavya, M. G. Gatti, U. T. Uthappa, G. M. Neelgund, H. Y. Jung, T. Altalhi, Madhuprasad, and M. D. Kurkuri, ‘Current Trends in Nanoporous Anodized Alumina Platforms for Biosensing Applications,’ *J. Nanomater.*, vol. 2016, 2016, ISSN: 16874129.

[63] G. E. J. Poinern, N. Ali, and D. Fawcett, ‘Progress in Nano-Engineered Anodic Aluminum Oxide Membrane Development,’ *Materials (Basel).*, vol. 4, no. 3, pp. 487–526, Feb. 2011, ISSN: 1996-1944.

[64] G. D. Sulka, ‘Highly Ordered Anodic Porous Alumina Formation by Self-Organized Anodizing,’ in *Nanostructured Mater. Electrochem.* Weinheim, Germany: Wiley-VCH Verlag GmbH & Co. KGaA, 2008, pp. 1–116, ISBN: 9783527318766.

[65] T. Kumeria, A. Santos, and D. Losic, ‘Nanoporous anodic alumina platforms: Engineered surface chemistry and structure for optical sensing applications,’ *Sensors (Switzerland)*, vol. 14, no. 7, pp. 11 878–11 918, 2014, ISSN: 14248220.

[66] G. Thompson, ‘Porous anodic alumina: fabrication, characterization and applications,’ *Thin Solid Films*, vol. 297, no. 1-2, pp. 192–201, Apr. 1997, ISSN: 0040-6090.

[67] D. Losic and A. Santos, *Nanoporous Alumina*, D. Losic and A. Santos, Eds., ser. Springer Series in Materials Science. Cham: Springer International Publishing, 2015, vol. 219, ISBN: 978-3-319-20333-1.

[68] H. Buff, ‘Ueber das electrische Verhalten des Aluminiums,’ *Ann. der Chemie und Pharm.*, vol. 102, no. 3, pp. 265–284, Jan. 1857, ISSN: 00754617.

[69] F. Keller, M. S. Hunter, and D. L. Robinson, ‘Structural Features of Oxide Coatings on Aluminum,’ *J. Electrochem. Soc.*, vol. 100, no. 9, p. 411, 1953, ISSN: 00134651.

[70] H. Masuda and K. Fukuda, ‘Ordered Metal Nanohole Arrays Made by a Two-Step Replication of Honeycomb Structures of Anodic Alumina,’ *Science (80-.).*, vol. 268, no. 5216, pp. 1466–1468, Jun. 1995, ISSN: 0036-8075.

[71] H. Masuda and M. Satoh, ‘Fabrication of Gold Nanodot Array Using Anodic Porous Alumina as an Evaporation Mask,’ *Jpn. J. Appl. Phys.*, vol. 35, no. Part 2, No. 1B, pp. L126–L129, Jan. 1996, ISSN: 00214922.

[72] R. O. Al-Kaysi, T. H. Ghaddar, and G. Guirado, 'Fabrication of One-Dimensional Organic Nanostructures Using Anodic Aluminum Oxide Templates,' *J. Nanomater.*, vol. 2009, pp. 1–14, 2009, ISSN: 1687-4110.

[73] J. Martín, J. Maiz, J. Sacristan, and C. Mijangos, 'Tailored polymer-based nanorods and nanotubes by "template synthesis": From preparation to applications,' *Polymer (Guildf).*, vol. 53, no. 6, pp. 1149–1166, Mar. 2012, ISSN: 00323861.

[74] K. Nielsch, J. Choi, K. Schwirn, R. B. Wehrspohn, and U. Gösele, 'Self-ordering Regimes of Porous Alumina: The 10% Porosity Rule,' *Nano Lett.*, vol. 2, no. 7, pp. 1–4, 2002, ISSN: 15306984.

[75] G. Sulka and K. Parkoła, 'Temperature influence on well-ordered nanopore structures grown by anodization of aluminium in sulphuric acid,' *Electrochim. Acta*, vol. 52, no. 5, pp. 1880–1888, Jan. 2007, ISSN: 00134686.

[76] C. H. Voon, M. N. Derman, U. Hashim, K. R. Ahmad, and K. L. Foo, 'Effect of Temperature of Oxalic Acid on the Fabrication of Porous Anodic Alumina from Al-Mn Alloys,' *J. Nanomater.*, vol. 2013, pp. 1–8, 2013, ISSN: 1687-4110.

[77] W. J. Stępniowski and Z. Bojar, 'Synthesis of anodic aluminum oxide (AAO) at relatively high temperatures. Study of the influence of anodization conditions on the alumina structural features,' *Surf. Coatings Technol.*, vol. 206, no. 2-3, pp. 265–272, Oct. 2011, ISSN: 02578972.

[78] M. Pashchanka and J. J. Schneider, 'Self-Ordering Regimes of Porous Anodic Alumina Layers Formed in Highly Diluted Sulfuric Acid Electrolytes,' *J. Phys. Chem. C*, vol. 120, no. 27, pp. 14 590–14 596, Jul. 2016, ISSN: 1932-7447.

[79] X.-j. Liu and L.-f. Li, 'Research on Interpore Distance of Anodic Aluminum Oxide Template,' Jan. 2013.

[80] S. Z. Chu, K. Wada, S. Inoue, M. Isogai, Y. Katsuta, and A. Yasumori, 'Large-Scale Fabrication of Ordered Nanoporous Alumina Films with Arbitrary Pore Intervals by Critical-Potential Anodization,' *J. Electrochem. Soc.*, vol. 153, no. 9, B384, Sep. 2006, ISSN: 00134651.

[81] C. T. Sousa, D. C. Leitao, M. P. Proenca, J. Ventura, A. M. Pereira, and J. P. Araujo, 'Nanoporous alumina as templates for multifunctional applications,' *Appl. Phys. Rev.*, vol. 1, no. 3, 2014, ISSN: 19319401.

[82] H. Han, S.-J. Park, J. S. Jang, H. Ryu, K. J. Kim, S. Baik, and W. Lee, 'In Situ Determination of the Pore Opening Point during Wet-Chemical Etching of the Barrier Layer of Porous Anodic Aluminum Oxide: Nonuniform Impurity Distribution in Anodic Oxide,' *ACS Appl. Mater. Interfaces*, vol. 5, no. 8, pp. 3441–3448, Apr. 2013, ISSN: 1944-8244.

[83] M. Shaban, H. Hamdy, F. Shahin, J. Park, and S.-W. Ryu, 'Uniform and Reproducible Barrier Layer Removal of Porous Anodic Alumina Membrane,' *J. Nanosci. Nanotechnol.*, vol. 10, no. 5, pp. 3380–3384, May 2010, ISSN: 15334880.

[84] L. P. Hernández-Eguía, J. Ferré-Borrull, G. Macias, J. Pallarès, and L. F. Marsal, 'Engineering optical properties of gold-coated nanoporous anodic alumina for biosensing,' *Nanoscale Res. Lett.*, vol. 9, no. 1, p. 414, Aug. 2014, ISSN: 1556-276X.

[85] N. Yuan, H. Zhao, C. Zheng, X. Zheng, Q. Fu, M. Wu, and Y. Lei, 'An efficient nanopatterning strategy for controllably fabricating ultra-small gaps as a highly sensitive surface-enhanced Raman scattering platform,' *Nanotechnology*, vol. 31, no. 4, p. 045 301, Jan. 2020, ISSN: 0957-4484.

[86] M. Pellin, P. Stair, G. Xiong, J. Elam, J. Birrell, L. Curtiss, S. George, C. Han, L. Iton, H. Kung, M. Kung, and H.-H. Wang, 'Mesoporous catalytic membranes: Synthetic control of pore size and wall composition,' *Catal. Letters*, vol. 102, no. 3-4, pp. 127–130, Aug. 2005, ISSN: 1011-372X.

[87] G. Pardon, H. K. Gatty, G. Stemme, W. van der Wijngaart, and N. Roxhed, 'Pt–Al_2O_3 dual layer atomic layer deposition coating in high aspect ratio nanopores,' *Nanotechnology*, vol. 24, no. 1, p. 015 602, Jan. 2013, ISSN: 0957-4484.

[88] W. Cheng, M. Steinhart, U. Gösele, and R. B. Wehrspohn, 'Tree-like alumina nanopores generated in a non-steady-state anodization,' *J. Mater. Chem.*, vol. 17, no. 33, p. 3493, Aug. 2007, ISSN: 0959-9428.

[89] C. Cheng and A. H. Ngan, 'Fast fabrication of self-ordered anodic porous alumina on oriented aluminum grains by high acid concentration and high temperature anodization,' *Nanotechnology*, vol. 24, no. 21, 2013, ISSN: 09574484.

[90] E. Choudhary and V. Szalai, 'Two-step cycle for producing multiple anodic aluminum oxide (AAO) films with increasing long-range order,' *RSC Adv.*, vol. 6, no. 72, pp. 67 992–67 996, 2016, ISSN: 2046-2069.

[91] J. Randon, P. Mardilovich, A. Govyadinov, and R. Paterson, 'Computer Simulation of Inorganic Membrane Morphology Part 3. Anodic Alumina Films and Membranes,' *J. Colloid Interface Sci.*, vol. 169, no. 2, pp. 335–341, Feb. 1995, ISSN: 00219797.

[92] R. Hillebrand, F. Müller, K. Schwirn, W. Lee, and M. Steinhart, 'Quantitative analysis of the grain morphology in self-assembled hexagonal lattices,' *ACS Nano*, vol. 2, no. 5, pp. 913–920, 2008, ISSN: 19360851.

[93] H. Masuda, 'Self-Ordering of Cell Arrangement of Anodic Porous Alumina Formed in Sulfuric Acid Solution,' *J. Electrochem. Soc.*, vol. 144, no. 5, p. L127, 1997, ISSN: 00134651.

[94] H. Masuda, K. Yada, and A. Osaka, ‘Self-Ordering of Cell Configuration of Anodic Porous Alumina with Large-Size Pores in Phosphoric Acid Solution,’ *Jpn. J. Appl. Phys.*, vol. 37, no. Part 2, No. 11A, pp. L1340–L1342, Nov. 1998.

[95] E. O. Gordeeva, I. V. Roslyakov, A. I. Sadykov, T. A. Suchkova, D. I. Petukhov, T. B. Shatalova, and K. S. Napolskii, ‘Formation Efficiency of Porous Oxide Films in Aluminum Anodizing,’ *Russ. J. Electrochem.*, vol. 54, no. 11, pp. 990–998, Nov. 2018, ISSN: 1023-1935.

[96] L. Sacco, I. Florea, M. Châtelet, and C.-s. Cojocaru, ‘Investigation of porous anodic alumina templates formed by anodization of single-crystal aluminum substrates,’ *Thin Solid Films*, vol. 660, pp. 213–220, Aug. 2018, ISSN: 00406090.

[97] C. Cheng, K. Y. Ng, and A. H. W. Ngan, ‘Quantitative characterization of acid concentration and temperature dependent self-ordering conditions of anodic porous alumina,’ *AIP Adv.*, vol. 1, no. 4, p. 042 113, Dec. 2011, ISSN: 2158-3226.

[98] L. Zaraska, W. J. Stępniowski, M. Jaskuła, and G. D. Sulka, ‘Analysis of nanopore arrangement of porous alumina layers formed by anodizing in oxalic acid at relatively high temperatures,’ *Appl. Surf. Sci.*, vol. 305, pp. 650–657, Jun. 2014, ISSN: 01694332.

[99] I. V. Roslyakov, D. S. Koshkodaev, A. A. Eliseev, D. Hermida-Merino, V. K. Ivanov, A. V. Petukhov, and K. S. Napolskii, ‘Growth of Porous Anodic Alumina on Low-Index Surfaces of Al Single Crystals,’ *J. Phys. Chem. C*, vol. 121, no. 49, pp. 27 511–27 520, 2017, ISSN: 19327455.

[100] J. Liao, Z. Ling, Y. Li, and X. Hu, ‘The Role of Stress in the Self-Organized Growth of Porous Anodic Alumina,’ *ACS Appl. Mater. Interfaces*, vol. 8, no. 12, pp. 8017–8023, 2016, ISSN: 19448252.

[101] J. E. Houser, ‘Modeling the steady-state growth of porous anodic alumina,’ Ph.D. dissertation, Iowa State University, Digital Repository, Ames, Jan. 2008.

[102] C. Wang, Y. Ishida, K.-i. Saitoh, T. Shimizu, S. Shingubara, and S. Tanaka, ‘Fabrication of an ordered anodic aluminum oxide pore arrays with an interpore distance smaller than the nano-indentation pitch formed by ion beam etching,’ in *2012 IEEE Int. Meet. Futur. Electron Devices, Kansai*, IEEE, May 2012, pp. 1–2, ISBN: 978-1-4673-0836-6.

[103] H. Masuda, H. Yamada, M. Satoh, H. Asoh, M. Nakao, and T. Tamamura, ‘Highly ordered nanochannel-array architecture in anodic alumina,’ *Appl. Phys. Lett.*, vol. 71, no. 19, pp. 2770–2772, Nov. 1997, ISSN: 0003-6951.

[104] A. P. Li, F. Müller, and U. Gösele, ‘Polycrystalline and Monocrystalline Pore Arrays with Large Interpore Distance in Anodic Alumina,’ *Electrochem. Solid-State Lett.*, vol. 3, no. 3, p. 131, Jan. 1999, ISSN: 10990062.

[105] C. Dell'Oca, D. Pulfrey, and L. Young, 'Anodic Oxide Films,' in *Phys. Thin Film.* Vol. 6, Elsevier, Jan. 1971, pp. 1–79, ISBN: 9780125330060.

[106] J. A. Davies, B. Domeij, J. P. S. Pringle, and F. Brown, 'The Migration of Metal and Oxygen during Anodic Film Formation,' *J. Electrochem. Soc.*, vol. 112, no. 7, p. 675, 1965, ISSN: 00134651.

[107] W. D. Mackintosh, F. Brown, and H. H. Plattner, 'Mobility of Metallic Foreign Atoms during the Anodic Oxidation of Aluminum,' *J. Electrochem. Soc.*, vol. 121, no. 10, p. 1281, 1974, ISSN: 00134651.

[108] J. Perrière, J. Siejka, and S. Rigo, 'Investigation of ionic movements during anodic oxidation of superimposed metallic layers by the use of rutherford backscattering techniques and nuclear microanalysis,' *Corros. Sci.*, vol. 20, no. 1, pp. 91–102, Jan. 1980, ISSN: 0010938X.

[109] J. Perrière and J. Siejka, 'Study of the Anodization of Niobium and Tantalum Superimposed Layers by ^{18}O Tracing Techniques and Nuclear Microanalysis: II . Discussion,' *J. Electrochem. Soc.*, vol. 130, no. 6, pp. 1267–1273, Jun. 1983, ISSN: 0013-4651.

[110] S. Rigo and J. Siejka, 'Long range migration of niobium during the anodic oxidation of tantalum on niobium and aluminum on niobium duplex layers,' *Solid State Commun.*, vol. 15, no. 2, pp. 259–264, Jul. 1974, ISSN: 00381098.

[111] J. Pringle, 'The anodic oxidation of superimposed metallic layers: theory,' *Electrochim. Acta*, vol. 25, no. 11, pp. 1423–1437, Nov. 1980, ISSN: 00134686.

[112] K. Shimizu, K. Kobayashi, P. Skeldon, G. Thompson, and G. Wood, 'Anodic oxidation of zirconium covered with a thin layer of aluminium,' *Thin Solid Films*, vol. 295, no. 1-2, pp. 156–161, Feb. 1997, ISSN: 00406090.

[113] P. Skeldon, K. Shimizu, G. E. Thompson, and G. C. Wood, 'Direct observation of anodic film growth on superimposed aluminium and tantalum metallic layers,' *Philos. Mag. B*, vol. 61, no. 5, pp. 927–938, May 1990, ISSN: 1364-2812.

[114] J. Pringle, 'The anodic oxidation of superimposed niobium and tantalum layers: theory,' *Electrochim. Acta*, vol. 25, no. 11, pp. 1403–1421, Nov. 1980, ISSN: 00134686.

[115] M. Lohrengel, 'Thin anodic oxide layers on aluminium and other valve metals: high field regime,' *Mater. Sci. Eng. R Reports*, vol. 11, no. 6, pp. 243–294, Dec. 1993, ISSN: 0927796X.

[116] V. Surganov, S. Arzhankov, N. Tatarenko, G. Gorokh, and V. Lastochkina, 'Method of preparing anodic oxide films on aluminum for spectroscopic and sctructural examination.,' *Ind. Lab.*, vol. 52, no. 8, pp. 753–755, 1986.

[117] V. F. Surganov, A. M. Mozalev, and V. A. Lastochkina, ‘Investigating the composition of periodic nano-size column structures of anodic titanium oxide by the method of IR spectroscopy,’ *J. Appl. Spectrosc.*, vol. 65, no. 6, pp. 891–897, Nov. 1998, ISSN: 0021-9037.

[118] N. I. Tatarenko, V. a. Solntsev, and a. N. Rodionov, ‘Novel nanoscale field emission structures: Fabrication technology, experimental, and calculated characteristics,’ *J. Vac. Sci. Technol. B Microelectron. Nanom. Struct.*, vol. 17, no. 2, p. 647, 1999, ISSN: 0734211X.

[119] M. Bendova, J. Kolar, M. Marik, T. Lednicky, and A. Mozalev, ‘Influence of nitrogen species on the porous-alumina-assisted growth of TiO_2 nanocolumn arrays,’ *Electrochim. Acta*, vol. 281, pp. 796–809, Aug. 2018, ISSN: 00134686.

[120] A. Mozalev, M. Sakairi, I. Saeki, and H. Takahashi, ‘Nucleation and growth of the nanostructured anodic oxides on tantalum and niobium under the porous alumina film,’ *Electrochim. Acta*, vol. 48, no. 20-22, pp. 3155–3170, Sep. 2003, ISSN: 00134686.

[121] A. Mozalev, R. M. Vázquez, C. Bittencourt, D. Cossement, F. Gispert-Guirado, E. Llobet, and H. Habazaki, ‘Formation–structure–properties of niobium-oxide nanocolumn arrays via self-organized anodization of sputter-deposited aluminum-on-niobium layers,’ *J. Mater. Chem. C*, vol. 2, no. 24, p. 4847, May 2014, ISSN: 2050-7526.

[122] A. Mozalev, M. Bendova, F. Gispert-Guirado, Z. Pytlicek, and E. Llobet, ‘Metal-substrate-supported tungsten-oxide nanoarrays via porous-alumina-assisted anodization: from nanocolumns to nanocapsules and nanotubes,’ *J. Mater. Chem. A*, vol. 4, no. 21, pp. 8219–8232, May 2016, ISSN: 2050-7488.

[123] Y.-H. Chang, Y.-T. Chen, C.-S. Huang, C.-L. Lu, S.-H. Lee, B.-R. Huang, and C. Chen, ‘Growth Mechanism of Self-Assembled Ti_xW_yO Nanotubes Fabricated by TiW Alloy Anodization,’ *J. Electrochem. Soc.*, vol. 165, no. 10, pp. D477–D481, Aug. 2018, ISSN: 0013-4651.

[124] A. Mozalev, V. Khatko, C. Bittencourt, A. W. Hassel, G. Gorokh, E. Llobet, and X. Correig, ‘Nanostructured Columnlike Tungsten Oxide Film by Anodizing Al/W/Ti Layers on Si,’ *Chem. Mater.*, vol. 20, no. 20, pp. 6482–6493, Oct. 2008, ISSN: 0897-4756.

[125] S. H. Park, Y. H. Kim, T. G. Lee, H. K. Shon, H. M. Park, and J. Y. Song, ‘Synthesis and electrochemical capacitance of long tungsten oxide nanorod arrays grown vertically on substrate,’ *Mater. Res. Bull.*, vol. 47, no. 11, pp. 3612–3618, Nov. 2012, ISSN: 00255408.

[126] K. Kamnev, J. Prasek, and A. Mozalev, ‘Anodic formation and SEM characterization of zirconium oxide nanostructured films,’ 2020, pp. 631–636.

[127] A. Mozalev, Z. Pytlicek, K. Kamnev, J. Prasek, F. Gispert-Guirado, and E. Llobet, 'Zirconium oxide nanoarrays via the self-organized anodizing of Al/Zr bilayers on substrates,' *Mater. Chem. Front.*, vol. 5, no. 4, pp. 1917–1931, Feb. 2021, ISSN: 2052-1537.

[128] P. Gong and R. Levicky, 'DNA surface hybridization regimes,' *Proc. Natl. Acad. Sci.*, vol. 105, no. 14, pp. 5301–5306, Apr. 2008, ISSN: 0027-8424.

[129] S.-Z. Chu, S. Inoue, K. Wada, S. Hishita, and K. Kurashima, 'Self-Organized Nanoporous Anodic Titania Films and Ordered Titania Nanodots/Nanorods on Glass,' *Adv. Funct. Mater.*, vol. 15, no. 8, pp. 1343–1349, Aug. 2005, ISSN: 1616-301X.

[130] T. Kondo, S. Nagao, S. Hirano, T. Yanagishita, N. T. Nguyen, P. Schmuki, and H. Masuda, 'Fabrication of ideally ordered anodic porous TiO_2 by anodization of pretextured two-layered metals,' *Electrochem. commun.*, vol. 72, pp. 100–103, Nov. 2016, ISSN: 13882481.

[131] A. B. Murphy, P. R. F. Barnes, L. K. Randeniya, I. C. Plumb, I. E. Grey, M. D. Horne, and J. A. Glasscock, 'Efficiency of solar water splitting using semiconductor electrodes,' *Int. J. Hydrogen Energy*, vol. 31, no. 14, pp. 1999–2017, 2006, ISSN: 03603199.

[132] M. Sepúlveda, J. Castaño, and F. Echeverría, 'Fabrication of highly-ordered TiO_2 nanocolumns by two-step anodizing of an Al/Ti layer in etidronic acid,' *Mater. Chem. Phys.*, vol. 216, pp. 51–57, Sep. 2018, ISSN: 02540584.

[133] T. Sjöström, N. Fox, and B. Su, 'A study on the formation of titania nanopillars during porous anodic alumina through-mask anodization of Ti substrates,' *Electrochim. Acta*, vol. 56, no. 1, pp. 203–210, Dec. 2010, ISSN: 00134686.

[134] T. Sjöström, N. Fox, and B. Su, 'Through-mask anodization of titania dot- and pillar-like nanostructures on bulk Ti substrates using a nanoporous anodic alumina mask,' *Nanotechnology*, vol. 20, no. 13, p. 135 305, Apr. 2009, ISSN: 0957-4484.

[135] L.-k. Tsui, N. T. Nguyen, L. Wang, R. Kirchgeorg, G. Zangari, and P. Schmuki, 'Hierarchical decoration of anodic TiO_2 nanorods for enhanced photocatalytic degradation properties,' *Electrochim. Acta*, vol. 155, pp. 244–250, Feb. 2015, ISSN: 00134686.

[136] P.-L. Chen, C.-T. Kuo, T.-G. Tsai, B.-W. Wu, C.-C. Hsu, and F.-M. Pan, 'Self-organized titanium oxide nanodot arrays by electrochemical anodization,' *Appl. Phys. Lett.*, vol. 82, no. 17, p. 2796, 2003, ISSN: 00036951.

[137] A. Mozalev, H. Habazaki, and J. Hubálek, 'The superhydrophobic properties of self-organized microstructured surfaces derived from anodically oxidized Al/Nb and Al/Ta metal layers,' *Electrochim. Acta*, vol. 82, pp. 90–97, Nov. 2012, ISSN: 00134686.

[138] M. Bendova, J. Kolar, F. Gispert-Guirado, and A. Mozalev, ‘Porous-Alumina-Assisted Growth of Nanostructured Anodic Films on Tiâ'Nb Alloys,’ *ChemElectroChem*, vol. 5, no. 19, pp. 2825–2835, Oct. 2018, ISSN: 21960216.

[139] J. M. Macák, H. Tsuchiya, and P. Schmuki, ‘High-aspect-ratio TiO_2 nanotubes by anodization of titanium,’ *Angew. Chemie - Int. Ed.*, vol. 44, no. 14, pp. 2100–2102, 2005, ISSN: 14337851.

[140] M. Marik, A. Mozalev, J. Hubalek, and M. Bendova, ‘Resistive switching in TiO_2 nanocolumn arrays electrochemically grown,’ *J. Phys. Conf. Ser.*, vol. 829, no. 1, p. 012 001, Apr. 2017, ISSN: 1742-6588.

[141] I. Gablech, V. Svatoš, O. Caha, M. Hrabovský, J. Prášek, J. Hubálek, and T. Šikola, ‘Preparation of (001) preferentially oriented titanium thin films by ion-beam sputtering deposition on thermal silicon dioxide,’ *J. Mater. Sci.*, vol. 51, no. 7, pp. 3329–3336, Apr. 2016, ISSN: 0022-2461.

[142] G. C. Schwartz, ‘An Anodic Process for Forming Planar Interconnection Metallization for Multilevel LSI,’ *J. Electrochem. Soc.*, vol. 122, no. 11, p. 1508, 1975, ISSN: 00134651.

[143] W. Lee and S.-J. Park, ‘Porous Anodic Aluminum Oxide: Anodization and Templated Synthesis of Functional Nanostructures,’ *Chem. Rev.*, vol. 114, no. 15, pp. 7487–7556, Aug. 2014, ISSN: 0009-2665.

[144] G. D. Sulka, ‘Highly Ordered Anodic Porous Alumina Formation by Self-Organized Anodizing,’ in *Nanostructured Mater. Electrochem.* Weinheim, Germany: Wiley-VCH Verlag GmbH & Co. KGaA, 2008, pp. 1–116, ISBN: 9783527318766.

[145] E. Białek, M. Włodarski, and M. Norek, ‘Influence of Anodization Temperature on Geometrical and Optical Properties of Porous Anodic Alumina(PAA)-Based Photonic Structures,’ *Materials (Basel).*, vol. 13, no. 14, p. 3185, Jul. 2020, ISSN: 1996-1944.

[146] K. Chernyakova, B. Tzaneva, I. Vrublevsky, and V. Videkov, ‘Effect of Aluminum Anode Temperature on Growth Rate and Structure of Nanoporous Anodic Alumina,’ *J. Electrochem. Soc.*, vol. 167, no. 10, p. 103 506, Jun. 2020, ISSN: 1945-7111.

[147] L. Zaraska, W. J. Stępniowski, E. Ciepiela, and G. D. Sulka, ‘The effect of anodizing temperature on structural features and hexagonal arrangement of nanopores in alumina synthesized by two-step anodizing in oxalic acid,’ *Thin Solid Films*, vol. 534, pp. 155–161, May 2013, ISSN: 00406090.

[148] T. W. Clyne and S. C. Troughton, ‘A review of recent work on discharge characteristics during plasma electrolytic oxidation of various metals,’ *Int. Mater. Rev.*, vol. 64, no. 3, pp. 127–162, Apr. 2019.

[149] C. Dunleavy, I. Golosnoy, J. Curran, and T. Clyne, 'Characterisation of discharge events during plasma electrolytic oxidation,' *Surf. Coatings Technol.*, vol. 203, no. 22, pp. 3410–3419, Aug. 2009.

[150] Z. J. Liu, X. Zhong, J. Walton, and G. E. Thompson, 'Anodic Film Growth of Titanium Oxide Using the 3-Electrode Electrochemical Technique: Effects of Oxygen Evolution and Morphological Characterizations,' *J. Electrochem. Soc.*, vol. 163, no. 3, E75–E82, Dec. 2016.

[151] I. Milošv, H.-H. Strehblow, B. Navinšek, and M. Metikoš-Huković, 'Electrochemical and thermal oxidation of TiN coatings studied by XPS,' *Surf. Interface Anal.*, vol. 23, no. 7-8, pp. 529–539, Jul. 1995, ISSN: 0142-2421.

[152] R. Beranek, '(Photo)electrochemical Methods for the Determination of the Band Edge Positions of TiO_2 -Based Nanomaterials,' *Adv. Phys. Chem.*, vol. 2011, pp. 1–20, 2011, ISSN: 1687-7985.

[153] J. C. Alexander, *Surface modifications and growth of titanium dioxide for photo-electrochemical water splitting*, November. 2014, ISBN: 9783319342276.

[154] 'Basic Theories of Semiconductor Electrochemistry,' in *Electrochem. Silicon Its Oxide*, Boston: Kluwer Academic Publishers, 2004, pp. 1–43.

[155] S. Tengeler, 'Cubic Silicon Carbide For Direct Photoelectrochemical Water Splitting,' Ph.D. dissertation, Technische Universität, Darmstadt, 2017.

[156] M. Diamanti, S. Codeluppi, A. Cordioli, and M. Pedeferri, 'Effect of thermal oxidation on titanium oxides' characteristics,' *J. Exp. Nanosci.*, vol. 4, no. 4, pp. 365–372, Dec. 2009, ISSN: 1745-8080.

[157] D. A. H. Hanaor and C. C. Sorrell, 'Review of the anatase to rutile phase transformation,' *J. Mater. Sci.*, vol. 46, no. 4, pp. 855–874, Feb. 2011, ISSN: 0022-2461.

[158] P. Hones, C. Zakri, P. E. Schmid, F. Lévy, and O. R. Shojaei, 'Oxidation resistance of protective coatings studied by spectroscopic ellipsometry,' *Appl. Phys. Lett.*, vol. 76, no. 22, pp. 3194–3196, May 2000.

[159] Y. Paz, 'Application of TiO_2 photocatalysis for air treatment: Patents' overview,' *Appl. Catal. B Environ.*, vol. 99, no. 3-4, pp. 448–460, 2010, ISSN: 09263373.

[160] R. Asahi, T. Morikawa, H. Irie, and T. Ohwaki, 'Nitrogen-Doped Titanium Dioxide as Visible-Light-Sensitive Photocatalyst: Designs, Developments, and Prospects,' *Chem. Rev.*, vol. 114, no. 19, pp. 9824–9852, Oct. 2014, ISSN: 0009-2665.

[161] Y. J. Jin, J. Linghu, J. Chai, C. S. Chua, L. M. Wong, Y. P. Feng, M. Yang, and S. Wang, 'Defect Evolution Enhanced Visible-Light Photocatalytic Activity in Nitrogen-Doped Anatase TiO_2 Thin Films,' *J. Phys. Chem. C*, vol. 122, no. 29, pp. 16 600–16 606, Jul. 2018, ISSN: 1932-7447.

[162] J. A. Seabold and K.-S. Choi, 'Effect of a Cobalt-Based Oxygen Evolution Catalyst on the Stability and the Selectivity of Photo-Oxidation Reactions of a WO_3 Photoanode,' *Chem. Mater.*, vol. 23, no. 5, pp. 1105–1112, Mar. 2011, ISSN: 0897-4756.

[163] I. S. Cho, Z. Chen, A. J. Forman, D. R. Kim, P. M. Rao, T. F. Jaramillo, and X. Zheng, 'Branched TiO_2 Nanorods for Photoelectrochemical Hydrogen Production,' *Nano Lett.*, vol. 11, no. 11, pp. 4978–4984, Nov. 2011, ISSN: 1530-6984.

[164] M. L. Vera, M. R. Rosenberger, C. E. Schvezov, and A. E. Ares, 'Fabrication of TiO_2 Crystalline Coatings by Combining Ti-6Al-4V Anodic Oxidation and Heat Treatments,' *Int. J. Biomater.*, vol. 2015, pp. 1–9, 2015, ISSN: 1687-8787.

[165] J. M. Gregoire, C. Xiang, X. Liu, M. Marcin, and J. Jin, 'Scanning droplet cell for high throughput electrochemical and photoelectrochemical measurements,' *Rev. Sci. Instrum.*, vol. 84, no. 2, p. 024 102, 2013, ISSN: 00346748.

[166] J.-S. Lee, C. C. Mardare, A. I. Mardare, and A. W. Hassel, 'Electrochemical Screening of Tungsten Trioxide–Nickel Oxide Thin Film Combinatorial Library at Low Nickel Concentrations,' *ACS Comb. Sci.*, vol. 22, no. 2, pp. 61–69, Feb. 2020, ISSN: 2156-8952.

[167] A. I. Mardare, C. C. Mardare, J. P. Kollender, S. Huber, and A. W. Hassel, 'Basic properties mapping of anodic oxides in the hafnium-niobium-tantalum ternary system,' *Sci. Technol. Adv. Mater.*, vol. 19, no. 1, pp. 554–568, Dec. 2018, ISSN: 1468-6996.

[168] R. E. Scholten, 'Enhanced laser shutter using a hard disk drive rotary voice-coil actuator,' *Rev. Sci. Instrum.*, vol. 78, no. 2, p. 026 101, Feb. 2007, ISSN: 0034-6748.

[169] R. Beranek, H. Tsuchiya, T. Sugishima, J. M. Macak, L. Taveira, S. Fujimoto, H. Kisch, and P. Schmuki, 'Enhancement and limits of the photoelectrochemical response from anodic TiO_2 nanotubes.,' vol. 243114, no. 2005, pp. 98–101, 2016.

[170] Z. Jiao, T. Chen, J. Xiong, T. Wang, G. Lu, J. Ye, and Y. Bi, 'Visible-light-driven photoelectrochemical and photocatalytic performances of Cr-doped $SrTiO_3/TiO_2$ heterostructured nanotube arrays.,' *Sci. Rep.*, vol. 3, p. 2720, 2013, ISSN: 2045-2322.

[171] T. O'Keeke, 'Pourbaix Diagrams,' in *Encycl. Mater. Sci. Technol.* Elsevier, Jan. 2001, pp. 7774–7781, ISBN: 9780080431529.

[172] Y.-T. Sul, C. B. Johansson, Y. Jeong, and T. Albrektsson, 'The electrochemical oxide growth behaviour on titanium in acid and alkaline electrolytes,' *Med. Eng. Phys.*, vol. 23, no. 5, pp. 329–346, Jun. 2001.

[173] J. R. Birch and T. D. Burleigh, 'Oxides Formed on Titanium by Polishing, Etching, Anodizing, or Thermal Oxidizing,' *CORROSION*, vol. 56, no. 12, pp. 1233–1241, Dec. 2000, ISSN: 0010-9312.

[174] H.-Y. Chen and F.-H. Lu, 'Oxidation behavior of titanium nitride films,' *J. Vac. Sci. Technol. A Vacuum, Surfaces, Film.*, vol. 23, no. 4, pp. 1006–1009, Jul. 2005, ISSN: 0734-2101.

[175] K. Hinode, Y. Homma, M. Horiuchi, and T. Takahashi, 'Morphology-dependent oxidation behavior of reactively sputtered titanium-nitride films,' *J. Vac. Sci. Technol. A Vacuum, Surfaces, Film.*, vol. 15, no. 4, pp. 2017–2022, Jul. 1997, ISSN: 0734-2101.

[176] M. Jarosz, K. Syrek, J. Kapusta-Kołodziej, J. Mech, K. Małek, K. Hnida, T. Łojewski, M. Jaskuła, and G. D. Sulka, 'Heat Treatment Effect on Crystalline Structure and Photoelectrochemical Properties of Anodic TiO_2 Nanotube Arrays Formed in Ethylene Glycol and Glycerol Based Electrolytes,' *J. Phys. Chem. C*, vol. 119, no. 42, pp. 24 182–24 191, Oct. 2015, ISSN: 1932-7447.

[177] J. Zhang, P. Zhou, J. Liu, and J. Yu, 'New understanding of the difference of photocatalytic activity among anatase, rutile and brookite TiO_2,' *Phys. Chem. Chem. Phys.*, vol. 16, no. 38, pp. 20 382–20 386, Aug. 2014, ISSN: 1463-9076.

[178] M. Licklederer, R. Mohammadi, N. T. Nguyen, H. Park, S. Hejazi, M. Halik, N. Vogel, M. Altomare, and P. Schmuki, 'Dewetted Au Nanoparticles on TiO_2 Surfaces: Evidence of a Size-Independent Plasmonic Photoelectrochemical Response,' *J. Phys. Chem. C*, vol. 123, no. 27, pp. 16 934–16 942, Jul. 2019, ISSN: 1932-7447.

[179] O. A. Krysiak, P. J. Barczuk, K. Bienkowski, T. Wojciechowski, and J. Augustynski, 'The photocatalytic activity of rutile and anatase TiO_2 electrodes modified with plasmonic metal nanoparticles followed by photoelectrochemical measurements,' *Catal. Today*, vol. 321-322, pp. 52–58, Feb. 2019, ISSN: 09205861.

[180] D. Thompson, 'Michael Faraday's recognition of ruby gold: the birth of modern nanotechnology,' *Gold Bull.*, vol. 40, no. 4, pp. 267–269, Dec. 2007, ISSN: 0017-1557.

[181] M. Jahn, S. Patze, I. J. Hidi, R. Knipper, A. I. Radu, A. Mühlig, S. Yüksel, V. Peksa, K. Weber, T. Mayerhöfer, D. Cialla-May, and J. Popp, 'Plasmonic nanostructures for surface enhanced spectroscopic methods,' *Analyst*, vol. 141, no. 3, pp. 756–793, Jan. 2016, ISSN: 0003-2654.

[182] H. Oka and Y. Ohdaira, 'Simple model of saturable localised surface plasmon,' *Sci. Rep.*, vol. 8, no. 1, p. 2643, Dec. 2018, ISSN: 2045-2322.

[183] E. Petryayeva and U. J. Krull, 'Localized surface plasmon resonance: Nanostructures, bioassays and biosensing—A review,' *Anal. Chim. Acta*, vol. 706, no. 1, pp. 8–24, Nov. 2011, ISSN: 00032670.

[184] Y.-C. Yeh, B. Creran, and V. M. Rotello, 'Gold nanoparticles: preparation, properties, and applications in bionanotechnology,' *Nanoscale*, vol. 4, no. 6, pp. 1871–1880, Mar. 2012, ISSN: 2040-3364.

[185] M. Loos, 'Nanoscience and Nanotechnology,' in *Carbon Nanotub. Reinf. Compos.* Elsevier, Jan. 2015, pp. 1–36, ISBN: 978-1-4557-3195-4.

[186] T. Lednický and A. Bonyár, 'Large Scale Fabrication of Ordered Gold Nanoparticle-Epoxy Surface Nanocomposites and Their Application as Label-Free Plasmonic DNA Biosensors,' *ACS Appl. Mater. Interfaces*, vol. 12, no. 4, pp. 4804–4814, Jan. 2020, ISSN: 1944-8244.

[187] A. Bonyár, 'Label-Free Nucleic Acid Biosensing Using Nanomaterial-Based Localized Surface Plasmon Resonance Imaging: A Review,' *ACS Appl. Nano Mater.*, vol. 3, no. 9, pp. 8506–8521, Sep. 2020, ISSN: 2574-0970.

[188] C. V. Thompson, 'Solid-State Dewetting of Thin Films,' *Annu. Rev. Mater. Res.*, vol. 42, no. 1, pp. 399–434, 2012, ISSN: 1531-7331.

[189] T. L. Temple and S. Dligatch, 'Role of the spacer layer in plasmonic antireflection coatings comprised of gold or silver nanoparticles,' *J. Photonics Energy*, vol. 5, no. 1, p. 053 095, 2015, ISSN: 1947-7988.

[190] F. Leroy, Borowik, F. Cheynis, Y. Almadori, S. Curiotto, M. Trautmann, J. C. Barbé, and P. Müller, 'How to control solid state dewetting: A short review,' *Surf. Sci. Rep.*, vol. 71, no. 2, pp. 391–409, 2016, ISSN: 01675729.

[191] P. Farzinpour, A. Sundar, K. D. Gilroy, Z. E. Eskin, R. A. Hughes, and S. Neretina, 'Altering the dewetting characteristics of ultrathin gold and silver films using a sacrificial antimony layer,' *Nanotechnology*, vol. 23, no. 49, 2012, ISSN: 09574484.

[192] T. Kim, H. Im, T. J. Kang, and Y. H. Kim, 'Preferential dewetting of gold thin films on single walled carbon nanotubes to produce nanogap electrodes,' *J. Mater. Chem. C*, vol. 4, no. 24, pp. 5725–5730, 2016, ISSN: 20507526.

[193] M. Yoshino, Y. Kubota, Y. Nakagawa, and M. Terano, 'Efficient fabrication process of ordered metal nanodot arrays for infrared plasmonic sensor,' *Micromachines*, vol. 10, no. 6, pp. 27–30, 2019, ISSN: 2072666X.

[194] M. Naffouti, R. Backofen, M. Salvalaglio, T. Bottein, M. Lodari, A. Voigt, T. David, A. Benkouider, I. Fraj, L. Favre, A. Ronda, I. Berbezier, D. Grosso, M. Abbarchi, and M. Bollani, 'Complex dewetting scenarios of ultrathin silicon films for large-scale nanoarchitectures,' *Sci. Adv.*, vol. 3, no. 11, pp. 1–11, 2017, ISSN: 23752548.

[195] J. Ye, 'Fabrication of ordered arrays of micro- and nanoscale features with control over their shape and size via templated solid-state dewetting,' *Sci. Rep.*, vol. 5, no. 5, pp. 1–8, 2015, ISSN: 20452322.

[196] A. L. Giermann and C. V. Thompson, 'Solid-state dewetting for ordered arrays of crystallographically oriented metal particles,' *Appl. Phys. Lett.*, vol. 86, no. 12, p. 121 903, Mar. 2005, ISSN: 0003-6951.

[197] J. Basu, C. B. Carter, R. Divakar, B. Mukherjee, and N. Ravishankar, 'Nanopatterning by solid-state dewetting on reconstructed ceramic surfaces,' *Appl. Phys. Lett.*, vol. 94, no. 17, pp. 1–4, 2009, ISSN: 00036951.

[198] A. Plaud, A. Sarrazin, J. Béal, J. Proust, P. Royer, J. L. Bijeon, J. Plain, P. M. Adam, and T. Maurer, 'Copolymer template control of gold nanoparticle synthesis via thermal annealing,' *J. Nanoparticle Res.*, vol. 15, no. 12, 2013, ISSN: 13880764.

[199] S. Yang, F. Xu, S. Ostendorp, G. Wilde, H. Zhao, and Y. Lei, 'Template-confined dewetting process to surface nanopatterns: Fabrication, structural tunability, and structure-related properties,' *Adv. Funct. Mater.*, vol. 21, no. 13, pp. 2446–2455, 2011, ISSN: 1616301X.

[200] M. Altomare, N. T. Nguyen, and P. Schmuki, 'Templated dewetting: designing entirely self-organized platforms for photocatalysis,' *Chem. Sci.*, vol. 7, no. 12, pp. 6865–6886, 2016, ISSN: 20416539.

[201] H. Ikeda, M. Iwai, D. Nakajima, T. Kikuchi, S. Natsui, N. Sakaguchi, and R. O. Suzuki, 'Nanostructural characterization of ordered gold particle arrays fabricated via aluminum anodizing, sputter coating, and dewetting,' *Appl. Surf. Sci.*, vol. 465, pp. 747–753, Jan. 2019, ISSN: 01694332.

[202] A. Bonyár, T. Lednický, and J. Hubálek, 'LSPR Nanosensors with Highly Ordered Gold Nanoparticles Fabricated on Nanodimpled Aluminium Templates,' *Procedia Eng.*, vol. 168, pp. 1160–1163, Jan. 2016, ISSN: 18777058.

[203] X. Fan, Q. Hao, R. Jin, H. Huang, Z. Luo, X. Yang, Y. Chen, X. Han, M. Sun, Q. Jing, Z. Dong, and T. Qiu, 'Assembly of gold nanoparticles into aluminum nanobowl array,' *Sci. Rep.*, vol. 7, no. 1, p. 2322, Dec. 2017, ISSN: 2045-2322.

[204] V. G. Kravets, A. V. Kabashin, W. L. Barnes, and A. N. Grigorenko, 'Plasmonic Surface Lattice Resonances: A Review of Properties and Applications,' *Chem. Rev.*, vol. 118, no. 12, pp. 5912–5951, Jun. 2018, ISSN: 0009-2665.

[205] J. Liu, H. He, D. Xiao, S. Yin, W. Ji, S. Jiang, D. Luo, B. Wang, and Y. Liu, 'Recent Advances of Plasmonic Nanoparticles and their Applications,' *Materials (Basel).*, vol. 11, no. 10, p. 1833, Sep. 2018, ISSN: 1996-1944.

[206] J. Homola, Ed., *Surface Plasmon Resonance Based Sensors*, ser. Springer Series on Chemical Sensors and Biosensors. Berlin, Heidelberg: Springer Berlin Heidelberg, 2006, vol. 4, ISBN: 978-3-540-33918-2.

[207] A. Dmitriev, Ed., *Nanoplasmonic Sensors.* New York, NY: Springer New York, 2012, ISBN: 978-1-4614-3932-5.

[208] S. A. Maier, *Plasmonics: Fundamentals and Applications.* New York, NY: Springer US, 2007, ISBN: 978-0-387-33150-8.

[209] R. B. M. Schasfoort, Ed., *Handbook of Surface Plasmon Resonance.* Cambridge: Royal Society of Chemistry, May 2017, ISBN: 978-1-78262-730-2.

[210] F. Vallée, 'Optical Properties of Metallic Nanoparticles,' in *Nanomater. Nanochemistry*, ser. Springer Series in Materials Science, vol. 232, Berlin, Heidelberg: Springer Berlin Heidelberg, 2007, pp. 197–227, ISBN: 978-3-319-25072-4.

[211] F. Ligmajer, 'Advanced plasmonic materials for metasurfaces and photochemistry,' Ph.D. dissertation, 2018, p. 142.

[212] J. Dai, 'Design and Characterization of Plasmonic Absorbers Based on Gold Nanospheres,' Ph.D. dissertation, KTH, School of Information and Communication Technology (ICT), 2012, p. 69.

[213] N. Jiang, X. Zhuo, and J. Wang, 'Active Plasmonics: Principles, Structures, and Applications,' *Chem. Rev.*, vol. 118, no. 6, pp. 3054–3099, Mar. 2018, ISSN: 0009-2665.

[214] E. Kretschmann and H. Raether, 'Notizen: Radiative Decay of Non Radiative Surface Plasmons Excited by Light,' *Zeitschrift für Naturforsch. A*, vol. 23, no. 12, pp. 2135–2136, Dec. 1968, ISSN: 1865-7109.

[215] V. Amendola, R. Pilot, M. Frasconi, O. M. Maragò, and M. A. Iatì, 'Surface plasmon resonance in gold nanoparticles: a review,' *J. Phys. Condens. Matter*, vol. 29, no. 20, p. 203 002, May 2017, ISSN: 0953-8984.

[216] A. Bonyár, I. Csarnovics, and G. Szántó, 'Simulation and characterization of the bulk refractive index sensitivity of coupled plasmonic nanostructures with the enhancement factor,' *Photonics Nanostructures - Fundam. Appl.*, vol. 31, pp. 1–7, Sep. 2018, ISSN: 15694410.

[217] E. Martinsson, B. Sepulveda, P. Chen, A. Elfwing, B. Liedberg, and D. Aili, 'Optimizing the Refractive Index Sensitivity of Plasmonically Coupled Gold Nanoparticles,' *Plasmonics*, vol. 9, no. 4, pp. 773–780, Aug. 2014, ISSN: 1557-1955.

[218] J. Jatschka, A. Dathe, A. Csáki, W. Fritzsche, and O. Stranik, 'Propagating and localized surface plasmon resonance sensing — A critical comparison based on measurements and theory,' *Sens. Bio-Sensing Res.*, vol. 7, pp. 62–70, Mar. 2016, ISSN: 22141804.

[219] J. A. Ruemmele, W. P. Hall, L. K. Ruvuna, and R. P. Van Duyne, 'A Localized Surface Plasmon Resonance Imaging Instrument for Multiplexed Biosensing,' *Anal. Chem.*, vol. 85, no. 9, pp. 4560–4566, May 2013, ISSN: 0003-2700.

[220] A. Csáki, O. Stranik, and W. Fritzsche, 'Localized surface plasmon resonance based biosensing,' *Expert Rev. Mol. Diagn.*, vol. 18, no. 3, pp. 279–296, Mar. 2018, ISSN: 1473-7159.

[221] S. Unser, I. Bruzas, J. He, and L. Sagle, 'Localized Surface Plasmon Resonance Biosensing: Current Challenges and Approaches,' *Sensors*, vol. 15, no. 7, pp. 15 684–15 716, Jul. 2015, ISSN: 1424-8220.

[222] J. D. Jackson, *Classical electrodynamics*. Wiley, 1999, p. 808, ISBN: 9780471309321.

[223] C. F. Bohren and D. R. Huffman, *Absorption and Scattering of Light by Small Particles*. Wiley, Apr. 1998, p. 530, ISBN: 9780471293408.

[224] G. Mie, 'Beiträge zur Optik trüber Medien, speziell kolloidaler Metallösungen,' *Ann. Phys.*, vol. 330, no. 3, pp. 377–445, Jan. 1908, ISSN: 00033804.

[225] X. Chong, N. Jiang, Z. Zhang, S. Roy, and J. R. Gord, 'Plasmonic resonance-enhanced local photothermal energy deposition by aluminum nanoparticles,' *J. Nanoparticle Res.*, vol. 15, no. 6, p. 1678, Jun. 2013, ISSN: 1388-0764.

[226] M. Dalarsson, S. Nordebo, D. Sjöberg, and R. Bayford, 'Absorption and optimal plasmonic resonances for small ellipsoidal particles in lossy media,' *J. Phys. D. Appl. Phys.*, vol. 50, no. 34, p. 345 401, Aug. 2017, ISSN: 0022-3727.

[227] N. M. Figueiredo and A. Cavaleiro, 'Dielectric Properties of Shape-Distributed Ellipsoidal Particle Systems,' *Plasmonics*, vol. 15, no. 2, pp. 379–397, Apr. 2020, ISSN: 1557-1955.

[228] M. Alsawafta, M. Wahbeh, and V.-V. Truong, 'Plasmonic Modes and Optical Properties of Gold and Silver Ellipsoidal Nanoparticles by the Discrete Dipole Approximation,' *J. Nanomater.*, vol. 2012, pp. 1–10, 2012, ISSN: 1687-4110.

[229] C. L. Haynes, A. D. McFarland, L. Zhao, R. P. Van Duyne, G. C. Schatz, L. Gunnarsson, J. Prikulis, B. Kasemo, and M. Käll, 'Nanoparticle Optics: The Importance of Radiative Dipole Coupling in Two-Dimensional Nanoparticle Arrays,' *J. Phys. Chem. B*, vol. 107, no. 30, pp. 7337–7342, Jul. 2003, ISSN: 1520-6106.

[230] A. D. Humphrey and W. L. Barnes, 'Plasmonic surface lattice resonances on arrays of different lattice symmetry,' *Phys. Rev. B*, vol. 90, no. 7, p. 075 404, Aug. 2014, ISSN: 1098-0121.

[231] S. Rodriguez, M. Schaafsma, A. Berrier, and J. Gómez Rivas, 'Collective resonances in plasmonic crystals: Size matters,' *Phys. B Condens. Matter*, vol. 407, no. 20, pp. 4081–4085, Oct. 2012, ISSN: 09214526.

[232] R. Borah and S. W. Verbruggen, 'Coupled Plasmon Modes in 2D Gold Nanoparticle Clusters and Their Effect on Local Temperature Control,' *J. Phys. Chem. C*, vol. 123, no. 50, pp. 30 594–30 603, Dec. 2019, ISSN: 1932-7447.

[233] S. Lal, N. K. Grady, J. Kundu, C. S. Levin, J. B. Lassiter, and N. J. Halas, 'Tailoring plasmonic substrates for surface enhanced spectroscopies,' *Chem. Soc. Rev.*, vol. 37, no. 5, p. 898, Apr. 2008, ISSN: 0306-0012.

[234] G. V. P. Kumar, 'Plasmonic nano-architectures for surface enhanced Raman scattering: a review,' *J. Nanophotonics*, vol. 6, no. 1, p. 064 503, May 2012, ISSN: 1934-2608.

[235] F. Le, D. W. Brandl, Y. A. Urzhumov, H. Wang, J. Kundu, N. J. Halas, J. Aizpurua, and P. Nordlander, 'Metallic Nanoparticle Arrays: A Common Substrate for Both Surface-Enhanced Raman Scattering and Surface-Enhanced Infrared Absorption,' *ACS Nano*, vol. 2, no. 4, pp. 707–718, Apr. 2008, ISSN: 1936-0851.

[236] V. Mondes, E. Antonsson, J. Plenge, C. Raschpichler, I. Halfpap, A. Menski, C. Graf, M. F. Kling, and E. Rühl, 'Plasmonic electric near-field enhancement in self-organized gold nanoparticles in macroscopic arrays,' *Appl. Phys. B*, vol. 122, no. 6, p. 155, Jun. 2016, ISSN: 0946-2171.

[237] M. B. Ross, C. A. Mirkin, and G. C. Schatz, 'Optical Properties of One-, Two-, and Three-Dimensional Arrays of Plasmonic Nanostructures,' *J. Phys. Chem. C*, vol. 120, no. 2, pp. 816–830, Jan. 2016, ISSN: 1932-7447.

[238] B. Liedberg, C. Nylander, and I. Lunström, 'Surface plasmon resonance for gas detection and biosensing,' *Sensors and Actuators*, vol. 4, no. C, pp. 299–304, Jan. 1983, ISSN: 02506874.

[239] H. Nguyen, J. Park, S. Kang, and M. Kim, 'Surface Plasmon Resonance: A Versatile Technique for Biosensor Applications,' *Sensors*, vol. 15, no. 5, pp. 10 481–10 510, May 2015, ISSN: 1424-8220.

[240] J. Homola, 'Surface Plasmon Resonance Sensors for Detection of Chemical and Biological Species,' *Chem. Rev.*, vol. 108, no. 2, pp. 462–493, Feb. 2008, ISSN: 0009-2665.

[241] C. L. Wong and M. Olivo, 'Surface Plasmon Resonance Imaging Sensors: A Review,' *Plasmonics*, vol. 9, no. 4, pp. 809–824, Aug. 2014, ISSN: 1557-1955.

[242] T. M. Chinowsky, S. D. Soelberg, P. Baker, N. R. Swanson, P. Kauffman, A. Mactutis, M. S. Grow, R. Atmar, S. S. Yee, and C. E. Furlong, 'Portable 24-analyte surface plasmon resonance instruments for rapid, versatile biodetection,' *Biosens. Bioelectron.*, vol. 22, no. 9-10, pp. 2268–2275, Apr. 2007, ISSN: 09565663.

[243] B. Feltis, B. Sexton, F. Glenn, M. Best, M. Wilkins, and T. Davis, 'A hand-held surface plasmon resonance biosensor for the detection of ricin and other biological agents,' *Biosens. Bioelectron.*, vol. 23, no. 7, pp. 1131–1136, Feb. 2008, ISSN: 09565663.

[244] T. M. Chinowsky, J. G. Quinn, D. U. Bartholomew, R. Kaiser, and J. L. Elkind, 'Performance of the Spreeta 2000 integrated surface plasmon resonance affinity sensor,' *Sensors Actuators B Chem.*, vol. 91, no. 1-3, pp. 266–274, Jun. 2003, ISSN: 09254005.

[245] A. N. Naimushin, S. D. Soelberg, D. U. Bartholomew, J. L. Elkind, and C. E. Furlong, 'A portable surface plasmon resonance (SPR) sensor system with temperature regulation,' *Sensors Actuators B Chem.*, vol. 96, no. 1-2, pp. 253–260, Nov. 2003, ISSN: 09254005.

[246] J. Cao, T. Sun, and K. T. Grattan, 'Gold nanorod-based localized surface plasmon resonance biosensors: A review,' *Sensors Actuators B Chem.*, vol. 195, pp. 332–351, May 2014, ISSN: 09254005.

[247] M. Tu, T. Sun, and K. Grattan, 'LSPR optical fibre sensors based on hollow gold nanostructures,' *Sensors Actuators B Chem.*, vol. 191, pp. 37–44, Feb. 2014, ISSN: 09254005.

[248] B. Sepúlveda, P. C. Angelomé, L. M. Lechuga, and L. M. Liz-Marzán, 'LSPR-based nanobiosensors,' *Nano Today*, vol. 4, no. 3, pp. 244–251, Jun. 2009, ISSN: 17480132.

[249] M. P. Raphael, J. A. Christodoulides, J. B. Delehanty, J. P. Long, P. E. Pehrsson, and J. M. Byers, 'Quantitative LSPR Imaging for Biosensing with Single Nanostructure Resolution,' *Biophys. J.*, vol. 104, no. 1, pp. 30–36, Jan. 2013, ISSN: 00063495.

[250] G. A. Lopez, M.-C. Estevez, M. Soler, and L. M. Lechuga, 'Recent advances in nanoplasmonic biosensors: applications and lab-on-a-chip integration,' *Nanophotonics*, vol. 6, no. 1, pp. 123–136, Jan. 2016, ISSN: 2192-8614.

[251] J. Jiang, X. Wang, S. Li, F. Ding, N. Li, S. Meng, R. Li, J. Qi, Q. Liu, and G. L. Liu, 'Plasmonic nano-arrays for ultrasensitive bio-sensing,' *Nanophotonics*, vol. 7, no. 9, pp. 1517–1531, Sep. 2018, ISSN: 2192-8614.

[252] J. Roether, K.-Y. Chu, N. Willenbacher, A. Q. Shen, and N. Bhalla, 'Real-time monitoring of DNA immobilization and detection of DNA polymerase activity by a microfluidic nanoplasmonic platform,' *Biosens. Bioelectron.*, vol. 142, p. 111 528, Oct. 2019, ISSN: 09565663.

[253] S. Thamm, A. Csàki, and W. Fritzsche, 'LSPR Detection of Nucleic Acids on Nanoparticle Monolayers,' in *Methods Mol. Biol.* Vol. 1811, 2018, pp. 163–171.

[254] T. Stakenborg and L. Lagae, 'Gold nanoring as a sensitive plasmonic biosensor for on-chip DNA detection,' *Appl. Phys. Lett.*, vol. 100, no. 17, p. 173 114, Apr. 2012, ISSN: 0003-6951.

[255] T. Schneider, N. Jahr, J. Jatschka, A. Csaki, O. Stranik, and W. Fritzsche, 'Localized surface plasmon resonance (LSPR) study of DNA hybridization at single nanoparticle transducers,' *J. Nanoparticle Res.*, vol. 15, no. 4, p. 1531, Apr. 2013, ISSN: 1388-0764.

[256] X. Qi and J. Bi, 'Plasmonic sensors relying on nanoparticle arrays created by a template-directed dewetting process,' *Opt. Commun.*, vol. 453, p. 124 328, Dec. 2019, ISSN: 00304018.

[257] H. Su, X. R. Cheng, T. Endo, and K. Kerman, 'Photonic crystals on copolymer film for label-free detection of DNA hybridization,' *Biosens. Bioelectron.*, vol. 103, pp. 158–162, Apr. 2018, ISSN: 09565663.

[258] L. Soares, A. Csáki, J. Jatschka, W. Fritzsche, O. Flores, R. Franco, and E. Pereira, 'Localized surface plasmon resonance (LSPR) biosensing using gold nanotriangles: detection of DNA hybridization events at room temperature,' *Analyst*, vol. 139, no. 19, pp. 4964–4973, Oct. 2014, ISSN: 0003-2654.

[259] S. Kaye, Z. Zeng, M. Sanders, K. Chittur, P. M. Koelle, R. Lindquist, U. Manne, Y. Lin, and J. Wei, 'Label-free detection of DNA hybridization with a compact LSPR-based fiber-optic sensor,' *Analyst*, vol. 142, no. 11, pp. 1974–1981, Jun. 2017, ISSN: 0003-2654.

[260] S. Zhu, H. Li, M. Yang, and S. W. Pang, 'Label-free detection of live cancer cells and DNA hybridization using 3D multilayered plasmonic biosensor,' *Nanotechnology*, vol. 29, no. 36, p. 365 503, Sep. 2018, ISSN: 0957-4484.

[261] M. R. Gartia, A. Hsiao, A. Pokhriyal, S. Seo, G. Kulsharova, B. T. Cunningham, T. C. Bond, and G. L. Liu, 'Colorimetric Plasmon Resonance Imaging Using Nano Lycurgus Cup Arrays,' *Adv. Opt. Mater.*, vol. 1, no. 1, pp. 68–76, Jan. 2013, ISSN: 21951071.

[262] M. Svedendahl, S. Chen, A. Dmitriev, and M. Käll, 'Refractometric Sensing Using Propagating versus Localized Surface Plasmons: A Direct Comparison,' *Nano Lett.*, vol. 9, no. 12, pp. 4428–4433, Dec. 2009, ISSN: 1530-6984.

[263] A. V. Kabashin, P. Evans, S. Pastkovsky, W. Hendren, G. A. Wurtz, R. Atkinson, R. Pollard, V. A. Podolskiy, and A. V. Zayats, 'Plasmonic nanorod metamaterials for biosensing,' *Nat. Mater.*, vol. 8, no. 11, pp. 867–871, Nov. 2009, ISSN: 1476-1122.

[264] H. Xu and M. Käll, 'Modeling the optical response of nanoparticle-based surface plasmon resonance sensors,' *Sensors Actuators B Chem.*, vol. 87, no. 2, pp. 244–249, Dec. 2002, ISSN: 09254005.

[265] H. Chen, X. Kou, Z. Yang, W. Ni, and J. Wang, 'Shape- and Size-Dependent Refractive Index Sensitivity of Gold Nanoparticles,' *Langmuir*, vol. 24, no. 10, pp. 5233–5237, May 2008, ISSN: 0743-7463.

[266] O. Saison-Francioso, G. Lévêque, R. Boukherroub, S. Szunerits, and A. Akjouj, 'Dependence between the Refractive-Index Sensitivity of Metallic Nanoparticles and the Spectral Position of Their Localized Surface Plasmon Band: A Numerical and Analytical Study,' *J. Phys. Chem. C*, vol. 119, no. 51, pp. 28 551–28 559, Dec. 2015, ISSN: 1932-7447.

[267] N. Hooshmand, J. A. Bordley, and M. A. El-Sayed, 'The Sensitivity of the Distance Dependent Plasmonic Coupling between Two Nanocubes to their Orientation: Edge-to-Edge versus Face-to-Face,' *J. Phys. Chem. C*, vol. 120, no. 8, pp. 4564–4570, Mar. 2016, ISSN: 1932-7447.

[268] Y. Chen, 'Nanofabrication by electron beam lithography and its applications: A review,' *Microelectron. Eng.*, vol. 135, pp. 57–72, Mar. 2015, ISSN: 01679317.

[269] S. Zhu and W. Zhou, 'Plasmonic properties of two-dimensional metallic nanoholes fabricated by focused ion beam lithography,' *J. Nanoparticle Res.*, vol. 14, no. 3, p. 652, Mar. 2012, ISSN: 1388-0764.

[270] S. Krishnamoorthy, S. Krishnan, P. Thoniyot, and H. Y. Low, 'Inherently Reproducible Fabrication of Plasmonic Nanoparticle Arrays for SERS by Combining Nanoimprint and Copolymer Lithography,' *ACS Appl. Mater. Interfaces*, vol. 3, no. 4, pp. 1033–1040, Apr. 2011, ISSN: 1944-8244.

[271] C.-C. Yu and H.-L. Chen, 'Nanoimprint technology for patterning functional materials and its applications,' *Microelectron. Eng.*, vol. 132, pp. 98–119, Jan. 2015, ISSN: 01679317.

[272] S. Dickreuter, J. Gleixner, A. Kolloch, J. Boneberg, E. Scheer, and P. Leiderer, 'Mapping of plasmonic resonances in nanotriangles,' *Beilstein J. Nanotechnol.*, vol. 4, no. 1, pp. 588–602, Sep. 2013, ISSN: 2190-4286.

[273] D. T. Nguyen, D.-J. Kim, and K.-S. Kim, 'Controlled synthesis and biomolecular probe application of gold nanoparticles,' *Micron*, vol. 42, no. 3, pp. 207–227, Apr. 2011, ISSN: 09684328.

[274] N. E. Cant, K. Critchley, H.-L. Zhang, and S. D. Evans, 'Surface functionalisation for the self-assembly of nanoparticle/polymer multilayer films,' *Thin Solid Films*, vol. 426, no. 1-2, pp. 31–39, Feb. 2003, ISSN: 00406090.

[275] J. Magura, A. Zeleňáková, V. Zeleňák, and M. Kaňuchová, 'Thiol-modified gold nanoparticles deposited on silica support using dip coating,' *Appl. Surf. Sci.*, vol. 315, no. 1, pp. 392–399, Oct. 2014, ISSN: 01694332.

[276] A. Bonyár, I. Csarnovics, M. Veres, L. Himics, A. Csik, J. Kámán, L. Balázs, and S. Kökényesi, 'Investigation of the performance of thermally generated gold nanoislands for LSPR and SERS applications,' *Sensors Actuators B Chem.*, vol. 255, pp. 433–439, Feb. 2018, ISSN: 09254005.

[277] N. Bhalla, S. Sathish, C. J. Galvin, R. A. Campbell, A. Sinha, and A. Q. Shen, 'Plasma-Assisted Large-Scale Nanoassembly of Metal-Insulator Bioplasmonic Mushrooms,' *ACS Appl. Mater. Interfaces*, vol. 10, no. 1, pp. 219–226, Jan. 2018, ISSN: 1944-8244.

[278] E. Hutter and M.-P. Pileni, 'Detection of DNA Hybridization by Gold Nanoparticle Enhanced Transmission Surface Plasmon Resonance Spectroscopy,' *J. Phys. Chem. B*, vol. 107, no. 27, pp. 6497–6499, Jul. 2003, ISSN: 1520-6106.

[279] T. Zhang, H. Li, S. Hou, Y. Dong, G. Pang, and Y. Zhang, 'Construction of Plasmonic Core-Satellite Nanostructures on Substrates Based on DNA-Directed Self-Assembly as a Sensitive and Reproducible Biosensor,' *ACS Appl. Mater. Interfaces*, vol. 7, no. 49, pp. 27 131–27 139, Dec. 2015, ISSN: 1944-8244.

[280] R. Singh, A. Feltmeyer, O. Saiapina, J. Juzwik, B. Arenz, and A. Abbas, 'Rapid and PCR-free DNA Detection by Nanoaggregation-Enhanced Chemiluminescence,' *Sci. Rep.*, vol. 7, no. 1, p. 14 011, Dec. 2017, ISSN: 2045-2322.

[281] D. Zopf, A. Pittner, A. Dathe, N. Grosse, A. Csáki, K. Arstila, J. J. Toppari, W. Schott, D. Dontsov, G. Uhlrich, W. Fritzsche, and O. Stranik, 'Plasmonic Nanosensor Array for Multiplexed DNA-based Pathogen Detection,' *ACS Sensors*, vol. 4, no. 2, pp. 335–343, Feb. 2019, ISSN: 2379-3694.

[282] S.-G. Park, X. Xiao, J. Min, C. Mun, H. S. Jung, V. Giannini, R. Weissleder, S. A. Maier, H. Im, and D. Kim, 'Self-Assembly of Nanoparticle-Spiked Pillar Arrays for Plasmonic Biosensing,' *Adv. Funct. Mater.*, vol. 29, no. 43, p. 1 904 257, Oct. 2019, ISSN: 1616-301X.

[283] Y. Ozaki, K. Kneipp, and R. Aroca, *Frontiers of Surface-Enhanced Raman Scattering*, Y. Ozaki, K. Kneipp, and R. Aroca, Eds. Chichester, UK: John Wiley & Sons, Ltd, Mar. 2014, vol. 9781118359, pp. 1–313, ISBN: 9781118703601.

[284] H. M. Jin, J. Y. Kim, M. Heo, S.-J. Jeong, B. H. Kim, S. K. Cha, K. H. Han, J. H. Kim, G. G. Yang, J. Shin, and S. O. Kim, 'Ultralarge Area Sub-10 nm Plasmonic Nanogap Array by Block Copolymer Self-Assembly for Reliable High-Sensitivity SERS,' *ACS Appl. Mater. Interfaces*, vol. 10, no. 51, pp. 44 660–44 667, Dec. 2018, ISSN: 1944-8244.

[285] N. D. Israelsen, C. Hanson, and E. Vargis, 'Nanoparticle Properties and Synthesis Effects on Surface-Enhanced Raman Scattering Enhancement Factor: An Introduction,' *Sci. World J.*, vol. 2015, pp. 1–12, 2015, ISSN: 2356-6140.

[286] T. Lednický, 'Template Assisted Electrodeposition of Multilayer Nanostructures,' Master's Thesis, Brno University of Technology, 2014, p. 83, ISBN: 0824758498.

[287] W. Yingwei, W. Fei, F. Liping, F. Jingyue, W. Guang, C. Shengli, and Z. Xueao, 'Self-assembled Au nanoparticles arrays by porous anodic alumina oxide and optical properties,' *Infrared Laser Eng.*, vol. 42, no. 11, pp. 3047–3052, Nov. 2013, ISSN: 1007-2276.

[288] H. Jo, D. Yoon, A. Sohn, D.-W. Kim, Y. Choi, T. Kang, D. Choi, S.-W. Kim, and L. P. Lee, 'Asymmetrically Coupled Plasmonic Core and Nanotriplet Satellites,' *J. Phys. Chem. C*, vol. 118, no. 32, pp. 18 659–18 667, Aug. 2014, ISSN: 1932-7447.

[289] L. Zaraska, G. D. Sulka, J. Szeremeta, and M. Jaskuła, ‘Porous anodic alumina formed by anodization of aluminum alloy (AA1050) and high purity aluminum,’ *Electrochim. Acta*, vol. 55, no. 14, pp. 4377–4386, 2010, ISSN: 00134686.

[290] M. Michalska-Domańska, W. J. Stępniowski, and L. R. Jaroszewicz, ‘Characterization of nanopores arrangement of anodic alumina layers synthesized on low-(AA1050) and high-purity aluminum by two-step anodizing in sulfuric acid with addition of ethylene glycol at low temperature,’ *J. Porous Mater.*, vol. 24, no. 3, pp. 779–786, 2017, ISSN: 15734854.

[291] C. K. Ng and A. H. Ngan, ‘Precise control of nanohoneycomb ordering over anodic aluminum oxide of square centimeter areas,’ *Chem. Mater.*, vol. 23, no. 23, pp. 5264–5268, 2011, ISSN: 08974756.

[292] R. W. Revie, Ed., *Uhlig’s Corrosion Handbook*. Hoboken, NJ, USA: John Wiley & Sons, Inc., Mar. 2011, ISBN: 9780470872864.

[293] C. Y. Liu, A. Datta, and Y. L. Wang, ‘Ordered anodic alumina nanochannels on focused-ion-beam-prepatterned aluminum surfaces,’ *Appl. Phys. Lett.*, vol. 78, no. 1, pp. 120–122, Jan. 2001, ISSN: 0003-6951.

[294] B. Chen, K. Lu, and Z. Tian, ‘Novel Patterns by Focused Ion Beam Guided Anodization,’ *Langmuir*, vol. 27, no. 2, pp. 800–808, Jan. 2011, ISSN: 0743-7463.

[295] W. CE, T. S, S. K, S. T, and S. S, ‘Fabrication of Ordered Arrays of Anodic Aluminum Oxide Pores with Interpore Distance Smaller than the Pitch of Nanopits formed by Ion Beam Etching,’ *J. Mater. Sci. Nanotechnol.*, vol. 1, no. 1, p. 1, Aug. 2014, ISSN: 23489812.

[296] W. Lee, R. Ji, C. A. Ross, U. Gösele, and K. Nielsch, ‘Wafer-Scale Ni Imprint Stamps for Porous Alumina Membranes Based on Interference Lithography,’ *Small*, vol. 2, no. 8-9, pp. 978–982, Aug. 2006, ISSN: 1613-6810.

[297] T. S. Kustandi, W. W. Loh, H. Gao, and H. Y. Low, ‘Wafer-Scale Near-Perfect Ordered Porous Alumina on Substrates by Step and Flash Imprint Lithography,’ *ACS Nano*, vol. 4, no. 5, pp. 2561–2568, May 2010, ISSN: 1936-0851.

[298] W. Jiang, Y. Wang, D. J. Srolovitz, and W. Bao, ‘Solid-state dewetting on curved substrates,’ *Phys. Rev. Mater.*, vol. 2, no. 11, pp. 1–13, 2018, ISSN: 24759953.

[299] M. Syed, ‘Surface Morphology of Gold Thin Films using RF Magnetron Sputtering,’ May 2018.

[300] S. Wu, H. Chen, X. Du, and Z. Liu, ‘Effect of deposition power and pressure on rate deposition and resistivity of titanium thin films grown by DC magnetron sputtering,’ *Spectrosc. Lett.*, vol. 49, no. 8, pp. 514–519, Sep. 2016, ISSN: 0038-7010.

[301] A. M. Stoneham and P. W. Tasker, ‘Understanding oxide-metal interfaces,’ *Le J. Phys. Colloq.*, vol. 49, no. C5, pp. C5–99–C5–113, Oct. 1988, ISSN: 0449-1947.

[302] N. Cabrera and N. F. Mott, 'Theory of the oxidation of metals,' *Reports Prog. Phys.*, vol. 12, no. 1, p. 308, Jan. 1949, ISSN: 00344885.

[303] J. Evertsson, F. Bertram, F. Zhang, L. Rullik, L. Merte, M. Shipilin, M. Soldemo, S. Ahmadi, N. Vinogradov, F. Carlà, J. Weissenrieder, M. Göthelid, J. Pan, A. Mikkelsen, J.-O. Nilsson, and E. Lundgren, 'The thickness of native oxides on aluminum alloys and single crystals,' *Appl. Surf. Sci.*, vol. 349, pp. 826–832, Sep. 2015, ISSN: 01694332.

[304] L. P. H. Jeurgens, W. G. Sloof, F. D. Tichelaar, and E. J. Mittemeijer, 'Growth kinetics and mechanisms of aluminum-oxide films formed by thermal oxidation of aluminum,' *J. Appl. Phys.*, vol. 92, no. 3, pp. 1649–1656, Aug. 2002, ISSN: 0021-8979.

[305] W. W. Smeltzer, 'Oxidation of Aluminum in the Temperature Range 400 °C–600 °C,' *J. Electrochem. Soc.*, vol. 103, no. 4, p. 209, Apr. 1956, ISSN: 00134651.

[306] M. P. Seah and S. J. Spencer, 'Ultrathin SiO_2 on Si. I. Quantifying and removing carbonaceous contamination,' *J. Vac. Sci. Technol. A Vacuum, Surfaces, Film.*, vol. 21, no. 2, pp. 345–352, Mar. 2003, ISSN: 0734-2101.

[307] E. Forrest, R. Schulze, C. Liu, and D. Dombrowski, 'Influence of surface contamination on the wettability of heat transfer surfaces,' *Int. J. Heat Mass Transf.*, vol. 91, pp. 311–317, Dec. 2015, ISSN: 00179310.

[308] N. Eustathopoulos, 'Wetting by Liquid Metals–Application in Materials Processing: The Contribution of the Grenoble Group,' *Metals (Basel).*, vol. 5, no. 1, pp. 350–370, Mar. 2015, ISSN: 2075-4701.

[309] H. Okamoto and T. B. Massalski, 'The Au-C (Gold-Carbon) system,' *Bull. Alloy Phase Diagrams*, vol. 5, no. 4, pp. 378–379, Aug. 1984, ISSN: 0197-0216.

[310] X. Sun and H. Li, 'Gold nanoisland arrays by repeated deposition and post-deposition annealing for surface-enhanced Raman spectroscopy,' *Nanotechnology*, vol. 24, no. 35, p. 355 706, Sep. 2013, ISSN: 0957-4484.

[311] M. Kang, S.-G. Park, and K.-H. Jeong, 'Repeated Solid-state Dewetting of Thin Gold Films for Nanogap-rich Plasmonic Nanoislands,' *Sci. Rep.*, vol. 5, no. 1, p. 14 790, Dec. 2015, ISSN: 2045-2322.

[312] U. Eduok, O. Faye, and J. Szpunar, 'Recent developments and applications of protective silicone coatings: A review of PDMS functional materials,' *Prog. Org. Coatings*, vol. 111, pp. 124–163, Oct. 2017, ISSN: 03009440.

[313] J. Friend and L. Yeo, 'Fabrication of microfluidic devices using polydimethylsiloxane,' *Biomicrofluidics*, vol. 4, no. 2, p. 026 502, Jun. 2010, ISSN: 1932-1058.

[314] I. Byun, A. W. Coleman, and B. Kim, 'Transfer of thin Au films to polydimethylsiloxane (PDMS) with reliable bonding using (3-mercaptopropyl)trimethoxysilane (MPTMS) as a molecular adhesive,' *J. Micromechanics Microengineering*, vol. 23, no. 8, p. 085 016, Aug. 2013, ISSN: 0960-1317.

[315] H. Li, J. Wu, X. Huang, Z. Yin, J. Liu, and H. Zhang, 'A Universal, Rapid Method for Clean Transfer of Nanostructures onto Various Substrates,' *ACS Nano*, vol. 8, no. 7, pp. 6563–6570, Jul. 2014, ISSN: 1936-0851.

[316] Y. Chen, K. Bi, Q. Wang, M. Zheng, Q. Liu, Y. Han, J. Yang, S. Chang, G. Zhang, and H. Duan, 'Rapid Focused Ion Beam Milling Based Fabrication of Plasmonic Nanoparticles and Assemblies via "Sketch and Peel" Strategy,' *ACS Nano*, vol. 10, no. 12, pp. 11 228–11 236, Dec. 2016, ISSN: 1936-0851.

[317] S. M. Rossnagel, J. J. Cuomo, and W. D. W. D. Westwood, *Handbook of plasma processing technology : fundamentals, etching, deposition, and surface interactions.* Noyes Publications, 1990, p. 523, ISBN: 9780815512202.

[318] N. Posseme, *Plasma etching processes for CMOS device realization*, N. Posseme, Ed. ISTE Press - Elsevier, 2017, p. 121, ISBN: 978-1-78548-096-6.

[319] H. Jansen, H. Gardeniers, M. de Boer, M. Elwenspoek, and J. Fluitman, 'A survey on the reactive ion etching of silicon in microtechnology,' *J. Micromechanics Microengineering*, vol. 6, no. 1, pp. 14–28, Mar. 1996, ISSN: 0960-1317.

[320] S. Hill, W. Qian, W. Chen, and J. Fu, 'Surface micromachining of polydimethylsiloxane for microfluidics applications,' *Biomicrofluidics*, vol. 10, no. 5, pp. 1–12, 2016, ISSN: 19321058.

[321] J. N. Lee, C. Park, and G. M. Whitesides, 'Solvent Compatibility of Poly(dimethylsiloxane)-Based Microfluidic Devices,' *Anal. Chem.*, vol. 75, no. 23, pp. 6544–6554, Dec. 2003, ISSN: 0003-2700.

[322] M. P. Anenden, M. Svehla, N. H. Lovell, and G. J. Suaning, 'Process development for dry etching polydimethylsiloxane for neural electrodes,' in *2011 Annu. Int. Conf. IEEE Eng. Med. Biol. Soc.*, IEEE, Aug. 2011, pp. 2977–2980, ISBN: 978-1-4577-1589-1.

[323] W. Chen, R. H. W. Lam, and J. Fu, 'Photolithographic surface micromachining of polydimethylsiloxane (PDMS),' *Lab Chip*, vol. 12, no. 2, pp. 391–395, 2012, ISSN: 1473-0197.

[324] B. Gorissen, C. Van Hoof, D. Reynaerts, and M. De Volder, 'SU8 etch mask for patterning PDMS and its application to flexible fluidic microactuators,' *Microsystems Nanoeng.*, vol. 2, no. 1, p. 16 045, Dec. 2016, ISSN: 2055-7434.

[325] C. Zhang, C. Yang, and D. Ding, 'Deep reactive ion etching of commercial PMMA in O_2/CHF_3, and O_2/Ar-based discharges,' *J. Micromechanics Microengineering*, vol. 14, no. 5, pp. 663–666, May 2004, ISSN: 0960-1317.

[326] L. M. Fischer, M. Tenje, A. R. Heiskanen, N. Masuda, J. Castillo, A. Bentien, J. Émneus, M. H. Jakobsen, and A. Boisen, 'Gold cleaning methods for electrochemical detection applications,' *Microelectron. Eng.*, vol. 86, no. 4-6, pp. 1282–1285, Apr. 2009, ISSN: 01679317.

[327] S. Yunus, C. d. C. de Looringhe, C. Poleunis, and A. Delcorte, 'Diffusion of oligomers from polydimethylsiloxane stamps in microcontact printing: Surface analysis and possible application,' *Surf. Interface Anal.*, vol. 39, no. 12-13, pp. 922–925, Dec. 2007, ISSN: 01422421.

[328] L. J. Millet, A. Jain, and M. U. Gillette, 'Less is More: Oligomer extraction and hydrothermal annealing increase PDMS bonding forces for new microfluidics assembly and for biological studies,' *bioRxiv*, p. 150 953, Jun. 2017.

[329] N. Vandencasteele, D. Merche, and F. Reniers, 'XPS and contact angle study of N_2 and O_2 plasma-modified PTFE, PVDF and PVF surfaces,' *Surf. Interface Anal.*, vol. 38, no. 4, pp. 526–530, Apr. 2006, ISSN: 0142-2421.

[330] K. Ma, P. Chen, B. Wang, G. Cui, and X. Xu, 'A study of the effect of oxygen plasma treatment on the interfacial properties of carbon fiber/epoxy composites,' *J. Appl. Polym. Sci.*, vol. 118, no. 3, pp. 1606–1614, Jun. 2010, ISSN: 00218995.

[331] J. M. Grace and L. J. Gerenser, 'Plasma Treatment of Polymers,' *J. Dispers. Sci. Technol.*, vol. 24, no. 3-4, pp. 305–341, Jan. 2003, ISSN: 0193-2691.

[332] C. Cardinaud, 'Fluorine-based plasmas: Main features and application in micro- and nanotechnology and in surface treatment,' *Comptes Rendus Chim.*, vol. 21, no. 8, pp. 723–739, Aug. 2018, ISSN: 16310748.

[333] A. Krauklis and A. Echtermeyer, 'Mechanism of Yellowing: Carbonyl Formation during Hygrothermal Aging in a Common Amine Epoxy,' *Polymers (Basel).*, vol. 10, no. 9, p. 1017, Sep. 2018, ISSN: 2073-4360.

[334] E. Yousif and R. Haddad, 'Photodegradation and photostabilization of polymers, especially polystyrene: review,' *Springerplus*, vol. 2, no. 1, p. 398, Dec. 2013, ISSN: 2193-1801.

[335] A. Mata, A. J. Fleischman, and S. Roy, 'Characterization of Polydimethylsiloxane (PDMS) Properties for Biomedical Micro/Nanosystems,' *Biomed. Microdevices*, vol. 7, no. 4, pp. 281–293, Dec. 2005, ISSN: 1387-2176.

[336] K. Efimenko, W. E. Wallace, and J. Genzer, 'Surface Modification of Sylgard-184 Poly(dimethyl siloxane) Networks by Ultraviolet and Ultraviolet/Ozone Treatment,' *J. Colloid Interface Sci.*, vol. 254, no. 2, pp. 306–315, Oct. 2002, ISSN: 00219797.

[337] B. Schnyder, T. Lippert, R. Kötz, A. Wokaun, V.-M. Graubner, and O. Nuyken, 'UV-irradiation induced modification of PDMS films investigated by XPS and spectroscopic ellipsometry,' *Surf. Sci.*, vol. 532-535, pp. 1067–1071, Jun. 2003, ISSN: 00396028.

[338] S. Ichikawa, 'Photooxidation of plasma polymerized polydimethylsiloxane film by 172nm vacuum ultraviolet light irradiation in dilute oxygen,' *J. Appl. Phys.*, vol. 100, no. 3, p. 033 510, Aug. 2006, ISSN: 0021-8979.

[339] G. Nansé, E. Papirer, P. Fioux, F. Moguet, and A. Tressaud, 'Fluorination of carbon blacks: An X-ray photoelectron spectroscopy study: I. A literature review of XPS studies of fluorinated carbons. XPS investigation of some reference compounds,' *Carbon N. Y.*, vol. 35, no. 2, pp. 175–194, Jan. 1997, ISSN: 00086223.

[340] Y.-G. Lei, K.-M. Ng, L.-T. Weng, C.-M. Chan, and L. Li, 'XPS C 1s binding energies for fluorocarbon-hydrocarbon microblock copolymers,' *Surf. Interface Anal.*, vol. 35, no. 10, pp. 852–855, Oct. 2003, ISSN: 0142-2421.

[341] W. Zhou, R. Apkarian, Z. L. Wang, and D. Joy, 'Fundamentals of Scanning Electron Microscopy (SEM),' in *Scanning Microsc. Nanotechnol.* New York, NY: Springer New York, 2006, pp. 1–40.

[342] A. Ul-Hamid, *A Beginners' Guide to Scanning Electron Microscopy.* SPRINGER, 2019, p. 402, ISBN: 978-3-030-07498-2.

[343] J. I. Goldstein, D. E. Newbury, P. Echlin, D. C. Joy, C. E. Lyman, E. Lifshin, L. Sawyer, and J. R. Michael, *Scanning Electron Microscopy and X-ray Microanalysis.* Boston, MA: Springer US, 2003, ISBN: 978-1-4613-4969-3.

[344] P. Echlin, *Handbook of Sample Preparation for Scanning Electron Microscopy and X-Ray Microanalysis.* Boston, MA: Springer US, 2009, ISBN: 978-0-387-85730-5.

[345] H. Lüth, *Solid Surfaces, Interfaces and Thin Films*, ser. Graduate Texts in Physics. Berlin, Heidelberg: Springer Berlin Heidelberg, 2010, ISBN: 978-3-642-13591-0.

[346] I. Müllerová and I. Konvalina, 'Collection of secondary electrons in scanning electron microscopes,' *J. Microsc.*, vol. 236, no. 3, pp. 203–210, Dec. 2009, ISSN: 00222720.

[347] A. J. Schwartz, M. Kumar, B. L. Adams, and D. P. Field, *Electron Backscatter Diffraction in Materials Science*, A. J. Schwartz, M. Kumar, B. L. Adams, and D. P. Field, Eds. Boston, MA: Springer US, 2009, p. 403, ISBN: 978-0-387-88135-5.

[348] H. Sun, M. Ye, and W. Sun, 'High Resolution AFM and Its Applications,' in *At. Force Microsc. Mol. Cell Biol.* Singapore: Springer Singapore, 2018, pp. 179–235.

[349] 'NanoWizard ® AFM Handbook JPK Instruments NanoWizard ® Handbook Version 2.2a 1,' Tech. Rep., 2012, p. 55.

[350] B. Voigtländer, *Scanning Probe Microscopy*, ser. NanoScience and Technology. Berlin, Heidelberg: Springer Berlin Heidelberg, 2015, p. 382, ISBN: 978-3-662-45239-4.

[351] G. Haugstad, *Atomic Force Microscopy.* Hoboken, NJ, USA: John Wiley & Sons, Inc., Aug. 2012, p. 464, ISBN: 9781118360668.

[352] A. Einstein, 'Über einen die Erzeugung und Verwandlung des Lichtes betreffenden heuristischen Gesichtspunkt,' *Ann. Phys.*, vol. 322, no. 6, pp. 132–148, Jan. 1905, ISSN: 00033804.

[353] P. van der Heide, *X-Ray Photoelectron Spectroscopy.* Hoboken, NJ, USA: John Wiley & Sons, Inc., Nov. 2011, ISBN: 9781118162897.

[354] J. M. Wagner, *X-ray photoelectron spectroscopy.* Nova Science Publishers, 2011, p. 277, ISBN: 1617282405.

LIST OF ABBREVIATIONS

a-MO$_x$	anodic metal-oxide
AAO	anodic aluminium oxide
AFM	atomic force microscopy/microscope
AuNP	gold nanoparticle
BD	breakdown
BSE	backscattered electrons
CCP	capacitively coupled plasma
CE	counter electrode
CPE	constant phase element
CV	cyclic voltammetry
DL	dielectric layer
DNA	deoxyribonucleic acid
EBL	electron-beam lithography
EBSD	electron backscatter diffraction
EDX	energy-dispersive X-ray spectroscopy
EIS	electrochemical impedance spectroscopy
FIB	focused ion beam
HER	hydrogen evolution reaction
IPA	isopropyl alcohol
IPCE	incident photon-to-current efficiency
IPF	inverse pole figure
LED	light emitting diode
LSP	localized surface plasmon
LSPR	localized surface plasmon resonance
LSPRi	localized surface plasmon resonance imaging
M–S	Mott–Schottky
MAO	micro-arc anodic oxide
MO$_x$	metal-oxide
NIL	nanoimprint lithography
NIR	near-infrared
NP	nanoparticle
OER	oxide evolution reaction
PAA	porous anodic alumina
PDMS	polydimethysiloxane
PE-SDCM	photoelectrochemical scanning droplet cell microscopy
PEC	photoelectrochemical cell
PMMA	polymethyl methacrylate

PVD	physical vapor deposition
QCM	quartz crystal microbalance
RE	reference electrode
RHE	reversible hydrogen electrode
RI	refractive index
RIE	reactive ion etching
SDCM	scanning droplet cell microscopy
SE	secondary electrons
SEM	scanning electron microscopy/microscope
SERS	surface-enhanced Raman spectroscopy
SIERA	surface enhanced infrared absorption
SPM	scanning probe microscopy/microscope
SPP	surface plasmon polariton
SPR	surface plasmon resonance
SPRi	surface plasmon resonance imaging
SSD	solid-state dewetting
ssDNA	single-stranded deoxyribonucleic acid
STEM	scanning transmission electron microscopy
TEM	transmission electron microscopy/microscope
TNT	titanium dioxide nanotube
UV	ultraviolet
VIS	visible
WE	working electrode
XPS	X-ray photoelectron spectroscopy
XRR	X-ray reflectometry

LIST OF APPENDICES

A METHODOLOGY

A.1 Scanning electron microscopy

Scanning Electron Microscopy (SEM) is one of the most common observation techniques used for micro-/nanostructures imaging and characterization. Only the basics will be discussed in this section to cover the experiments conducted in this thesis. For a more in-depth insight into physics, instrumentation, operation, image interpretation, and sample preparation, the reader is referred to professional books.[341–344]

Electron microscopy is often related to optical microscopy since there is a close analogy between electron and photon optics. The electron microscopy was developed to overcome the diffraction limits of the light, which are negligible for highly accelerated electrons. Despite all similarities, the image construction in SEM is entirely different, as indicated by the term ‘scanning’. The electron beam rasters across the specimen and detects the produced signal of interaction between incident electrons and the specimen material. When an electron of the incident beam hits and penetrates the specimen, it is deflected in an elastic or inelastic scattering way. It generates a variety of signals within a pear-shaped interaction volume that includes secondary electrons (SE), backscattered electrons (BSE), Auger electrons, and X-rays (Figure A.1:A).

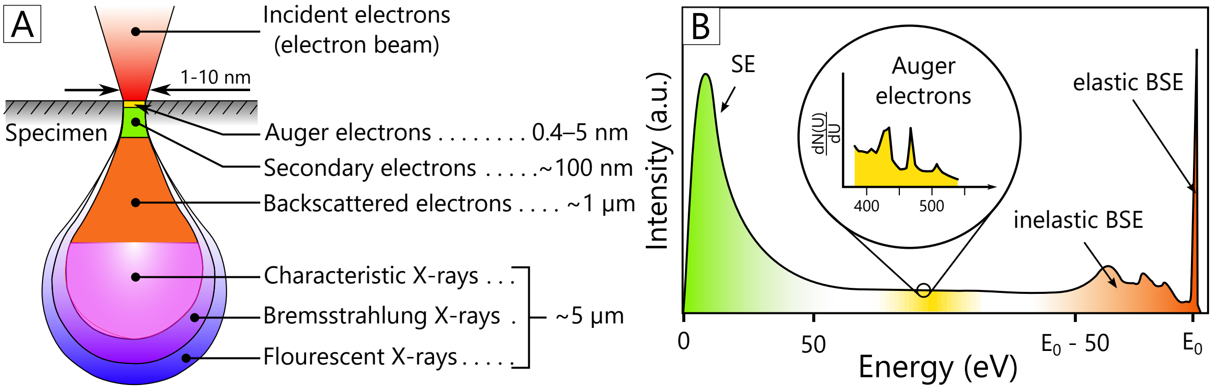

Figure A.1: (A) Schematic illustration of depth origin for signals generated in SEM and (B) the illustrative energy distribution of electrons emitted from a surface irradiated by the electron beam of primary energy E_0 (90 % of SE have energy below 10 eV). Adapted from ref.[345].

A.1.1 Secondary electrons

Secondary electrons (SE) are created when the inelastic scattering of the beam electrons ejects weakly bound electrons (from the valence or conducting bands), which have binding energies of ≈1–15 eV with the parent atom/s.[343] An essential characteristic of SE is their low kinetic energy (Figure A.1:B) that has a strong influence on their escape depth. SEs generated further from the surface beyond the escape depth cannot escape the specimen as they suffer a rapid energy loss with the distance travelled. Therefore, the SE image information is only from the top few nanometres, around 1 nm in metals and up to 20 nm in insulators.[342] Thanks to this, SEs are considered to constitute the most appropriate signal for studying the surface topography of the specimen. Hence, SE imaging is the most common type of imaging that is used in the SEM. Nowadays, SEMs are standardly equipped with Everhart-Thornley (ET) detector, representing a scintillator photomultiplier system side-positioned inside the SEM chamber. The scheme and working principle are illustrated in Figure A.2: Low-energy SE are pulled towards the detector by a weak electrostatic field of a wired grid (Faraday cage), then they are accelerated towards the scintillator where they convert into photons. These travel through the waveguide, at which end they are absorbed by a photocathode of the electron multiplier. Here, the generated electrons are amplified to levels suitable for image formation. Afterwards, the output electrical signal is digitalized into the 2D intensity map (SEM image).

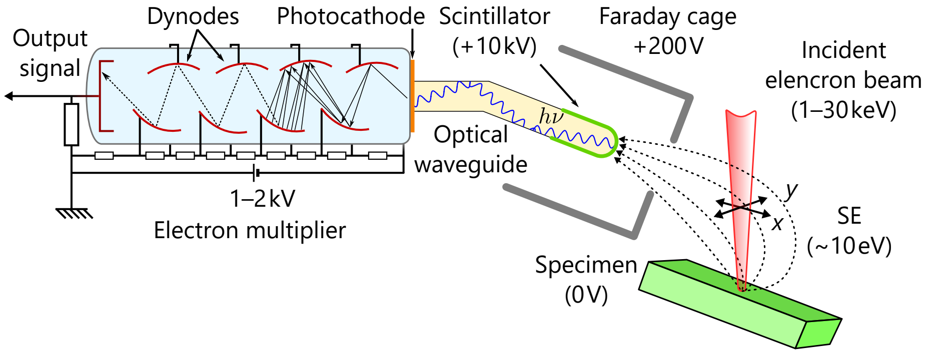

Figure A.2: The Everhart-Thornley (ET) detector scheme used in scanning electron microscopes and the principle of SE detection.

Modern SEMs have improved their image resolution by the so-called immersion systems with a strong magnetic field penetrating the specimen region to decrease the aberration coefficients of the objective lens.[346] Its utilization usually requires a low working distance between the objective lens and the specimen. In the presence of a strong magnetic field, the SE are easily 'sucked' into the objective lens, where they are detected by an additional SE detector (in-lens/through the lens/in-beam).

The formed SEM images have a 3D appearance due to differences in contrast between various structural features of the specimen displayed by a SE detector. This feature may be used better to understand the behaviour and morphology of the studied specimen. However, it may be a double-edged tool leading to many misinterpretations caused by insufficient understanding of the signal origin.

The contrast of the image arises from varying intensities of the detected SE over different parts of the specimen. This intensity is composed of two attributes: the amount of generated SE and their detection efficiency. While the yield of SE depends on the incident electron energy, material, and surface tilt, the detection efficiency is a complex process that originates from the role of escape depth and position of the SE detector with respect to the specimen. Examples of material contrast and morphology are shown and described in Figure A.3:A–B.

However, the SE contrast can also be affected by the charging of the observed specimen. The specimen charging is a common issue for insulating or poorly grounded specimens. It usually manifests as recognizable fast changes of the image, such as drifting, scanning dependent artefacts, or image deformations. Even though this is a common SEM issue, there is not a simple workaround. The most common solution is to make the specimen electrically conducting by depositing a thin (nanometres) conductive layer (e.g., gold, carbon) over it. This method has a few significant drawbacks; the loss of fine specimen structure, the loss of material contrast, and, naturally, the contamination of the sample by the deposited layer. Another method used in this work is to tune the scanning parameters to suppress or partly compensate for the charging effects. This task is pleasantly simplified with the rapid development and novel features (e.g., charge neutralisation mode, drift correction, various modes of image acquisition) of current SEMs.

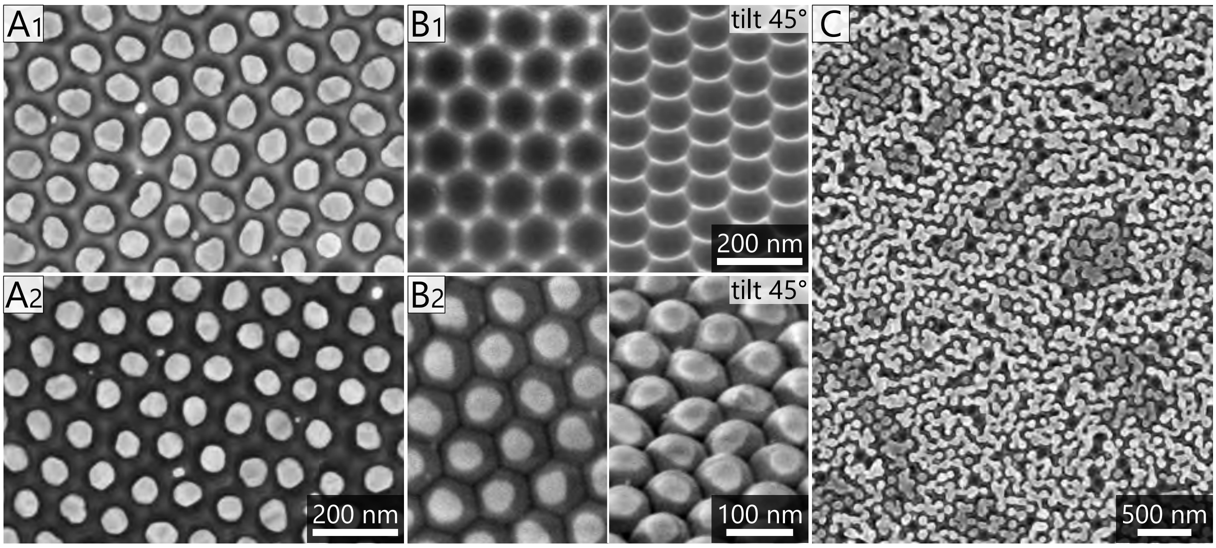

Figure A.3: Secondary electron SEM images showing a difference in contrast between AuNPs on (A1) Al with native oxide and (A2) with an additional thin carbon layer due to different SE yield between the materials. (B1) Shows contrast between bright protrusion boundaries and dark concave centres of nanobowled Al surface due to the specimen morphology. In comparison, reverse morphology of (B2) AuNPs embedded in epoxy substrate gives dark contrast for narrow, deep boundaries of the hemispheres. (C) Shows effect of the charging on interconnected AuNPs; darker insulated particles/agglomerates are being positively charged by the observation leading to lower SE emission.

Besides these effects, the charging may lead to a more peculiar behaviour shown in Figure A.3:C. The SE contrast of isolated AuNPs clusters originates from their charging and thus a consecutive lower SE emission compared to the surrounding master cluster that is presumably well grounded. Another more visual effect is the electrostatic attraction induced by the charging, shown in Figure A.4. This effect is illustrated on TiO_2 nanocolumns, where one (red-masked) of the separated nanocolumns is selectively irradiated (4 s), resulting in a strong electrostatic attraction between neighbouring column/s follow-up by their bending and permanent touch.

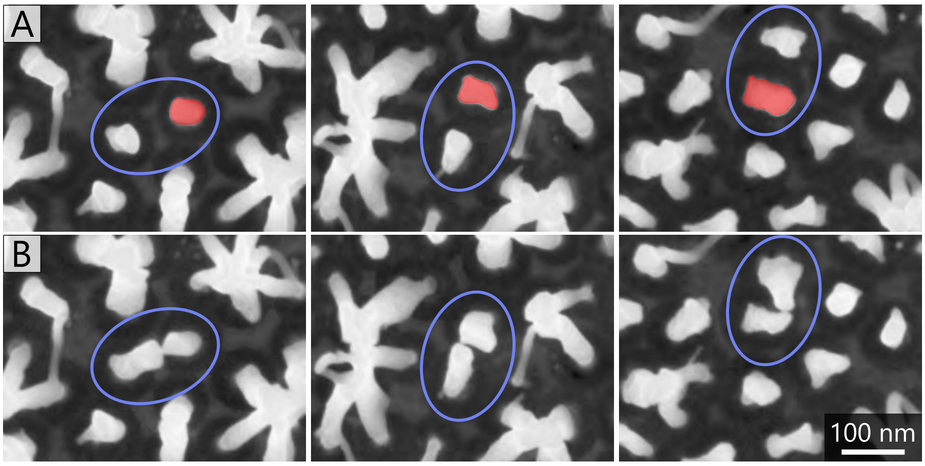

Figure A.4: SEM images showing an electrostatic attraction: (A) initial state, (B) resulting state. This electrostatic interaction was induced by a single column (red-masked) selective charging by an electron beam inside SEM (≈0.2 nC). Columns are 422 nm tall formed by PAA-assisted anodising of Ti substrate with a 13 % of Nb content (Figure 2.12).

A.1.2 Backscattered electrons

Backscattered electrons (BSE) were utilized in this work for Scanning Transmission Electron Microscopy (STEM) imaging and Electron Backscatter Diffraction (EBSD). BSE imaging reveals the distribution of phases/compounds with different compositions based on their mean atomic number.

STEM images are formed by a signal from the BSE transmitted through the specimen. Therefore, the specimen thickness must be very thin (<200 nm), and the acceleration voltage must be high (20–30 keV). It requires a unique sample preparation that usually involves dual-beam SEM with a Focused Ion Beam (FIB). In return, higher resolution is achievable thanks to a smaller interaction volume. However, the primary motivation for this technique was the enhanced material contrast between AuNPs and the polymeric substrate. FFor this, it was utilized a segmented annular detector placed below the specimen. This detector collects the signal from individual rings that allows a selection of desired BSE scattering angle. Analogous to the optical bright/dark field (BF/DF) mode, the same effect can be achieved by isolating the signal from the central segment (BF) or the outer segment (DF).

EBSD was employed to display individual grains of the material and their crystallographic orientation. EBSD uses backscatter diffraction of high-energy electrons from a volume of crystal material approximately 20 nm deep in the specimen (Figure A.5). Diffracted electrons form a Kikuchi pattern over a phosphor screen that is digitalized by a CCD camera. The geometry of the Kikuchi pattern can be interpreted as a gnomonic projection of the crystal lattice on the plate of the phosphor screen. This geometry is unique for a particular crystal structure and crystal lattice orientation.[347] Nowadays, obtaining results is just a matter of suitable sample preparation thanks to fully automatized pattern evaluation by specialized software.

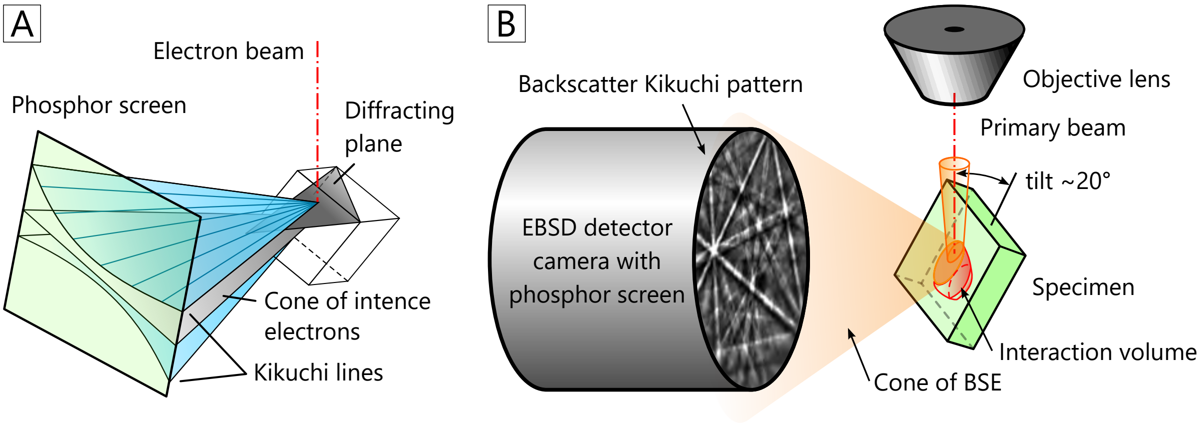

Figure A.5: Schematic of (A) the diffracting cones with respect to reflecting plane, the specimen, and the phosphor screen (adapted from ref.[347]) and (B) a layout of the EBSD system.

Experimental instrumentation:

SEM was performed with either a high-resolution SEM, FEI Verios 460L or Focused Ion Beam/Scanning Electron Microscope (FIB/SEM) FEI Helios NanoLab 660 that was also used for STEM observation. Standard observations were done in the immersion mode with a through-the-lens detector (TLD). The electron acceleration voltage was 5 keV with a beam current of 25 pA. In the case of non-conductive samples, such as PAA or nanoparticles on polymer substrates, the charge-neutralisation mode was also applied. The images were processed in the Gwyddion software.

EBSD mapping was performed on the SEM FEI Verios using EDAX DigiView EBSD camera. The samples were tilted at 70° with the acceleration voltage of 20 keV and the beam current of a few nanoamps. Data were collected, and EBSD patterns were indexed using the EDAX TeamTM software. Further postprocessing (e.g., stitching, cleaning) and evaluation (e.g., IPF map) were done in OIM Analysis™.

A.1.3 Nanoparticle size

The size of AuNPs was evaluated using the Gwyddion software. The grains (the example is shown in Figure A.6) were picked from an SEM image with 5 µm view-field by the threshold value and then filtered to exclude any defective grains (e.g., merged, small remains). The statistical sample was over 2500 and 1250 grains for 25 V and 40 V templates, respectively. The NP size was taken as the mean radius from the centre of the mass of the grain multiplied by two, if not specified otherwise. A different approach using the minimum circumcircle of grain (illustrated in Figure A.6:a) was used in the published article [**LeBo20**], which gives different results.

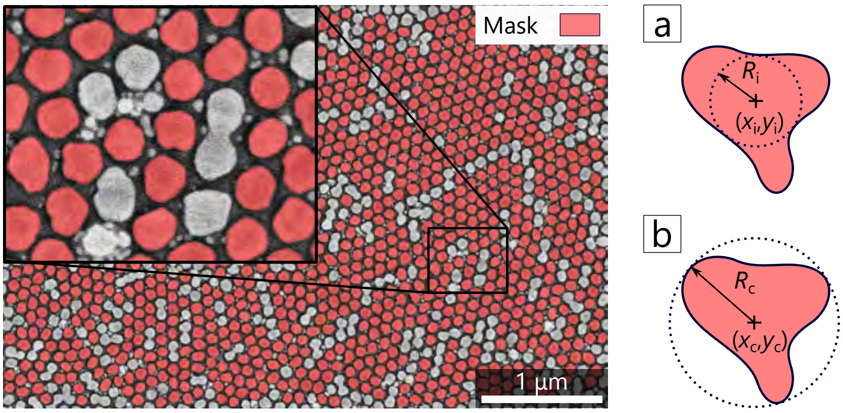

Figure A.6: Example of grain marking for the NP size evaluation and illustration of (a) maximum inscribe disc radius and (b) minimum circumcircle radius of a grain.

The notation (NP diameter and bounding length) is presented in the form of $x \pm \sigma$, where x is the centre (x_c) of the Gaussian function fitter over a statistic sample and σ represent the standard deviation ($\sigma = \mathrm{fwhm}/2\sqrt{2\ln 2}$).

The circularity (C) of the grains is calculated as

$$C = \frac{4\pi A}{P^2} \tag{A.1}$$

where A is the area of the grain and P is the perimeter of the grain. However, the software (Gwyddion version 2.51 or 2.55) estimates a larger boundary length (perimeter) of grain (5–6 %) when compared to the real value (tested on artificial structures). This error originates from the estimation method and may vary based on the resolution, shape, and angle of the boundary with respect to the pixel mesh. Even though this error was counted in, the estimated values serve just for a rough comparison. Higher circularity values correspond to more circular shapes. In the ideal case: $C_{\bigcirc} = 1$, $C_{\hexagon} = 0.907$, $C_{\square} = 0.785$.

A.2 Atomic Force Microscopy

Atomic Force Microscopy (AFM) is a scanning probe microscopies (SPM) that uses a probe that scans over the specimen surface. Based on interactions between the probe and the specimen, various properties can be observed with a sub-nanometre spatial resolution. The basic idea of an AFM is that the local attractive or repulsive forces between the tip and the specimen are converted into bending or deflection of the cantilever. These tiny changes are commonly measured by the deflection of a laser beam reflected from the backside of the cantilever to a quad photodiode (optical level principle). Figure A.7 illustrates this working principle with a diagram of fundamental interactions between the tip and the surface. Even though it is possible to scan over the surface without changing the height of the cantilever, this method is not common since it generates excessive force, especially on the fragile tip of the cantilever.

Nowadays, AFMs are equipped with advanced electronics that use a feedback loop to monitor the cantilever response and adjust the height of the cantilever accordingly to the surface changes. In contrast to the static mode, AFM imaging can be performed in a dynamic mode when the cantilever is excited to oscillations by a piezo actuator. Frequency then changes corresponding to the tip-surface interactions. However, this, along with other AFM techniques, is out of the scope of this work. Readers are referred to other books for more information.[348–351]

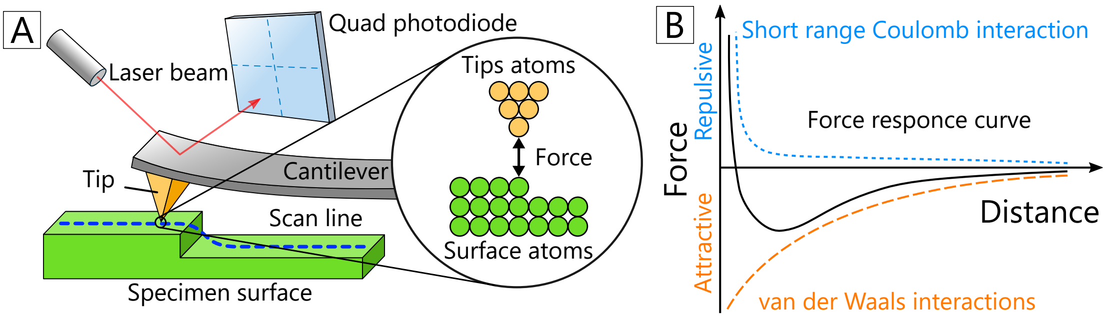

Figure A.7: (A) Schematic of the AFM setup and (B) diagram to illustrate the interaction between two objects according to their distance (adapted from ref.[348]).

Experimental instrumentation:

AFM was performed with a Scanning Probe Microscope (SPM) Bruker Dimensional Icon. The basic topography characterizations were done by a ScanAsyst® mode that is a Peak-Force Tapping® based image optimization technique developed by Bruker. For a low aspect ratio topography, standard Bruker ScanAsyst-Air probes were used. While in the case of high aspect ratio structures, NANOSENSORS™ uniqprobe – HeartBeatCantilever (qp-HBC) type probes were used with much better success. The image postprocessing was done in the Gwyddion software.

A.3 X-ray Reflectometry

X-ray Reflectometry (XRR) was used to analyse the thickness of the deposited gold layers precisely. For this purpose, the deposition was done over a piece of Si wafer. Before deposition, the native oxide was etched in a buffered oxide etch (BOE) solution for 2 minutes. XRR was performed in a Rigaku SmartLab 3 kW X-ray diffractometer, using Cu Kα radiation (40 kV, 30 mA), and the data were fitted in the GlobalFit software.

A.4 X-ray Photoelectron Spectroscopy

X-ray Photoelectron Spectroscopy (XPS) utilizes a photoelectric effect, firstly explained in 1905 by A. Einstein.[352] Photoelectron production in its simplest form describes a single-step process in which an electron initially bound to an atom/ion is ejected by a photon.[353] If the photon energy is sufficient, then this will result in electron ejection from the atom/ion as well as the specimen (illustrated in Figure A.8).

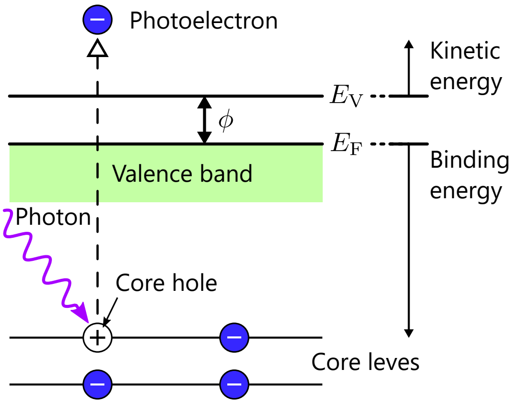

Figure A.8: Schematic of the photoemission process.

Thanks to a complete energy transfer during the process, it is possible to estimate the binding energy (E_B) from the formula:

$$E_B = h\nu - E_K - \phi \tag{A.2}$$

where $h\nu$ is the photon energy, ϕ is the work function of the instrument spectrometer, and E_K is the measured kinetic energy of an electron. Since the binding energy of an electron in a particular shell of an atom is unique to each element, the elements present on the material surface (other than Hydrogen and Helium) can be identified, and their relative composition can be determined.[354] Additionally, chemical bounding can be estimated based on the shift of the spectral lines. Like secondary electron generated in SEM, the escape depth plays a significant contribution in determining the high surface sensitivity of the method. Similarly, the emission of photoelectrons from the specimen leads to the specimen charging that deforms the shape and shifts the position of the spectral lines for non-conductive or insulated samples. This effect can be compensated mainly by a charge neutralization achieved by an electron bombardment from an electron source (charge neutraliser).

Experimental instrumentation:

XPS was conducted with a Kratos Analytical AXIS Supra instrument with a monochromatic Al Kα X-ray source (1486.6 eV) using a pass energy of 80 and 20 eV for wide and narrow spectra, respectively. The maximum lateral dimension of the analysed area was 0.7 mm. The spectra were acquired with a charge neutralization in the overcompensated mode to avoid most of the charging effects. Calibration of the binding energy scale was performed by shifting the hydrocarbon component CH_x to 284.8 eV. The concentrations were estimated from peak intensities in the CasaXPS software (version 2.3.18) using the Shirley-type background.

A.5 Optical spectrometry

This work utilized absorption spectroscopy in the VIS region to measure the bulk RI sensitivity of AuNP layers on selected substrates. A basic setup to measure absorption spectra is illustrated in Figure A.9.

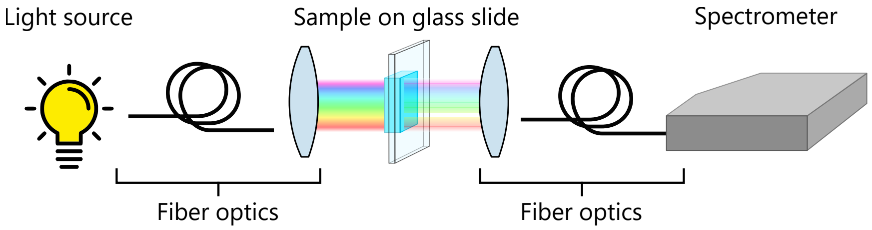

Figure A.9: Schematic of the absorption spectroscopy measurements.

Experimental instrumentation:

The optical spectroscopy measurements were performed either with a UV–VIS optical spectrometer (Ocean Optics JAZ 3-channel) with a tungsten halogen light source or an Avantes Avaspec 2048-4DT spectrometer with an Avantes Avalight DHS halogen light source (measured by Dr Attila Bonyár at BUTE).

B INCLUDED ARTICLES

Lednický, T.; Bonyár, A. 'Large Scale Fabrication of Ordered Gold Nanoparticle-Epoxy Surface Nanocomposites and Their Application as Label-Free Plasmonic DNA Biosensors' *ACS Applied Materials and Interfaces*, vol. 12, no. 4, 2020, pp. 4804–4814, doi:10.1021/acsami.9b20907.

ACS APPLIED MATERIALS & INTERFACES

www.acsami.org

Research Article

Large Scale Fabrication of Ordered Gold Nanoparticle−Epoxy Surface Nanocomposites and Their Application as Label-Free Plasmonic DNA Biosensors

Tomáš Lednický and Attila Bonyár*

Cite This: *ACS Appl. Mater. Interfaces* 2020, 12, 4804−4814

Read Online

ACCESS | Metrics & More | Article Recommendations | Supporting Information

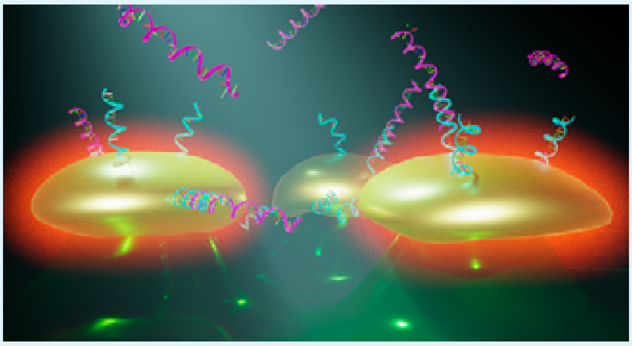

ABSTRACT: A robust and scalable technology to fabricate ordered gold nanoparticle arrangements on epoxy substrates is presented. The nanoparticles are synthesized by solid-state dewetting on nanobowled aluminum templates, which are prepared by the selective chemical etching of porous anodic alumina (PAA) grown on an aluminum sheet with controlled anodic oxidation. This flexible fabrication technology provides proper control over the nanoparticle size, shape, and interparticle distance over a large surface area (several cm^2), which enables the fine-tuning and optimization of their plasmonic absorption spectra for LSPR and SERS applications between 535 and 625 nm. The nanoparticles are transferred to the surface of epoxy substrates, which are subsequently selectively etched. The resulting nanomushrooms arrangements consist of ordered epoxy nanopillars with flat, disk-shaped nanoparticles on top, and their bulk refractive index sensitivity is between 83 and 108 nm RIU^{-1}. Label-free DNA detection is successfully demonstrated with the sensors by using a 20 base pair long specific DNA sequence from the parasite *Giardia lamblia*. A red-shift of 6.6 nm in the LSPR absorbance spectrum was detected after the 2 h hybridization with 1 μM target DNA, and the achievable LOD was around 5 nM. The reported plasmonic sensor is one of the first surface AuNP/polymer nanocomposites ever reported for the successful label-free detection of DNA.

KEYWORDS: *localized surface plasmon resonance, nanoparticle lattice, DNA biosensor, surface nanocomposite, nanobowled aluminum*

1. INTRODUCTION

Surface plasmon polaritons (SPPs) are the collective oscillation of delocalized electrons at a metallic surface in response to an external electric field. Since their first application for sensing purposes in the early 1980s,[1] surface plasmon resonance (SPR) based instruments became one of the most widely used tools of our time for the label-free characterization of biomolecular interactions.[2] The major advantages of SPR based chemical and biosensors are their excellent sensitivity (even in the range of 10^{-7} RIU)[3] to the changes in the refractive index of the medium close to the metal−dielectric interface and that they yield real-time information regarding the molecular interactions. Also, by use of a defocused laser illumination and a CCD camera as a detector, it is possible to image a larger area of the sensor surface, which enables a high-throughput multianalyte/multibiosensor concept, called SPR imaging.[4] Besides the obvious success and the widespread distribution of SPRi instruments, a disadvantage of the configuration is that the classical Kretschmann-type reflective optical setup is hard to be integrated into small, hand-held point-of-care (PoC) devices, which is the main reason for the comparatively limited success of integrated SPR constructions[5−8] and for the lack of hand-held SPRi devices on the market. The most significant difference between LSPR and classic SPR is that localized surface plasmon resonance on nanoparticles is more easily excitable, and thus simpler measurement configurations can be used.[9,10] In the chip based LSPR setup the nanoparticles are used on a surface of a transparent substrate;[10] the transmissive optical setup enables the integration of this principle into small, hand-held point-of-care LSPR imaging devices.[11,12]

There are several recent reviews focusing on the advances of plasmonic nanoparticle[13,14] and nanoarray[15] based LSPR sensors and their application for biosensing purposes. Out of these applications, label-free DNA sensing is one of the most challenging because of the inherently small size of target molecules. Although higher bulk RI sensitivity generally means higher sensitivity to target molecules, the relationship between the RI sensitivity and molecular sensitivity is not trivial in LSPR. The reported bulk RI sensitivity values[16] for LSPR sensors range between 71 and 1933 nm RIU^{-1}, and although it

Received: November 17, 2019
Accepted: January 6, 2020
Published: January 6, 2020

https://dx.doi.org/10.1021/acsami.9b20907
ACS Appl. Mater. Interfaces 2020, 12, 4804−4814

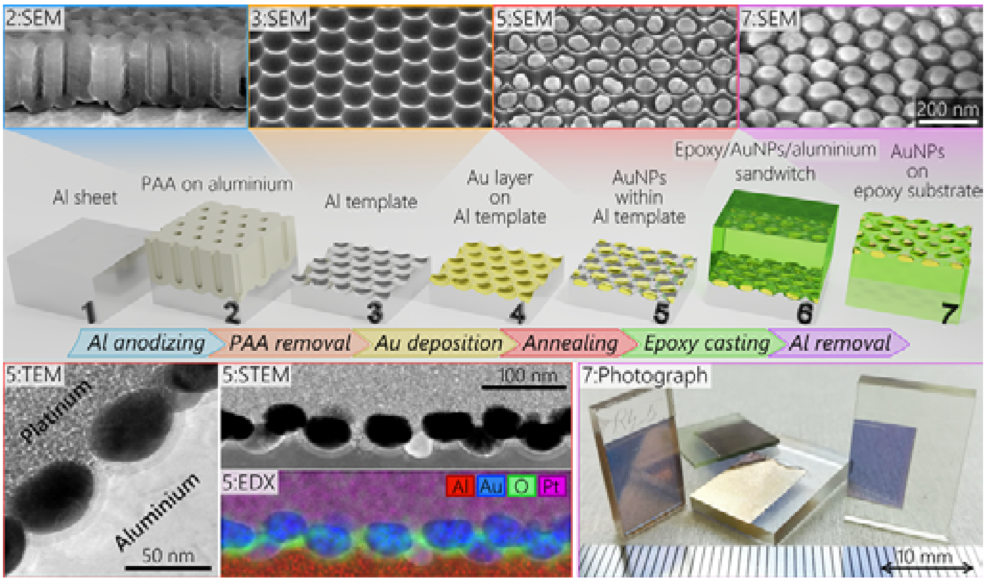

Figure 1. Comprehensive illustration of the technology to fabricate ordered nanoparticle arrangements on epoxy substrates. The main steps of the process are the following: (1) Preparation (cleaning, mechanical and electrochemical polishing) of the Al sheets. (2) Formation of PAA on aluminum through controlled anodic oxidation. (3) Nanobowled aluminum template formation after PAA removal. (4) Thin film deposition of gold on the template. (5) Nanoparticle arrangement formation through solid-state dewetting. (6) Epoxy casting and curing on top of the gold arrangement. (7) After the removal of the Al sheet the nanoparticles are transferred to the epoxy substrate. The SEM/TEM/EDX/optical images illustrate the various phases of fabrication.

can still be considered low compared to the equivalent bulk refractive index sensitivity of thin film based classical SPR instruments (which can be above 3300 nm RIU^{-1}),[17] concerning molecular sensitivity, LSPR can match the standard thin film based SPR instruments.[17,18] The near field decay length of nanoparticles is at least 1 order of magnitude smaller than the exponentially decaying evanescent field length in thin film SPR; in other words, LSPR is more focused on the molecular scale interactions, which take place in the near vicinity of the particle surface.[19] The near field intensity and its decay around the particles depend on the size, shape, and material properties of the nanostructures.[20,21] Coupling and interparticle distances also play a major role in near field intensity and thus sensitivity enhancement.[22,23]

All of the listed aspects should be considered when selecting a nanofabrication method for LSPR sensor construction, which usually requires compromises. Control over the particles' size, shape, and distribution in a sufficiently large surface area (several cm^2), preferably with a cheap and reproducible technology, could be considered optimal. With electron beam[24] or ion beam[25] lithography it is possible to control the size and distribution of the nanostructures, resulting in high sensitivity,[26] but patterning large surface areas is too expensive with this method. This is also true for nanoimprint lithography (NIL), where the hard masks are usually prepared with these technologies.[27−29] Colloidal lithography[30] and hole-mask colloidal lithography (HCL)[11] are often used to pattern somewhat larger surface areas; however, there are some limitations regarding the size/shape of the fabricated structures, resulting in mediocre/small surface coverage and thus sensitivity.[31,32] Precise control over the size and shape could be achieved through the colloidal synthesis of the nanoparticles.[33] Here, the challenge is the subsequent binding of the nanoparticles to a substrate (through silanization[34] or thiol chemistry[35]); the control over the distribution of the nanoparticle array is limited, and the uncoupled spherical nanoparticles usually have lower molecular sensitivities.[2,36,37] Thermal annealing of a previously deposited thin film on glass or silicon is a simple technique to produce nanoislands,[38] also combined with subsequent etching of the substrate to produce nanomushrooms,[39,40] but the control over the arrangement is limited;[39] because gold does not adhere well with SiO_2, fluidic environments can remove the NPS from the surface. Drawbacks of the listed technologies which enable extra high sensitivities are either the small fabrication area (EBL[26]) or the inhomogeneous surface.[41] A recently introduced reversal nanoimprint lithography excelled in most of these aspects, with high sensitivities in the NIR range.[42]

Our proposed method (illustrated in Figure 1) is based on the controlled, template-assisted solid-state dewetting synthesis of nanoparticles and their transfer to a polymer; namely, epoxy support has the following distinct advantages compared to other technologies: (1) *Controlled synthesis*: the particle size and interparticle distance can be precisely controlled in a fixed hexagonal distribution, and thus the plasmonic absorption peak (and sensitivity) can be fine-tuned for individual applications. Besides plasmonic sensing, the absorption peak should be tuned for surface-enhanced Raman scattering (SERS) applications as well, where the relation between the resonance peak of the substrate and the excitation wavelength defined by the laser has an effect on the SERS enhancement.[38,43] (2) *Large scale fabrication*: the lateral size of the substrate is not limited, sensors with several cm^2 surface area can be easily prepared, and the nanoparticle size/distribution is homogeneous on the whole surface. Such large sensor areas are required for LSPR imaging (LSPRi) applications[12] and also beneficial for SERS.[44,45] (3) *Robustness*: the prepared nanocomposite—gold nanoparticle arrangement on fixed on epoxy pillars—is completely stable; there, is no particle removal exposed to fluidic environments. The surface of the gold can be cleaned multiple times with low-power O_2 plasma without any significant drop in sensitivity.

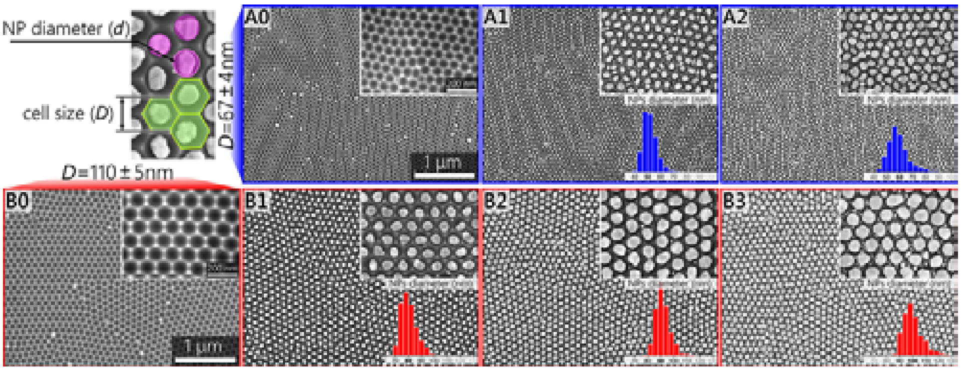

Figure 2. SEM images illustrating the control over the nanoparticle arrangement and sizes on two types of nanobowled Al templates formed by anodization at 25 V in sulfuric acid with cell sizes D = 67 ± 4 nm (A type) and at 40 V in oxalic acid with D = 110 ± 5 nm (B type). The size distributions (d) of particles are the following: 51 ± 5 nm (A1), 60 ± 7 nm (A2), 79 ± 6 nm (B1), 92 ± 6 nm (B2), and 102 ± 9 nm (B3).

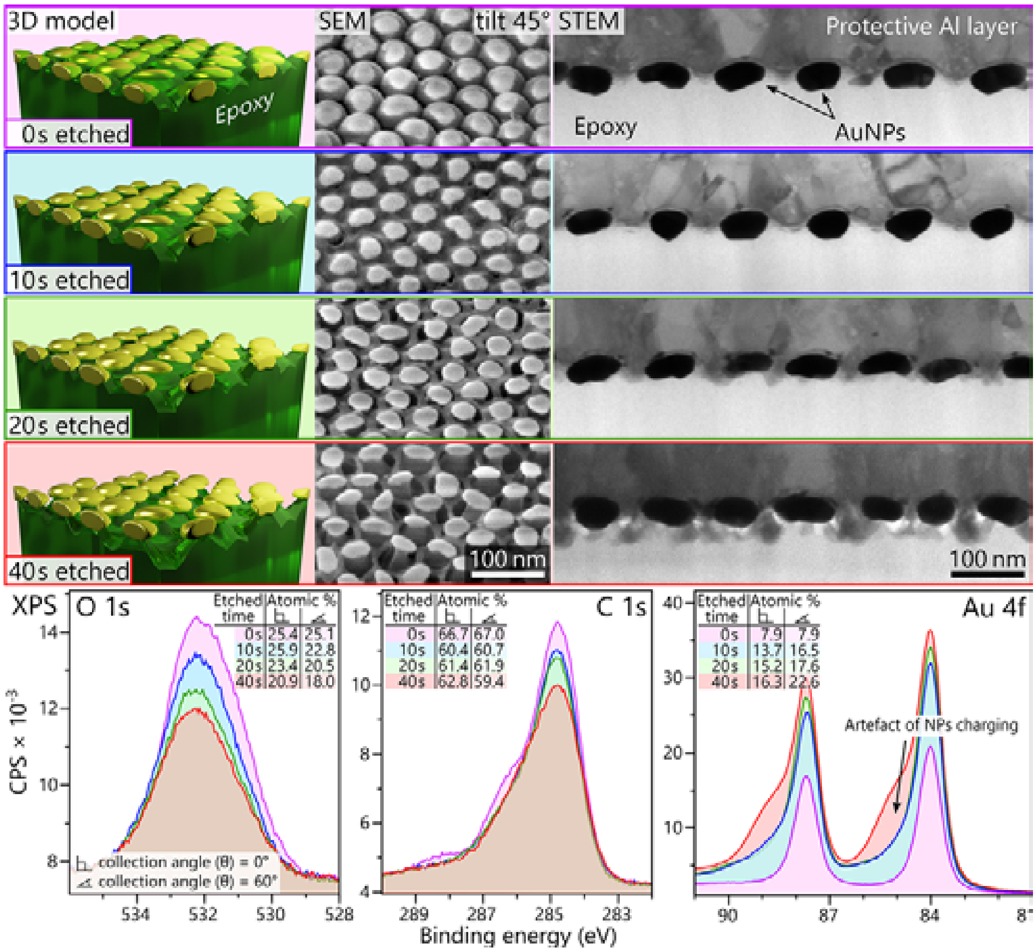

Figure 3. Illustration and the effect of selective epoxy etching on B1 type samples. Top row, left: 3D models. Middle: tilted (45°) SEM views. Right: STEM cross-sectional images (bright mode). Etching times from top to bottom: 0, 10, 20, and 40 s. Bottom graphs: detailed XPS spectra of O 1s, C 1s, and Au 4f peaks; collection angle (θ) = 60°. The tables show the estimated atomic concentrations for both standard (θ = 0°) and tilted (θ = 60°) measurements.

It also has to be noted that—to the best of our knowledge except for the Ag/PET based nano-Lycurgus cup arrays of Gartia et al.[41]—ours is one of the first surface Au-NP/polymer nanocomposite LSPR sensor successfully used for label-free DNA detection. Surface Au/Ag-NP/polymer nanocomposites were successfully utilized for other applications,[46] for example as protein LSPR sensors.[47,48]

2. EXPERIMENTAL SECTION

2.1. Preparation of the Nanobowled Aluminum Template.

High-purity Al foils (99.999%, 250 μm thick, tempered as-rolled, Goodfellow) were cut into 25 mm × 50 mm samples that were mechanically polished, finishing with a 3 μm suspension. After the mechanical polishing, the foils were ultrasonicated in acetone and deionized water (MilliPore, 18.2 MΩ), dried, and annealed in vacuum (~4 × 10^{-4} Pa) at 550 °C for 15 h with a heating ramp of 10 °C min^{-1} and natural cooling of ~6 h. One side of the Al foils were then electrochemically polished in a mixture (0.6 dm^3) of perchloric acid (70% w/w) and ethanol (96% w/w) with a volume ratio of 1:4 at 0 °C. The electrochemical polishing were performed potentiostatically, in a two-electrode setup with a stainless mesh as a cathode, at 20 V for 1−2 min. After rinsing in deionized water and drying, Al foils were prepared for anodizing (Figure 1: phase 1).

The one-step anodizing was performed in the same setup as the electrochemical polishing by using oxalic acid solution (0.3 M) at 7 °C with a potential of 40 V for 20 h or sulfuric acid solution (0.3 M) at 0 °C with a potential of 25 V for 15 h. To avoid unnecessary consumption of Al from unpolished side, the anodization was interrupted after the first 30 min, the foil was cleaned and dried, and Kapton tape was applied on unpolished side to mask it from further anodizing. This resulted in an over 50 μm thick porous anodic alumina (PAA) layer (Figure 1: phase 2) with hexagonally ordered cells of 67 ± 4 and 110 ± 5 nm size for 25 and 40 V, respectively.

To obtain the nanostructured (nanobowled) Al surface (Figure 1: phase 3), the PAA was selectively dissolved (from both sides) in a vigorously stirred mixture of phosphoric acid (0.42 M) and chromium trioxide (0.2 M) at 65 °C for 2 h, followed by thorough cleaning and ultrasonication in deionized water and methanol.

2.2. Formation of Gold Nanoparticle Arrangements. AuNPs were fabricated by utilizing the nanobowled Al template as substrate for controlled solid-state dewetting of a thin gold film (Figure 1: phase 4−5). First, a thin Au film was deposited by RF magnetron sputtering (BESTEC, magnetron sputtering system) with a rate of 0.035 nm s^{-1} (in an argon atmosphere of 10^{-1} Pa), 200 mm distance, and 30° angle between the Al template and the Au target (99.99%, Kurt J. Lesker Company). The deposition rate was monitored in situ by a quartz crystal microbalance and ex situ by calibration sample profilometry measurements (discussed in detail in the Supporting Information S5). Afterward, the foils with Au films was thermally annealed on a hot plate at 300 °C for 5 min (discussed in the Supporting Information S3). Various distributions or sizes of AuNPs (example shown in Figure 2) were obtained by tuning the thickness of Au film and repeating these processes (deposition and annealing) for multiple times.

2.3. Transfer of Gold Nanoparticles. To utilize the fabricated AuNPs layers as a LSPR sensor element, they were transferred to an electrically nonconductive and optically transparent substrate (Figure 1: phase 6−7). A two-compound epoxy resin (Elan-tron EC 570 and W 363, weight ratio of 100:33) was cast over the AuNP layer in a thickness of a few millimeters and cured in an oven for 12 h at 50 °C. Then, the Al substrate was dissolved in a hydrochloric acid (35% w/w) and copper(II) chloride (2 M) water solution. After that, the samples were immersed subsequently into iron(III) chloride (2 M) and sodium hydroxide (1 M) water solution for 10 min to remove copper and aluminum oxide residues, respectively.

2.4. Epoxy Substrate Etching. The epoxy substrate was dry etched in a PlasmaPro 80 RIE chamber (Oxford Instruments Plasma Technology), which uses capacitively coupled plasma (CCP). Prior to etching, samples were cut into square based pieces with 10 mm edge length and washed subsequently in deionized water, ethanol, and methanol, finished with drying under nitrogen steam. The RIE was performed for different time periods in an oxygen plasma at a pressure of 6.7 Pa, power of 50 W, and O_2 flow rate of 50 sccm.

2.5. Characterization. Scanning electron microscopy (SEM) was performed with a high-resolution SEM (FEI Verios 460L) in secondary electron detector mode and an acceleration voltage of 5 keV. Thin lamellae (thickness of ~100 nm) for transmission electron microscopy (TEM) were prepared by a dual-beam system (FIB-SEM Tescan LYRA3) (Figure 1) and a FEI Helios NanoLab 660 (Figure 3). Transmission electron microscopy (TEM) and scanning transmission microscopy (STEM) with energy-dispersive X-ray spectroscopy (EDS) in Figure 1 were performed with a Carl Zeiss LIBRA200FE (with a Bruker Quantax 200, 30 mm^2 EDS detector). The STEM images in Figure 3 were obtained with a FEI Helios NanoLab 660 in bright field mode and operating voltage of 30 keV.

X-ray photoelectron spectroscopy (XPS) was conducted with a Kratos Analytical AXIS Supra instrument with a monochromatic Al Kα X-ray source (1486.6 eV) by using pass energy of 20 eV. The maximum lateral dimension of the analyzed area was 0.7 mm. The spectra were acquired with a charge neutralization in overcompensated mode to avoid most of the charging effects. The calibration of binding energy (BE) scale was performed by shifting the hydrocarbon component CHx to 284.8 eV. The concentrations were estimated from peak intensities in the CasaXPS software (version 2.3.18) by using the Shirley-type background.

The optical spectroscopy measurements were performed either with an Avantes Avaspec 2048-4DT spectrometer and an Avantes Avalight DHS halogen light source (at BUTE) or with an UV−vis optical spectrometer (Ocean Optics JAZ 3-channel) with a tungsten halogen light source.

2.6. LSPR Sensor Tests. The bulk refractive index sensitivity of the plasmonic sensors was tested by changing the medium above the samples between air, deionized water, and a sucrose dilution series (25%, 50%, and 75% in deionized water). The sensor surface was illuminated in a circular area with a diameter of 8 mm, and a glass microscope sheet was used to cover the dispersed media on the samples.

2.7. DNA Experiments. The same protocols were followed, which were used and tested in a previous work.[49] The oligomers were purchased from Sigma-Aldrich (Germany), and the stock solutions were prepared by using NaCl (0.5 M)−Na_2HPO_4 (0.05 M), pH 6.8, buffer (termed running buffer, RB, from now on). The base sequences of the probe and target ss-DNA, which form a specific sequence from the parasite *Giardia lamblia* (the β-giardin gene),[50] are the following (from 5′ to 3′): Giardia_probe: CGTACATCTTCTTCCTTTTT-[ThiC6]; Giardia_target: AGGAAGAAGATGTACGACCA. The probe and target ss-DNAs are both 20 bases long, and the complementary sequence in the target is 16 bases. As a negative control, the following 20 bases long noncomplementary DNA sequence was used: CTGTGTCGATCAGTTCTCCA. Prior to surface functionalization, the sensor surfaces were freshly cleaned with low-power O_2 plasma by using a Diener Atto chamber at a pressure of 40 Pa at 20 W power for 15 s. For probe immobilization the sensors surfaces were immersed into a solution of thiol modified ss-DNA (1 μM Giardia_probe) for an overnight (~16 h) incubation. The ionic strength of the buffer was varied between 0.5, 0.75, and 1 M NaCl, as indicated at the discussion of the results. After probe immobilization the surface of the sensor was thoroughly rinsed with the same buffer that was used for the immobilization. Subsequently, the whole sensor surface was passivated with 6-mercapto-1-hexanol (1 mM, MCH, in the same buffer) for 30 min to reduce nonspecific binding of probe-DNA on the gold surface. After MCH treatment, the sensor surface was rinsed again. Finally, the target ss-DNA (Giardia_target, in various concentrations between 1 nM and 3 μM) diluted in the same buffer as the immobilization solution was added. The hybridization time was 2 h; after that, the surface was rinsed again with the corresponding buffer extensively. All optical spectroscopy measurements (on a bare sensors surface, after probe-DNA immobilization, after MCH treatment, and after hybridization with target-DNA) were done in RB medium (after washing) as well, so the effect of DNA binding can be compared to the same baseline. The immobilization and hybridization steps were performed by drop coating the surface of the samples with the respective DNA solutions. The incubation was performed in a humidified, hermetically sealed dish to avoid the evaporation of the solutions. All experiments were performed at laboratory ambient temperatures (22 °C).

3. RESULTS AND DISCUSSION

3.1. Nanoparticle Arrangement Control. In the ideal case the solid-state dewetting of an Au thin film on the aluminum nanobowled template leads to the formation of one nanoparticle per a single bowl, with the volume corresponding to the dimple area and thickness of the deposited film. This process is primarily governed by the template's hexagonal protrusions; these sharp and uniform structures confine areas for NP growth. The driving force behind nanoparticle formation can be explained by the theory of surface energy minimization, previously explained on the same structures by Fan and others.[51] Therefore, the most important parameters to control the NPs uniformity, distribution, and size are the template morphology and deposited layer thickness (and its morphology), as it was also investigated and demonstrated in our previous work,[52] or other publications.[51,53]

In this work we focused on utilizing the aluminum nanobowled template, whose morphology is inherited from the PAA. However, the hexagonally self-ordered PAA structure can be achieved within a relatively narrow window of anodizing conditions. For the given electrolyte system there is an optimal anodizing potential which determines the PAA cell size and thus the nanobowl's diameter (proportional constant of 2.5 nm V^{-1}). In this work, the most conventional processes were chosen: 0.3 M sulfuric acid (U = 25 V) and 0.3 M oxalic acid (U = 40 V), resulting in template morphologies shown in Figures 2(A0) and 2(B0), respectively. The images show defect-free domains whose lateral size is limited to only a several micrometers (tens of cells).[54] Although this is a major cause of NP lattice defects, this could be considered as a common drawback of any self-ordering processes (for example, it also happens with self-ordering PS ball based techniques as well).[55] Technologies that can overcome these issues (for example, soft imprinting) are either not applicable for this work or are very expensive for large surface area patterning (for example, e-beam lithography).

In the case of ideal dewetting, the Al template determines NPs arrangement (hexagonal) and interparticle distances (center to center) are given by the cell size. Although the size of NPs can be tuned by the thickness of the deposited Au film, it was experimentally observed that only a narrow range of thickness leads to an ideal dewetting process with respect to the Al template morphology (cell size). In our case it was experimentally established that the ideal thicknesses are approximately 6 and 8 nm for type A and type B templates (shown in Figure 2(A1,B1)), respectively. For smaller layer thicknesses more voids can be observed after annealing, especially at the side of the protrusions, which causes undesirable separation and formation of NPs independently from the nanobowled template (shown in Figure S1: 6 nm). On the other side, increasing the thickness above the optimum leads to incomplete NPs separation: the NPs can remain connected through bridges over sharp template protrusions. Other groups reported similar observations regarding the dewetting process on different substrates.[55−57] To match the arrangement of the NPs with the pattern defined by the template, it is important to control not only the deposited film thickness but also the film morphology (explained in more detail in the Supporting Information S1−S3). The morphology of the film may vary based on the selected deposition technique and its parameters. Here vacuum sputtering was selected since it yields smoother films compared to vacuum evaporation (as demonstrated in Figure S5), but the in-depth investigation of other deposition techniques was not the aim of our current work.

However, as seen in Figure 2(A1,B1) with these optimal initial layer thicknesses the resulting NPs have undesirably large interparticle distances which would not yield substantial sensitivity enhancement by plasmon coupling. To decrease the distance between nanoparticles and at the same time increase their size, the deposition and annealing processes were repeated multiple times. The examples in Figure 2 were prepared by sequential deposition and annealing, where the deposited layer thicknesses were the following: (A2) 6 nm + 5 nm, (B2) 8 nm + 7 nm, and (B3) 8 nm + 7 nm + 5.5 nm. An analogous method is present by Kang and others by using a template-less dewetting technique.[58] As the result of these procedures, it is possible to achieve well-ordered, uniform, and closely packed NP layers with gap distances under 10 nm (Figure 2(A2,B3)). If the separation between the particles is sufficiently small, interparticle plasmon coupling will occur, which could lead to a significant increase in the near field intensity in the gap and also to a significant increase in LSPR bulk refractive index sensitivity (or SERS enhancement in other applications).[38] Efforts to further decrease the interparticle gap resulted in predominant defect formation and merging of the NPs. Compared to the first layer, tuning the thickness for subsequent films is even more challenging, which leads to a compromise including possible NP merging and formation of small, secondary NPs (as illustrated in Figure S4). This NP merging is not desirable, since the change in the particle shape would add other components into the plasmonic absorbance spectrum of the arrangement, causing red-shift and widening of the absorbance peak. Such tightly packed nanoparticles, synthesized by a distantly similar technique utilizing porous alumina templates, were proved to be sufficiently sensitive for molecular scale sensing to detect biomarkers.[59]

3.2. Nanoparticle Transfer to Epoxy and Nanocomposite Stability.

To use the synthesized AuNP arrangements as plasmonic biosensors (working in fluidic environments), it is necessary to fix the NPs onto a different substrate. A general problem with the solid state dewetting based NP synthesis methods is that the NPs do not adhere well to the substrate used for synthesis and can be washed away easily. Also, in this case the NPs are electrically coupled to the aluminum substrate, which hinders their plasmon resonance. Third, having a transparent substrate under the AuNP arrangement is beneficial, for in this case the sensors can be used in a simpler transmission based optical setup.

For these practical reasons the NPs were transferred after synthesis onto an electrically nonconductive and optically transparent substrate via simple polymer casting. Although several substrate materials were tested—including PDMS and PMMA—epoxy was found to be the most suitable candidate for this purpose unanimously. The main reason for this is that after the transfer of the NPs a subsequent polymer etching step is required to remove the casted polymer from the surface of the NPs. This etching can be easily performed in the case of epoxy with simple O_2 plasma, while it requires more aggressive etchants and complex procedures for sturdier polymers, such as PDMS. On the other hand, we observed that thermoplastics (like PMMA) are not suitable for this kind of plasma etching due to their low glass transition and melting temperatures. These temperatures can be locally reached due to the heating of NPs, caused by the microwave irradiation. In comparison, thermoset epoxy is much more stable in this regards. Today O_2 plasma is a commonly used cleaning protocol for sensor surfaces; thus, the selective etching of epoxy with O_2 plasma can be considered compatible with standard laboratory protocols.

Figure 3 gives a comprehensive illustration regarding the selective etching of epoxy with O_2 plasma. Directly after polymer casting the transferred NPs are partially covered with a thin epoxy layer, as can be clearly seen on the SEM images.

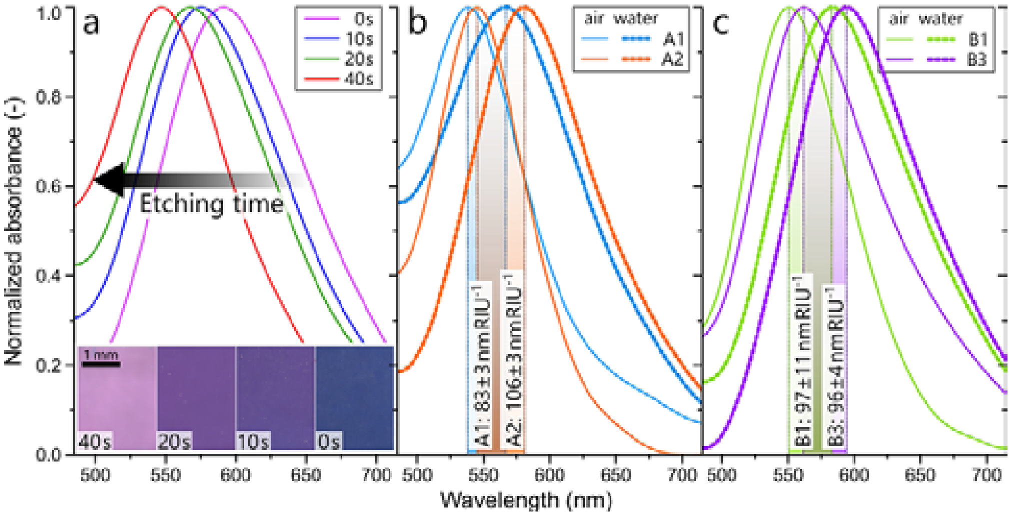

Figure 4. Normalized absorbance spectra of (a) A1 type nanocomposites after different times of selective epoxy etching with O_2 plasma, measured in air (data corresponding to Figure 3) with inset of optical microscopy images (transmission) of corresponding samples; (b) A1 and A2 type samples after 30 s selective etching measured in air and in water; (c) B1 and B3 type samples after 30 s selective etching measured in air and in water, respectively.

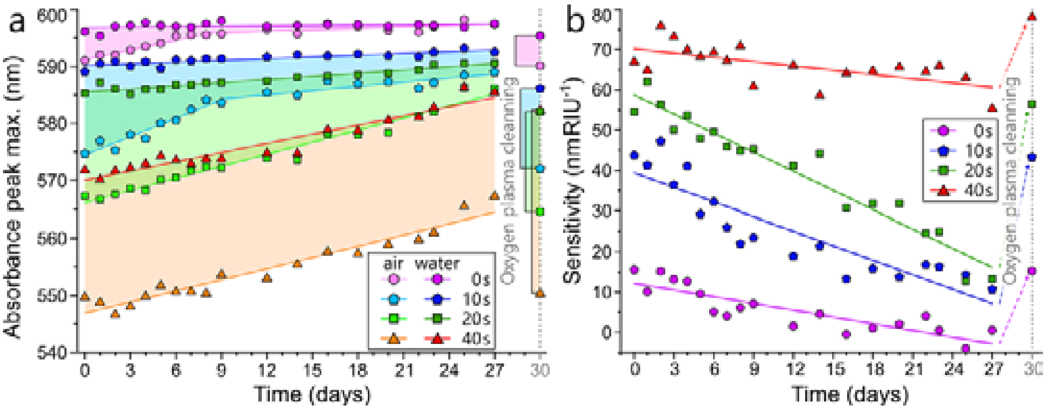

Figure 5. (a) Position of the LSPR absorbance peak maxima of the etched A1 type nanocomposite samples measured in air and in water, respectively. (b) Calculated bulk refractive index sensitivities of the same sensors. The values on the right side of the graphs represent the condition of the samples after cleaning them with low-power O_2 plasma after 30 days. The samples correspond to the ones presented in Figure 3 and Figure 4a.

This is also confirmed by the color of the samples (Figure 4) and the very small bulk refractive index sensitivities, measured directly after the transfer (around 15 nm RIU^{-1}, Figure 5). Etching the epoxy samples in O_2 plasma (at a pressure of 6.7 Pa, power of 50 W, and O_2 flow rate of 50 sccm) for 10, 20, and 40 s gradually removes the epoxy from between the particles (Figure 3), as confirmed by the SEM and STEM images. Because the AuNPs mask the underlying areas of epoxy from etching, the resulting structures will resemble mushroom-like shapes, with gradually narrowing epoxy pillars holding the NPs on top. The 3D models of Figure 3 were reconstructed based on the SEM and STEM images. It is also worth mentioning that judging by the cross-sectional STEM images the shape of the AuNPs is closer to flattened disks (resembling red blood cells) than spheres. With such flattened shapes interparticle interactions and coupling are expected to be stronger in the lateral plane compared to spherical NPs.[60]

The successful selective removal of the epoxy from the top and between the particles is also confirmed by XPS measurements, presented in Figure 3. Longer etching times gradually decrease the atomic percentage of oxygen and carbon on the surface (based on the O 1s and C 1s peaks, respectively), while at the same time increasing the atomic percentage of gold (Au 4f peaks). Parallel optical spectrophotometry measurements were done on the same samples (from the B1 line). The normalized absorbance spectra of Figure 4a also confirm the successful removal of the epoxy. The absorbance peak measured in air decreased from the initial 590 nm to 575, 567.5, and 547 nm after 10, 20, and 40 s selective etching, respectively (Figure 4a). The changes in the color of the samples upon etching are visible to the naked eye as well (inset of Figure 4a). As can be seen in Figure 5, this change goes hand in hand with increasing bulk RI sensitivity, from the initial 15 nm RIU^{-1} to around 80 nm RIU^{-1}, for this particular B1 type sample. Because for other applications, like SERS, the position of the LSPR peak alone could be important, it has to be mentioned that by varying the particle size, interparticle distance, and epoxy etching, it was possible to tune the plasmonic peak of the sensors elements between 535 and 625 nm, measured in air.

The best achievable RI sensitivities were found to be 83 ± 3 nm RIU^{-1} for A1, 106 ± 3 nm RIU^{-1} for A2, 97 ± 11 nm

https://dx.doi.org/10.1021/acsami.9b20907
ACS Appl. Mater. Interfaces 2020, 12, 4804−4814

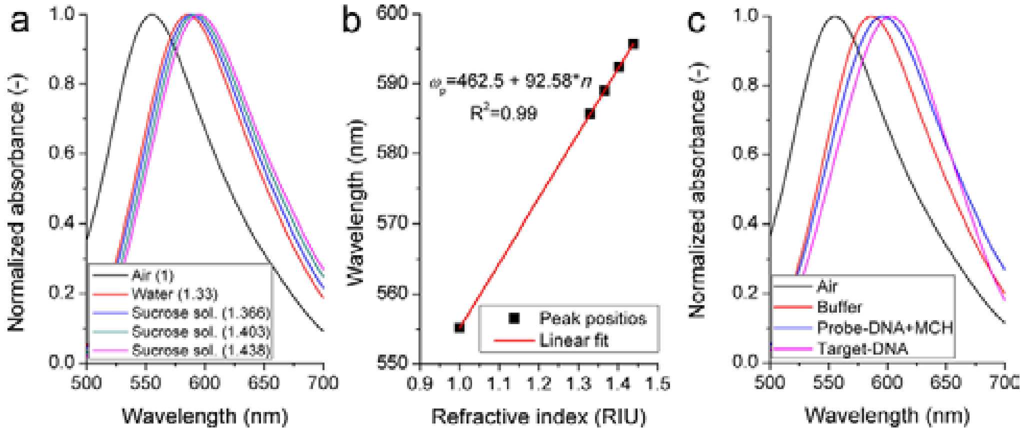

Figure 6. (a) Normalized absorbance spectra of a B3 type nanocomposite sample, measured in different media (sucrose solutions). (b) Linear regression of the LSPR peak maxima shown in (a). (c) Normalized absorbance spectra measured in different phases of probe-DNA immobilization and target-DNA hybridization, measured on a B3 type nanocomposite, by using a 0.75 M NaCl−50 mM Na_2HPO_4 buffer.

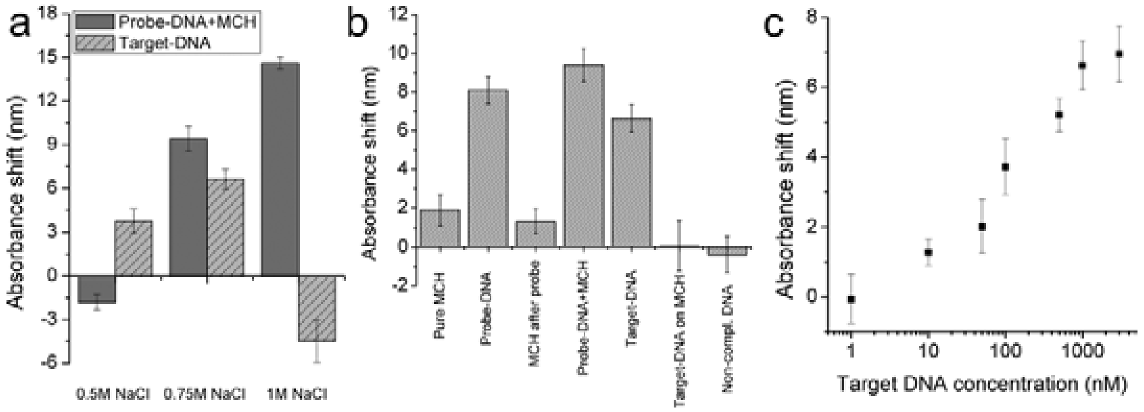

Figure 7. (a) Absolute LSPR absorbance shift measured after DNA immobilization and subsequent DNA hybridization by using buffers with different ionic strengths on the B3 type nanocomposite. (b) Results of control experiments (performed in a buffer with 0.75 M ionic strength, B3 type composite) aiming to distinguish between the signal contribution of MCH and probe-DNA during immobilization and also negative controls with noncomplementary DNA. (c) Calibration curve of the B3 type nanocomposite. All data are an average of 4−5 measurements.

RIU^{-1} for B1, and 96 ± 4 nm RIU^{-1} for the B3 sample, all after 30 s etching time (illustrated in Figures 4b and 4c). It has to be noted that overetching these samples in O_2 plasma could destabilize the AuNP arrangement's integrity by narrowing the epoxy pillars below a critical point, resulting in NP removal during washing, leading to decreased sensitivity. The 30 s O_2 plasma etching always resulted in stable samples, with reproducible spectra and reversible changes after multiple steps of washing and drying. Adhesion tests were also performed on the etched samples, and the NPs could not be removed by the classic Scotch tape method (see Supporting Information S7).

The stability (robustness) and cleanability of the fabricated plasmonic sensors are of outmost importance since before the immobilization of receptor molecules the surface of the gold has to be cleaned sufficiently. For this, this long-term stability of the sensors was tested. Figure 5 shows the absorbance peak maxima (in air and water, Figure 5a) and respective bulk RI sensitivities (Figure 5b) monitored for 27 consecutive days, measured on the same samples as in Figures 3 and 4a. Upon storage at normal office ambient conditions the bulk RI sensitivity of the sensors gradually decreased with the elapsed time, which is not surprising, knowing that the surface of gold can easily be contaminated by numerous ambient agents.[61] Despite the significant drop in sensitivity with time, the samples could be easily regenerated with short, low-power O_2 plasma cleaning (20 W power at 0.4 mbar for 15 s), to retain their initial sensitivities. Other long-term tests performed with multiple cleaning steps demonstrated that the sensors could be effectively cleaned with such low-power O_2 plasma several times (3−5), without any significant drop in sensitivity. The robustness and cleanability of the fabricated sensors elements thus enable their application as LSPR biosensors.

3.3. Detection of DNA Hybridization. To test the fabricated epoxy−Au nanocomposites as LSPR sensors for DNA hybridization detection, a 20 bp long specific sequence from the parasite *Giardia lamblia* (the β-giardin gene) was used. This particular sequence and probe-target DNA pair were extensively tested in a previous work with both an SPR and a capacitive sensor.[49] Here, the exact same probe immobilization and target hybridization protocols were used. For these experiments we only used nanocomposites from the B3 batch. Figures 6a and 6b present bulk refractive index calibration results for one of the samples, performed with a dilution series of sucrose dissolved in water. The LSPR sensor has a linear response in the relevant refractive index range of 1−1.44 RIU, with a bulk RI sensitivity of 92.58 nm RIU^{-1}.

Figure 6c presents the resulting absolute shift of the absorbance spectra after Giardia_probe + MCH immobilization (overnight from 1 μM solution) and the subsequent hybridization with 1 μM Giardia_target for 2 h. The spectra were always measured in the specified running buffer. The shifts are defined between the subsequent phases; for example, probe immobilization is compared to the spectra measured in empty buffer prior immobilization, while the shift caused by hybridization is compared to the spectra measured after immobilization. Buffers with three different ionic strengths were investigated, namely 0.5, 0.75, and 1 M; the resulting absorbance shifts are given in Figure 7a. The first set of experiments were performed in the same buffer which was used in the mentioned reference,[49] namely 0.5 M NaCl−50 mM Na_2HPO_4, pH 6.8. In this buffer a small, but reproducible, blue-shift (1.8 ± 0.5 nm) of the spectra was observed after probe-DNA immobilization and a subsequent 3.8 ± 0.8 nm red-shift after the hybridization with the target-DNA. Although it is known that the presence of DNA on the nanoparticle's surface increases the effective refractive index in the surrounding media and causes a red-shift in absorbance, such a blue-shift upon DNA binding is not entirely unexpected or unprecedented in LSPR systems. Roether et al. also measured a 2−3 nm blue-shift upon DNA immobilization,[39] while others explained their observed blue-shifts with plasmon uncoupling between particles.[13,48] In our nanoparticle arrangement (B3 type) the average interparticle gap between the nanoparticles is around 10 nm, while due to the irregular shape of the particles it can sometimes be below 5 nm in hot spots. Because the length of the Giardia_probe is around 7 nm, it is possible that the repulsion between the negatively charged DNA strands in these gaps causes the particles to shift out of the coupling plane (by slightly bending the epoxy pillars), resulting in plasmonic uncoupling and the observed blue-shift in the spectra. To test this theory, the measurements were repeated in buffers with increased ionic strength (0.75 and 1 M NaCl; both with 50 mm Na_2HPO_4). Higher ionic strength was proven to be effective in decreasing the repulsion between the DNA strands by screening the charges of their sugar−phosphate backbone and thus decreasing their Debye length,[62] resulting in more tightly packed DNA layers.[63] NaCl in high concentration (such as 1 M) is particularly used for this purpose.[64,65]

As can be seen in Figure 7a, in higher ionic buffers the immobilization of Giardia_probe resulted in a red-shifts of 9.4 ± 0.8 and 14.6 ± 0.4 nm in buffers with 0.75 and 1 M ionic strength, respectively. For the 0.75 M buffer the 6.6 ± 0.7 nm red-shift signal resulting from target-DNA hybridization was also significantly higher compared to the 0.5 M buffer. In the case of the buffer with 1 M ionic strength the hybridization resulted in a blue-shift of 4.5 ± 1.5 nm, but this time this can be associated with damaged NP integrity. During the washing step after target-hybridization some AuNPs were visibly washed away from the surface. This phenomenon never happened with buffers of lower ionic strength (and as it was discussed in section 3.2 the nanocomposite was found to be quite robust with stable NPs), while it was reproducible in 1 M ionic strength; thus, it can be accounted for the instability caused by the too tightly packed DNA molecules. This phenomenon is investigated in more detail in Supporting Information S7. Figure 6c presents normalized absorption spectra measured in the 0.75 M buffer, illustrating the 9.4 ± 0.8 nm red-shift upon immobilization of probe (compared to empty buffer) and subsequent 6.6 ± 0.7 nm red-shift upon hybridization with the target.

Figure 7b presents the result of control experiments—all performed in a buffer with 0.75 M ionic strength. The deposition of a pure MCH monolayer resulted in a 1.88 ± 0.8 nm shift, while a pure probe-DNA layer in 8.08 ± 0.7 nm. Adding the MCH after the probe results in a smaller 1.31 ± 0.6 nm shift compared to the pure MCH monolayer. Based on these values, the probe surface density was roughly estimated to be around $(2-5) \times 10^{12}$ molecules cm^{-2} (details of the calculations are presented in the Supporting Information S9). Upon comparison of the signals of probe-DNA (8.08 ± 0.7 nm) and subsequent target-DNA hybridization (6.62 ± 0.7 nm), the signal ratio is around 80%, which corresponds well with the work of Gong et al., who predicted a hybridization efficiency between 70−90% for buffers between 0.33−1 M on a probe coverage between $(2-8) \times 10^{12}$ molecules cm^{-2}.[63]

The calibration curve for a B3 type nanocomposite is presented in Figure 7c. The target-DNA signal starts to saturate around 1 μM concentration, and the characteristic is linear (as a function of a logarithmic target concentration) between 10 nM and 1 μM, mostly consistent with previous works on such SPR/LSPR DNA biosensors.[36,49,66] It has to be noted that the measured variation of the signal (between ±0.3−0.8 nm) originates from the variation between samples/sample areas, since the sample is removed/replaced in the spectrometer in each step of the experiment. By integrating the LSPR chip into a microfluidic setup and monitoring a fixed area constantly, we could significantly reduce these errors. The standard deviation of the blank signal (measured by monitoring the same sensor area in a blank buffer for 10 min) is around 0.1 nm. Based on this, the LOD (defined as the signal from the blank sample plus 3 times the standard deviation of the signal from the blank sample) is around 5 nM. The same probe-target DNA system was measured previously with a commercial SPR instrument, resulting in sub-nanomolar detection limit.[49] However, this detection limit and maximum signal response for a 20 bases long target are comparable and even better than several LSPR sensor solutions which were previously presented for label-free DNA detection.[32,36,37,39]

4. CONCLUSIONS

The fabrication technology and plasmonic sensor application of an AuNP-epoxy based surface nanocomposites were presented. It was extensively demonstrated that with this versatile, nanopatterned template based fabrication technology the large scale production of robust plasmonic sensors with tunable properties is possible. The main advantage of the proposed fabrication technology is the large (several cm^2) surface area, in which the nanoparticle size/distribution is homogeneous and also tunable with the technological properties. Other strengths of the nanocomposite are the stability of the arranged AuNPs on the epoxy pillars in fluidic environments and also their repeated cleanability with reproducible sensitivities. The LSPR sensors were successfully used for the label-free detection of a 20 bp long DNA molecule, making it one of the first NP-polymer surface nanocomposite sensors ever demonstrated for the plasmonic detection of DNA.

■ ASSOCIATED CONTENT

Supporting Information

The Supporting Information is available free of charge at https://pubs.acs.org/doi/10.1021/acsami.9b20907.

S1: solid state dewetting of Au films with various thicknesses on the nanobowled templates; S2: influence of the native aluminum oxide on the morphology of the deposited thin film; S3: influence of the annealing temperature on the resulting NP layers; S4: repeated Au thin film deposition and annealing on the nanobowled templates; S5: thickness estimation of gold thin films; S6: estimation of the nanoparticles' size and distribution; S7: adhesion tests; S8: structural instability after DNA immobilization in high (1 M) ionic strength buffer; S9: assessment of probe-DNA coverage (PDF)

■ AUTHOR INFORMATION

Corresponding Author

Attila Bonyár – *Budapest University of Technology and Economics, Budapest, Hungary;* orcid.org/0000-0002-6976-7846; Email: bonyar@ett.bme.hu

Other Author

Tomáš Lednický – *Brno University of Technology, Brno, Czech Republic*

Complete contact information is available at: https://pubs.acs.org/10.1021/acsami.9b20907

Author Contributions

The manuscript was written through contributions of all authors. All authors have given approval to the final version of the manuscript. The detailed contributions of the authors are the following: Tomáš Lednický: PhD student, developed and optimized the nanocomposite fabrication technology, performed and evaluated SEM, STEM, XPS, and optical spectroscopy measurements, and wrote parts of the paper. Attila Bonyár: PhD, associate professor, coordinated the development of the plasmonic sensor, performed the DNA experiments, performed and evaluated optical spectroscopy measurements, and wrote parts of the paper.

Funding

Part of the work was performed with the support of CEITEC Nano Research Infrastructure (ID LM2015041, MEYS CR, 2016–2019), CEITEC Brno University of Technology. The research reported in this paper was partially supported by the Higher Education Excellence Program of the Ministry of Human Capacities in the frame of Nanotechnology and Materials Science (BME FIKP-NAT) and also Biotechnology (BME-FIKP-BIO) research areas of Budapest University of Technology and Economics. Tomáš Lednický acknowledges the financial support of GACR Project GA16-11140S from the Czech Republic. The support of the Hungarian Electronic Information Service National Programme (EISZ) is also acknowledged.

Notes

The authors declare no competing financial interest.

■ ACKNOWLEDGMENTS

Attila Bonyár is grateful for the support of the János Bolyai Research Scholarship of the Hungarian Academy of Sciences. We thank Jan Michalička (CEITEC BUT) for lamella preparation and TEM/STEM/EDS analysis.

■ REFERENCES

(1) Liedberg, B.; Nylander, C.; Lunström, I. Surface Plasmon Resonance for Gas Detection and Biosensing. *Sens. Actuators* **1983**, *4* (C), 299–304.

(2) Nguyen, H.; Park, J.; Kang, S.; Kim, M. Surface Plasmon Resonance: A Versatile Technique for Biosensor Applications. *Sensors* **2015**, *15* (5), 10481–10510.

(3) Homola, J. Surface Plasmon Resonance Sensors for Detection of Chemical and Biological Species. *Chem. Rev.* **2008**, *108* (2), 462–493.

(4) Wong, C. L.; Olivo, M. Surface Plasmon Resonance Imaging Sensors: A Review. *Plasmonics* **2014**, *9* (4), 809–824.

(5) Chinowsky, T. M.; Quinn, J. G.; Bartholomew, D. U.; Kaiser, R.; Elkind, J. L. Performance of the Spreeta 2000 Integrated Surface Plasmon Resonance Affinity Sensor. *Sens. Actuators, B* **2003**, *91* (1–3), 266–274.

(6) Chinowsky, T. M.; Soelberg, S. D.; Baker, P.; Swanson, N. R.; Kauffman, P.; Mactutis, A.; Grow, M. S.; Atmar, R.; Yee, S. S.; Furlong, C. E. Portable 24-Analyte Surface Plasmon Resonance Instruments for Rapid, Versatile Biodetection. *Biosens. Bioelectron.* **2007**, *22* (9–10), 2268–2275.

(7) Naimushin, A. N.; Soelberg, S. D.; Bartholomew, D. U.; Elkind, J. L.; Furlong, C. E. A Portable Surface Plasmon Resonance (SPR) Sensor System with Temperature Regulation. *Sens. Actuators, B* **2003**, *96* (1–2), 253–260.

(8) Feltis, B. N.; Sexton, B. A.; Glenn, F. L.; Best, M. J.; Wilkins, M.; Davis, T. J. A Hand-Held Surface Plasmon Resonance Biosensor for the Detection of Ricin and Other Biological Agents. *Biosens. Bioelectron.* **2008**, *23* (7), 1131–1136.

(9) *Nanoplasmonic Sensors*; Dmitriev, A., Ed.; Springer: New York, 2012.

(10) Sepúlveda, B.; Angelomé, P. C.; Lechuga, L. M.; Liz-Marzán, L. M. LSPR-Based Nanobiosensors. *Nano Today* **2009**, *4* (3), 244–251.

(11) Ruemmele, J. A.; Hall, W. P.; Ruvuna, L. K.; Van Duyne, R. P. A Localized Surface Plasmon Resonance Imaging Instrument for Multiplexed Biosensing. *Anal. Chem.* **2013**, *85* (9), 4560–4566.

(12) Raphael, M. P.; Christodoulides, J. A.; Delehanty, J. B.; Long, J. P.; Pehrsson, P. E.; Byers, J. M. Quantitative LSPR Imaging for Biosensing with Single Nanostructure Resolution. *Biophys. J.* **2013**, *104* (1), 30–36.

(13) Liu, J.; He, H.; Xiao, D.; Yin, S.; Ji, W.; Jiang, S.; Luo, D.; Wang, B.; Liu, Y. Recent Advances of Plasmonic Nanoparticles and Their Applications. *Materials* **2018**, *11* (10), 1833.

(14) Lopez, G. A.; Estevez, M.-C.; Soler, M.; Lechuga, L. M. Recent Advances in Nanoplasmonic Biosensors: Applications and Lab-on-a-Chip Integration. *Nanophotonics* **2017**, *6* (1), 123–136.

(15) Jiang, J.; Wang, X.; Li, S.; Ding, F.; Li, N.; Meng, S.; Li, R.; Qi, J.; Liu, Q.; Liu, G. L. Plasmonic Nano-Arrays for Ultrasensitive Bio-Sensing. *Nanophotonics* **2018**, *7* (9), 1517–1531.

(16) Tu, M. H.; Sun, T.; Grattan, K. T. V. LSPR Optical Fibre Sensors Based on Hollow Gold Nanostructures. *Sens. Actuators, B* **2014**, *191*, 37–44.

(17) Svedendahl, M.; Chen, S.; Dmitriev, A.; Käll, M. Refractometric Sensing Using Propagating versus Localized Surface Plasmons: A Direct Comparison. *Nano Lett.* **2009**, *9* (12), 4428–4433.

(18) Kabashin, A. V.; Evans, P.; Pastkovsky, S.; Hendren, W.; Wurtz, G. A.; Atkinson, R.; Pollard, R.; Podolskiy, V. A.; Zayats, A. V. Plasmonic Nanorod Metamaterials for Biosensing. *Nat. Mater.* **2009**, *8* (11), 867–871.

(19) Xu, H.; Käll, M. Modeling the Optical Response of Nanoparticle-Based Surface Plasmon Resonance Sensors. *Sens. Actuators, B* **2002**, *87* (2), 244–249.

(20) Chen, H.; Kou, X.; Yang, Z.; Ni, W.; Wang, J. Shape- and Size-Dependent Refractive Index Sensitivity of Gold Nanoparticles. *Langmuir* **2008**, *24* (10), 5233–5237.

(21) Saison-Francioso, O.; Lévêque, G.; Boukherroub, R.; Szunerits, S.; Akjouj, A. Dependence between the Refractive-Index Sensitivity of

Metallic Nanoparticles and the Spectral Position of Their Localized Surface Plasmon Band: A Numerical and Analytical Study. *J. Phys. Chem. C* **2015**, *119* (51), 28551−28559.

(22) Martinsson, E.; Sepulveda, B.; Chen, P.; Elfwing, A.; Liedberg, B.; Aili, D. Optimizing the Refractive Index Sensitivity of Plasmonically Coupled Gold Nanoparticles. *Plasmonics* **2014**, *9* (4), 773−780.

(23) Hooshmand, N.; Bordley, J. A.; El-Sayed, M. A. The Sensitivity of the Distance Dependent Plasmonic Coupling between Two Nanocubes to Their Orientation: Edge-to-Edge versus Face-to-Face. *J. Phys. Chem. C* **2016**, *120* (8), 4564−4570.

(24) Chen, Y. Nanofabrication by Electron Beam Lithography and Its Applications: A Review. *Microelectron. Eng.* **2015**, *135*, 57−72.

(25) Zhu, S.; Zhou, W. Plasmonic Properties of Two-Dimensional Metallic Nanoholes Fabricated by Focused Ion Beam Lithography. *J. Nanopart. Res.* **2012**, *14* (3), 652.

(26) Kaye, S.; Zeng, Z.; Sanders, M.; Chittur, K.; Koelle, P. M.; Lindquist, R.; Manne, U.; Lin, Y.; Wei, J. Label-Free Detection of DNA Hybridization with a Compact LSPR-Based Fiber-Optic Sensor. *Analyst* **2017**, *142* (11), 1974−1981.

(27) Yu, C.-C.; Chen, H.-L. Nanoimprint Technology for Patterning Functional Materials and Its Applications. *Microelectron. Eng.* **2015**, *132*, 98−119.

(28) Su, H.; Cheng, X. R.; Endo, T.; Kerman, K. Photonic Crystals on Copolymer Film for Label-Free Detection of DNA Hybridization. *Biosens. Bioelectron.* **2018**, *103*, 158−162.

(29) Krishnamoorthy, S.; Krishnan, S.; Thoniyot, P.; Low, H. Y. Inherently Reproducible Fabrication of Plasmonic Nanoparticle Arrays for SERS by Combining Nanoimprint and Copolymer Lithography. *ACS Appl. Mater. Interfaces* **2011**, *3* (4), 1033−1040.

(30) Dickreuter, S.; Gleixner, J.; Kolloch, A.; Boneberg, J.; Scheer, E.; Leiderer, P. Mapping of Plasmonic Resonances in Nanotriangles. *Beilstein J. Nanotechnol.* **2013**, *4* (1), 588−602.

(31) Stakenborg, T.; Lagae, L. Gold Nanoring as a Sensitive Plasmonic Biosensor for On-Chip DNA Detection. *Appl. Phys. Lett.* **2012**, *100* (17), 173114.

(32) Qi, X.; Bi, J. Plasmonic Sensors Relying on Nanoparticle Arrays Created by a Template-Directed Dewetting Process. *Opt. Commun.* **2019**, *453*, 124328.

(33) Nguyen, D. T.; Kim, D.-J.; Kim, K.-S. Controlled Synthesis and Biomolecular Probe Application of Gold Nanoparticles. *Micron* **2011**, *42* (3), 207−227.

(34) Cant, N. E.; Critchley, K.; Zhang, H.-L.; Evans, S. D. Surface Functionalisation for the Self-Assembly of Nanoparticle/Polymer Multilayer Films. *Thin Solid Films* **2003**, *426* (1−2), 31−39.

(35) Magura, J.; Zeleňáková, A.; Zeleňák, V.; Kaňuchová, M. Thiol-Modified Gold Nanoparticles Deposited on Silica Support Using Dip Coating. *Appl. Surf. Sci.* **2014**, *315* (1), 392−399.

(36) Schneider, T.; Jahr, N.; Jatschka, J.; Csaki, A.; Stranik, O.; Fritzsche, W. Localized Surface Plasmon Resonance (LSPR) Study of DNA Hybridization at Single Nanoparticle Transducers. *J. Nanopart. Res.* **2013**, *15* (4), 1531.

(37) Thamm, S.; Csàki, A.; Fritzsche, W. LSPR Detection of Nucleic Acids on Nanoparticle Monolayers. *Methods Mol. Biol.* **2018**, *1811*, 163−171.

(38) Bonyár, A.; Csarnovics, I.; Veres, M.; Himics, L.; Csik, A.; Kámán, J.; Balázs, L.; Kökényesi, S. Investigation of the Performance of Thermally Generated Gold Nanoislands for LSPR and SERS Applications. *Sens. Actuators, B* **2018**, *255*, 433−439.

(39) Roether, J.; Chu, K.-Y.; Willenbacher, N.; Shen, A. Q.; Bhalla, N. Real-Time Monitoring of DNA Immobilization and Detection of DNA Polymerase Activity by a Microfluidic Nanoplasmonic Platform. *Biosens. Bioelectron.* **2019**, *142*, 111528.

(40) Bhalla, N.; Sathish, S.; Galvin, C. J.; Campbell, R. A.; Sinha, A.; Shen, A. Q. Plasma-Assisted Large-Scale Nanoassembly of Metal−Insulator Bioplasmonic Mushrooms. *ACS Appl. Mater. Interfaces* **2018**, *10* (1), 219−226.

(41) Gartia, M. R.; Hsiao, A.; Pokhriyal, A.; Seo, S.; Kulsharova, G.; Cunningham, B. T.; Bond, T. C.; Liu, G. L. Colorimetric Plasmon Resonance Imaging Using Nano Lycurgus Cup Arrays. *Adv. Opt. Mater.* **2013**, *1* (1), 68−76.

(42) Zhu, S.; Li, H.; Yang, M.; Pang, S. W. Label-Free Detection of Live Cancer Cells and DNA Hybridization Using 3D Multilayered Plasmonic Biosensor. *Nanotechnology* **2018**, *29* (36), 365503.

(43) Ozaki, Y.; Kneipp, K.; Aroca, R. *Frontiers of Surface-Enhanced Raman Scattering*; Ozaki, Y., Kneipp, K., Aroca, R., Eds.; John Wiley & Sons, Ltd.: Chichester, UK, 2014; Vol. *9781118359*.

(44) Israelsen, N. D.; Hanson, C.; Vargis, E. Nanoparticle Properties and Synthesis Effects on Surface-Enhanced Raman Scattering Enhancement Factor: An Introduction. *Sci. World J.* **2015**, *2015*, 1−12.

(45) Jin, H. M.; Kim, J. Y.; Heo, M.; Jeong, S.-J.; Kim, B. H.; Cha, S. K.; Han, K. H.; Kim, J. H.; Yang, G. G.; Shin, J.; Kim, S. O. Ultralarge Area Sub-10 Nm Plasmonic Nanogap Array by Block Copolymer Self-Assembly for Reliable High-Sensitivity SERS. *ACS Appl. Mater. Interfaces* **2018**, *10* (51), 44660−44667.

(46) Badilescu, S.; Prakash, J.; Packirisamy, M. Surface Gold and Silver-Polymer Nanocomposite Self-Standing Films. In *Handbook of Polymer and Ceramic Nanotechnology*; Springer International Publishing: Cham, 2019; pp 1−20.

(47) SadAbadi, H.; Badilescu, S.; Packirisamy, M.; Wüthrich, R. Integration of Gold Nanoparticles in PDMS Microfluidics for Lab-on-a-Chip Plasmonic Biosensing of Growth Hormones. *Biosens. Bioelectron.* **2013**, *44* (1), 77−84.

(48) Scarano, S.; Berlangieri, C.; Carretti, E.; Dei, L.; Minunni, M. Tunable Growth of Gold Nanostructures at a PDMS Surface to Obtain Plasmon Rulers with Enhanced Optical Features. *Microchim. Acta* **2017**, *184* (9), 3093−3102.

(49) Spiga, F. M.; Bonyár, A.; Ring, B.; Onofri, M.; Vinelli, A.; Sántha, H.; Guiducci, C.; Zuccheri, G. Hybridization Chain Reaction Performed on a Metal Surface as a Means of Signal Amplification in SPR and Electrochemical Biosensors. *Biosens. Bioelectron.* **2014**, *54*, 102−108.

(50) Guy, R. A.; Xiao, C.; Horgen, P. A. Real-Time PCR Assay for Detection and Genotype Differentiation of Giardia Lamblia in Stool Specimens. *J. Clin. Microbiol.* **2004**, *42* (7), 3317−3320.

(51) Fan, X.; Hao, Q.; Jin, R.; Huang, H.; Luo, Z.; Yang, X.; Chen, Y.; Han, X.; Sun, M.; Jing, Q.; Dong, Z.; Qiu, T. Assembly of Gold Nanoparticles into Aluminum Nanobowl Array. *Sci. Rep.* **2017**, *7* (1), 2322.

(52) Bonyár, A.; Lednický, T.; Hubálek, J. LSPR Nanosensors with Highly Ordered Gold Nanoparticles Fabricated on Nanodimpled Aluminium Templates. *Procedia Eng.* **2016**, *168*, 1160−1163.

(53) Ikeda, H.; Iwai, M.; Nakajima, D.; Kikuchi, T.; Natsui, S.; Sakaguchi, N.; Suzuki, R. O. Nanostructural Characterization of Ordered Gold Particle Arrays Fabricated via Aluminum Anodizing, Sputter Coating, and Dewetting. *Appl. Surf. Sci.* **2019**, *465*, 747−753.

(54) Lee, W.; Park, S.-J. Porous Anodic Aluminum Oxide: Anodization and Templated Synthesis of Functional Nanostructures. *Chem. Rev.* **2014**, *114* (15), 7487−7556.

(55) Yang, S.; Xu, F.; Ostendorp, S.; Wilde, G.; Zhao, H.; Lei, Y. Template-Confined Dewetting Process to Surface Nanopatterns: Fabrication, Structural Tunability, and Structure-Related Properties. *Adv. Funct. Mater.* **2011**, *21* (13), 2446−2455.

(56) Müller, C. M.; Mornaghini, F. C. F.; Spolenak, R. Ordered Arrays of Faceted Gold Nanoparticles Obtained by Dewetting and Nanosphere Lithography. *Nanotechnology* **2008**, *19* (48), 485306.

(57) Hao, Q.; Huang, H.; Fan, X.; Yin, Y.; Wang, J.; Li, W.; Qiu, T.; Ma, L.; Chu, P. K.; Schmidt, O. G. Controlled Patterning of Plasmonic Dimers by Using an Ultrathin Nanoporous Alumina Membrane as a Shadow Mask. *ACS Appl. Mater. Interfaces* **2017**, *9* (41), 36199−36205.

(58) Kang, M.; Park, S.-G.; Jeong, K.-H. Repeated Solid-State Dewetting of Thin Gold Films for Nanogap-Rich Plasmonic Nanoislands. *Sci. Rep.* **2015**, *5* (1), 14790.

(59) Bae, Y. M.; Jin, S. O.; Kim, I.; Shin, K. Y.; Heo, D.; Kang, D.-G. Detection of Biomarkers Using LSPR Substrate with Gold Nanoparticle Array. *J. Nanomater.* **2015**, *2015*, 1−6.

(60) Kravets, V. G.; Kabashin, A. V.; Barnes, W. L.; Grigorenko, A. N. Plasmonic Surface Lattice Resonances: A Review of Properties and Applications. *Chem. Rev.* **2018**, *118* (12), 5912−5951.

(61) Fischer, L. M.; Tenje, M.; Heiskanen, A. R.; Masuda, N.; Castillo, J.; Bentien, A.; Émneus, J.; Jakobsen, M. H.; Boisen, A. Gold Cleaning Methods for Electrochemical Detection Applications. *Microelectron. Eng.* **2009**, *86* (4−6), 1282−1285.

(62) Hsieh, C. C.; Balducci, A.; Doyle, P. S. Ionic Effects on the Equilibrium Dynamics of DNA Confined in Nanoslits. *Nano Lett.* **2008**, *8* (6), 1683−1688.

(63) Gong, P.; Levicky, R. DNA Surface Hybridization Regimes. *Proc. Natl. Acad. Sci. U. S. A.* **2008**, *105* (14), 5301−5306.

(64) Zhang, X.; Servos, M. R.; Liu, J. Surface Science of DNA Adsorption onto Citrate-Capped Gold Nanoparticles. *Langmuir* **2012**, *28* (8), 3896−3902.

(65) Jia, S.; Bian, C.; Sun, J.; Tong, J.; Xia, S. A Wavelength-Modulated Localized Surface Plasmon Resonance (LSPR) Optical Fiber Sensor for Sensitive Detection of Mercury(II) Ion by Gold Nanoparticles-DNA Conjugates. *Biosens. Bioelectron.* **2018**, *114*, 15−21.

(66) Drozd, M.; Pietrzak, M. D.; Malinowska, E. SPRi-Based Biosensing Platforms for Detection of Specific DNA Sequences Using Thiolate and Dithiocarbamate Assemblies. *Front. Chem.* **2018**, *6*, 173.

C LIST OF AUTHOR’S SCIENTIFIC ACHIEVEMENTS

Author’s scientific identifiers

Researcher ID:	AAE-6679-2020
ORCID ID:	0000-0003-0564-1862
SCOPUS ID:	57188768803

C.1 Publications in impact journals

1. **Lednický, T.**; Bonyár, A. ‘Large Scale Fabrication of Ordered Gold Nanoparticle-Epoxy Surface Nanocomposites and Their Application as Label-Free Plasmonic DNA Biosensors’ *ACS Applied Materials and Interfaces*, vol. 12, no. 4, 2020, pp. 4804–4814. doi:10.1021/acsami.9b20907.

   ISSN 1944-8244. Impact factor (2019): 8.758.

   My contribution: fabrication of samples, design of experiments, sample preparation, measurements and evaluation of experiments (except detection of DNA hybridization), partially writing the manuscript.

2. Simunkova, H.; **Lednický, T.**; Whitehead, A.H.; Kalina, L.; Simunek, P.; Hubalek, J. ‘Tantalum-based nanotube arrays via porous-alumina-assisted electrodeposition from ionic liquid: Formation and electrical characterization’, *Applied Surface Science*, vol. 548, no. 9, 2021, pp. 149264. doi:10.1016/j.apsusc.2021.149264.

   ISSN 0169-4332. Impact factor (2019): 6.182.

   My contribution: SEM measurements and design of experiments, revision of the manuscript.

3. Vallejos Vargas, S.; Grácia, I.; **Lednický, T.**; Vojkůvka, L.; Figueras, E.; Hubálek, J.; Cané, C. ‘Highly hydrogen sensitive micromachined sensors based on aerosol-assisted chemical vapor deposited ZnO rods’, *Sensors and Actuators B: Chemical*, vol. 268, 2018, pp. 15–21. doi:10.1016/j.snb.2018.04.033.

   ISSN 0925-4005. Impact factor (2019): 7.100.

   My contribution: XPS measurements and design of experiments, revision of the manuscript.

4. Bendová, M.; Kolář, J.; Márik, M.; **Lednický, T.**; Mozalev, A. ‘Influence of nitrogen species on the porous-alumina-assisted growth of TiO_2 nanocolumn arrays.’,

Electrochimica Acta, vol. 281, no. 1, 2018, pp. 796–809. doi:10.1016/j.electacta.2018.05.197.

ISSN 0013-4686. Impact factor (2019): 6.215.

My contribution: XPS analyses and the manuscript revision.

5. Bezdekova, J.; Vlcnovska, M.; Zemankova, K.; Bacova, R.; Kolackova, M.; **Lednický, T.**; Pribyl, J.; Richtera, L.; Vanickova, L.; Adam, V.; Vaculovicova, 'Molecularly imprinted polymers and capillary electrophoresis for sensing phytoestrogens in milk', *Journal of Dairy Science*, vol. 103, no. 6, 2020, pp. 4941–4950, doi:10.3168/jds.2019-17367.

   ISSN 0022-0302. Impact factor (2019): 3.333.

   My contribution: XPS measurements, minor manuscript revision.

C.2 Contributions to conference proceedings indexed in WoS or Scopus

1. Zangana, S.; **Lednický, T.**; Rigó, I.; Csarnovics, I.; Veres, M.; Bonyár, A. 'Surface-Enhanced Raman Spectroscopy Investigation of DNA Molecules on Gold/Epoxy Nanocomposite Substrates', *IEEE 26th International Symposium for Design and Technology in Electronic Packaging (SIITME)*, 21–24 October 2020, ISSN: 2642-7036, doi:10.1109/SIITME50350.2020.9292267.

2. **Lednický, T.**; Mozalev, A.; Bendová, M. 'Electrochemical characterization of pure and nitrogen- containing anodic TiO_2 nanocolumn arrays', *8th International Conference on Nanomaterials - Research and Application (NANOCON2016)*, 2017, pp. 669–674, ISBN: 978-80-87294-71-0.

3. Bonyár, A.; **Lednický, T.**; Hubálek, J. 'LSPR Nanosensors with Highly Ordered Gold Nanoparticles Fabricated on Nanodimpled Aluminium Templates', *Procedia Engineering*, vol. 168, 2016, pp. 1160–1163, doi:10.1016/j.proeng.2016.11.390.

4. **Lednický, T.**; Mozalev, A. 'Optimization of Self-organized Growth of Nanoporous Anodic Alumina Templates for Capacitor Application.', *NANOCON 2015: 7th International Conference on Nanomaterials - Research and Application*, 2015, pp. 265–269, ISBN: 978-80-87294-59-8.

C.3 Contributions to conference proceedings and meetings

1. **Lednický, T.**; Plichta, T.; Fohlerová, Z.; Bonyár, A. ‘PDMS degradation detection by LSPR of embedded AuNPs array’, *18th International Conference on Thin Films & 18th Joint Vacuum Conference*, 22–26 November 2020.

2. **Lednický, T.**; Bonyár, A.; ‘Highly-ordered gold nanoparticles surface fabrication for localized surface plasmon resonance sensors’, *Curie - Pasteur - CEITEC joint young scientist retreat*, 2017, p. 73.

3. **Lednický, T.**; Bonyár, A.; ‘Highly-ordered gold nanoparticle surfaces for localized surface plasmon resonance sensors’, *CEITEC PhD Retreat II. Book of abstracts*, 2017, p. 90, ISBN: 978-80-210-8550-3.

4. **Lednický, T.**; Mozalev, A.; Bendová, M. ‘Electro- and Photoelectrochemistry on TiO_2-based Nanorod Arrays via Anodizing Al/Ti and Al/TiN_x Layers’, *21st Topical Meeting of the International Society of Electrochemistry; Photoelectrochemistry of semiconductors at the nanoscale: from fundamental aspects to practical applications. International Society of Electrochemistry*, 2017, p. 117.

5. **Lednický, T.**; Mozalev, A.; Bendová, M. ‘TiO_2-based Nanocolumn Arrays for Photoelectrochemical Water Splitting: Electrochemical Characterization’, *International Conference on Advances in Semiconductors and Catalysts for Photoelectrochemical Fuel Production (SolarFuel16)*, 2016.

6. Kynclová, H.; **Lednický, T.**; Hrdý, R.; Prášek, J.; Hubálek, J. ‘Gold nanostructured surfaces based on alumina template.’, *In XVI. Workshop of Physical Chemists and Electrochemists*, 2016, pp. 101–103, ISBN: 978-80-210-8267-0.

7. **Lednický, T.** ‘Solid-state synthesis of gold nanoparticles films for spectroscopic measurement enhancement’, *In XVI. Workshop of Physical Chemists and Electrochemists*, 2016, pp. 104–107, ISBN: 978-80-210-8267-0.

8. **Lednický, T.** ‘Solid-state Synthesis of Gold Nanoparticles on Dimpled Aluminum Surfaces and Their Transfer to Transparent Substrates’, *Proceedings of the 22nd Conference STUDENT EEICT 2016*, 2016, pp. 670–674, ISBN: 978-80-214-5350-0.

9. **Lednický, T.**; Mozalev, A. ‘On the growth behavior of nanoporous anodic films on aluminium in citric acid electrolytes’, *In Proceedings of the International Con-*

ference on Advances in Electronic and Photonic Technologies (ADEPT 2015), 2015, pp. 202–205, ISBN: 978-80-554-1033-3.

10. **Lednický, T.**; Mozalev, A. ‘On the anodizing behaviour of aluminium in citric acid Electrolytes’, *XV. Workshop of Physical Chemists and Electrochemists*, 2015, pp. 111–114, ISBN: 978-80-210-7857.

11. **Lednický, T.**; Mozalev, A. ‘Effect of pretreatment parameters on the anodizing behaviour of Al foils in citric acid electrolytes’, *In CEITEC PhD Retreat, 23-24 April 2015, Valtice, Czech Republic*, 2015, p. 100, ISBN: 978-80-210-7825-3.

12. Kynclová, H.; Majzlíková, P.; Prášek, J.; **Lednický, T.**; Hrdý, R.; Hubálek, J. ‘Production and study of nanoporous alumina membranes by electrochemical methods’, *47th Heyrovsky Discussion on Electrochemistry of Organic and Bioactive Compounds*, 2014, p. 36, ISBN: 978-80-87351-29-1.